Lecture Notes in Computational Vision and Biomechanics 22

Fei Gao
Kuangyu Shi
Shuo Li *Editors*

Computational Methods for Molecular Imaging

Springer

Lecture Notes in Computational Vision and Biomechanics

Volume 22

The research related to the analysis of living structures (Biomechanics) has been a source of recent research in several distinct areas of science, for example, Mathematics, Mechanical Engineering, Physics, Informatics, Medicine and Sport. However, for its successful achievement, numerous research topics should be considered, such as image processing and analysis, geometric and numerical modelling, biomechanics, experimental analysis, mechanobiology and enhanced visualization, and their application to real cases must be developed and more investigation is needed. Additionally, enhanced hardware solutions and less invasive devices are demanded.

On the other hand, Image Analysis (Computational Vision) is used for the extraction of high level information from static images or dynamic image sequences. Examples of applications involving image analysis can be the study of motion of structures from image sequences, shape reconstruction from images, and medical diagnosis. As a multidisciplinary area, Computational Vision considers techniques and methods from other disciplines, such as Artificial Intelligence, Signal Processing, Mathematics, Physics and Informatics. Despite the many research projects in this area, more robust and efficient methods of Computational Imaging are still demanded in many application domains in Medicine, and their validation in real scenarios is matter of urgency.

These two important and predominant branches of Science are increasingly considered to be strongly connected and related. Hence, the main goal of the LNCV&B book series consists of the provision of a comprehensive forum for discussion on the current state-of-the-art in these fields by emphasizing their connection. The book series covers (but is not limited to):

- Applications of Computational Vision and Biomechanics
- Biometrics and Biomedical Pattern Analysis
- Cellular Imaging and Cellular Mechanics
- Clinical Biomechanics
- Computational Bioimaging and Visualization
- Computational Biology in Biomedical Imaging
- Development of Biomechanical Devices
- Device and Technique Development for Biomedical Imaging
- Digital Geometry Algorithms for Computational Vision and Visualization
- Experimental Biomechanics
- Gait & Posture Mechanics
- Multiscale Analysis in Biomechanics
- Neuromuscular Biomechanics
- Numerical Methods for Living Tissues
- Numerical Simulation
- Software Development on Computational Vision and Biomechanics
- Grid and High Performance Computing for Computational Vision and Biomechanics
- Image-based Geometric Modeling and Mesh Generation
- Image Processing and Analysis
- Image Processing and Visualization in Biofluids
- Image Understanding
- Material Models
- Mechanobiology
- Medical Image Analysis
- Molecular Mechanics
- Multi-Modal Image Systems
- Multiscale Biosensors in Biomedical Imaging
- Multiscale Devices and Biomems for Biomedical Imaging
- Musculoskeletal Biomechanics
- Sport Biomechanics
- Virtual Reality in Biomechanics
- Vision Systems

More information about this series at http://www.springer.com/series/8910

Fei Gao · Kuangyu Shi · Shuo Li
Editors

Computational Methods for Molecular Imaging

Springer

Editors
Fei Gao
Siemens Medical Solutions
Knoxville, TN
USA

Kuangyu Shi
Department of Radiotherapy and Radiooncology
Technical University of Munich
München
Germany

Shuo Li
GE Healthcare
University of Western Ontario
London, ON
Canada

ISSN 2212-9391 ISSN 2212-9413 (electronic)
Lecture Notes in Computational Vision and Biomechanics
ISBN 978-3-319-18430-2 ISBN 978-3-319-18431-9 (eBook)
DOI 10.1007/978-3-319-18431-9

Library of Congress Control Number: 2015939665

Springer Cham Heidelberg New York Dordrecht London

Printed on acid-free paper

Springer International Publishing AG Switzerland is part of Springer Science+Business Media (www.springer.com)

Contents

Part I
Computational Methods

Computational Methods for Molecular Imaging

Fei Gao and Pengcheng Shi

Abstract Molecular imaging is a new research discipline enabling the visualization, characterization and quantification of biologic processes taking place at the cellular and subcellular levels within intact living subjects. Applications of molecular imaging techniques will benefit various clinical practices including classification and tracking of chemotherapy and treatment planning of radiotherapy, as well as drug discovery and development. Molecular imaging typically includes two or three dimensional imaging with quantification over time, and is often applied on molecular imaging modalities, such as Positron Emission Tomography (PET), and Single Photon Emission Computed Tomography (SPECT). Computational methods serve as an essential part in molecular imaging. Various computational methods are developed to accelerate image processing, identify underlying diseases hidden in the image volumes, evaluate the effectiveness of drug and radiotherapy etc. Computational methods for molecular imaging are in a fast growing field and full of potentials and challenges, and related topics have attracted many researchers from both academia and industry. This book covers the selected topics in computational methods for molecular imaging. As the start, this review provides a brief introduction to the current status of computational methods for molecular imaging and their applications.

Keywords Computational methods · Molecular imaging · Positron emission tomography (PET) · Clinical applications

1 Introduction to Molecular Imaging

Molecular imaging provides the images of molecular and cellular level activities inside the body. Molecular imaging enables doctors to measure the biological processes quantitatively and reflects the functionality of organs and tissues inside

F. Gao · P. Shi (✉)
Rochester Institute of Technology, 102 Lomb Memorial Drive,
Rochester, NY 14623-5608, USA
e-mail: pengcheng.shi@rit.edu

F. Gao et al. (eds.), *Computational Methods for Molecular Imaging*,
Lecture Notes in Computational Vision and Biomechanics 22,
DOI 10.1007/978-3-319-18431-9_1

patients. According to the definition from the Society of Nuclear Medicine and Molecular Imaging (SNMMI), molecular imaging is the visualization, characterization, and measurement of biological processes at the molecular and cellular levels in humans and other living systems [52]. Molecular imaging is a noninvasive procedure and can be used to study and diagnose cancer, brain diseases and disorders, cardiology, and various disorders in different organs and tissues. Major molecular imaging modalities are Positron Emission Tomography (PET) and Single Photon Emission Computed Tomography (SPECT), furthermore, hybrid modalities, i.e. hybrid PET/CT [73], PET/MRI [64], PET/SPECT/CT [50] significantly enrich the ability of molecular imaging.

PET as a biomedical research technique and clinical diagnostic procedure is one of the most important part in nuclear medical imaging devices. In the past three decades, there have been significant advancements in PET scanners and image processing methods [4, 75, 77]. Currently, PET scans are most commonly used to detect cancer, heart problems, brain disorders and other central nervous system disorders. PET scan can be used to track the spread of disease inside body and patient response to drugs and therapies, which help to determine the more effective treatment plans for individual patient. PET scans can also be used to follow-up and manage ongoing cares. Quantitative dynamic PET imaging also offers good promise for personalized drug treatment by accurate pharmacokinetic analysis and will enable medicine to be tailored to each person's needs, and improve the safety, quality and effectiveness of healthcare for every patient.

PET scans rely on the injected radiotracers which circulate inside the body. Different radiotracers will reveal different diseases. Besides ^{18}F-FDG, which is widely used for cancer diagnosis, cardiology, neurology, there are many other radiotracers used in research and clinical applications, for example, ^{18}F-FLT (3′-fluoro-3′-deoxy-l-thymidine) is developed to image tumor cell proliferation [12], ^{11}C-acetate is developed to localize prostate cancer [57], ^{13}N-ammonia is developed to quantify the myocardial blood flow [46], ^{11}C-dihydrotetrabenazine (DTBZ) is developed for brain imaging, which can be used for differentiating Alzheimer's disease from dementia and Parkinson's disease [45]. Labeling drugs with various biomarkers is always a hot topic for pharmaceutical studies, where critical quantitative information can be generated by using dynamic PET imaging.

SPECT scan uses a gamma camera that rotates around the patient to detect the radiotracer inside body. SPECT will also produce a set of 3D images but generally have a lower resolution. The radiotracers commonly used for SPECT scan include ^{99m}Tc [54], ^{188}Re [39], ^{68}Ga [84], ^{82}Rb [24], etc. Electrocardiography (ECG)-Gated ^{82}Rb can also be used for myocardial perfusion PET [6]. Hybrid SPECT/CT is also designed to provide more accurate anatomical and functional information [71]. SPECT scan differs from PET scan in that the tracer stays in your blood stream rather than being absorbed by surrounding tissues, therefore, SPECT scan can show how blood flows to the heart and brain are effective or not. SPECT scan is cheaper and more readily available than higher resolution PET scan. Tests have shown that SPECT scan might be more sensitive to brain injury than either MRI or CT scanning because it can

detect reduced blood flow to injured sites. SPECT scan is also useful for presurgical evaluation of medically uncontrolled seizures and diagnosing stress fractures in the spine (spondylolysis), blood deprived (ischemic) areas of brain following a stroke, and tumors [5, 9].

2 Computational Methods for Molecular Imaging

Computational methods play a critical role in the development of molecular imaging, from image synthesis to data analysis and from clinical diagnosis to therapy individualization. They continuously deepen the visualization depth, enhance the imaging resolution, extend the molecular scope and improve the precision. The applications of computational methods can be in both generating images and understanding images, with the aim to improve the accuracy and efficiency. This section will provide a brief introduction to computational methods for molecular imaging within our topic coverage.

2.1 Data Correction and Image Reconstruction

The first step of all processing is to generate the image from raw data, which includes but not limit to data correction, system modeling and image reconstruction. The computational methods are designed to either improve the quantification accuracy or accelerate the processing. The challenges in PET data analysis come from the change of statistical properties of measurement data after various data corrections. The quality of results from all image reconstruction algorithms depends on the accuracy of statistical models in each data correction and image reconstruction. However, due to the complexity of PET scan, it is nearly impossible to propose a perfect model. Furthermore, a complicated model will apparently slow down the whole image reconstruction process. The modeling and processing in data correction includes scatter correction [37, 43, 80], attenuation correction [38, 68], partial volume effect correction [23, 67], etc. The image reconstruction includes analytical reconstruction and model-based reconstruction [2, 26]. In the studies involving a large amount of images from different patients, normalizing these images is also critical to the quantification of the studies [28].

2.2 Dynamic PET Imaging and Pharmacokinetic Analysis

Dynamic PET imaging is a combination of short interval PET scans and reflects the dynamic metabolism of injected radiotracers. Dynamic PET brings more challenges to PET imaging due to the poorer statistical property and low SNR from the low count

PET data. The series of acquisitions can be used to estimate the kinetic parameters which represent the metabolism of radiotracers in vivo.

In order to obtain the kinetic parameters, a traditional approach is first to reconstruct the activity distributions from the dynamic PET data, and then to fit the calculated time activity curve (TAC) to a predefined kinetic model. The accuracy of this kind of approaches relies on the reconstructed activity distributions. The complicated statistical noise properties, especially in the low-count dynamic PET imaging, and the uncertainties introduced by various PET data corrections will affect the activity reconstruction and lead to a suboptimal estimation of kinetic parameters [31]. There are also many efforts that try to estimate the kinetic parameters from PET projection data directly and achieve better bias and variance including both linear and nonlinear models [56, 74, 83]. The optimization algorithms are generally very complicated. Kamasak et al. applied the coordinate descent algorithm for optimization but it is still limited to specific kinetic models [41]. Wang et al. applied a generalized algorithm for reconstruction of parametric images [79], however, estimating individual kinetic parameter is still a challenging issue, which will be critical to clinical research, drug discovery and drug development [14, 27, 75].

In drug discovery and development, quantitative pharmacokinetic analysis with dynamic PET imaging now plays a promising role as determinants of in vivo drug action to help select drug candidate. Fast and accurate pharmacokinetic analysis with rapid information feedback in the early stage of drug discovery and development is critical to obtain the in vitro and in vivo drug properties [13, 81].

2.3 Mathematical and Statistical Modeling

Mathematical and statistical models have long been used in molecular imaging [47]. For static reconstruction, researchers unitized various system probability models [3], statistical models for data acquisition [86] and prior models [1]. For dynamic studies, compartment models are used in many fields including pharmacokinetics, biology, engineering etc. Compartment models are the type of mathematical models to describe the way materials (radiotracers and their metabolite in PET and SPECT scan) are transmitted among the compartments (different organs and tissues). Inside each compartment, the concentration of radiotracers is assumed to be uniformly equal. Due to their simplicity and plausibility, compartment models are widely used in the dynamic PET scans to describe the tracer/drug kinetics. Drug kinetic models include simple drug transport model, which generally contains equal or less than three compartments and can be solved directly, and complicated biological models, which can contain up to twenty compartments and generally require prior knowledge to solve [32, 33]. Most of the complicated models with many compartments can usually be decomposed into a combination of simple models with less than four compartments. The most basic compartment models include two compartment blood flow model, standard two tissue three compartment Phelps 4 K model with reversible target tissue and Sokoloff 3 K model with irreversible target tissue, three tissue five

parameter bertoldo model, standard three tissue four compartment model. More complicated models with more compartments and parallel model with multiple injection can be extended from aforementioned standard models [25, 42].

2.4 Feature Selection

Feature selection is widely used in computer aided diagnosis. Correctly selected features from a large set of clinical data can be used to improve the diagnosis accuracy of various diseases and provide a guidance for future clinical trials. The most commonly used method is Principal Component Analysis (PCA), which is a statistical procedure to convert a set of observation of possibly correlated variables to a set of linearly uncorrelated variables, i.e. principal components. These principle components can then be used as the feature for following studies, for example, comparing the functional connectivities in human brain studies [62, 70]. Machine learning and data mining techniques have also been applied to molecular imaging by various researchers. Researchers extract features to analyze cancer treatment outcome [20], utilize FDG-PET scan in lymphoma by WHO classification [21], classify the tissue in PET/MR scan with the potential for attenuation correction [53]. For clinical applications, support vector machine can also be used to identify imaging biomarkers of neurological and psychiatric diseases [59], and in therapy decision [58]. The application of machine learning is also very active in cancer prediction and prognosis [16].

2.5 Disease Specific Analysis and Image Quantification

In molecular imaging, the high activity concentrations (hot spots) are identified and analyzed as Region of Interest (ROI). In some clinical studies, different diseases may show similar activity concentrations inside the same organ tissue, then disease specific dynamic analysis become a superior tool to differentiate these different diseases [18, 27]. Disease specific dynamic analysis utilizes predefined disease models and the time activity curves from molecular imaging to classify the studies into proper disease categories. However, the accuracy of quantitative dynamic PET studies depends on various factors including kinetic models, quantitative methods and the approximation of arterial input function from blood sampling. The most general kinetic models used are compartment model with assumptions that physiological process and molecular interactions are not influenced by injected radioligand. Current clinical adopted quantitative methods are actually semi-quantitative methods, which include methods using reference regions or calculating Standard Uptake Value (SUV) [8]. Methods using reference regions are easy to implement but have several drawbacks, e.g. the reference tissue is hard to define and has low SNR due to the low resolution of PET and SPECT scans, and the uptake of the reference tissue may

change after the radiotherapy. SUV now is included in every clinical study, which is calculated as a ratio of tissue radioactivity concentration and injected dose divided by body weight, the advantage of SUV in clinical study is that the blood sampling is not required. However, the full quantitative analysis requires both dynamic PET scans and tracer concentration in the arterial blood plasma. The gold standard of blood sampling is serial arterial sampling of a superficial artery, and clinical alternative methods include venous blood sampling, image derived input function and population based input function [34, 48]. The drawback of the full quantitative method is only one FOV/bed position can be taken into consideration at one time. For metastasized disease, not all lesions can be quantified simultaneously [69, 76].

2.6 Other Conventional Image Processing Applications

1. Image Segmentation. Image segmentation is the process of partitioning an image into multiple different segments (group of pixels). Especially in molecular imaging, the image segmentation is used to simplify the representation of an image and extract Region of Interest (ROI) that is more meaningful and followed by image analysis. Image segmentation is also important to find the boundaries of different regions and organs by applying different labels. Image segmentation can also be applied to 3D image stacks to help 3D image reconstruction [17, 87]. Computational methods for image segmentation including basic thresholding methods [19, 22, 40], cluster based methods, which are multivariate data analysis methods using predefined criteria to partition a large number of objects into a smaller number of clusters [82], gradient based methods, which are to find the boundary of an object of interest with the gradient intensity observed in the images [29], level set based methods [51, 60], 3D level set methods [85], and kinetic model guided segmentation methods, which assume different ROIs have different tracer kinetic properties to separate different functional regions [11].
2. Image Registration. Image registration is the process to transform different sets of data into one coordinate system. Image registration is widely used in molecular imaging, e.g. patient radiotherapy follow-up by transforming PET images from a series of studies, diagnosis by images from multiple imaging modalities [15, 35, 36, 65]. Major computational methods include intense based methods, which compare intensity patterns in multiple images and register the reference image and target image by defining correlation metrics [44], feature-based image registration, which extract common features from the anatomical information of organs and tissues as references [63], this method can also be used for multiple imaging modalities [30, 49, 55]. The image registration can be improved by different patient preparation and pre-positioning [7], respiratory gating [10], various tracking devices, etc. [66].

3. Image Fusion. Image fusion is the combination of relevant information from two or more images into one single image. The fused image will provide more information than any single input image. Accurate image fusion from combined PET, CT, MRI scans can significantly improve the diagnosis and provide better understandings of diseases. Image fusion generally works together and shares similar technologies with image registration [61, 72, 78].

3 Future Directions

Molecular imaging is a relatively new but fast-growing area for both research and clinical applications. Although with some technical limitations, molecular imaging modalities show the superior ability to quantitatively measure the biologic processes in a functional way at the cellular and subcellular level within living subjects, and this significantly improved our understanding of various diseases and greatly benefited the clinical diagnosis. The emerging new scanner systems with new detectors will further enhance their abilities, and bring new challenges in data correction and image analysis at the same time.

Computational methods play a critical role in processing the images, from data processing based on the physical natures of the molecular imaging modalities to image reconstruction, analysis and understanding. The data processing algorithms need to be adjusted with the properties of new system design, and new features in detector system correspondingly. Monte Carlo simulation is a faithful way to study the new design and provide references for validation of new methods. Application-specific statistical models will greatly improve the image qualities of certain disease compared with generic models, and new techniques like machine learning have shown promising prospects in classifying diseases, generating atlas based models etc. The image post-processing including image analysis and understanding must also adopt related changes. Researchers are actively using computing methods to guide applicable pathological studies from a series of patient studies using dynamic analysis, this has the great potential to apply to personalized treatment. Pharmaceutical companies are also interested in the accurate quantitative pharmacokinetic analysis using PET to study the metabolism of new drugs, which has the potentials to shorten the drug development cycle and save tons of money for the industry and patients. With the evolution of both image pre-processing and post-processing methods, molecular imaging is believed to be able to study more complicated diseases currently in the unknown area, and computational methods for molecular imaging will help us to mine the potentials buried in the data and images.

References

1. Alenius, S., Ruotsalainen, U.: Bayesian image reconstruction for emission tomography based on median root prior. Eur. J. Nucl. Med. **24**(3), 258–265 (1997)
2. Alessio, A., Kinahan, P.: Pet image reconstruction. Nucl. Med., **2** (2006)
3. Alessio, A.M., Stearns, C.W., Tong, S., Ross, S.G., Kohlmyer, S., Ganin, A., Kinahan, P.E.: Application and evaluation of a measured spatially variant system model for pet image reconstruction. IEEE Trans. Med. Imaging **29**(3), 938–949 (2010)
4. Bailey, D., Townsend, D., Valk, P., Maisey, M.: Positron Emission Tomography: Basic Sciences. Springer, New York (2005)
5. Bartenstein, P., Minoshima, S., Hirsch, C., Buch, K., Willoch, F., Mösch, D., Schad, D., Schwaiger, M., Kurz, A., et al.: Quantitative assessment of cerebral blood flow in patients with Alzheimer's disease by SPECT. J. Nucl. Med. **38**(7), 1095 (1997)
6. Bateman, T.M., Heller, G.V., McGhie, A.I., Friedman, J.D., Case, J.A., Bryngelson, J.R., Hertenstein, G.K., Moutray, K.L., Reid, K., Cullom, S.J.: Diagnostic accuracy of rest/stress ECG-gated Rb-82 myocardial perfusion PET: comparison with ECG-gated Tc-99m sestamibi SPECT. J. Nucl. Cardiol. **13**(1), 24–33 (2006)
7. Beyer, T., Tellmann, L., Nickel, I., Pietrzyk, U.: On the use of positioning aids to reduce misregistration in the head and neck in whole-body PET/CT studies. J. Nucl. Med. **46**(4), 596–602 (2005)
8. Boellaard, R., O'Doherty, M.J., Weber, W.A., Mottaghy, F.M., Lonsdale, M.N., Stroobants, S.G., Oyen, W.J., Kotzerke, J., Hoekstra, O.S., Pruim, J., et al.: FDG PET and PET/CT: Eanm procedure guidelines for tumour pet imaging: version 1.0. Eur. J. Nucl. Med. Mol. Imaging **37**(1), 181–200 (2010)
9. Bonte, F.J., Weiner, M.F., Bigio, E.H., White, C., et al.: Brain blood flow in the dementias: SPECT with histopathologic correlation in 54 patients. Radiology **202**(3), 793–797 (1997)
10. Boucher, L., Rodrigue, S., Lecomte, R., Bénard, F.: Respiratory gating for 3-dimensional PET of the thorax: feasibility and initial results. J. Nucl. Med. **45**(2), 214–219 (2004)
11. Brankov, J.G., Galatsanos, N.P., Yang, Y., Wernick, M.N.: Segmentation of dynamic PET or fMRI images based on a similarity metric. IEEE Trans. Nucl. Sci. **50**(5), 1410–1414 (2003)
12. Buck, A.K., Halter, G., Schirrmeister, H., Kotzerke, J., Wurziger, I., Glatting, G., Mattfeldt, T., Neumaier, B., Reske, S.N., Hetzel, M.: Imaging proliferation in lung tumors with PET: 18F-FLT Versus 18F-FDG. J. Nucl. Med. **44**(9), 1426–1431 (2003)
13. Catafau, M., Bullich, S.: Molecular imaging PET and SPECT approaches for improving productivity of antipsychotic drug discovery and development. Curr. Med. Chem. **20**(3), 378–388 (2013)
14. Cobelli, C., Foster, D., Toffolo, G.: Tracer Kinetics in Biomedical Research: From Data to Model. Kluwer Academic/Plenum Publishers, New York (2000)
15. Crum, W., Hartkens, T., Hill, D.: Non-rigid image registration: theory and practice. Br. J. Radiol. **77**(suppl 2), S140–S153 (2004)
16. Cruz, J.A., Wishart, D.S.: Applications of machine learning in cancer prediction and prognosis. Cancer Inf. **2**, 59 (2006)
17. Daisne, J.F., Sibomana, M., Bol, A., Doumont, T., Lonneux, M., Grégoire, V.: Tri-dimensional automatic segmentation of PET volumes based on measured source-to-background ratios: influence of reconstruction algorithms. Radiother. Oncol. **69**(3), 247–250 (2003)
18. Dimitrakopoulou-Strauss, A., Strauss, L.G., Heichel, T., Wu, H., Burger, C., Bernd, L., Ewerbeck, V.: The role of quantitative 18F-FDG PET studies for the differentiation of malignant and benign bone lesions. J. Nucl. Med. **43**(4), 510–518 (2002)
19. Drever, L., Roa, W., McEwan, A., Robinson, D.: Iterative threshold segmentation for PET target volume delineation. Med. Phys. **34**, 1253 (2007)
20. El Naqa, I., Grigsby, P., Apte, A., Kidd, E., Donnelly, E., Khullar, D., Chaudhari, S., Yang, D., Schmitt, M., Laforest, R., et al.: Exploring feature-based approaches in pet images for predicting cancer treatment outcomes. Pattern Recognit. **42**(6), 1162–1171 (2009)

21. Elstrom, R., Guan, L., Baker, G., Nakhoda, K., Vergilio, J.A., Zhuang, H., Pitsilos, S., Bagg, A., Downs, L., Mehrotra, A., et al.: Utility of FDG-PET scanning in lymphoma by who classification. Blood **101**(10), 3875–3876 (2003)
22. Erdi, Y.E., Mawlawi, O., Larson, S.M., Imbriaco, M., Yeung, H., Finn, R., Humm, J.L.: Segmentation of lung lesion volume by adaptive positron emission tomography image thresholding. Cancer **80**(S12), 2505–2509 (1997)
23. Erlandsson, K., Buvat, I., Pretorius, P.H., Thomas, B.A., Hutton, B.F.: A review of partial volume correction techniques for emission tomography and their applications in neurology, cardiology and oncology. Phys. Med. Biol. **57**(21), R119 (2012)
24. Freedman, N., Schechter, D., Klein, M., Marciano, R., Rozenman, Y., Chisin, R.: SPECT attenuation artifacts in normal and overweight persons: insights from a retrospective comparison of Rb-82 positron emission tomography and Tl-201 SPECT myocardial perfusion imaging. Clin. Nucl. Med. **25**(12), 1019–1023 (2000)
25. Gao, F., Liu, H., Jian, Y., Shi, P.: Dynamic dual-tracer PET reconstruction. In: Information Processing in Medical Imaging, pp. 38–49. Springer (2009)
26. Gao, F., Liu, H., Shi, P.: Efficient robust reconstruction of dynamic PET activity maps with radioisotope decay constraints. Med. Image Comput. Comput.-Assist. Interv. (MICCAI 2010) **3**, 571–578 (2010)
27. Gao, F., Liu, H., Shi, P.: Robust estimation of kinetic parameters in dynamic PET imaging. Med. Image Comput. Comput.-Assist. Interv. - MICCAI 2011, **6891**, 492–499 (2011)
28. Gee, J., Ding, L., Xie, Z., Lin, M., DeVita, C., Grossman, M.: Alzheimer's disease and frontotemporal dementia exhibit distinct atrophy-behavior correlates: a computer-assisted imaging study1. Acad. Radiol. **10**(12), 1392–1401 (2003)
29. Geets, X., Lee, J.A., Bol, A., Lonneux, M., Grégoire, V.: A gradient-based method for segmenting FDG-PET images: methodology and validation. Eur. J. Nucl. Med. Mol. Imaging **34**(9), 1427–1438 (2007)
30. Goerres, G.W., Kamel, E., Heidelberg, T.N.H., Schwitter, M.R., Burger, C., von Schulthess, G.K.: PET-CT image co-registration in the thorax: influence of respiration. Eur. J. Nucl. Med. Mol. Imaging **29**(3), 351–360 (2002)
31. Gunn, R., Gunn, S., Turkheimer, F., Aston, J., Cunningham, V.: Tracer kinetic modeling via basis pursuit. In: Senda, M., Kimura, Y., Herscovitch, P. (eds.) Brain Imaging Using PET. Academic Press (2002)
32. Gunn, R.N., Gunn, S.R., Cunningham, V.J.: Positron emission tomography compartmental models. J. Cereb. Blood Flow Metab. **21**(6), 635–652 (2001)
33. Gunn, R.N., Gunn, S.R., Turkheimer, F.E., Aston, J.A., Cunningham, V.J.: Positron emission tomography compartmental models: A basis pursuit strategy for kinetic modeling. J. Cereb. Blood Flow Metab. **22**(12), 1425–1439 (2002)
34. Gunn, R.N., Lammertsma, A.A., Hume, S.P., Cunningham, V.J.: Parametric imaging of ligand-receptor binding in pet using a simplified reference region model. Neuroimage **6**(4), 279–287 (1997)
35. Hajnal, J.V.: Medical Image Registration. CRC Press LLC (2001)
36. Huang, X., Hill, N.A., Ren, J., Guiraudon, G., Boughner, D., Peters, T.M.: Dynamic 3D ultrasound and MR image registration of the beating heart. In: Medical Image Computing and Computer-Assisted Intervention-MICCAI 2005, pp. 171–178. Springer (2005)
37. Hutton, B.F., Buvat, I., Beekman, F.J.: Review and current status of SPECT scatter correction. Phys. Med. Biol. **56**(14), R85 (2011)
38. Iida, H., Narita, Y., Kado, H., Kashikura, A., Sugawara, S., Shoji, Y., Kinoshita, T., Ogawa, T., Eberl, S.: Effects of scatter and attenuation correction on quantitative assessment of regional cerebral blood flow with spect. J. Nucl. Med. Off. Publ. Soc. Nucl. Med. **39**(1), 181–189 (1998)
39. Iznaga-Escobar, N.: ^{188}Re-direct labeling of monoclonal antibodies for radioimmunotherapy of solid tumors: Biodistribution, normal organ dosimetry, and toxicology. Nucl. Med. Biol. **25**(5), 441–447 (1998)
40. Jentzen, W., Freudenberg, L., Eising, E.G., Heinze, M., Brandau, W., Bockisch, A.: Segmentation of PET volumes by iterative image thresholding. J. Nucl. Med. **48**(1), 108–114 (2007)

41. Kamasak, M.E., Bouman, C.A., Morris, E.D., Sauer, K.: Direct reconstruction of kinetic parameter images from dynamic PET data. IEEE Trans. Med. Imaging **25**, 636–650 (2005)
42. Kelly, C.J., Brady, M.: A model to simulate tumour oxygenation and dynamic [18F]-Fmiso PET data. Phys. Med. Biol. **51**(22), 5859 (2006)
43. Kinahan, P., Townsend, D., Beyer, T., Sashin, D.: Attenuation correction for a combined 3D PET/CT scanner. Med. Phys. **25**(10), 2046–2053 (1998)
44. Klein, S., Staring, M., Murphy, K., Viergever, M.A., Pluim, J.P., et al.: Elastix: a toolbox for intensity-based medical image registration. IEEE Trans. Med. Imaging **29**(1), 196–205 (2010)
45. Koeppe, R.A., Gilman, S., Junck, L., Wernette, K., Frey, K.A., et al.: Differentiating Alzheimer's disease from dementia with Lewy bodies and Parkinson's disease with (+)-[11C] dihydrotetrabenazine positron emission tomography. Alzheimer's Dement. J. Alzheimer's Assoc. **4**(1 Suppl 1), S67 (2008)
46. Krivokapich, J., Smith, G., Huang, S.C., Hoffman, E., Ratib, O., Phelps, M., Schelbert, H.: 13N ammonia myocardial imaging at rest and with exercise in normal volunteers. Quantification of absolute myocardial perfusion with dynamic positron emission tomography. Circulation **80**(5), 1328–1337 (1989)
47. Li, T., Thorndyke, B., Schreibmann, E., Yang, Y., Xing, L.: Model-based image reconstruction for four-dimensional PET. Med. Phys. **33**(5), 1288–1298 (2006)
48. Logan, J., Fowler, J.S., Volkow, N.D., Wang, G.J., Ding, Y.S., Alexoff, D.L.: Distribution volume ratios without blood sampling from graphical analysis of pet data. J. Cereb. Blood Flow Metab. **16**(5), 834–840 (1996)
49. Maes, F., Collignon, A., Vandermeulen, D., Marchal, G., Suetens, P.: Multimodality image registration by maximization of mutual information. IEEE Trans. Med. Imaging **16**(2), 187–198 (1997)
50. Magota, K., Kubo, N., Kuge, Y.: Nishijima, K.i., Zhao, S., Tamaki, N.: Performance characterization of the Inveon preclinical small-animal PET/SPECT/CT system for multimodality imaging. Eur. J. Nucl. Med. Mol. Imaging **38**(4), 742–752 (2011)
51. Malladi, R., Sethian, J.A., Vemuri, B.C.: Shape modeling with front propagation: a level set approach. IEEE Trans. Pattern Anal. Mach. Intell. **17**(2), 158–175 (1995)
52. Mankoff, D.A.: A definition of molecular imaging. J. Nucl. Med. **48**(6), 18N–21N (2007)
53. Martinez-Möller, A., Souvatzoglou, M., Delso, G., Bundschuh, R.A., Chefd'hotel, C., Ziegler, S.I., Navab, N., Schwaiger, M., Nekolla, S.G.: Tissue classification as a potential approach for attenuation correction in whole-body PET/MRI: evaluation with PET/CT data. J. Nucl. Med. **50**(4), 520–526 (2009)
54. Maruyama, A., Hasegawa, S., Paul, A.K., Xiuli, M., Yoshioka, J., Maruyama, K., Hori, M., Nishimura, T.: Myocardial viability assessment with gated SPECT Tc-99m tetrofosmin wall thickening: Comparison with F-18 FDG-PET. Ann. Nucl. Med. **16**(1), 25–32 (2002)
55. Mattes, D., Haynor, D.R., Vesselle, H., Lewellen, T.K., Eubank, W.: PET-CT image registration in the chest using free-form deformations. IEEE Trans. Med. Imaging **22**(1), 120–128 (2003)
56. Mattes, D., Haynor, D.R., Vesselle, H., Lewellen, T.K., Eubank, W.: PET-CT image registration in the chest using free-form deformations. IEEE Trans. Med. Imaging **22**(1), 120–128 (2003)
57. Mena, E., Turkbey, B., Mani, H., Adler, S., Valera, V.A., Bernardo, M., Shah, V., Pohida, T., McKinney, Y., Kwarteng, G., Daar, D., Lindenberg, M.L., Eclarinal, P., Wade, R., Linehan, W.M., Merino, M.J., Pinto, P.A., Choyke, P.L., Kurdziel, K.A.: 11C-Acetate PET/CT in localized prostate cancer: A study with MRI and histopathologic correlation. J. Nucl. Med. **53**(4), 538–545 (2012)
58. Naumann, R., Beuthien-Baumann, B., Reiss, A., Schulze, J., Hänel, A., Bredow, J., Kühnel, G., Kropp, J., Hänel, M., Laniado, M., et al.: Substantial impact of FDG PET imaging on the therapy decision in patients with early-stage Hodgkin's lymphoma. Br. J. Cancer **90**(3), 620–625 (2004)
59. Orrù, G., Pettersson-Yeo, W., Marquand, A.F., Sartori, G., Mechelli, A.: Using support vector machine to identify imaging biomarkers of neurological and psychiatric disease: a critical review. Neurosci. Biobehav. Rev. **36**(4), 1140–1152 (2012)

60. Osher, S., Fedkiw, R.P.: Level set methods: an overview and some recent results. J. Comput. Phys. **169**(2), 463–502 (2001)
61. Pajares, G.: Manuel de la Cruz, J.: A wavelet-based image fusion tutorial. Pattern Recognit. **37**(9), 1855–1872 (2004)
62. Paus, T., Jech, R., Thompson, C.J., Comeau, R., Peters, T., Evans, A.C.: Transcranial magnetic stimulation during positron emission tomography: a new method for studying connectivity of the human cerebral cortex. J. Neurosci. **17**(9), 3178–3184 (1997)
63. Pellizzari, C., Levin, D.N., Chen, G.T., Chen, C.T.: Image registration based on anatomic surface matching. In: Interactive Image-Guided Neurosurgery pp. 47–62 (1993)
64. Pichler, B.J., Kolb, A., Nagele, T., Schlemmer, H.P.: PET/MRI: paving the way for the next generation of clinical multimodality imaging applications. J. Nucl. Med. **51**(3), 333–336 (2010)
65. Pietrzyk, U., KarlHerholz, G., AndreasJacobs, R.: Image registration: validation for PET, SPECT, MRI and CT brain studies. J. Nucl. Med. **35**(12), 2011–2018 (1994)
66. Rahmim, A., Rousset, O., Zaidi, H.: Strategies for motion tracking and correction in PET. PET Clinics **2**(2), 251–266 (2007)
67. Rousset, O.G., Ma, Y., Evans, A.C., et al.: Correction for partial volume effects in PET: principle and validation. J. Nucl. Med. **39**(5), 904–911 (1998)
68. Samarin, A., Burger, C., Wollenweber, S.D., Crook, D.W., Burger, I.A., Schmid, D.T., von Schulthess, G.K., Kuhn, F.P.: PET/MR imaging of bone lesions-implications for pet quantification from imperfect attenuation correction. Eur. J. Nucl. Med. Mol. Imaging **39**(7), 1154–1160 (2012)
69. Strother, S.C., Anderson, J., Hansen, L.K., Kjems, U., Kustra, R., Sidtis, J., Frutiger, S., Muley, S., LaConte, S., Rottenberg, D.: The quantitative evaluation of functional neuroimaging experiments: the NPAIRS data analysis framework. NeuroImage **15**(4), 747–771 (2002)
70. Strother, S.C., Anderson, J.R., Schaper, K.A., Sidtis, J.J., Liow, J.S., Woods, R.P., Rottenberg, D.A.: Principal component analysis and the scaled subprofile model compared to intersubject averaging and statistical parametric mapping: I. Functional connectivity of the human motor system studied with [150] water pet. J. Cereb. Blood Flow Metab. **15**(5), 738–753 (1995)
71. Tharp, K., Israel, O., Hausmann, J., Bettman, L., Martin, W., Daitzchman, M., Sandler, M., Delbeke, D.: Impact of 131I-SPECT/CT images obtained with an integrated system in the follow-up of patients with thyroid carcinoma. Eur. J. Nucl. Med. Mol. Imaging **31**(10), 1435–1442 (2004)
72. Townsend, D.W., Beyer, T.: A combined PET/CT scanner: the path to true image fusion. Br. J. Radiol. **75**(suppl 9), S24–S30 (2002)
73. Townsend, D.W., Carney, J.P., Yap, J.T., Hall, N.C.: PET/CT today and tomorrow. J. Nucl. Med. **45**(1 suppl), 4S–14S (2004)
74. Tsoumpas, C., Turkheimer, F., Thielemans, K.: A survey of approaches for direct parametric image reconstruction in emission tomography. Med. Phys. **35**, 3963 (2008)
75. Valk, P., Delbeke, D., Bailey, D., Townsend, D., Maisey, M.: Positron Emission Tomography: Clinical Practice. Springer (2006)
76. Varrone, A., Sjöholm, N., Eriksson, L., Gulyás, B., Halldin, C., Farde, L.: Advancement in PET quantification using 3D-OP-OSEM point spread function reconstruction with the HRRT. Eur. J. Nucl. Med. Mol. Imaging **36**(10), 1639–1650 (2009)
77. Wahl, R.L., Buchanan, J.W.: Principles and Practice of Positron Emission Tomography. Lippincott Williams & Wilkins (2002)
78. Wahl, R.L., Quint, L.E., Cieslak, R.D., Aisen, A.M., Koeppe, R.A., Meyer, C.R., et al.: Anatometabolic tumor imaging: fusion of FDG PET with CT or MRI to localize foci of increased activity. J. Nucl. Med. **34**(7), 1190 (1993)
79. Wang, G., Qi, J.: Generalized algorithms for direct reconstruction of parametric images from dynamic PET data. IEEE Trans. Med. Imaging **28**(11), 1717–1726 (2009)
80. Watson, C.C.: New, faster, image-based scatter correction for 3D PET. IEEE Trans. Nucl. Sci. **47**(4), 1587–1594 (2000)
81. Willmann, J.K., Van Bruggen, N., Dinkelborg, L.M., Gambhir, S.S.: Molecular imaging in drug development. Nat. Rev. Drug Discov. **7**(7), 591–607 (2008)

82. Wong, K.P., Feng, D., Meikle, S.R., Fulham, M.J.: Segmentation of dynamic PET images using cluster analysis. IEEE Trans. Nucl. Sci. **49**(1), 200–207 (2002)
83. Yan, J., Planeta-Wilson, B., Gallezot, J., Carson, R.: Initial evaluation of direct 4D parametric reconstruction with human PET data. In: Nuclear Science Symposium Conference Record (NSS/MIC), 2009 IEEE, pp. 2503–2506. IEEE (2010)
84. Yang, D.J., Azhdarinia, A., Kim, E.E.: Tumor specific imaging using Tc-99m and Ga-68 labeled radiopharmaceuticals. Curr. Med. Imaging Rev. **1**(1), 25–34 (2005)
85. Yang, J., Staib, L.H., Duncan, J.S.: Neighbor-constrained segmentation with level set based 3-D deformable models. IEEE Trans. Med. Imaging **23**(8), 940–948 (2004)
86. Yavuz, M., Fessler, J.A.: Statistical image reconstruction methods for randoms-precorrected pet scans. Med. Image Anal. **2**(4), 369–378 (1998)
87. Zaidi, H., El Naqa, I.: PET-guided delineation of radiation therapy treatment volumes: a survey of image segmentation techniques. Eur. J. Nucl. Med. Mol. Imaging **37**, 2165–2187 (2010)

Fuzzy Connectedness Image Co-segmentation for Hybrid PET/MRI and PET/CT Scans

Ziyue Xu, Ulas Bagci, Jayaram K. Udupa and Daniel J. Mollura

Abstract In this paper, we presented a 3-D computer-aided co-segmentation tool for tumor/lesion detection and quantification from hybrid PET/MRI and PET/CT scans. The proposed method was designed with a novel modality-specific visibility weighting scheme built upon a fuzzy connectedness (FC) image segmentation algorithm. In order to improve the determination of lesion margin, it is necessary to combine the complementary information of tissues from both anatomical and functional domains. Therefore, a robust image segmentation method that simultaneously segments tumors/lesions in each domain is required. However, this task, named co-segmentation, is a challenging problem due to (1) unique challenges brought by each imaging modality, and (2) a lack of one-to-one region and boundary correspondences of lesions in different imaging modalities. Owing to these hurdles, the algorithm is desired to have a sufficient flexibility to utilize the strength of each modality. In this work, seed points were first selected from high uptake regions within PET images. Then, lesion boundaries were delineated using a hybrid approach based on novel affinity function design within the FC framework. Further, an advanced extension of FC algorithm called iterative relative FC (IRFC) was used with automatically identified background seeds. The segmentation results were compared to the reference truths provided by radiologists. Experimental results showed that the proposed method effectively utilized multi-modality information for co-segmentation, with a high accuracy (mean DSC of 85 %) and can be a viable alternative to the state-of-the art joint segmentation method of random walk (RW) with higher efficiency.

U. Bagci (✉)
Center for Research in Computer Vision (CRCV), HEC 221, Computer Science,
University of Central Florida, Orlando, FL 32816, USA
e-mail: bagci@crcv.ucf.edu

Z. Xu · D.J. Mollura
Center for Infectious Disease Imaging, Radiology and Imaging Sciences
National Institutes of Health, Bethesda, MD 20892, USA

J.K. Udupa
Department of Radiology, University of Pennsylvania,
Philadelphia, PA 19104, USA

F. Gao et al. (eds.), *Computational Methods for Molecular Imaging*,
Lecture Notes in Computational Vision and Biomechanics 22,
DOI 10.1007/978-3-319-18431-9_2

Keywords Co-segmentation · Fuzzy connectedness · PET/MRI · PET/CT · Image segmentation

1 Introduction

Multimodal imaging techniques make use of different but complementary imaging modalities within a single system. While PET/CT sequentially acquires computed tomography (CT) and positron emission tomography (PET) images from a patient, PET/MRI simultaneously acquires PET and magnetic resonance (MR) images, and provides very accurate spatial and temporal image fusion. With PET/MRI and PET/CT, the spatial distribution of radiotracer activity from PET can be precisely analyzed with anatomical details revealed by MRI or CT, leading to more accurate localization and characterization of pathology. PET/MR and PET/CT have thus emerged as a mean of achieving higher sensitivity and specificity than either component modality alone. Most automated tumor/lesion segmentation methods are either solely based on PET images and ignore complementary MRI or CT information, or vice versa. Lately, the requirements for joint analysis of lesions in both structural and functional image domains led researchers to develop co-segmentation methods for robust quantification of lesions [1, 2].

In this paper, as an alternative to the state-of-the-art methods, we propose an efficient framework for hybrid imaging modalities segmentation. Our proposed method is based on a fuzzy connectedness (FC) image segmentation [3], which effectively utilizes a modality-specific visibility weighting scheme through a novel fuzzy affinity function. Our method is flexible to withstand various visibility conditions of the object of interest in different modalities. In clinical routines, high uptake regions of radiotracers in PET images are usually determined by the visual assessment of radiologists based on the fused information. This process is labor intensive and time consuming. Thresholding, edge detection, region growing, and watershed approaches have also been employed to determine the region boundaries [4], but these algorithms were developed solely on functional images without incorporating anatomical information. Therefore, the methods are limited in accuracy, robustness, and reproducibility. Recently, a few co-segmentation methods have been proposed for quantification of PET/CT images [1, 2, 5, 6]. Feature extraction and classification, considering both PET and CT information for distinguishing tumor from normal tissue in the head and neck regions, is presented in [5]. In [6], localization and initial segmentation were performed over PET images, which is further refined by voxel classification in CT. The above methods [5, 6] are based on classification, which lack the capability of concurrent segmentation from both modalities. Markov Random Field (MRF) model was employed for PET/CT co-segmentation in [1]; graph optimization was performed to simultaneously minimize the total MRF energy obtained from both PET and CT images. The MRF-based method was shown to be effective; however, it works on a 2-D slice plane and requires a precisely defined seed set provided by user interaction. In [2], random walk (RW) co-segmentation was applied to find the correct anatomical

boundaries in CT images, driven by the uptake regions from the corresponding PET images. The RW-based algorithm was shown to perform better than MRF in both accuracy and speed. In this paper, we propose an alternative method to these state-of-the-art methods [1, 2]. An automatic 3-D co-segmentation method was designed based on the FC framework with a novel fuzzy affinity function. Our method has the flexibility to segment tumors/lesions jointly through a modality-specific weight mechanism; experiments have been conducted on images from hybrid PET/MRI and PET/CT scans.

2 Methods

In this section, the theory of FC is presented, followed by co-segmentation formulation.

In the FC framework, a fuzzy topological construct characterizes how voxels of an image hang together to form an object through a predefined function called *affinity* [7]. Assuming $\mathcal{V} \subset \mathbb{Z}^3$ denotes a 3-D cubic grid representing the *image space*, where each element of $\mathcal{V}$ is called a *voxel*, a topology on an image is given in terms of an *adjacency* relation (μ_α). Theoretically, if p and q are α-adjacent to each other, then $\mu_\alpha(p, q) = 1$, '0' otherwise. In practice, we set $\alpha = 26$ for 3-D analysis. While affinity is intended to be a local relation, a global fuzzy relation called fuzzy connectedness, is induced on the image domain by the affinity functions. This is done by considering all possible paths between any two voxels p and q in the image domain, and assigning a strength of fuzzy connectedness to each path. The level of the fuzzy connectedness between any two voxels p and q is considered to be the maximum of the strengths of all paths between p and q.

An *affinity relation* κ is the most fundamental measure of local hanging togetherness of nearby voxels. For a path π, which is a sequence of voxels $\langle p_1, p_2, \ldots, p_l \rangle$ with every two successive voxels being adjacent, given *fuzzy affinity function* $\mu_\kappa(p_i, p_{i+1})$, the strength of the path is defined as the minimum affinity along the path:

$$\mu_{\mathcal{N}}(\pi) = \min_{1 \le i < l} \mu_\kappa(p_i, p_{i+1}). \tag{1}$$

Then, the strength of connectedness $\mu_{\mathcal{K}}(p, q)$ between any two voxels p and q is the strength of the strongest path between them as

$$\mu_{\mathcal{K}}(p, q) = \max_{\pi \in \mathcal{P}(p,q)} \mu_{\mathcal{N}}(\pi), \tag{2}$$

where $\mathcal{P}(p, q)$ denotes the set of all paths between p and q. Therefore, a fuzzy connected object $\mathcal{O}$ in an image can be defined for a predetermined set of seeds S. Since the level of FC between any two voxels p and q is considered to be the maximum of the strengths of all paths between them, for multiple seeds, the fuzzy object membership function for $\mathcal{O}$ or the strength of connectedness of $\mathcal{O}$ is defined

as follows:

$$\mu_{\mathcal{O}}(p) = \max_{s \in S} \mu_{\mathcal{K}}(p, s). \tag{3}$$

An efficient computational solution is presented in [3] for computing $\mu_{\mathcal{O}}(p)$, given κ and S and an image.

Absolute FC segmentation is based on computing the FC strength between a set of seed points and all other voxels within the image and set a proper threshold to the resulting FC image for generating the binary segmentation result. However, the threshold determination is usually manual. On the other hand, IRFC method is based on several seed sets $S_i, i = 1, 2, \ldots, k$. FC strength is first computed at every voxel for each of the seed sets individually, and then the voxel is labeled as belonging the seed set with maximum FC value. In this way, the thresholding step is avoided. In this study, we investigated both the application of FC and IRFC.

2.1 Image Co-segmentation with Novel Affinity Function

Effectiveness of the FC/RFC algorithm depends on the choice of the affinity function. The most prominent affinities used so far are (i) adjacency-based μ_α, (ii) homogeneity-based μ_ψ, and (iii) object feature-based μ_ϕ such that fuzzy affinity is defined as

$$\mu_\kappa(p, q) = \begin{cases} 1, & \text{if } p = q; \\ \mu_\alpha(p, q)\sqrt{\mu_\psi(p, q)\mu_\phi(p, q)}, & \text{otherwise,} \end{cases} \tag{4}$$

where $\mu_\psi(p, q)$ captures the homogeneity between p and q, with a higher value for similar pairs. For object feature-based affinity, $\mu_\phi(p, q)$ defines the hanging-togetherness of p and q in the target object based on likeliness of their feature values with respect to the expected feature distribution of the target object. The general form of $\mu_\psi(p, q)$ and $\mu_\phi(p, q)$ are

$$\mu_\psi(p, q) = e^{-\frac{|f(p)-f(q)|^2}{2\sigma_\psi^2}}, \tag{5}$$

$$\mu_\phi(p, q) = \min\left(e^{-\frac{|f(p)-m|^2}{2\sigma_\phi^2}}, e^{-\frac{|f(q)-m|^2}{2\sigma_\phi^2}}\right), \tag{6}$$

where σ_ψ and σ_ϕ are two different standard deviation parameters used for homogeneity and object feature distribution, m is the mean object feature value, and f denotes image intensity function: $f : \mathcal{V} \to \mathcal{L} \subset \mathbb{Z}$.

In order to introduce a co-segmentation framework, we introduce two intensity functions corresponding to anatomical ($\mathcal{A}$: MRI or CT) and functional ($\mathcal{F}$: PET)

image domain, $f^{\mathcal{A}}$ and $f^{\mathcal{F}}$, respectively. Similarly, for each image modality $\mathcal{A}$ and $\mathcal{F}$, we define a new fuzzy affinity function by combining fuzzy affinity functions corresponding to anatomical and functional images (i.e., $\mu_\kappa^{\mathcal{A}}(p,q)$ and $\mu_\kappa^{\mathcal{F}}(p,q)$) as

$$\mu_\kappa(p,q) = \begin{cases} 0, & \text{if } \mu_\kappa^{\mathcal{A}}(p,q) \text{ or } \mu_\kappa^{\mathcal{F}}(p,q) = 0; \\ w_{\mathcal{A}}\mu_\kappa^{\mathcal{A}}(p,q) + w_{\mathcal{F}}\mu_\kappa^{\mathcal{F}}(p,q), & \text{otherwise;} \end{cases} \tag{7}$$

where weights $w_{\mathcal{A}}$ and $w_{\mathcal{F}}$ are used to combine affinities, and were determined by considering target visibility of different modalities such that they were constrained as $0 \leq w_{\mathcal{A}}, w_{\mathcal{F}} \leq 1$, and $w_{\mathcal{A}} + w_{\mathcal{F}} = 1$.

We also designed a new object feature-based affinity function specific to the image modality by analyzing the characteristics of individual imaging modalities. A non-uniform Gaussian formulation was utilized for this purpose. The functions designed for this purpose are illustrated in Fig. 1. As can be seen from the first row of the figure that since the *hot* regions are more active for a PET image, thus inferring more reliable target volume, we can define an expected value m from the image intensity distribution that shapes the non-uniform Gaussian formulation as

$$\mu_\phi^{\mathcal{F}}(x) = \begin{cases} 1, & \text{if } f^{\mathcal{F}}(x) > m; \\ e^{-\frac{|f^{\mathcal{F}}(x)-m|^2}{2\sigma_\phi^2}}, & \text{otherwise.} \end{cases} \tag{8}$$

In a similar fashion, to model the object feature-based affinity function, higher and lower intensity variations can be combined with respect to an object feature as

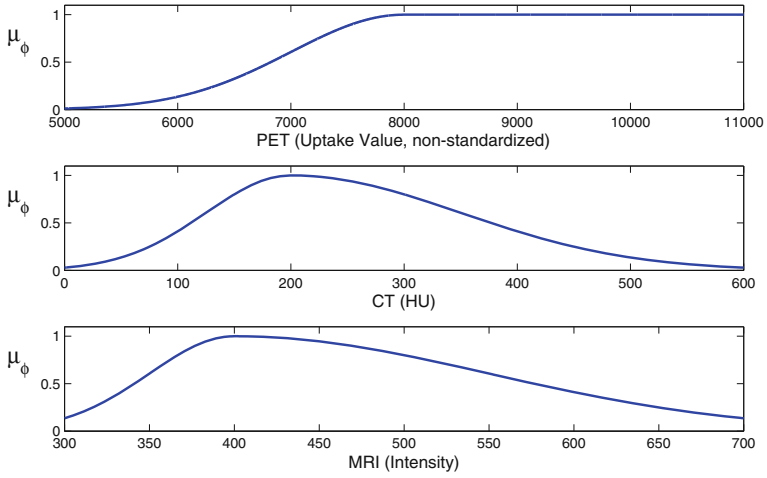

Fig. 1 Non-uniform Gaussian formulation for object feature similarity μ_ϕ

$$\mu_{\phi}^{\mathcal{A}}(x) = \begin{cases} e^{-\frac{|f^{\mathcal{A}}(x)-m|^2}{2\sigma_{\phi_{\mathrm{H}}}^2}}, & \text{if } f^{\mathcal{A}}(x) > m; \\ e^{-\frac{|f^{\mathcal{A}}(x)-m|^2}{2\sigma_{\phi_{\mathrm{L}}}^2}}, & \text{otherwise,} \end{cases} \tag{9}$$

where $\sigma_{\phi_{\mathrm{L}}} < \sigma_{\phi_{\mathrm{H}}}$. Second and third rows in Fig. 1 demonstrate the object feature-based affinity functions used for CT and MRI modalities, respectively. Once all affinity functions were defined, Eq. 3 was solved to obtain segmentation results.

3 Experiments and Results

Data and Evaluation Metrics: A retrospective study was performed on 9 PET/MRI and 9 PET/CT images. For comparison with the state-of-the-art algorithm of RW [2], we have used **the same dataset, reference segmentation, and evaluation criterion**. For PET/MRI scans, voxel sizes were $1.1 \times 1.1 \times 6$ mm^3 for MR images and $4.17 \times 4.17 \times 2$ mm^3 for PET images. For PET/CT scans, voxel sizes were $0.97 \times 0.97 \times 1.5$ mm^3 for CT images and $2.65 \times 2.65 \times 3$ mm^3 for PET images. Each patient's scan was positive for at least one mass tumor in the neck, thorax, abdomen, or pelvis pertaining to Von Hippel-Lindau disease, pheochromocytoma, or hereditary leiomyomatosis and renal cell cancer, as previously identified (but not circumscribed) by a radiologist. Manual delineations from two expert observers on PET/CT and PET/MR images were used as reference for evaluation, and the segmentation performance was evaluated using two conventional segmentation metrics, the Dice Similarity Coefficient (DSC) and Hausdorff Distance (HD). Note that DSC calculates the ratio of overlap between two segmentation results and HD measures the boundary mismatch between two segmentations. Higher DSC and lower HD are desirable for a segmentation algorithm. Seed points are manually determined, and variations are allowed given that FC is the most robust method for seed selection [8].

3.1 Qualitative and Quantitative Evaluation

The experiments were conducted on a machine with 2.7 GHz CPU, 16GB memory, and Mac OS X system. Average running time for the proposed co-segmentation algorithm was less than 10 seconds. RFC doubles the time complexity of FC, and we found no statistical significant difference between FC and IRFC results regarding segmentation accuracy. Figure 2 shows examples of the co-segmentation results from PET/MR images under different visibility conditions of the target object. The second column displays the fused images overlaid by segmentation results (green boundaries) and manual references (blue boundaries). The first and the third columns show corresponding PET and MR images. As illustrated, the visibility of the target object and contrast with surrounding tissues are more prominent in PET for the first row (showing a small tumor); the target object is almost equally visible for the second row

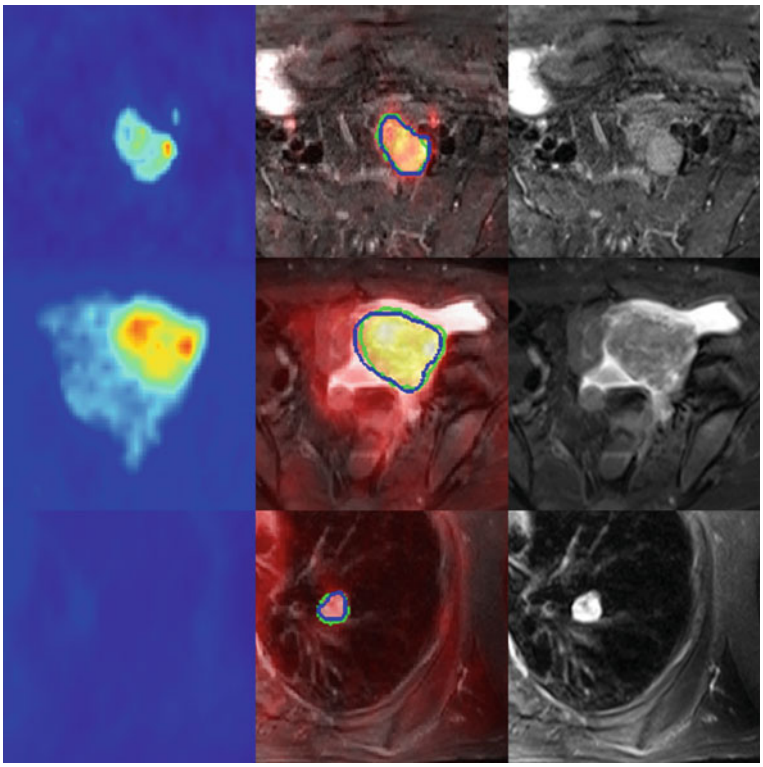

Fig. 2 Co-segmentation results for PET/MR images under different visibility conditions. *The first column* PET images in three different anatomical levels. *The second column* hybrid PET/MR image with segmentation results (*green contours*) and manual references (*blue contours*) overlaid. *The third column* corresponding MR images. Target object is more visible in PET for the first row (*small tumor*); almost equally visible for the second row (*big tumor*); and more visible in MRI for the third row (lung mass)

(showing a larger tumor); and the target object is more prominent in MRI for the third row (showing lung mass). Qualitatively, the co-segmentation results agree well with the anatomical boundaries, as well as hot regions from functional images. Similarly, results for PET/CT images are qualitatively presented in Fig. 3. The second column is the fused images overlaid by segmentation results (green boundaries) and manual references (blue boundaries). The first and the third columns are corresponding PET and CT images. The first row illustrates a consolidation case where the contrast between consolidation region and surrounding tissue in CT image is subtle for the human eye, as pointed out by the red arrow (consolidation) and the yellow arrows (blood vessels). The second row presents a tree-in-bud case where the contrast is higher, but the infected region contains complex structures in the CT image. As can be observed, when contrast between the target region and the surrounding tissue is subtle, human observers tend to rely more on the PET image, while the automatic algorithm is able to capture the difference in both images. Note that in the

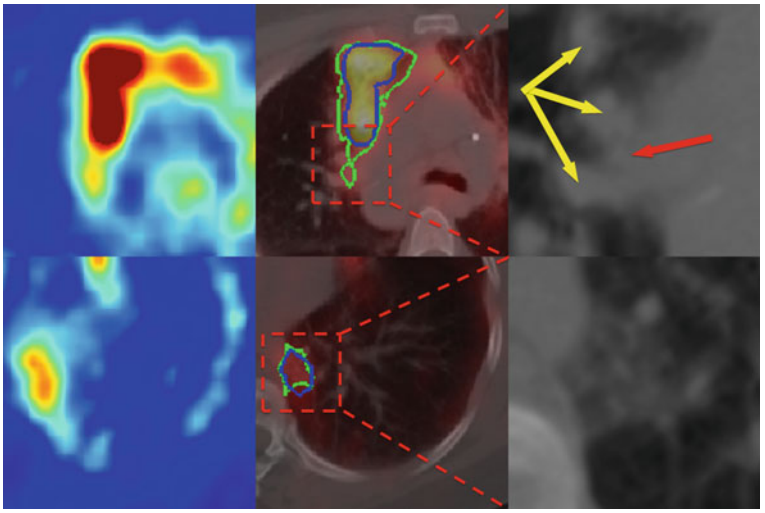

Fig. 3 Co-segmentation results for two PET/CT images. *The first column* PET images in two different anatomical levels. *The second column* hybrid PET/CT image with segmentation results (*green contours*) and manual references (*blue contours*) overlaid. *The third column* corresponding CT images. Contrast between target region and surrounding tissue is subtle for the first row (consolidation), as pointed out by the *red arrow* (consolidation) and the *yellow arrows* (blood vessels), differentiating vessels and consolidations is almost impossible visually. Target region has higher contrast but contains complex structures in the second row (tree-in-bud)

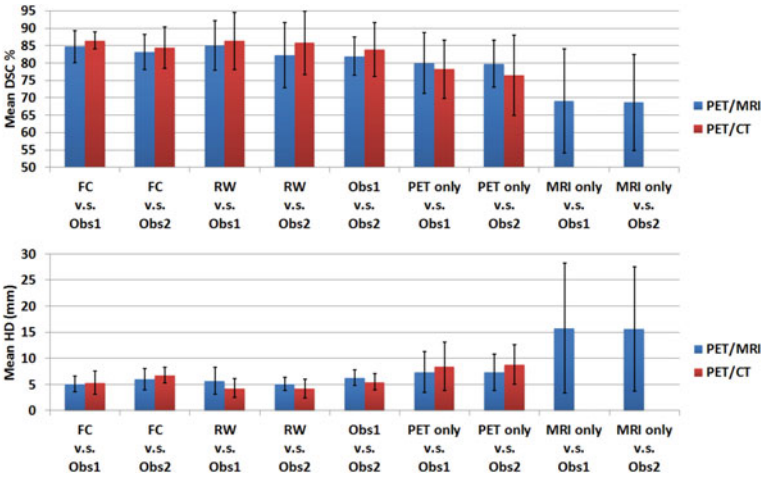

Fig. 4 DSCs and HDs for segmentation results, given by different methods and manual delineations

CT images in Fig. 3, the target object is only partially defined by lung and is discriminant from the surrounding soft tissues with subtle contrast; therefore, segmentation solely based on CT images is often not feasible for the experimental data. Mean and standard deviation of the delineations' DSCs and HDs are presented in Fig. 4. As illustrated, co-segmentation on PET/MR and PET/CT images helps to improve the results over MRI, CT, or PET alone, and it performs better than or comparable to inter-observer variation. Also, although CT alone has poor intensity resolution and gives partial description of the target object, it helps to improve the segmentation with additional boundary constraint.

4 Discussion and Conclusion

In this paper, we proposed a co-segmentation framework using both anatomical and functional images. The proposed method was performed in 3-D image domain, with flexibility to segment various lesions under different visibility conditions. The performance of the method was evaluated using PET/MR and PET/CT images, and high accuracy was achieved. In comparison with the RW image co-segmentation [2], which achieves a DSC of 86 %, our proposed method had a similar performance with heightened efficiency; therefore, our method can be an alternative to the state-of-the-art method. Indeed, the proposed framework performs delineation of the lesions about four times faster than the RW co-segmentation method. Note that perfect registration is assumed for the input anatomical and functional images, and proper registration is needed in presence of mismatches. Also, motion correction could be applied before segmentation to account for inter- and intra-scan motions during imaging. These two issues are important factors for the final accuracy, although they are out of the scope of the proposed framework. Furthermore, it will be meaningful in our future work to test the proposed method on heterogeneous tumors considering the strength of FC in handling variations of local image intensities.

Acknowledgments This research is supported by CIDI, the intramural research program of the National Institute of Allergy and Infectious Diseases (NIAID) and the National Institute of Biomedical Imaging and Bioengineering (NIBIB).

References

1. Han, D., Bayouth, J., Song, Q., Taurani, A., Sonka, M., Buatti, J., Wu, X.: Globally optimal tumor segmentation in PET-CT images: a graph-based co-segmentation method. Inf. Process. Med. Imaging **22**, 245–256 (2011)
2. Bagci, U., Udupa, J.K., Mendhiratta, N., Foster, B., Xu, Z., Yao, J., Chen, X., Mollura, D.J.: Joint segmentation of anatomical and functional images: applications in quantification of lesions from PET, PET-CT, MRI-PET, and MRI-PET-CT images. Med. Image Anal. **17**(8), 929–945 (2013)

3. Udupa, J.K., Samarasekera, S.: Fuzzy connectedness and object definition: theory, algorithms, and applications in image segmentation. CVGIP **58**(3), 246–261 (1996)
4. Drever, L., Robinson, D., McEwan, A., Roa, W.: A comparison of three image segmentation techniques for PET target volume delineation. J. Appl. Clin. Med. Phys. **8**(2), 93–109 (2007)
5. Yu, H., Caldwell, C., Mah, K.: Coregistered FDG PET/CT-based textural characterization of head and neck cancer for radiation treatment planning. IEEE Trans. Med. Imaging. **28**(3), 374–383 (2009)
6. Potesil, V., Huang, X., Zhou, X.S.: Automated tumor delineation using joint PET/CT information. In: SPIE Med. Imaging (2007)
7. Saha, P.K., Udupa, J.K.: Fuzzy connected object delineation: axiomatic path strength definition and the case of multiple seeds. Comput. Vis. Image Underst. **83**(3), 275–295 (2001)
8. Ciesielski, K., Udupa, J., Falco, A., Miranda, P.: Fuzzy connectedness image segmentation in graph cut formulation: a linear-time algorithm and a comparative analysis. J. Math. Imaging Vis. **44**(3), 375–398 (2012)

PET/MRI/VCT: Restoration of Virtual CT from Transmission Scan on PET/MRI Using Joint-Anisotropic Diffusion

Kuangyu Shi, Xiaoyin Cheng, Nassir Navab, Stefan Foerster and Sibylle I. Ziegler

Abstract CT is a mandatory imaging modality for radiation treatment planning (RTP) while MRI and PET have advantages in tumor delineation and dose prescriptions. To avoid multiple scanning and additional high radiation doses, this paper proposes to integrate low dose transmission scan (TX) into a PET/MRI machine for the synthesis of virtual CT (VCT) for treatment planning. TX is usually extremely noisy with artifact spots and it is necessary to smooth the sinogram to obtain interpretable images. However this results in blurred low resolution images. This study introduces a novel joint-anisotropic diffusion (JAD) method which restores VCT images without loss of resolution using additional anatomical images to regularize the filtering. Through reshaping the anisotropic diffusion tensor using MRI, this method guides the diffusion flux to favor the similarity between VCT and MRI leading to an increase of mutual information. For proof of concept, virtual PET/MRI/VCT system with conventional ^{68}Ga ring source was implemented on GATE and realistic TX data were simulated and tested. The results demonstrate that the new approach improves the geometrical accuracy of VCT and provides a potential application for RTP.

Keywords PET/MRI · Virtual CT · Transmission scan · Anisotropic diffusion · Treatment planning

1 Introduction

PET/MRI is an evolving hybrid imaging modality that incorporates magnetic resonance imaging (MRI) and positron-emission tomography (PET) imaging [1, 2]. It has advantages of simultaneous acquisition of soft tissue morphological imaging and molecular imaging, which provides advanced information supporting clinical diagnosis and therapy planning.

K. Shi (✉) · X. Cheng · S. Foerster · S.I. Ziegler
Nuclear Medicine, Technische Universität München, Munich, Germany
e-mail: shi@lrz.tum.de

N. Navab
Computer Aided Medical Procedures, Technische Universität München, Munich, Germany

F. Gao et al. (eds.), *Computational Methods for Molecular Imaging*,
Lecture Notes in Computational Vision and Biomechanics 22,
DOI 10.1007/978-3-319-18431-9_3

Computed tomography (CT) serves as basis for modern radiotherapy treatment planning (RTP) which provides X-ray absorption information for radiation dose calculation [3]. For many cancers such as brain tumors, MRI and PET are often necessary to provide enough soft tissue contrast as well as physiological information for tumor delineation and dose prescription. To avoid multiple scanning as well as additional high radiation dose of CT, RTP based on *only* MRI images has been investigated for several decades [4, 5]. However, MRI signal is based on the proton density of tissues and is not directly related to the electron density. Thus it is not possible for direct estimation of radiation absorption. Virtual CT (VCT) images must be synthesized based on tissue classifications of MRI. However, structures such as bone or air are difficult to exact in MRI and many bone or cavity structures are missing in synthesized VCT. Although RTP can be generated based on VCT of missing structures, which is closely related to a CT-based planning in some situations [5], the application in a wide range is restricted. An atlas can be employed to interpolate the missing structures. However, it depends on many factors and is insensitive to anatomical variations, in particular abnormalities.

Transmission scan (TX) is the traditional way for PET attenuation correction (AC), which compensates the influence of inhomogeneous γ-ray attenuation inside the body [6]. It acquires the radiation absorption data via an external source of annihilative radioactivities (^{68}Ge/Ga) or single photon emitters of higher energy (^{137}Cs). A transmission scan takes usually 2–10 min and the dose is generally insignificant (brain: 1.6 % and cardiac: 2.4 % compared to CT) [7]. In current PET/MRI machines such as Siemens mMR, TX is usually not offered. Bone and air cavity structures can be ignored for AC purpose and MRI based classification is enough for the accuracy of PET imaging [8].

Concerning the high requirements on geometrical and radiological accuracy of RTP, VCT based on MRI alone is generally not enough. Radiation absorption information is necessary for VCT synthesis. Without significant system modification, this can be achieved for PET/MRI, which is already equipped with radiation detectors. In contrast to current main stream PET/MRI, this paper proposes to bring TX back into the scanner for the acquisition of radiation absorption data and generate VCT for RTP accordingly.

One main challenge here is that TX measures the radiation absorption via lines-of-response (LOR) of detector pairs in contrast to conventional CT. The directly reconstructed images are extremely noisy with lots of artifact spots due to low imaging statistics. Smoothing the sinogram can generate interpretable images with the sacrifice of resolution. We propose a novel approach to include the MRI structural information in the restoration of VCT using a joint-anisotropic diffusion (JAD), which filters out the irrelevant spots while preserving the anatomical similarity to MRI. Mutual information between VCT and MRI is introduced to select a proper input MRI image and to control the number of iterations of diffusion. For the proof of concept of PET/MRI/VCT, conventional ^{68}Ga ring sources were configured on a virtual PET/MRI machine implemented using a dedicated imaging system simulation software GATE [9]. The restored VCT demonstrated improved geometrical accuracy and provides potential for RTP.

2 Joint-Anisotropic Diffusion

Anisotropic diffusion (AD) is an image restoration method which reduces noise while preserving structures [10]. However, it is not possible to filter out artifact spots, which are not distinguishable from structures. Joint-anisotropic diffusion (JAD) is developed here to filter out such spots with additional structural information. Given an noisy image $u(x)$ with artifact spots and a structural image $g(x)$, where $x \in \Omega$ and $u(x)$ and $g(x)$ capture the same object with different modalities, JAD is achieved by solving a diffusion equation,

$$\begin{cases} \partial u/\partial t = (1-\alpha) div(\mathcal{D}(u)\nabla u) + \alpha div(\mathcal{D}(g)\nabla u) \\ u(x,0) = u(x) \\ < [(1-\alpha)\mathcal{D}(u) + \alpha\mathcal{D}(g)]\nabla u, \mathbf{n} >= 0 \end{cases} \tag{1}$$

where $\mathcal{D}(u)$ and $\mathcal{D}(g)$ are anisotropic diffusion tensors obtained from the corresponding images and div is the divergence operator. $\mathbf{n}$ denotes the norm direction of image board and the flux across the board is 0, which makes sure that the mass conserves. α is a constant to control the influence of image $g(x)$ during the restoration and $\alpha = 0$ is equivalent to conventional AD. The diffusion tensor $\mathcal{D}(f)$ of image f (f can be u or g) is constructed based on a structure tensor $J_\rho(f) = \nabla f_\rho \nabla f_\rho{}^T$, where ∇ is the gradient operator and f_ρ is the image after convolution of a Gaussian kernel ρ. Suppose λ_1 and λ_2 ($\lambda_1 > \lambda_2$) are two eigenvalues of J_ρ, and thus $\mathcal{D}$ is configured as following:

$$\begin{cases} \zeta_1(\lambda_1) = \begin{cases} 1 & (\lambda_1 \le 0) \\ 1 - exp\left(\frac{-C_m}{(\lambda_1/s)^m}\right) & (\lambda_1 > 0) \end{cases} \\ \zeta_2 \quad = 1 \end{cases} \tag{2}$$

where ζ_1, ζ_2 are eigenvalues of $\mathcal{D}$ and C_m, m and s are constants to control the anisotropy of the diffusion tensor. The diffusion tensor $\mathcal{D}$ relates to the edge direction and contrast. It is mirror invariant ($\mathcal{D}(\nabla f_\rho) = \mathcal{D}(-\nabla f_\rho)$).

JAD reshapes the diffusion tensor $\mathcal{D} = (1-\alpha)\mathcal{D}(u) + \alpha\mathcal{D}(g)$ to combine the internal and external structural information for the filtering. For a spatial location x, if g and u have the same edge as shown in Fig. 1a, JAD will enhance the edge further; if the edge of g conflicts with u as shown in Fig. 1b, JAD leads to smoothing of the edge in u. In general, JAD will locally guide the diffusion flux to the direction which favors the common structure of u and g as shown in Fig. 1c. Globally JAD will lead to an increase of the similarity between the two images, which can be described using mutual information (MI) of u and g:

$$m(u(x), g(x)) = \int_{x\in\Omega} p(u(x), g(x)) log\left(\frac{p(u(x), g(x))}{p(u(x))p(g(x))}\right) dx \tag{3}$$

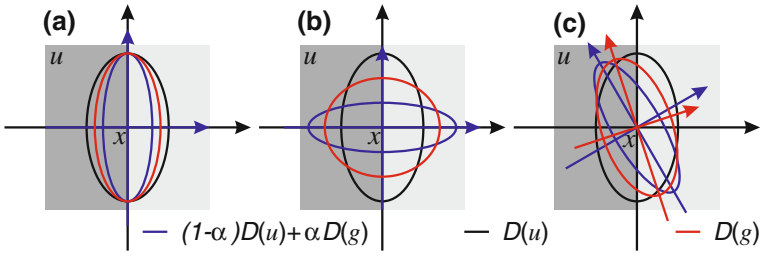

Fig. 1 Joint diffusion tensor when u and g has **a** similar edge **b** conflict edge **c** general relation in local coordinate system of u at position x

where $p(u)$ and $p(g)$ is the marginal probability density function and $p(u, g)$ is the joint probability density function [3]. MI can be used to control the number of iterations of JAD until the increase δm below a threshold ϵ. Note that during the iterations, the local reorganization of the mass may reduce the similarity temporally. MI may get fluctuated although its general trend increases. A smooth window of size L ($m_i = \sum_{j=i-L+1}^{i} m_j$) of MI is considered to avoid immature termination of the iterations.

3 Restoration of Virtual CT

TX measures tissue attenuation coefficients concerning γ-ray photons emitted by the transmission source while CT relates to attenuations of X-ray photons. To synthesize VCT from TX, the measured γ attenuation coefficients need be transformed into correct Hounsfield units (HU) [11]:

$$CT = \begin{cases} 1000\mu^{TX}/\mu_W^{TX} - 1000 & \mu^{TX} \leq \mu_W^{TX} \\ 1000(\mu^{TX} - \mu_W^{TX})(\mu_B^{CT} - \mu_W^{CT})/(\mu_B^{TX} - \mu_W^{TX}) & \mu^{TX} > \mu_W^{TX} \end{cases} \tag{4}$$

where μ^{TX} is the measured attenuation value, μ_W^{TX}, μ_B^{TX} are the known attenuation coefficients of water and bone for TX and μ_W^{CT}, μ_B^{CT} are the known attenuation coefficients of water and bone for CT.

Similar to PET, TX acquires the data via LOR of detector pairs. It is extremely noisy with lots of artifact spots, which are not distinguishable from normal structures [6]. A general smoothing of sinogram will lead to a sacrifice of image resolution. In PET/MRI, a series of MRI images can be acquired together with TX, which provides additional structural information. Instead of nonspecific smoothing, JAD is applied here to selectively filter the noise according to MRI structures using Eq. 1. A selection of MRI images with large starting MI is preferred for JAD.

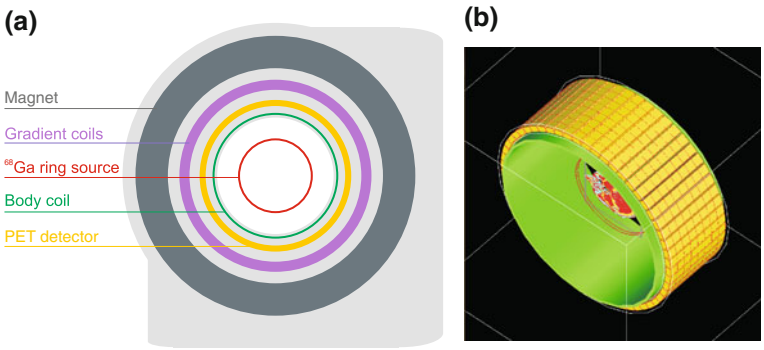

Fig. 2 **a** Configuration of transmission source in PET/MRI; **b** simulation of transmission scans with PET/MRI detector

3.1 PET/MRI/VCT System Configuration and TX Simulation

For the proof of concept, an example virtual machine is proposed with the integration of a ^{68}Ga ring source in a typical PET/MRI system as shown in Fig. 2. It was implemented in GATE, which is a dedicated simulation system for PET, CT or radiotherapy based on realistic modeling of radiologic interaction and detection process [9]. The system was modeled based on the Siemens Biograph mMR including 56×8 APDs, 8×8 LSO crystals per APD and a 1 cm thick body coil (Fig. 2b) [12]. A 100 MBq ^{68}Ga ring source (1 mm thick, 15 cm radius) was placed in the center. CT images were classified into bone, muscle, brain, adipose and air and then placed in the center of the field of view of the virtual PET/MRI/VCT system. The TX and blank scan were simulated for 6 min. The acquisitions were then binned into sinograms with 344 radial bins, 252 projection views without any smoothing and corrected with the blank scan. TX was reconstructed using maximum-likelihood expectation-maximization (MLEM) for 50 iterations.

4 Result

The algorithm was tested on a patient data set with CT and Dixon MRI images (fat, water, in phase, opposed phase) acquired on the same day. The CT image is transferred to the virtual PET/MRI/VCT system on GATE for simulation of realistic TX data. One example slice of CT and the corresponding simulated TX are shown in Fig. 3a, b. After mapping the γ-ray attenuation coefficients to HU values, a noisy VCT image is shown in Fig. 3c, where the artifact spots destroy the diagnostic quality. Figure 3d shows a VCT based on reconstructed TX with general sinogram smoothing. Figure 3e shows the restoration result using conventional AD ($C_m = 0.3314$, $m = 4$, $s = 3.6$, 500 iterations). The artifact spots become enhanced as well. JAD ($C_m = 0.3314$,

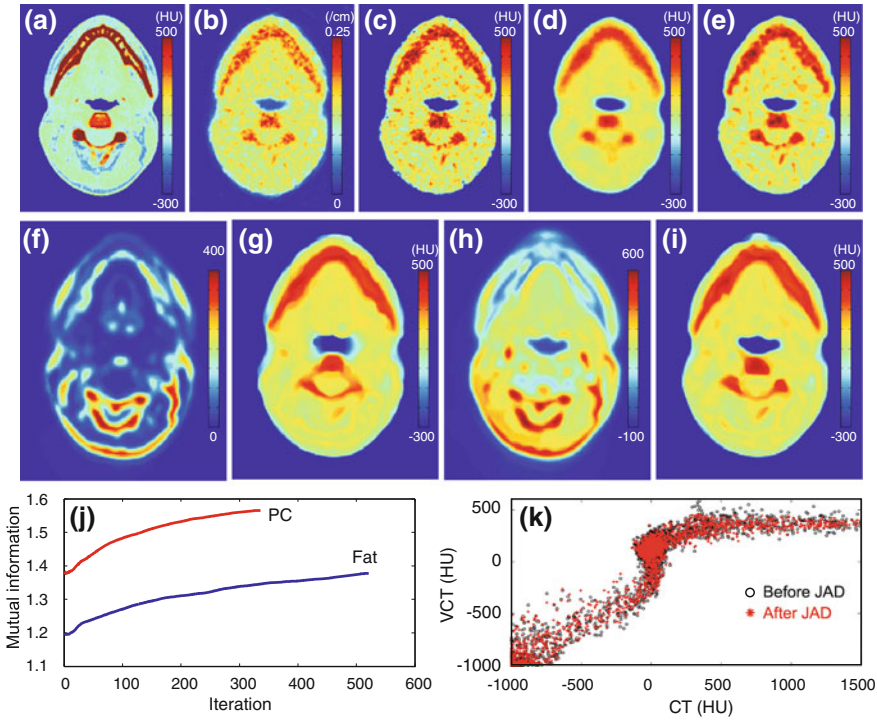

Fig. 3 Result of on example slice: **a** original CT; **b** simulated TX; **c** mapped VCT; **d** VCT using nonspecific smooth; **e** VCT using AD; **f**, **g** Dixon fat MRI and corresponding VCT using JAD; **h**, **i** strongest PC image after PCA on 4 Dixon MRI images and corresponding VCT using JAD; **j** MI course during JAD iterations; **k** correlation between VCT and original CT

$m = 4$, $s = 3.6$, $\alpha = 0.5$, $\epsilon = 10^{-10}$, L = 16) was applied with two different input of MRI image. Figure 3f shows the Dixon fat MRI image which highlights the fat structure. The corresponding VCT using JAD is shown in Fig. 3g. The diffusion stops after 521 iterations and the changes of MI during the iterations are displayed in Fig. 3i. Principal component analysis (PCA) was applied to the 4 MRI images and the strongest principal component (PC) image (Fig. 3g) was sent to JAD. The restored VCT and the corresponding MI development are illustrated in Fig. 3h, j. Although the intensities of fat and PC images are quite different, their influences on the results of JAD are not significant. JAD is stable even with a poor structural input. With more structural information, the PC image has higher MI to start JAD and the quality of the results is improved. A higher starting MI is preferred for JAD to select a good structural image.

From the restored VCT using JAD (Fig. 3i), the main bone structures and pharynx (air) are clearly distinguished, which are usually difficult to extract solely with MRI images. Figure 4a shows a result of MRI based classification by clustering of 4 Dixon MRI images. Each spatial location is associated with a 4 element vector

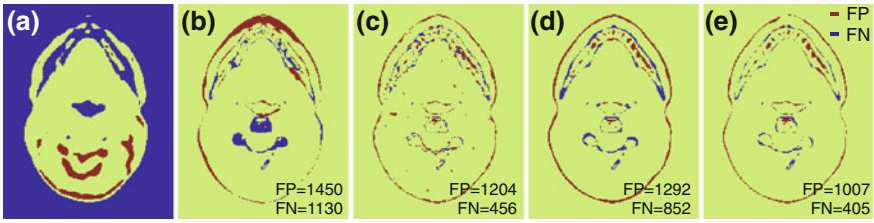

Fig. 4 **a** One tissue classification based on 4 Dixon MRI images; (**b**–**e**) maps of misclassifications without distinction of air and bone based on: **b** MRI, **c** VCT without restoration, **d** smooth VCT and **e** VCT using JAD

field and Euclidean distance was taken as similarity metrics for vector based K-Means algorithm. One cluster of the results denotes air and bone. Without additional information, it is not possible to separate bone further from air. The corresponding map of misclassifications without distinction of air and bone is shown in Fig. 4b. Similarly, maps of misclassifications using VCT in PET/MRI are displayed in Fig. 4c, d. The numbers of false positive (FP) and false negative (FN) voxels are displayed on the images accordingly. The TX based VCT has generally less misclassifications, even when mixing air and bone. Restored VCT using JAD can reduce both FP and FN compared to original VCT and smooth VCT. The test of overall 5 simulated TX data shows that VCT using JAD can improve the accuracy of 39.8–94.7 % compared to MRI classification, 1.1–27.6 % compared to noisy VCT and 38.3–74.5 % compared to smooth VCT. The differentiation of bone from air is obvious for VCT while not straightforward for MRI and the real improvements compared to MRI without Atlas support can be even larger.

Note that the contrasts of the real CT and the restored VCT are different here. The difference is already observable before JAD. A scatter plot of the correlation between VCT and CT (Fig. 3k) shows that the real CT has a wide value range (−1000 to 2000 HU) while VCT has even before JAD a range of −1000 to 500 HU. This is caused by the simulation of TX data which considers only 5 tissue materials offered by GATE. The detail materials such as high density bones are not possible to model and therefore reveal system bias, which is not a problem for real measurements. Nevertheless, the simulation is realistic in physical procedures and generates noisy images resembling real measurements. It is practical in testing the restoration algorithms and proving the system concept.

In general, JAD conserves the mass, where the total radiation absorption properties on a large scale do not vary. The difference between the original image and the restored image are constrained locally. This reduces the spread of possible errors for RTP.

5 Conclusion

This paper proposed a novel approach to restore proper VCT from noisy TX for the purpose of RTP. In particular, we have made the following contributions: (1) we proposed the concept to integrate low dose TX in PET/MRI system to generate virtual CT; (2) we developed a joint-anisotropic diffusion algorithm to regularize noise filtering with additional structural data; (3) we introduced mutual information as a criteria to select a proper structural image and to control the number of iterations for JAD. Our algorithm was tested on realistic simulated TX data and demonstrated an improved geometrical accuracy. This provides a potential application of PET/MRI/VCT in RTP.

There is still debate about the suitability of MRI based AC, additional TX information can enhance the AC for PET/MRI. The current TX is configured with a conventional ring source. More advanced TX configurations such as rotating rod source or single photon source can be adapted to PET/MRI/VCT system similarly. The simultaneous acquisition of TX during PET/MRI is potentially also possible [6].

Sophisticated MRI based classification methods such as pattern recognition with Atlas support [13] are not discussed here but can be extended as future work. The extraction of tissues such as fat can add more detail into VCT which may further improve the accuracy for RTP. Another limitation of the current approach is that the patient-specific geometrical distortion of MRI [4] is not corrected. With the available TX scan, it may be solved by an elastic registration [3] between MRI and TX. The application of PET/MRI/VCT in real RTP needs to be investigated and validated.

References

1. Judenhofer, M.S., Wehrl, H.F., Newport, D.F., Catana, C., Siegel, S.B., Becker, M., Thielscher, A., Kneilling, M., Lichy, M.P., Eichner, M., Klingel, K., Reischl, G., Widmaier, S., Röcken, M., Nutt, R.E., Machulla, H.J., Uludag, K., Cherry, S.R., Claussen, C.D., Pichler, B.J.: Simultaneous PET-MRI: a new approach for functional and morphological imaging. Nat. Med. **14**, 459–465 (2008)
2. Pedemonte, S., Bousse, A., Hutton, B.F., Arridge, S.R., Ourselin, S.: 4-D generative model for PET/MRI reconstruction. MICCAI **6891**(1), 581–588 (2011)
3. Risholm, P., Balter, J., Wells III, W.M.: Estimation of delivered dose in radiotherapy: the influence of registration uncertainty. MICCAI **6891**(1), 548–555 (2011)
4. Stanescu, T., Jans, H.S., Pervez, N., Stavrev, P., Fallone, B.G.: A study on the magnetic resonance imaging (MRI)-based radiation treatment planning of intracranial lesions. Phys. Med. Biol. **53**(13), 3579–3593 (2008)
5. Jonsson, J., Karlsson, M., Karlsson, M., Nyholm, T.: Treatment planning using MRI data: an analysis of the dose calculation accuracy for different treatment regions. Radiat. Oncol. **5**(1), 62–69 (2010)
6. Bailey, D.L., Townsend, D.W., Valk, P.E., Maisey, M.N.: Positron Emission Tomography: Basic Sciences. Springer, New York (2004)
7. Almeida, P., Bendriem, B., de Dreuille, O., Peltier, A., Perrot, C., Brulon, V.: Dosimetry of transmission measurements in nuclear medicine: a study using anthropomorphic phantoms and thermoluminescent dosimeters. Eur. J. Nucl. Med. **25**, 1435–1441 (1998)

8. Martinez-Möller, A., Souvatzoglou, M., Delso, G., Bundschuh, R.A., Chefd'hotel, C., Ziegler, S.I., Navab, N., Schwaiger, M., Nekolla, S.G.: Tissue classification as a potential approach for attenuation correction in whole-body PET/MRI: evaluation with PET/CT data. J. Nucl. Med. **50**(4), 520–526 (2009)
9. Santin, G., Strul, D., Lazaro, D., Simon, L., Krieguer, M., Martins, M., Breton, V., Morel, C.: GATE: a Geant4-based simulation platform for PET and SPECT integrating movement and time management. IEEE Trans. Nucl. Sci. **50**(5), 1516–1521 (2003)
10. Weickert, J.: Anisotropic Diffusion in Image Processing. Teuber Verlag, Stuttgart (1998)
11. Burger, C., Goerres, G., Schoenes, S., Buck, A., Lonn, A., von Schulthess, G.: PET attenuation coefficients from CT images: experimental evaluation of the transformation of CT into PET 511-keV attenuation coefficients. Eur. J. Nucl. Med. Mol. Imaging **29**, 922–927 (2002)
12. Delso, G., Fürst, S., Jakoby, B., Ladebeck, R., Ganter, C., Nekolla, S.G., Schwaiger, M., Ziegler, S.I.: Performance measurements of the Siemens mMR integrated whole-body PET/MR scanner. J. Nucl. Med. **52**(12), 1914–1922 (2011)
13. Hofmann, M., Steinke, F., Scheel, V., Charpiat, G, Farquhar, J., Aschoff, P., Brady, M., Schölkopf, B., Pichler, B.J.: MRI-based attenuation correction for PET/MRI: a novel approach combining pattern recognition and atlas registration. J. Nucl. Med. **49**(11), 1875–1883 (2008)

Large Scale Simplex Optimisation to Accelerate Kinetic Analysis

Nicholas Dowson, Paul Thomas, Jye Smith, Olivier Salvado and Stephen Rose

Abstract Although Positron Emission Tomography images are implicitly dynamic and the temporal variation of tracers often holds relevant information, kinetic analysis of the data is seldom performed due to its computational expense, especially when flexible ODE-based formulations are used. Kinetic analysis at the voxel scale remains expensive even with recent formulations relying on the closed form summation of convolution of exponentials. This work proposes a scheme to accelerate the kinetic analysis of large populations of time activity curves, by selectively sharing tailored simplex optimisations between them. Experiments on synthetic and real data demonstrate that the approach not only accelerates kinetic analysis, but maintains equivalent or better fitting accuracy than existing approaches that optimise time activity curves individually.

Keywords Kinetic analysis · Positron emission tomography · Optimisation

1 Introduction

The raw (list-mode) data of Positron Emission Tomography images is implicitly dynamic, and the temporal evolution of tracer activity holds potentially relevant information. The temporal information is typically discarded in the clinical setting, possibly because the reconstructed data needs further processing to obtain biologically meaningful parameters. Such processing can be computationally expensive when performed at the scale of voxels; when using ordinary differential equation

N. Dowson (✉) · O. Salvado · S. Rose
CSIRO Digital and Productivity Services Flagship, Australian eHealth Research Centre, Level 5, UQ Health Sciences Building, Royal Brisbane and Women's Hospital, Herston, QLD 4029, Australia
e-mail: Nicholas.Dowson@csiro.au
URL: http://aehrc.com/research/biomedical-imaging/

P. Thomas · J. Smith
Specialised PET Services Queensland, Royal Brisbane and Women's Hospital, Herston, QLD, Australia

F. Gao et al. (eds.), *Computational Methods for Molecular Imaging*, Lecture Notes in Computational Vision and Biomechanics 22,
DOI 10.1007/978-3-319-18431-9_4

(ODE) based formulations, optimisation can take several hours to optimise a typical 1.5 million voxel PET scan with 26 time frames (single-threaded). Although other more computationally efficient formulations exist such as Gjedde-Patlak analysis [2, 13] and Logan analysis [7], ODE formulations have the greatest flexibility in describing biological system and are hence the focus of this paper.

The temporal evolution of voxel intensities are referred to as a time activity curves (TACs), T_p, where p is a spatial index. The temporal resolution is limited to a set of time-frames, t_i, indexed by i. Typically an iterative process is used to generate simulated TACs, $S(\mathbf{k})$, based on a set of parameters, $\mathbf{k}$, and a blood input function, $B(t)$. Iterative optimisation is utilised to find a set of parameters that minimise a fitting score, D:

$$\mathbf{k}_p^{(opt)} \leftarrow \arg_{\mathbf{k}} \min D(T_p, S(\mathbf{k})). \tag{1}$$

In previous work, several authors have demonstrated strategies that reduce the expense of kinetic analysis. In the context of Magnetic Resonance (MR) imaging, Martel proposed generating a finite set of initial parameters and associated simulated TACs. The fit of each TAC, T_p, to each simulation, S_a, is measured in a brute force manner and the parameters of the best fitting simulation stored [9]. This approach is robust, but the size of the initial set of parameters scales with the resolution at which the parameter is explored to the power of the number of the parameter elements. Computational efficiency is also dependent on the formulation of the model used for kinetic analysis. After introducing a formulation using ordinary differential equations, Phelps et al. present an equivalent formulation relying on a summation of terms in which a blood input function is convolved with exponential functions [14]. Gunn et al. proposed creating a set of such convolution terms and storing them in a dictionary. Subsequently an efficient optimisation algorithm called basis pursuit is used to select a minimal number of dictionary entries and estimate their coefficients [3]. Smith et al. obtain simulations in closed form by restricting the blood input function to be a sum of exponentials [16]. Basis pursuit retains much of the flexibility of ODE formulations compromising only on the resolution with which parameters are known. Kadrmas and Oktay take the approach of performing optimisation only over the non-linear parameters, and internally performing a non-negative least squares optimisation to obtain the linear parameters [4].

Previous work has focused on improving the efficiency with which TACs can be optimised individually. This work proposes an alternative approach: to share the simulations generated during the optimisation of one TAC with other TACs. This approach is based on two observations. Firstly, many time activity curves closely resemble each other, so parameter updates that improve the cost function for one TAC are likely to have a similar effect on another. Secondly, the evaluation of D only requires simple element-wise operations and hence fewer computational cycles than the evaluation of S, which at the very least requires the convolution of B with one or more exponentials.

2 Method

The components of a kinetic analysis algorithm comprise: a model formulation, a fitting function, an initialisation method and an optimisation algorithm. The efficient formulation proposed by Kadrmas and Oktay [4] for a two compartment model is used here:

$$\begin{aligned} S(t_j;\mathbf{k}) = \kappa_0 B_j + \kappa_b \textstyle\int_{t=0}^{t_j} B(\tau)\mathrm{d}\tau + \kappa_1 \int_{t=0}^{t_j} e^{-\nu_1(t_j-\tau)} B(\tau)\mathrm{d}\tau \\ +\kappa_2 \textstyle\int_{t=0}^{t_j} (e^{-\nu_2(t_j-\tau)} - e^{-\nu_1(t_j-\tau)}) B(\tau)\mathrm{d}\tau \end{aligned}, \tag{2}$$

with the parameter vector being formulated as follows: $\mathbf{k} = (\kappa_0, \kappa_b, \kappa_1, \nu_1, \kappa_2, \nu_2)$. The non-linear parameters are ν_1 and ν_2; the remaining parameters are linear. (2) can be converted to a one compartment model by removing the fourth term, i.e. setting κ_2 to zero. The distance function selected is a normalised sum of square distance function:

$$D(T_p, S(\mathbf{k})) = \frac{\min_{\{\kappa_b,\kappa_0,\kappa_1,\kappa_2\}} \sum_i [T_p(t_i) - S(t_i;\mathbf{k})]^2}{\sum_i [T_p(t_i)]^2}. \tag{3}$$

The minimum function indicates the use of non-negative least squares, using [5] to minimise D as a function of the linear parameters in (2). The normalisation is included to remove the effect of magnitude from the individual TACs for the purposes of comparison, i.e. only mismatches in the shape of the TAC are reported. This has no influence on optimisation because of the use of non-negative least squares optimisation within each non-linear iteration (as proposed in [4]). Non-negative least squares is accompanied by a risk of bias when data is noisy [10], which must traded off against the improvement in computational efficiency.

For initialisation, a small set of parameters is generated on a grid within a region of values defined as plausible in the literature [15]. The linear parameters $\{\kappa_b, \kappa_0, \kappa_1, \kappa_2\}$ are all temporarily fixed to be one with the grid generated over the non-linear parameters. This approach is made possible by the use of non-negative least squares optimisation in evaluating D. Since there are two non-linear parameters (ν_1 and ν_2) the number of initial parameters only expands quadratically with the grid resolution. The parameters are stored with their corresponding simulation in an initialisation dictionary, $K = \{\mathbf{k}_a; S(\mathbf{k}_a) \,|\, a \in [1; N_a]\}$, where N_a is the number of dictionary elements. Each TAC is initialised by computing $D(T_p, S(\mathbf{k}_a))$ for every entry in K and ordering the results such that $D(T_p, S(\mathbf{k}_{r_1})) < D(T_p, S(\mathbf{k}_{r_2})) < D(T_p, S(\mathbf{k}_{r_3})) < D(T_p, S(\mathbf{k}_{\forall r \in [1,N_a] \setminus \{r_1,r_2,r_2\}})$. The collection of top ranked u indices is referred to as $R_{(u)}(K)$.

For the non-linear optimisation the simplex algorithm proposed by Nelder and Mead [12] is used. This algorithm relies on a set of heuristic rules for manipulating a set of points in the space of parameters. The number of points is the number of (non-linear) parameters plus one forming a simplex. For initialisation the three simplex points are obtained using the ranking operation, $R_{(3)}(\{\mathbf{k}^{(1)}, \mathbf{k}^{(2)}, \mathbf{k}^{(3)}, \mathbf{k}^{(new)}\})$.

The simplex algorithm is described, because the implementation used was modified. In each iteration, we calculate the centre of gravity $\mathbf{k}_c = \frac{1}{3}\sum_{a=1}^{3}\mathbf{k}^{(a)}$ of the simplex. Although the number of points (3) is explicitly stated, it is trivial to include more points for more complex model formulations. One of four transformations to the simplex can be performed to propose a new set of parameters (point in Fig. 1), $\mathbf{k}_{new}$, depending on the mode m_p: reflection of the entire simplex (the default transform), expansion of the simplex (if reflection successfully reduces D: $D(\mathbf{k}_{new}) < D(\mathbf{k}^{(1)})$), contraction (if reflection failed produce any improvement ($D(\mathbf{k}_{new}) > D(\mathbf{k}^{(3)})$) or reduction if contraction also failed ($D(\mathbf{k}_{new}) > D(\mathbf{k}^{(3)})$ again). In all cases, $\mathbf{k}_{new}$ replaces the worst ranked point if $D(\mathbf{k}_{new}) < D(\mathbf{k}^{(3)})$. Four parameters are used to control the extent of each transformation: *e.g.* $\alpha = 1$, $\gamma = 2$, $\rho = -\frac{1}{2}$ and $\sigma = \frac{1}{2}$. The simplex algorithm and mathematical expressions used for each operation are illustrated in Fig. 1.

Using the four components just described, kinetic analysis may be performed for individual voxels by iterating the selected optimisation algorithm until the variations in $\mathbf{k}$ or D fall below a predefined threshold, or until a certain number of iterations has been performed as illustrated in Fig. 2a.

The proposed approach differs in some ways from individual optimisation that are highlighted in Fig. 2b. Firstly, a TAC, T_p, is randomly selected from all the set of

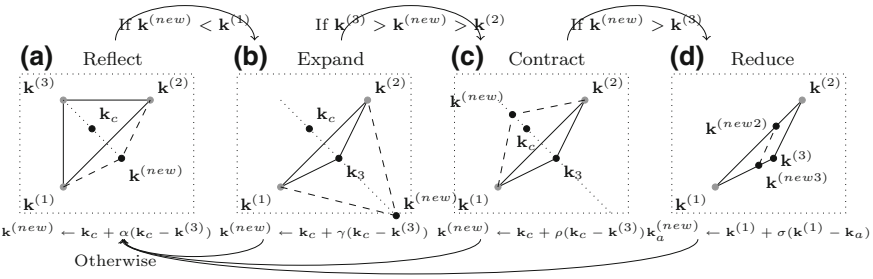

Fig. 1 The simplex algorithm consists of four modes. In all modes, existing points concatenated with $\mathbf{k}_{new}$ are reordered such that $(\mathbf{k}^{(1)}, \mathbf{k}^{(2)}, \mathbf{k}^{(3)}) \leftarrow R_{(3)}(\mathbf{k}^{(1)}, \mathbf{k}^{(2)}, \mathbf{k}^{(3)}, \mathbf{k}_{new})$. Note the $\mathbf{k}$ entries here consist solely of the nonlinear parameters ν_1 and ν_2

	(a) Individual Optimisation		**(b)** Proposed Approach
1	**For each** TAC	1	**For each** TAC
2	Initialise using $R_{(3)}(K)$ operation	2	Initialise using $R_{(3)}(K)$ operation
3	**For** $i \in [0; N_{iterations}]$	3	**For** $i \in [0; N_{iterations}]$
		X	Select random TAC T_p
		Y	$\mathbf{k}^{(new)} \leftarrow \text{Simplex}'(m_p, \mathbf{k}^{(1)}, \mathbf{k}^{(2)}, \mathbf{k}^{(3)}) + \epsilon$
4	**For each** TAC	4	**For each** TAC
Y	$\mathbf{k}^{(new)} \leftarrow \text{Simplex}(m_p, \mathbf{k}^{(1)}, \mathbf{k}^{(2)}, \mathbf{k}^{(3)})$		
5	Compute $D(T_p, S(\mathbf{k}^{(new)}))$	5	Compute $D(T_p, S(\mathbf{k}^{(new)}))$
6	$(\mathbf{k}^{(1)}, \mathbf{k}^{(2)}, \mathbf{k}^{(3)}) \leftarrow$ $R_{(3)}(\mathbf{k}^{(1)}, \mathbf{k}^{(2)}, \mathbf{k}^{(3)}, \mathbf{k}^{(new)})$	6	$(\mathbf{k}^{(1)}, \mathbf{k}^{(2)}, \mathbf{k}^{(3)}) \leftarrow$ $R_{(3)}(\mathbf{k}^{(1)}, \mathbf{k}^{(2)}, \mathbf{k}^{(3)}, \mathbf{k}^{(new)})$
7	Update simplex mode, m_p (Fig. 1)	7	Update simplex mode, m_p (Fig. 1)

Fig. 2 Differences between **a** individual optimisation and **b** the proposed approach

TACs. Secondly, *outside* the loop over TACs, a new set of parameters is generated using the simplex algorithm for T_p, illustrated by the shift in line Y to be above line 4 in Fig. 2b. Thirdly, a small random offset, ϵ, is added to the proposed point. Finally, in the reduction mode only $\mathbf{k}^{(3)}$ is reduced to generate a single $\mathbf{k}_{new}$.

The selection of a single TAC and generation of a single parameter set, relies on the observation that many TACs in images are similar to each-other. Hence, a new set of parameters that reduces D for one TAC is likely to reduce D for others. Also the evaluation of D is generally lower than the evaluation of S, even in efficient formulations. So in some cases it is more efficient to evaluate D multiple times than to evaluate S.

All the TACs are initialised from the same dictionary K, so several TACs may have the same combination of simplex points. On occasion two such TACs, p_1 and p_2 may be consecutively selected and $\mathbf{k}_{p_1}^{(new)}$ may be such that D improves for the T_{p_1}, but not for T_{p_2}. At some later stage when T_{p_2} is selected, $\mathbf{k}_{p_2}^{(new)}$ is generated, but this is the same as $\mathbf{k}_{p_1}^{(new)}$. Having been generated before, this will offer no improvement for any TACs, wasting the computational cycles expended on evaluating $S(\mathbf{k}_{p_2}^{(new)})$ and the overhead of the iteration. In practice, such occurrences are frequent, motivating for the insertion of a random offset, ϵ on line Y in Fig. 2b. The offset is generated from a normal distribution with standard deviation of 5 % of the magnitude of $\mathbf{k}^{(r_1)}$.

In the reduce phase of the simplex algorithm, the simplex points $\mathbf{k}^{(2)}$ and $\mathbf{k}^{(3)}$ are shifted towards the highest ranked point, $\mathbf{k}^{(1)}$. In the proposed approach, this is modified so that only the lowest ranked point, $\mathbf{k}^{(3)}$, is manipulated in this manner, because the algorithm as presented in Fig. 2b only caters for a single $\mathbf{k}^{(new)}$ each iteration. Modifying the proposed approach further to cater for multiple generated parameters and comparing TACs against both sets of parameters will be examined in future work.

The proposed approach and comparison methods were implemented in Matlab, but in all cases the code was vectorised to maintain efficiency. For comparison, a Levenberg-Marquardt [6, 8] algorithm for individual optimisation was also implemented.

3 Experiments and Results

Experiments were performed using synthetically generated data and real data. For the synthetic experiment a set of TACs were simulated from randomly generated parameters. The parameters were distributed uniformly in a biologically plausible range of values as reported in the literature [15]. The restriction that $\nu_2 < \nu_1$ [4] was enforced by sorting the non-linear parameters. Poisson distributed noise was added, but assuming large numbers of event counts, allowing approximation by a normal distribution. The standard deviations added ranged from 5 to 25 % as suggested by the literature [1, 11] (plus a margin).

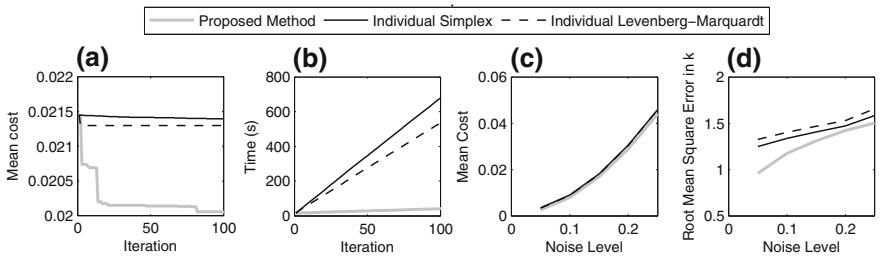

Fig. 3 Results of experiments on synthetic data. Plots of **a** mean cost function and **b** computational cost as a function of iteration are shown. Also **c** mean cost function and **d** mean root mean square error in **k** are shown as a function of noise level

The real-data experiment used an available image of a late stage glioma patient imaged using 6-[18F] fluoro-l-dopa (FDOPA) on a Phillips Gemini GXL scanner. The scan consisted of eight 15 s frames, two 30 s frames, two 1 min frames and fourteen 5 min frames. The final volume consisted of ninety 128×128 planes with isotropic voxels 2 mm on a side. The blood input function was extracted from 20 connected voxels in the left and right carotid arteries that had the highest intensity during the first 2 min of scanning. The blood input function and frame lengths were re-used for the synthetic experiments. Optimisation was performed using the proposed approach and by performing individual optimisation using the simplex and Levenberg-Marquardt optimisation algorithms.

The results of the synthetic experiment are presented in Fig. 3. Figure 3a, b respectively report the mean cost function and computational cost as a function of iteration. All the algorithms converge by 100 iterations, but the proposed approach obtains an improved mean cost in comparison to the other methods. The proposed approach has the lowest computational cost, by nearly an order of magnitude. The lower computational cost of the proposed method arises from the fact that it reduces the number of evaluations of S. The reduction in computational cost is only partly offset by the increased number of evaluations of D. Of the two individual optimisation approaches, Levenberg-Marquardt was more efficient, because a tolerance of 10^{-9} was applied to variations in new $\mathbf{k}$ values. New $\mathbf{k}$ values insufficiently distinctive from the $\mathbf{k}^{(1)}$ were not evaluated. The lower mean cost of the proposed approach could potentially arise from the existence of local minima. The sharing of simulations enables TACs to escape local minima, but this relies on TACs having some similarity to each-other, i.e. $\mathbf{k}_p^{(new)}$ is relevant to multiple TACs.

Figure 3c, d show mean cost and mean root mean square error (RMSE) in $\mathbf{k}$ as a function of noise. In both cases, error increases with noise as would be expected. In terms of mean cost, the bulk of the difference between the proposed approach and other methods resides at high noise levels, where local minima would be more likely. Notably, the differences between optimisation approaches are more distinctive for mean RMSE in $\mathbf{k}$ than for the cost function, D, implying that many choices of parameters give similar cost functions (i.e. local minima exist).

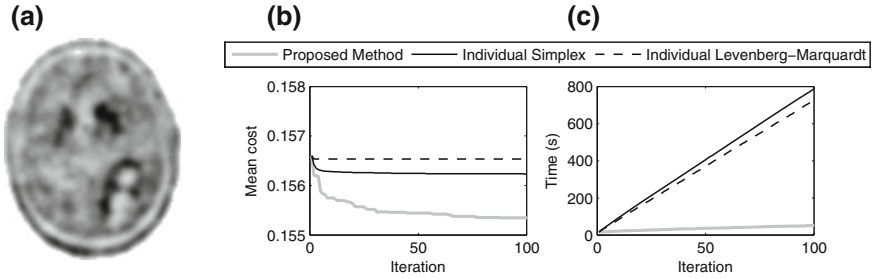

Fig. 4 Results of experiments on real data. **a** shows a single slice from the test data set. Plots of **b** mean cost function and **c** computational cost as a function of iteration are also shown

The upper range of noise was set relatively high to act as a proxy for the cases where poor outlier voxels were continually selected by the method, because the high noise ensures a many (if not most) samples have only a limited relationship to their neighbours. The model degrades gracefully as the noise levels are increased, even at high levels. The high noise also tests the case where the model is a poor reflection of the data. In addition, the synthetic experiment with its randomly selected parameters, acts a substitute for test data typified by different biological and tracer characteristics, or where tissue biology is heterogeneous.

The results of the real data experiment are shown in Fig. 4 along with a single slice from the data set in Fig. 4a. Figure 4b, c respectively report the mean cost function and computational cost as a function of iteration. One hundred iterations is sufficient for all algorithms to converge. As for the synthetic data, the proposed approach obtains a lower mean cost than when performing individual optimisation, with less computational expense.

4 Conclusion

This paper has proposed an alternative approach to improving computational efficiency, which instead of reducing the cost of evaluating S, relies on sharing the simulations between multiple time activity curves, reducing the number of evaluations of S. This is particularly advantageous for the flexible but computationally expensive ODE formulations for biological systems. Testing with synthetic and real data demonstrated that this approach improves computational efficiency by an order of magnitude while obtaining the same or better quality of fit as measured by the cost function. Synthetic experiments might not necessarily completely represent real-world cases of heterogeneous tissue or inappropriate model selection, and in future work a wider range of real test data will be sought. Comparisons to basis pursuit were not included due to limited space, but are also of interest as they may allow similar fit error at similar speeds. Future work will also explore more sophisticated strategies to select the TAC from which $\mathbf{k}$ is generated.

References

1. Dahlbom, M., Schiepers, C., Czernin, J.: Comparison of noise equivalent count rates and image noise. IEEE Trans. Nucl. Sci. **52**(5), 1386–1390 (2005). doi:10.1109/TNS.2005.858176
2. Gjedde, A.: High- and low-affinity transport of d-glucose from blood to brain. J. Neurochem. **36**(4), 1463–1471 (1981). doi:10.1111/j.1471-4159.1981.tb00587.x
3. Gunn, R.N., Gunn, S.R., Turkheimer, F.E., Aston, J.A.D., Cunningham, V.J.: Positron emission tomography compartmental models: a basis pursuit strategy for kinetic modeling. J. Cereb. Blood Flow Metab. **22**(12), 1425–1439 (2002). doi:10.1097/01.wcb.0000045042.03034.42
4. Kadrmas, D.J., Oktay, M.B.: Generalized separable parameter space techniques for fitting 1K–5K serial compartment models. Med. Phys. **40**(7), 072–502 (2013). doi:10.1118/1.4810937
5. Lawson, C.L., Hanson, R.J.: Society for Industrial and Applied Mathematics: Solving Least Squares Problems. SIAM, Philadelphia (1995)
6. Levenberg, K.: A method for the solution of certain problems in least squares. Q. Appl. Math. **2**, 164–168 (1944)
7. Logan, J., Fowler, J.S., Volkow, N.D., Wolf, A.P., Dewey, S.L., Schlyer, D.J., MacGregor, R.R., Hitzemann, R., Bendriem, B., Gatley, S.J.: Graphical analysis of reversible radioligand binding from time-activity measurements applied to [N-11C-methyl]-(-)-cocaine PET studies in human subjects. J. Cereb. Blood Flow Metab. **10**(5), 740–7 (1990). doi:10.1038/jcbfm.1990.127
8. Marquardt, D.: An algorithm for least-squares estimation of nonlinear parameters. SIAM J. Appl. Math. **11**, 431–441 (1963)
9. Martel, A.L.: A fast method of generating pharmacokinetic maps from dynamic contrast-enhanced images of the breast. In: Larsen, R., Nielsen, M., Sporring, J. (eds.) MICCAI, vol. 4191, pp. 101–108. Springer, Berlin Heidelberg (2006)
10. Meikle, S.R., Matthews, J.C., Brock, C.S., Wells, P., Harte, R.J., Cunningham, V.J., Jones, T., Price, P.: Pharmacokinetic assessment of novel anti-cancer drugs using spectral analysis and positron emission tomography: a feasibility study. Cancer Chemother. Pharmacol. **42**(3), 183–93 (1998). doi:10.1007/s002800050804
11. Mettivier, G., Tabacchini, V., Conti, M., Russo, P.: Signal-to-noise gain at variable randoms ratio in TOF PET. IEEE Trans. Nucl. Sci. **59**(5), 1948–1957 (2012). doi:10.1109/TNS.2012.2198833
12. Nelder, J.A., Mead, R.: A simplex method for function minimization. Comput. J. **7**(4), 308–313 (1965). doi:10.1093/comjnl/7.4.308
13. Patlak, C.S., Blasberg, R.G., Fenstermacher, J.D.: Graphical evaluation of blood-to-brain transfer constants from multiple-time uptake data. J. Cereb. Blood Flow Metabol. **3**(1), 1–7 (1983). doi:10.1038/jcbfm.1983.1
14. Phelps, M.E., Huang, S.C., Hoffman, E.J., Selin, C., Sokoloff, L., Kuhl, D.E.: Tomographic measurement of local cerebral glucose metabolic rate in humans with (f-18)2-fluoro-2-deoxy-d-glucose: Validation of method. Ann. Neurol. **6**(5), 371–388 (1979). doi:10.1002/ana.410060502
15. Schiepers, C., Chen, W., Cloughesy, T., Dahlbom, M., Huang, S.C.: 18F-FDOPA kinetics in brain tumors. J. Nucl. Med. **48**(10), 1651–1661 (2007). doi:10.2967/jnumed.106.039321
16. Smith, B., Hamarneh, G., Saad, A.: Fast GPU fitting of kinetic models for dynamic PET. In: MICCAI High Performance Workshop (2010)

Gradient Projection for Regularized Cryo-Electron Tomographic Reconstruction

Shadi Albarqouni, Tobias Lasser, Weaam Alkhaldi, Ashraf Al-Amoudi and Nassir Navab

Abstract Cryo-ET has recently emerged as a leading technique to investigate the three-dimensional (3D) structure of biological specimens at close-to-native state. The technique consists of acquiring many two-dimensional (2D) projections of the structure under scrutiny at various tilt angles under cryogenic conditions. The 3D structure is recovered through a number of steps including projection alignment and reconstruction. However, the resolution currently achieved by cryo-ET is well below the instrumental resolution mainly due to the contrast transfer function of the microscope, the limited tilt range and the high noise power. These limitations make the 3D reconstruction procedure very challenging. Here, we propose a new regularized reconstruction technique based on projected gradient algorithm. Using the gold-standard method for resolution assessment, the Fourier Shell Correlation, we show that the proposed technique outperforms the commonly used reconstruction methods in ET, including the filtered back projection and the algebraic reconstruction techniques.

Keywords Tomographic reconstruction · Gradient projection · Sparse regularization · Cryo-electron tomography

S. Albarqouni (✉) · T. Lasser · N. Navab
Computer Aided Medical Procedures (CAMP), Technische Universität München, Munich, Germany
e-mail: shadi.albarqouni@tum.de

S. Albarqouni · W. Alkhaldi · A. Al-Amoudi
Deutsches Zentrum Für Neurodegenerative Erkrankungen (DZNE), Bonn, Germany

N. Navab
Computer Aided Medical Procedures (CAMP), Johns Hopkins University, Baltimore, MD, USA

F. Gao et al. (eds.), *Computational Methods for Molecular Imaging*,
Lecture Notes in Computational Vision and Biomechanics 22,
DOI 10.1007/978-3-319-18431-9_5

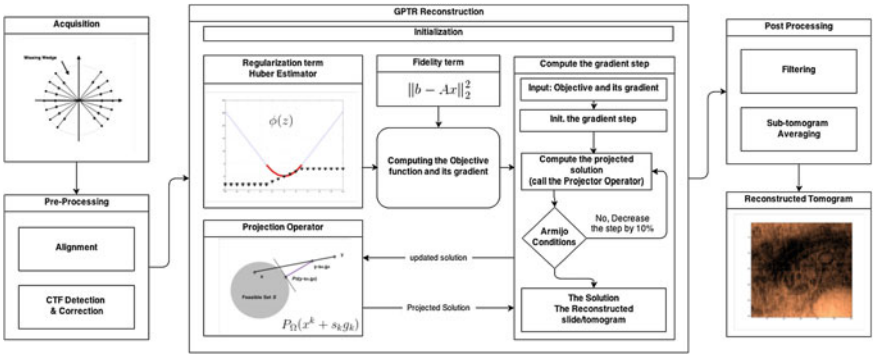

Fig. 1 Cryo-ET image processing pipeline

1 Introduction

Over the last decade, cryo-Electron Tomography (cryo-ET) has drawn the attention of researchers. It is considered the most powerful imaging technique to address fundamental questions on biological structures at both cellular and molecular levels [1]. It also bridges the gap between low-resolution imaging techniques (e.g. light microscopy) and high-resolution techniques (e.g. single particle electron microscopy). Cryo-ET merges the principles of transmission electron microscopy (TEM) and the principle of tomographic imaging by acquiring several two-dimensional projection images of biological structures at limited tilt range and close-to-native condition. These two-dimensional projection images are then reconstructed to a three-dimensional image (called tomogram), after passing through a pipeline of alignment and restoration procedure as shown in Fig. 1. For a more in-depth description of the cryo-ET and the associated image processing pipeline see [2].

The resolution of the reconstructed tomogram, however, is affected by the low signal to noise ratio (SNR) of the projection images (typically 0.1–0.01) and the limited angular coverage (typically ± 60–$70°$) resulting in wedge-shaped missing information in Fourier space, the so-called "missing wedge", making the reconstruction process very challenging and demanding [3]. Therefore, developing a reconstruction technique that incorporates the sparsely sampled data, the noise level, and that preserves the structural edges while pushing the limits of resolution further, is highly desirable.

One technique, that was recently investigated in the context of cryo-ET [4], is the direct Fourier reconstruction using a non-uniform fast Fourier transform, but it is still hampered by the high computational cost. Therefore, the current standard method in cryo-ET is the weighted (filtered) back projection (WBP) based on Radon transform [5], which backprojects the high-pass filtered projection data into the tomogram. One of the main drawbacks of WBP, however, are the typical streak artifacts due to the missing wedge of data, as well as the corresponding degraded resolution.

Recently, due to the increasing availability of high performance computing, variants of the algebraic reconstruction technique (ART) have been employed and extended in the context of cryo-ET [6–8], which formulate the reconstruction problem as a large system of linear equations to be solved iteratively. In this manner, the missing wedge effect can be minimized, but the reconstruction performance is still degraded due to the noisy input data.

The projected gradient-based algorithm [9] has recently been used in several applications such as compressed sensing [10], X-ray computed tomography [11] and in sparse signal recovery [12] to solve the $L_2 - L_1$ optimization problem (LASSO). In this paper, the reconstruction problem is formulated as an unconstrained, regularized optimization problem, using the projected gradient-based algorithm to solve the problem on a feasible bounded set. In the following we denote this approach as Gradient-based Projection Tomographic Reconstruction, in short GPTR.

2 Problem Formulation

2.1 Notation and Concept

The three-dimensional reconstructed tomogram is represented as a discretized, linearized vector $x \in \mathbb{R}^n$, with $n \in \mathbb{N}$. The forward problem can be formulated using the discrete version of the Radon Transform [5] for each measurement $j \in \{1, \ldots, m\}$:

$$b_j = \sum_{i=1}^{n} a_{ij} x_i \qquad \text{or in short} \qquad b = Ax, \tag{1}$$

where $b \in \mathbb{R}^m$ represents the measured projection data, $(a_{ji}) = A \in \mathbb{R}^{m \times n}$ represents the weighting matrix, where a_{ji} is the weight with which each voxel in the image vector $x \in \mathbb{R}^n$ contributes to the jth projection measurement.

For computational simplicity, we treat the three-dimensional tomogram as a stack of two-dimensional slices, which are reconstructed individually and then stacked together again to a three-dimensional tomogram.

2.2 Formulation as an Optimization Problem

The tomographic reconstruction problem of solving $b = Ax$ for the unknown x in cryo-ET is underdetermined due to the limited tilt angles, as well as ill-posed, for example due to the measurement noise. Hence a direct solution is not feasible. Instead, a least squares approach is adopted to find an approximate solution

$$x_{LS} = \arg\min_{x} \|b - Ax\|_2^2, \tag{2}$$

where $\|\cdot\|_2$ denotes the Euclidean norm. This least squares problem can be solved iteratively following a weighted gradient descent approach,

$$x^{k+1} = x^k + s_k g_k, \qquad k = 0, 1, \ldots, \tag{3}$$

with a starting value x^0, step size s_k and a weighted gradient $g_k = QA^T D(b - Ax^k)$. Standard techniques such as SIRT or SART can be expressed in this form by choosing s_k and g_k appropriately (for example we can get SIRT by setting Q and D to the identity matrix in g_k, and $s_k \in [0, 2]$). This is also true for the recently developed techniques I-SIRT, M-SART or W-SIRT [6–8]. To accelerate convergence, a standard numerical method like the LSQR variant of the conjugate gradient algorithm [13] can be used instead.

However, due to the strong measurement noise, a least squares approach will lead to noise amplification in later iterates x^k. To combat this, a regularization term $\phi(x)$ is added to stabilize the solution,

$$x_{opt} = \arg\min_{x \in \Omega} \|b - Ax\|_2^2 + \beta\phi(x) \tag{4}$$

with a Lagrangian multiplier $\beta > 0$ describing the strength of the regularizer, and further restricting the solution to a feasibility region $\Omega = \left\{x = (x_i) \in \mathbb{R}^n : x_i \in [l, u]\right\}$, where $l, u \in \mathbb{R}$ denote lower and upper bounds of the signal.

A popular choice for the regularization term is the isotropic total variation, $\phi(x) = \|Dx\|_1$, where D is an operator computing the gradient magnitude using finite differences and circular boundary conditions, and $\|\cdot\|_1$ denotes the ℓ_1-norm. However, isotropic TV is non-smooth and thus poses problems for the optimization procedure.

3 Methodology

3.1 Problem Statement

We investigate the regularized optimization problem as in Eq. (4), that is optimizing the objective function

$$f(x) = \|b - Ax\|_2^2 + \beta\phi(x). \tag{5}$$

To overcome the non-smoothness of isotropic total variation, we use the smooth Huber function ϕ_{huber} [14], replacing the ℓ_1-norm of total variation. ϕ_{huber} is illustrated in Fig. 1 and is expressed by

$$\phi_{huber}(z) = \begin{cases} 0.5\,|z|^2 & |z| \le \tau \\ \tau\,|z| - 0.5\tau^2 & \text{else,} \end{cases} \tag{6}$$

where the threshold parameter τ is estimated by the median absolute deviation, $\tau = median(|z - median(z)|)$. Using $\phi(x) := \phi_{\text{huber}}(Dx)$ the objective function $f(x)$ is now smooth and convex, so the projected gradient method can be applied to find a feasible solution $x \in \Omega$.

3.2 Projected Gradient Algorithm

The projected gradient method [9] is an extended version of gradient descent, where the solution is iteratively projected onto the convex feasible set Ω, as illustrated in Fig. 1. Starting with an initial value x_0, it is expressed by:

$$x^{k+1} = P_\Omega(x^k + s_k g_k), \qquad k = 0, 1, \ldots, n_{\text{iter}} \tag{7}$$

where $g_k = \nabla f(x)$ is the gradient of the objective function in (5), and s_k is the step size. The step size s_k is computed using an inexact line search, limiting the gradient step by the Armijo conditions [15], ensuring the curvature and a sufficient decrease of the objective function as follows:

$$f(x(s_k)) - f(x) \le \frac{\alpha}{s_k} \|x(s_k) - x\|^2, \tag{8}$$

where α is a scalar constant.

The algorithm *Gradient Projection for Tomographic Reconstruction (GPTR)* is illustrated in Fig. 1 and can be described as follows:

1. **Input**: The algorithm is fed with the aligned projections b associated with the tilt angle, and the forward projector matrix A [16].
2. **Set the initial conditions**: The initial reconstructed tomogram is set to $x^0 \in \Omega = \left\{x = (x_i) \in \mathbb{R}^n : x_i \in [l, u]\right\}$ with lower and upper bounds $l, u \in \mathbb{R}$, a tolerance and the maximum number of iterations n_{iter}.
3. **Iterate for** $k = 0, 1, \ldots, n_{\text{iter}}$
   a. **Compute the objective function** $f(x)$: The data fidelity term $\|b - Ax^k\|_2^2$ and the regularization term $\phi(x^k) = \phi_{\text{huber}}(Dx^k)$ are computed.
   b. **Compute the gradient** g_k: The gradient $g_k = \nabla f(x^k)$ is computed.
   c. **Compute the gradient step** s_k: Initialize $s_k = 1$. Check the Armijo condition in Eq. (8) and iteratively reduce s_k by 90 % until the condition is met (or a maximum number of iterations are performed).
   d. **Update the solution estimate** x^{k+1}: Compute x^{k+1} by computing the gradient descent update step $x^k + s_k g_k$ and projecting it onto Ω as in Eq. (7).

4. **Output**: x^{k+1} is the output once the iteration has converged (i.e. the tolerance was reached) or the maximum number of iterations has been reached.

Convergence of the GPTR algorithm with a regularized objective function has not been investigated yet. However, a detailed analysis for a similar problem can be found in [17].

4 Experiments and Results

The proposed reconstruction method has been examined on real data, a tomographic tilt series of a vitrified freeze-substituted section of HeLa cells [18], which were collected from −58 to 58° at 2° intervals and imaged at a pixel size of 1.568 nm using Tecani T10 TEM, equipped with 1k × 1k CCD camera. To keep the computational complexity manageable, the projection data was down-sampled by a factor of eight. The solution of the proposed technique GPTR was compared with those of the most commonly used techniques in the field of cryo-ET, namely WBP, LSQR, and SART. The parameters were set to $\beta = 0.1$, a tolerance of 10^{-2}, $n_{iter} = 50$ and $[u, l] = [0.01, 1000]$.

4.1 Fourier Shell Correlation

The Fourier Shell Correlation (FSC), the typical quantitative analysis of the resolution within the cryo-EM and cryo-ET community [19], was applied to the different reconstruction methods to assess the resolution. The tomograms were reconstructed from even and odd projections separately and the Fourier transform of each tomogram was calculated (F_n and G_n for even and odd tomograms respectively). Then the Fourier plane was binned into K shells from 0 to the Nyquist frequency as shown in Fig. 2b. The FSC is calculated as follows:

$$FSC(K) = \frac{\sum_{n \in K} F_n G_n^*}{\sqrt{\sum_{n \in K} |F_n|^2 \sum_{n \in K} |G_n|^2}}, \tag{9}$$

where K is the Fourier shell and $*$ is the conjugate Fourier transform.

The results are shown in Fig. 2a. The 0.5-FSC-criterion is usually used as an indicator of the achieved resolution. It is quite clear that the FSC of the GPTR method crosses the 0.5-FSC-line at high spatial frequencies, outperforming the FSCs of the traditional methods. Moreover, the high frequency components (noise) are attenuated in GPTR (indicating robustness to noise), while the noise was aligned with the data in the SART technique. Also, we observed that the GPTR reached the tolerance in 6–8 iterations, while the LSQR did not converge in 10 iterations.

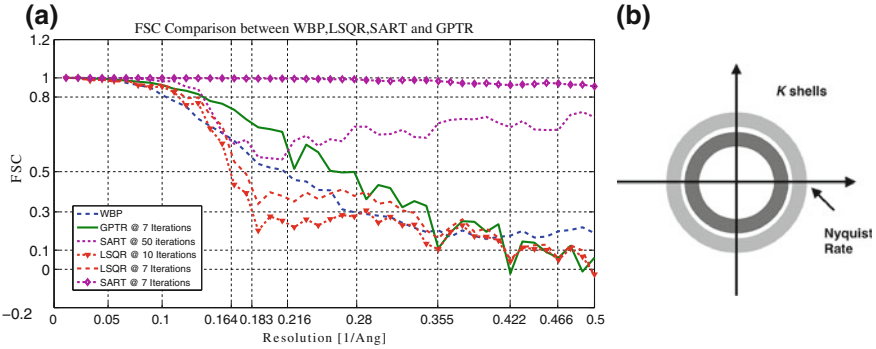

Fig. 2 FSC curves for different reconstruction techniques (WBP, LSQR, SART and GPTR) with their cutoff frequency 0.164, 0.216, 0.28 and Inf respectively. **a** FSC curves. **b** Fourier shells

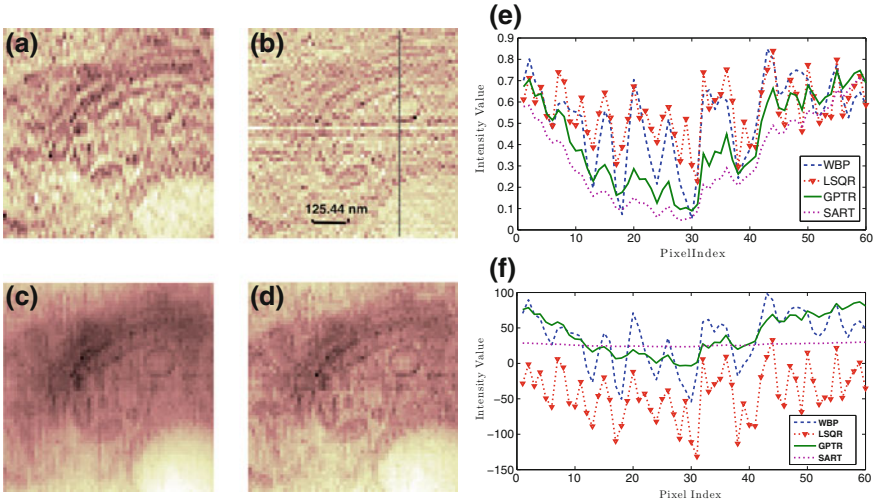

Fig. 3 Reconstructed tomograms and their line profiles (LP). **a** WBP. **b** LSQR. **c** SART. **d** GPTR. **e** The intensity LP. **f** The un-normalized intensity LP

4.2 Line Profile

Another experiment was performed using $n_{iter} = 7$, leaving the other parameters unchanged. Then an intensity line profile (LP), the dashed line in Fig. 3b, was drawn for the different reconstructed tomograms from Fig. 3a–d to investigate the edge preservation, the noise effects and the non-negativity of the intensity values. The LP was drawn for both the normalised sections in Fig. 3e and the un-normalised ones in Fig. 3f. It is clear from Fig. 3f that the LP behaviour of GPTR is similar to theSART,

which follows the underlying object smoothly, while the GPTR preserves the edges better. Additionally, GPTR by construction produces positive intensities, while WBP and LSQR are affected clearly by the noise and the negative values.

5 Conclusion

In this paper, the gradient projection for tomographic reconstruction (GPTR) was proposed to solve the regularized optimization problem for the Electron tomographic reconstruction. A proof of principle was demonstrated on real ET data using the gold standard for resolution measurement, FSC. A gain of several nanometers in resolution (0.5-FSC criterion) was achieved without affecting the sharpness of the structure (line-profile criterion). Extending the work for large data sets and/or in the field of cryo-ET is currently under development.

References

1. McEwen, B.F., Marko, M.: The emergence of electron tomography as an important tool for investigating cellular ultrastructure. J. Histochem. Cytochem. **49**(5), 553–563 (2001)
2. Frank, J.: Electron Tomography: Methods for Three-Dimensional Visualization of Structures in the Cell. Springer, New York (2006)
3. Diebolder, C.A., et al.: Pushing the resolution limits in cryo electron tomography of biological structures. J. Microsc. **248**(1), 1–5 (2012)
4. Chen, Y., Förster, F.: Iterative reconstruction of cryo-electron tomograms using nonuniform fast Fourier transforms. J. Struct. Biol. (2013)
5. Radon, J.: Über die Bestimmung von Funktionen durch ihre Integralwerte längs gewisser Mannigfaltigkeiten. Berichte über die Verhandlungen der Saechsischen Akad. der Wissenschaften zu Leipzig, Math. Naturwissenschaftliche Klasse. **69**, 262–277 (1917)
6. Wan, X. et al.: Modified simultaneous algebraic reconstruction technique and its parallelization in cryo-electron tomography. In: 15th International Conference on Parallel and Distributed Systems (ICPADS), pp. 384–390. IEEE (2009)
7. Qian, Z., et al.: Improving SIRT algorithm for computerized tomographic image reconstruction. Recent Advances in Computer Science and Information Engineering, pp. 523–528. Springer, Berlin (2012)
8. Wolf, D., et al.: Weighted simultaneous iterative reconstruction technique for single-axis tomography. Ultramicroscopy **136**, 15–25 (2014)
9. Calamai, P., Moré, J.: Projected gradient methods for linearly constrained problems. Math. Program. **39**(1), 93–116 (1987)
10. Figueiredo, M.A.T., et al.: Gradient projection for sparse reconstruction: application to compressed sensing and other inverse problems. IEEE J. Sel. Top. Signal Process. **1**(4), 586–597 (2007)
11. Jørgensen, J.H. et al.: Accelerated gradient methods for total-variation-based CT image reconstruction (2011). arXiv:1105.4002v1
12. Harmany, Z. et al.: Gradient projection for linearly constrained convex optimization in sparse signal recovery. In: 17th IEEE International Conference on Image Processing (ICIP), pp. 3361–3364 (2010)

13. Paige, C.C., Saunders, M.A.: LSQR: an algorithm for sparse linear equations and sparse least squares. ACM Trans. Math. Softw. **8**(1), 43–71 (1982)
14. Huber, P.: Robust estimation of a location parameter. Ann. Math. Stat. **35**(1), 73–101 (1964)
15. Armijo, L.: Minimization of functions having Lipschitz continuous first partial derivatives. Pac. J. Math. **16**(1), 1–3 (1966)
16. Hansen, P.C., Saxild-Hansen, M.: AIR tools-a MATLAB package of algebraic iterative reconstruction methods. J. Comput. Appl. Math. **236**(8), 216–2178 (2012)
17. Gong, P. et al.: A general iterative shrinkage and thresholding algorithm for non-convex regularized optimization problems (2013). arXiv Prepr. arXiv1303.4434
18. Dumoux, M., et al.: Chlamydiae assemble a pathogen synapse to hijack the host endoplasmic reticulum. Traffic **13**(12), 1612–1627 (2012)
19. Penczek, P.A.: Resolution measures in molecular electron microscopy, in Methods in Enzymology, pp. 73–100 (2010)

Joint Direct Motion Estimation/Kinetic Images Reconstruction from Gated PET Data

Alexandre Bousse, Jieqing Jiao, Kris Thielemans, David Atkinson, Simon Arridge, Sébastien Ourselin and Brian F. Hutton

Abstract In this paper we propose a unified framework for joint motion estimation/kinetic image reconstruction from gated dynamic PET data. The method is a generalisation of previous work to include gated data. The kinetic and motion parameters are estimated jointly by maximisation of the penalised likelihood. Kinetic parameters are estimated with an optimisation transfer approach, and the non-rigid motion is estimated with a quasi-Newton algorithm. Results on synthetic phantom data show that there is an advantage in jointly estimating motion and kinetics compared to pre-estimating the motion field for motion-compensated kinetic image reconstruction.

Alexandre Bousse and Jieqing Jiao are equally contributed to this work.

A. Bousse (✉) · K. Thielemans · B.F. Hutton
Institute of Nuclear Medicine, University College London, London, UK
e-mail: a.bousse@ucl.ac.uk

K. Thielemans
e-mail: k.thielemans@ucl.ac.uk

B.F. Hutton
e-mail: b.hutton@ucl.ac.uk

J. Jiao (✉) · S. Arridge · S. Ourselin
Centre for Medical Image Computing, University College London, London, UK
e-mail: j.jiao@ucl.ac.uk

S. Arridge
e-mail: s.arridge@cs.ucl.ac.uk

S. Ourselin
e-mail: s.ourselin@cs.ucl.ac.uk

D. Atkinson
Centre for Medical Imaging, University College London, London, UK
e-mail: d.atkinson@ucl.ac.uk

B.F. Hutton
Centre for Medical Radiation Physics, University of Wollongong,
Wollongong, Australia

F. Gao et al. (eds.), *Computational Methods for Molecular Imaging*,
Lecture Notes in Computational Vision and Biomechanics 22,
DOI 10.1007/978-3-319-18431-9_6

Keywords Dynamic PET · Parametric imaging · Optimisation transfer · Kinetic analysis · Gating · Non-rigid registration

1 Introduction

Respiratory and cardiac motion are severe sources of degradation in whole-body PET imaging. Since the motion is quasi-periodic and a PET acquisition lasts for multiple cycles, gating the data by a series of motion phases for PET image reconstruction can reduce the motion artefacts, but potentially leads to increased noise when only a subset of the data is used. Motion can be pre-estimated (for compensated reconstruction) or jointly estimated with the activity distribution [1, 2].

Furthermore, in a dynamic PET scan, where the data is recorded immediately after the injection of radioactive tracer to monitor the *in vivo* pharmacokinetic process, the tracer kinetics can be estimated directly from PET raw data. This problem is addressed in several papers (see [3] for a review), but to our knowledge the current direct methods do not estimate motion.

We addressed the problem of joint motion estimation/compensation kinetic image reconstruction in [4] for brain rigid motion. In this paper we extend our method to joint kinetic image reconstruction from gated data with non-rigid motion. The motion and kinetic parameters are estimated from raw data by penalised maximum likelihood. The algorithm is similar to [4] with extensions to handle gated data and to tackle non-rigid motion. Our joint kinetic motion estimation (JKM) algorithm was tested on a 2-D+t torso dynamic PET phantom for the reconstruction of the parametric image related to the influx rate. We compared our method with a motion-compensated kinetic image reconstruction with a pre-estimated motion field (PMK).

2 Method

2.1 Kinetic Model

In this work we use the Gjedde-Patlak approach [5] to model the irreversible tracer kinetics, although the same framework can be applied to other linear models. In whole-body PET, a significant number of the scans are intended to assess the irreversible retention of a tracer, for example FDG, an analogue of glucose widely used in cancer imaging and cardiac imaging. When at least one irreversible compartment exists, after the equilibrium is reached between the reversible compartments and plasma, the ratio of free tracer in tissue and in plasma becomes time-independent, and the total tracer concentration in tissue $C_{\mathrm{T}}(t)$ can be described as

$$C_{\mathrm{T}}(t) = K_{\mathrm{I}} \int_0^t C_{\mathrm{P}}(\tau)\,\mathrm{d}\tau + \kappa C_{\mathrm{P}}(t)$$

where $C_{\mathrm{P}}(t)$ is the tracer concentration in plasma, K_{I} is the influx rate that represents the irreversible uptake of the tracer and $\kappa C_{\mathrm{P}}(t)$ is the reversible component. For PET data that are divided into frames, the activity at frame m is

$$\int_{t_{\mathrm{s},m}}^{t_{\mathrm{e},m}} C_{\mathrm{T}}(t)\,\mathrm{d}t = \mathcal{F}_m(\boldsymbol{\vartheta}) = [\boldsymbol{B}\boldsymbol{\vartheta}]_m = \begin{bmatrix} b_{m,1} & b_{m,2} \end{bmatrix} \begin{bmatrix} \vartheta_1 \\ \vartheta_2 \end{bmatrix},$$

where $[\boldsymbol{\vartheta}]_q = \vartheta_q$, $\vartheta_1 = K_{\mathrm{I}}$, $\vartheta_2 = \kappa$, $[\boldsymbol{B}]_{m,1} = b_{m,1} = \int_{t_{\mathrm{s},m}}^{t_{\mathrm{e},m}} \int_0^t C_{\mathrm{P}}(\tau)\,\mathrm{d}\tau\,\mathrm{d}t$, $[\boldsymbol{B}]_{m,2} = b_{m,2} = \int_{t_{\mathrm{s},m}}^{t_{\mathrm{e},m}} C_{\mathrm{P}}(t)\,\mathrm{d}t$, $t_{\mathrm{s},m}$ and $t_{\mathrm{e},m}$ are the starting and ending times of frame m. Note that this linear representation is not FDG-specific and can be applied to other tracers [4].

2.2 Gating

The perpetual motion of the patient is assumed to be cyclic (e.g. respiratory or cardiac motion) in order to regroup PET data into n_{g} gates, each gate $l \in \{1, \ldots, n_{\mathrm{g}}\}$ corresponding to a patient position in the cycle. In dynamic PET, gating should be performed in accordance with the separation of dynamic data into frames $m \in \{1, \ldots, n_{\mathrm{t}}\}$. Since motion cycles are short compared to kinetic time frames, we will assume each frame covers at least one cycle. Figure 1 is an illustration of the double gate/frame time indexation: in this example each cycle comprises of 3 states; frame $m = 1$ contains 1 cycle and each gate corresponds to 1 dataset, $m = 3$ contains 5 cycles and each gate corresponds to 5 datasets, etc.

At gate l, frame m, the collected PET data is a vector $\boldsymbol{g}_{l,m} \in \mathbb{N}^{n_{\mathrm{b}}}$, where n_{b} is the number of detector bins, and $g^i_{l,m} = [\boldsymbol{g}_{l,m}]_i \in \mathbb{N}$ is the number of collected counts at bin i. For simplicity, a pair 'gate l-frame m' is referred to as a 'state' (l, m). The complete collection of data at each state is $\boldsymbol{g} = (\boldsymbol{g}_{l,m})_{l,m=1}^{n_{\mathrm{g}},n_{\mathrm{t}}} \in \mathbb{N}^{n_{\mathrm{g}} \times n_{\mathrm{t}} \times n_{\mathrm{b}}}$.

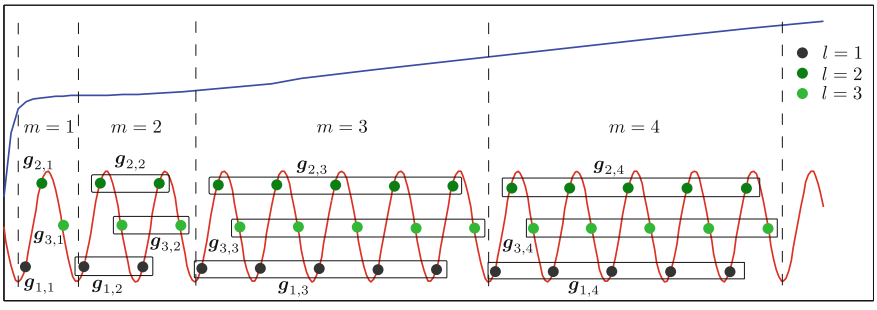

Fig. 1 Schematic representation of the gate/frame temporal indexation

2.3 Penalised Log-likelihood

In absence of motion, the PET dynamic activity is determined by the kinetic model $\boldsymbol{\mathcal{F}} = (\mathcal{F}_m)_{m=1}^{n_\mathrm{t}}$, $\mathcal{F}_m : \mathbb{R}^{n_\mathrm{k} \times n_\mathrm{v}} \to \mathbb{R}^{n_\mathrm{v}}$, and the parametric images $\boldsymbol{\Theta} = (\boldsymbol{\vartheta}_j)_{j=1}^{n_\mathrm{v}} \in \mathbb{R}^{n_\mathrm{k} \times n_\mathrm{v}}$, where $\boldsymbol{\vartheta}_j \in \mathbb{R}^{n_\mathrm{k}}$ is the collection of kinetic parameters in voxel j, and $n_\mathrm{t}, n_\mathrm{v}$ and n_k are respectively the number of time frames, voxels and kinetic parameters. The qth parameter value at voxel j is $[\boldsymbol{\Theta}]_{q,j} = [\boldsymbol{\vartheta}_j]_q = \vartheta_{q,j}$. Each row $[\vartheta_{q,1}, \ldots, \vartheta_{q,n_\mathrm{v}}]$ of $\boldsymbol{\Theta}$ is a parametric image. The activity volume distribution at frame m takes the form of a vector $\boldsymbol{\mathcal{F}}_m(\boldsymbol{\Theta}) = (\mathcal{F}_m(\boldsymbol{\vartheta}_j))_{j=1}^{n_\mathrm{v}} \in \mathbb{R}^{n_\mathrm{v}}$, and $\mathcal{F}_m(\boldsymbol{\vartheta}_j) = [\boldsymbol{B}\boldsymbol{\vartheta}_j]_m \in \mathbb{R}$ is the activity at frame m and voxel j. $\boldsymbol{B}$ is a $n_\mathrm{t} \times n_\mathrm{k}$ matrix. In this work $n_\mathrm{k} = 2$, but larger dimension models can be applied [4]. Note that although we focus on the influx constant K_I, the two components of each $\boldsymbol{\vartheta}_j$, $\vartheta_{1,j} = K_{\mathrm{I},j}$ and $\vartheta_{2,j} = \kappa_j$, are estimated.

When patient motion is present, the activity distribution is deformed by a mapping $\varphi_{\boldsymbol{\alpha}} : \mathbb{R}^3 \to \mathbb{R}^3$ parametrised by $\boldsymbol{\alpha} \in \mathbb{R}^{n_\mathrm{w}}$ where n_w is the number of parameters of the warping model. Introducing the voxel grid $\mathcal{G} = \{\boldsymbol{x}_k,\ k = 1, \ldots, n_\mathrm{v}\} \subset \mathbb{R}^3$ and using the framework from [1], the operator associated to $\varphi_{\boldsymbol{\alpha}}$ and $\mathcal{G}$ is the $n_\mathrm{v} \times n_\mathrm{v}$ square matrix $\boldsymbol{W}_{\boldsymbol{\alpha}}$ defined by $[\boldsymbol{W}_{\boldsymbol{\alpha}}]_{j,k} = w(\varphi_{\boldsymbol{\alpha}}(\boldsymbol{x}_j) - \boldsymbol{x}_k)$, where $w : \mathbb{R}^3 \to \mathbb{R}^+$ is an interpolating function. Assuming that PET data are divided into n_g gates and n_t time frames, and that the motion between the gates is consistent for all time frames, the activity distribution image at state (l, m) is $\boldsymbol{W}_{\boldsymbol{\alpha}_l}\boldsymbol{\mathcal{F}}_m(\boldsymbol{\Theta})$, where $\boldsymbol{\alpha}_l$ is the motion parameter at gate l.

The PET measured data at state (l, m) is a Poisson random vector $\boldsymbol{g}_{l,m} \in \mathbb{N}^{n_\mathrm{b}}$ with independent entries and of mean

$$\overline{\boldsymbol{g}}_{l,m}(\boldsymbol{\Theta}, \boldsymbol{\alpha}_l) = \boldsymbol{P}\boldsymbol{W}_{\boldsymbol{\alpha}_l}\boldsymbol{\mathcal{F}}_m(\boldsymbol{\Theta}) + \boldsymbol{r}_{l,m} \in \mathbb{R}^{n_\mathrm{b}}$$

where $\boldsymbol{P} \in \mathbb{R}^{n_\mathrm{b} \times n_\mathrm{v}}$ is the PET system matrix i.e. $[\boldsymbol{P}]_{i,j} = p_{i,j}$ is the probability that an annihilation occurring in j is detected in i, $\boldsymbol{r}_{l,m}$ is the average background at state (l, m). Let $\boldsymbol{A} = (\boldsymbol{\alpha}_l)_{l=1}^{n_\mathrm{g}} \in \mathbb{R}^{n_\mathrm{g} \times n_\mathrm{w}}$ be the collection of motion parameters at each gate. The log-likelihood given the complete dynamic gated data $\boldsymbol{g}$ is

$$L(\boldsymbol{g}|\boldsymbol{\Theta}, \boldsymbol{A}) = \sum_{l=1}^{n_\mathrm{g}} \sum_{m=1}^{n_\mathrm{t}} \sum_{i=1}^{n_\mathrm{b}} g_{l,m}^i \log \overline{g}_{l,m}^i(\boldsymbol{\Theta}, \boldsymbol{\alpha}_l) - \overline{g}_{l,m}^i(\boldsymbol{\Theta}, \boldsymbol{\alpha}_l)$$

in which $\overline{g}_{l,m}^i = [\overline{\boldsymbol{g}}_{l,m}]_i$ (constants were omitted). Penalised maximum-likelihood (PML) joint estimation of $\boldsymbol{\Theta}$, $\boldsymbol{A}$ consists of maximising

$$\Phi(\boldsymbol{\Theta}, \boldsymbol{A}) = L(\boldsymbol{g}|\boldsymbol{\Theta}, \boldsymbol{A}) + \beta U(\boldsymbol{\Theta}) + \gamma V(\boldsymbol{A}) \tag{1}$$

where $U(\boldsymbol{\Theta})$ and $V(\boldsymbol{A})$ are penalty terms on kinetic and warping parameters respectively. Here $U(\boldsymbol{\Theta})$ is a quadratic penalty function on the dynamic volumes $\boldsymbol{\mathcal{F}}_m(\boldsymbol{\Theta})$:

$$U(\boldsymbol{\Theta}) = -\frac{1}{8}\sum_{m=1}^{n_\mathrm{t}}\sum_{j=1}^{n_\mathrm{v}}\sum_{k\in\mathcal{N}_j}\omega_{j,k}(\mathcal{F}_m(\boldsymbol{\vartheta}_j) - \mathcal{F}_m(\boldsymbol{\vartheta}_k))^2$$

where $\mathcal{N}_j$ is neighbourhood of j and the $\omega_{j,m}$'s are weights satisfying $\omega_{j,k} = \omega_{k,j}$.

In this work the maximisation of $\Phi(\boldsymbol{\Theta}, \boldsymbol{A})$ is performed in alternation between $\boldsymbol{\Theta}$ and $\boldsymbol{A}$.

2.4 Kinetic Image Reconstruction

In this section $\boldsymbol{A}$ is fixed. We used the methodology from [6] with some modifications for gated data. For compactness, $\Phi(\boldsymbol{\Theta}, \boldsymbol{A})$, $L(\boldsymbol{g}|\boldsymbol{\Theta}, \boldsymbol{A})$ and $\overline{g}^i_{l,m}(\boldsymbol{\Theta}, \boldsymbol{\alpha}_l)$ are temporarily denoted $\Phi(\boldsymbol{\Theta})$, $L(\boldsymbol{\Theta})$ and $\overline{g}^i_{l,m}(\boldsymbol{\Theta})$. The motion compensated system matrix $\boldsymbol{P}\boldsymbol{W}_{\boldsymbol{\alpha}_l}$ is denoted $\boldsymbol{P}^l$, with $[\boldsymbol{P}^l]_{i,j} = p^l_{i,j}$. We focus on the maximisation of $\Phi(\boldsymbol{\Theta}) = L(\boldsymbol{\Theta}) + \beta U(\boldsymbol{\Theta})$.

Let $\boldsymbol{\Theta}^{\mathrm{old}} = (\boldsymbol{\vartheta}_j^{\mathrm{old}})_{j=1}^{n_\mathrm{v}}$ be a current estimate of $\boldsymbol{\Theta}$. To maximise $\Phi(\boldsymbol{\Theta})$, we proceed as in our previous work [4] but with gated dynamic data. As in [6], we followed [7, 8] to derive the voxel-separating surrogate functions $Q^L(\boldsymbol{\Theta}|\boldsymbol{\Theta}^{\mathrm{old}}) \leq L(\boldsymbol{\Theta})$ and $Q^U(\boldsymbol{\Theta}|\boldsymbol{\Theta}^{\mathrm{old}}) \leq U(\boldsymbol{\Theta})$ for L and U:

$$Q^L(\boldsymbol{\Theta}|\boldsymbol{\Theta}^{\mathrm{old}}) = \sum_{j=1}^{n_\mathrm{v}} q^L(\boldsymbol{\vartheta}_j; \boldsymbol{f}^{\mathrm{em},j}, \boldsymbol{p}_j),\ \ Q^U(\boldsymbol{\Theta}|\boldsymbol{\Theta}^{\mathrm{old}}) = \sum_{j=1}^{n_\mathrm{v}} q^U(\boldsymbol{\vartheta}_j; \boldsymbol{f}^{\mathrm{reg},j}, \omega_j), \tag{2}$$

$$\forall \boldsymbol{\vartheta}, \boldsymbol{f}^{\mathrm{em}}, \boldsymbol{p} = (p^l)_{l=1}^{n_\mathrm{g}},\quad q^L(\boldsymbol{\vartheta}; \boldsymbol{f}^{\mathrm{em}}, \boldsymbol{p}) = \sum_{l=1}^{n_\mathrm{g}} p^l \sum_{m=1}^{n_\mathrm{t}} f^{\mathrm{em}}_{l,m} \log \mathcal{F}_m(\boldsymbol{\vartheta}) - \mathcal{F}_m(\boldsymbol{\vartheta}), \tag{3}$$

$$\forall \boldsymbol{\vartheta}, \boldsymbol{f}^{\mathrm{reg}}, \omega,\quad q^U(\boldsymbol{\vartheta}; \boldsymbol{f}^{\mathrm{reg}}, \omega) = -\frac{1}{2}\omega \sum_{m=1}^{n_\mathrm{t}} (\mathcal{F}_m(\boldsymbol{\vartheta}) - f^{\mathrm{reg}}_m)^2,$$

and the parameters in (2) are $\boldsymbol{p}_j = (p^l_j)_{l=1}^{n_\mathrm{g}}$, $p^l_j = \sum_{i=1}^{n_\mathrm{b}} p^l_{i,j}$, $\omega_j = \sum_{k\in\mathcal{N}_j}\omega_{j,k}$. $\boldsymbol{f}^{\mathrm{em},j} = (f^{\mathrm{em},j}_{l,m})_{l,m=1}^{n_\mathrm{g},n_\mathrm{t}}$ and $\boldsymbol{f}^{\mathrm{reg},j} = (f^{\mathrm{reg},j}_m)_{m=1}^{n_\mathrm{t}}$ are defined for each voxel j and state (l, m) as

$$f^{\mathrm{em},j}_{l,m} = \frac{\mathcal{F}_m(\boldsymbol{\vartheta}_j^{\mathrm{old}})}{p^l_j}\sum_{i=1}^{n_\mathrm{b}} \frac{p^l_{i,j} g^i_{l,m}}{\overline{g}^i_{l,m}(\boldsymbol{\Theta}^{\mathrm{old}})},$$

$$f^{\mathrm{reg},j}_m = \frac{1}{2\omega_j}\sum_{k\in\mathcal{N}_j}\omega_{j,k}\left(\mathcal{F}_m(\boldsymbol{\vartheta}_j^{\mathrm{old}}) + \mathcal{F}_m(\boldsymbol{\vartheta}_k^{\mathrm{old}})\right).$$

Unlike [4], there are no time frame weights in the sum over m in (3), as the gates and frame indices are separated. The voxel separation in (2) allows to compute each $\boldsymbol{\vartheta}_j$ independently as

$$\boldsymbol{\vartheta}_j^{\text{new}} = \underset{\boldsymbol{\vartheta} \in \mathbb{R}_+^{n_\text{k}}}{\arg\max}\, q^L(\boldsymbol{\vartheta}; \boldsymbol{f}^{\text{em},j}, \boldsymbol{p}_j) + \beta q^U(\boldsymbol{\vartheta}; \boldsymbol{f}^{\text{reg},j}, \omega_j)\ . \tag{4}$$

Note that $u = q^L + \beta q^U$ is strictly concave as the Hessian matrix of q^U is $-\omega \boldsymbol{B}^\top \boldsymbol{B} < \boldsymbol{0}$ ($\boldsymbol{B}$ is a $n_\text{t} \times n_\text{k}$ matrix with strictly positive entries and $n_\text{t} > n_\text{k} = 2$). Besides, the set $\mathscr{D} = \{\boldsymbol{\vartheta} \in \mathbb{R}_+^{n_\text{k}},\ u(\boldsymbol{\vartheta}) \geq u(\boldsymbol{1})\} \subset \mathbb{R}_+^{n_\text{k}}$ is compact (u is continuous and coercive) and convex so the existence and uniqueness of $\boldsymbol{\vartheta}_j^{\text{new}} \in \mathscr{D}$ is guaranteed.

Again, in order to achieve (4), we applied the optimisation transfer from [6]. The task is the same for each voxel so index j is omitted. Given the hyper-parameters $\boldsymbol{f}^{\text{em}}$, $\boldsymbol{f}^{\text{reg}}$, $\boldsymbol{p}$ and ω in (4), we derive the parameter-separating surrogate function $H^L(\boldsymbol{\vartheta}|\boldsymbol{\vartheta}^{\text{old}}) \leq q^L(\boldsymbol{\vartheta}; \boldsymbol{f}^{\text{em}}, \boldsymbol{p})$ and $H^U(\boldsymbol{\vartheta}|\boldsymbol{\vartheta}^{\text{old}}) \leq q^U(\boldsymbol{\vartheta}; \boldsymbol{f}^{\text{reg}}, \omega)$:

$$H^L(\boldsymbol{\vartheta}|\boldsymbol{\vartheta}^{\text{old}}) = \sum_{q=1}^{n_\text{k}} h^L(\vartheta_q; \vartheta_q^{\text{em}}, c_q),\ \ H^U(\boldsymbol{\vartheta}|\boldsymbol{\vartheta}^{\text{old}}) = \sum_{q=1}^{n_\text{k}} h^U(\vartheta_q; \vartheta_q^{\text{reg}}, \omega a_q) \tag{5}$$

where the parameter-wise surrogate functions h^L and h^U are defined as

$$h^L(\vartheta; \vartheta^{\text{em}}, c) = c(\vartheta^{\text{em}} \log \vartheta - \vartheta), \quad h^U(\vartheta; \vartheta^{\text{reg}}, a) = -\frac{a}{2}(\vartheta - \vartheta^{\text{reg}})^2$$

and the hyper-parameters in (5) are $c_q = b_q \sum_{l=1}^{n_\text{g}} p^l$, $p^l = [\boldsymbol{p}]_l$, $b_q = \sum_{m=1}^{n_\text{t}} b_{m,q}$, $a_q = \sum_{m=1}^{n_\text{t}} b_{m,q} \sum_{q'=1}^{n_\text{k}} b_{m,q'}$,

$$\vartheta_q^{\text{em}} = \frac{\sum_{l=1}^{n_\text{g}} p^l \vartheta_q^{\text{em},l}}{\sum_{l=1}^{n_\text{g}} p^l} \text{ with } \vartheta_q^{\text{em},l} = \frac{\vartheta_q^{\text{old}}}{b_q} \sum_{m=1}^{n_\text{t}} \frac{b_{m,q} f_{l,m}^{\text{em}}}{[\boldsymbol{B}\boldsymbol{\vartheta}^{\text{old}}]_m}$$

and

$$\vartheta_q^{\text{reg}} = \vartheta_q^{\text{old}} - a_q^{-1} \sum_{m=1}^{n_\text{t}} \left(b_{m,q} [\boldsymbol{B}\boldsymbol{\vartheta}^{\text{old}}]_m - f_m^{\text{reg}} \right)\ .$$

Note that the intermediary parameter ϑ_q^{em} corresponds to a weighted average across the gates of the intermediary parameter found in [4]. Each parameter ϑ_q is updated from $\boldsymbol{\vartheta}^{\text{old}}$ independently as

$$\vartheta_q^{\text{new}} = \underset{\vartheta \in \mathbb{R}_+}{\arg\max} \left\{ h^L(\vartheta; \vartheta_q^{\text{em}}, c_q) + \beta h^U(\vartheta; \vartheta_q^{\text{reg}}, \omega a_q) \right\}$$

and corresponds to the unique positive root of a second degree polynomial (see [4]). The overall scheme is a nested algorithm with 2 iteration indices (one index per optimisation transfer). A complete algorithm description is given in [4].

2.5 Motion Estimation

Similarly to Sect. 2.4, $L(\boldsymbol{g}|\boldsymbol{\Theta}, \boldsymbol{A})$ is temporarily denoted $L(\boldsymbol{A})$. In addition, we denote $\boldsymbol{f}_m = \boldsymbol{\mathcal{F}}_m(\boldsymbol{\Theta})$, and $\overline{\boldsymbol{g}}_{l,m}(\boldsymbol{\Theta}, \boldsymbol{\alpha}_l)$ is replaced by $\overline{\boldsymbol{g}}_{l,m}(\boldsymbol{\alpha}_l) = \boldsymbol{P}\boldsymbol{W}_{\boldsymbol{\alpha}_l}\boldsymbol{f}_m + \boldsymbol{r}_{l,m}$. Similarly $\Phi(\boldsymbol{A})$ replaces $\Phi(\boldsymbol{\Theta}, \boldsymbol{A})$. The log-likelihood term $L(\boldsymbol{A})$ can be written as a sum over the gates, $L(\boldsymbol{A}) = \sum_{l=1}^{n_g} \Lambda_l(\boldsymbol{\alpha}_l)$ with

$$\Lambda_l(\boldsymbol{\alpha}_l) = \sum_{m=1}^{n_t} \sum_{i=1}^{n_b} g_{l,m}^i \log \overline{g}_{l,m}^i(\boldsymbol{\alpha}_l) - \overline{g}_{l,m}^i(\boldsymbol{\alpha}_l).$$

We also assume the penalty on $\boldsymbol{A}$ can be rewritten as

$$V(\boldsymbol{A}) = \sum_{l=1}^{n_g} v_l(\boldsymbol{\alpha}_l).$$

We have

$$\Phi(\boldsymbol{A}) = \sum_{l=1}^{n_g} \phi_l(\boldsymbol{\alpha}_l)$$

where $\phi_l = \Lambda_l + v_l$, so that each $\boldsymbol{\alpha}_l$ can be computed independently. We utilised a quasi-Newton (QN) algorithm, which requires the computation of $\nabla\phi_l$ and an approximation of the Hessian matrix $\nabla^2\phi_l$. For the rest of this section we assume the gradient and Hessian of v_l are tractable so we focus on Λ_l. The gradient is $\nabla\phi_l(\boldsymbol{\alpha}_l) = \nabla\Lambda_l(\boldsymbol{\alpha}_l) + \gamma\nabla v_l(\boldsymbol{\alpha}_l)$ with

$$\nabla\Lambda_l(\boldsymbol{\alpha}_l) = \sum_{m=1}^{n_t} \boldsymbol{J}(\boldsymbol{W}_{\boldsymbol{\alpha}_l}\boldsymbol{f}_m)\boldsymbol{P}^\top[\boldsymbol{g}_{l,m}/\overline{\boldsymbol{g}}_{l,m}(\boldsymbol{\alpha}_l) - \boldsymbol{1}],$$

where $\boldsymbol{J}(\boldsymbol{W}_{\boldsymbol{\alpha}_l}\boldsymbol{f}_m)$ is the Jacobian in $\boldsymbol{\alpha}_l$ of the warped volume. The gradient can be computed with n_t backprojections. For rigid motion (i.e. $\boldsymbol{\alpha}_l \in \mathbb{R}^6$), the Hessian of the likelihood term was approximated in [4] following

$$\nabla^2\Lambda_l(\boldsymbol{\alpha}_l) \simeq \sum_{m=1}^{n_t} \boldsymbol{J}(\boldsymbol{W}_{\boldsymbol{\alpha}_l}\boldsymbol{f}_m)^\top \boldsymbol{P}^\top \boldsymbol{D}_{l,m}\boldsymbol{P}\boldsymbol{J}(\boldsymbol{W}_{\boldsymbol{\alpha}_l}\boldsymbol{f}_m) \tag{6}$$

where $\boldsymbol{D}_{l,m} = -\text{diag}\left\{ g^i_{l,m}/\overline{g}^i_{l,m}(\boldsymbol{\alpha}_l),\ i = 1, \ldots, n_\text{b} \right\}$. Computing (6) is performed by projecting each of the 6 columns of $\boldsymbol{J}(\boldsymbol{W}_{\boldsymbol{\alpha}_l} \boldsymbol{f}_m)$. For large-dimensional $\boldsymbol{\alpha}_l$ (non-rigid motion), this approximation is not tractable. Instead we computed a QN step as $\boldsymbol{h}(\boldsymbol{\alpha}_l) = -\boldsymbol{G}_l(\boldsymbol{\alpha}_l)\nabla\phi_l(\boldsymbol{\alpha}_l)$ where $\boldsymbol{G}_l(\boldsymbol{\alpha}_l)$ is an approximation of $[\nabla^2\phi_l(\boldsymbol{\alpha}_l)]^{-1}$ using the limited memory Broyden-Fletcher-Goldfarb-Shanno (L-BFGS) algorithm [9]. The update on $\boldsymbol{\alpha}_l$ is

$$\boldsymbol{\alpha}_l^\text{new} = \boldsymbol{\alpha}_l^\text{old} + \delta^\star \boldsymbol{h}(\boldsymbol{\alpha}_l^\text{old})$$

with

$$\delta^\star = \underset{\delta \geq 0}{\arg\max}\, \phi_l(\boldsymbol{\alpha}_l^\text{old} + \delta \boldsymbol{h}(\boldsymbol{\alpha}_l^\text{old})).$$

3 Results

We compared JKM with a pre-estimated motion field motion-compensated kinetic image reconstruction (PMK), where $\boldsymbol{A}$ is estimated by registration of reconstructed activity images at each gate l (i.e. from the $\boldsymbol{g}_l = \sum_{m=1}^{n_\text{t}} \boldsymbol{g}_{l,m}$'s). The registrations were performed with Kullback-Leibler divergence minimisation. For a fixed $\boldsymbol{A}$, $\boldsymbol{\Theta}$ was estimated following the scheme presented in Sect. 2.4. This estimation of the motion does not account for kinetics.

We used a 2-D version of the torso PET phantom from [10]. It consists of 9 volumes at different phases of the respiratory cycle. For each volume, we generated 28 [^{18}F]FDG frames using a two-tissue compartment model with K_1, k_2 and k_3 values taken from clinical studies for various regions. The 9×28 volumes were projected with a blurred line integral operator to generate the noiseless $\boldsymbol{g}_{l,m}$ projections at each state (l, m). Poisson noise was added to each $\boldsymbol{g}_{l,m}$. We reconstructed K_I using both methods and compared it to the ground truth $K_\text{I}^\star = K_1 k_3/(k_2 + k_3)$.

The parametric image $\boldsymbol{\Theta}$ was reconstructed from 20 Poisson noise realisations, with 7 different values for β. Using the noise replicate, we estimated the mean variance of the PML estimator obtained with JKM and PMK. Figure 2 shows the estimated variance and the mean square error $\|K_\text{I}^\star - \hat{K}_\text{I}\|_2^2$ in a region of interest containing the liver and 3 tumours. Results show that for all variance levels, JKM has a lower square bias than PMK. Figure 3 shows reconstructed K_I using JKM, PMK and ignoring motion (i.e. PMK with $\boldsymbol{A} = \boldsymbol{0}$). The displayed JKM and PKM images correspond to 2 β values chosen using Fig. 2 such that the mean square bias is the same in both images. The PMK image appears to be more noisy than the JKM image.

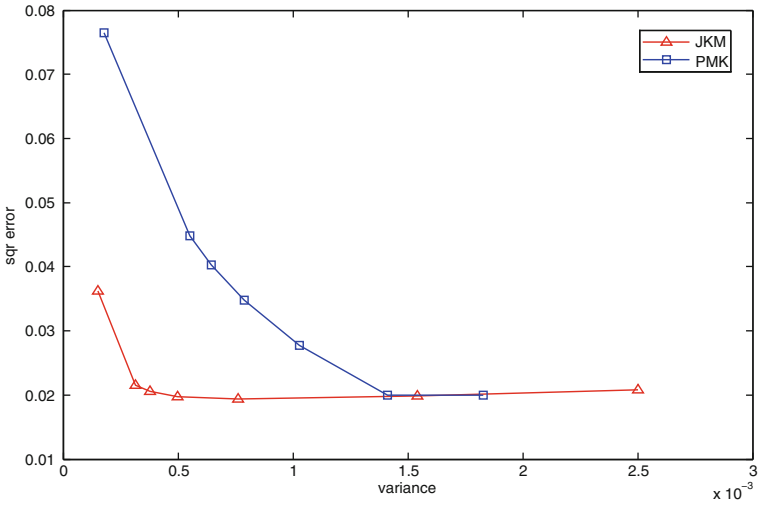

Fig. 2 Mean square error versus mean variance of the reconstructed images using JKM and PMK for different values of β. On both curves each data point corresponds to a single value of β

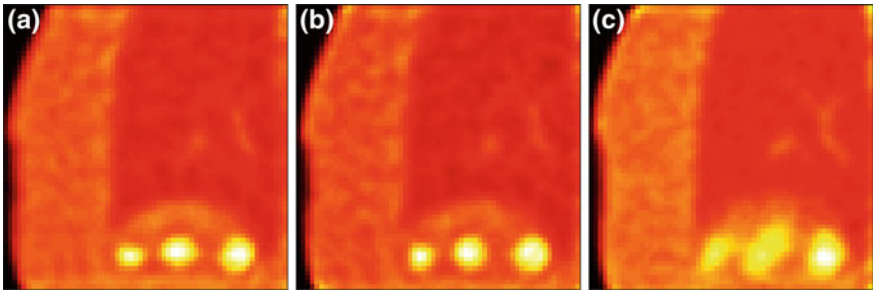

Fig. 3 Reconstructed images with: **a** JKM; **b** PMK; **c** no motion compensation. JKM and PMK images have the same mean square bias

4 Conclusion

We have presented a novel method to estimate the kinetic and non-rigid motion parameters directly from the dynamic gated PET raw data, by maximisation of the penalised log-likelihood. The maximisation is performed by alternating between the 2 parameters. A double optimisation transfer approach was used to derive an update of the kinetic parameters, and we utilised a quasi-newton algorithm to estimate the motion. Results on simulated [^{18}F]FDG data with respiratory motion show that estimating motion and kinetics jointly achieves better performance than using a pre-estimated motion field.

Acknowledgments This research was funded by UK EPSRC (EP/K005278/1) and supported by researchers at the National Institute for Health Research University College London Hospitals Biomedical Research Centre including its High Impact Initiative.

References

1. Jacobson, M.W., Fessler, J.A.: In: Nuclear Science Symposium Conference Record, pp. 3290–3294 (2003)
2. Blume, M., Keil, A., Navab, N., Rafecas, M.: IEEE Trans. Med. Imag. **29**(11), 1892 (2010)
3. Wang, G., Qi, J.: Theranostics **3**(10), 802 (2013)
4. Jiao, J., Bousse, A., Thielemans, K., Markiewicz, P., Burgos, N., Atkinson, D., Arridge, S., Hutton, B., Ourselin, S.: Med Image Comput. Comput. Assist. Interv. (2014)
5. Patlak, C., Blasberg, R.: J. Cereb. Blood Flow Metab. **5**(4), 584 (1985)
6. Wang, G., Qi, J.: IEEE Trans. Med. Imag. **31**(10), 1977 (2012)
7. De Pierro, A.R.: IEEE Trans. Med. Imag. **14**(1), 132 (1995)
8. Lange, K., Hunter, D.I.Y.: J. Comput. Graph. Stat. **9**(1), 1 (2000)
9. Nocedal, J., Wright, S.J.: Numerical Optimization, 2nd edn. Springer, New York (2006)
10. Tsoumpas, C., Buerger, C., King, A.P., Mollet, P., Keereman, V., Vandenberghe, S., Schulz, V., Schleyer, P., Schaeffter, T., Marsden, P.K.: Phys. Med. Biol. **56**, 6597 (2011)

The Effect of Mouth Motion on the Attenuation Correction in Neurological PET Studies

Joaquin L. Herraiz, Angel Torrado-Carvajal, Juan A. Hernandez-Tamames and Norberto Malpica

Abstract In each new generation of PET scanners, the axial field-of-view (FOV) has been increased as a way to improve their sensitivity and obtain better images, faster and with lower injected doses. Nevertheless, in neurological studies, the use of larger axial FOV can introduce errors in the PET attenuation correction (AC), as possible movements of the patient's mouth are not currently considered. This effect happens when oblique PET sinograms containing both the jaw and the brain are used. In this work we have studied the bias that mouth motion can introduce in the PET AC, for two different scanners. The average effect over large regions in the brain is around 1 % for a moderate mouth motion, although some voxels show differences of up to 18 %. These results indicate that if scanners with large axial FOV and acceptance angles are going to be used in the future, possible movements of patient's mouth should be considered in the AC procedure.

Keywords Attenuation correction · Dual modality · Extended FOV · Motion correction · PET/MR · Tissue classification

J.L. Herraiz (✉)
M+Visión Consortium, Research Laboratory of Electronics, Massachusetts Institute of Technology, 50 Vassar Street, Cambridge, MA 02139, USA
e-mail: herraiz@mit.edu

J.L. Herraiz
Grupo de Fisica Nuclear, Universidad Complutense de Madrid, Av. Complutense s/n, 28040 Madrid, Spain

A. Torrado-Carvajal · J.A. Hernandez-Tamames · N. Malpica
Madrid-MIT M+Visión Consortium, Calle Gran Va 6, 28013 Madrid, Spain

A. Torrado-Carvajal · J.A. Hernandez-Tamames · N. Malpica
Medical Image Analysis and Biometry Lab, Universidad Rey Juan Carlos, Calle Tulipán s/n, 28933 Madrid, Móstoles, Spain

F. Gao et al. (eds.), *Computational Methods for Molecular Imaging*,
Lecture Notes in Computational Vision and Biomechanics 22,
DOI 10.1007/978-3-319-18431-9_7

1 Introduction

Since the origins of Positron Emission Tomography (PET), the number of detectors in PET scanners has been increasing in the axial direction. Currently, there are clinical PET scanners with 64 rings, covering an axial FOV of more than 25 cm [1]. Even larger scanners have been proposed [2, 3]. The goal is to get higher sensitivity in order to obtain images with better signal-to-noise (SNR) ratio, and reduce the acquisition time or the amount of radioactivity injected to the patient. For the same reason, the maximum ring difference (MRD), which represents the maximum oblique angle that it is accepted in the data has been also increasing. In contrast to the initial 2D-mode acquisitions (with septa), now 3D-mode acquisition with large MRD are common. Despite these advantages, there is a potential source of error in the quantification of brain studies caused by the movement of the tongue and the mouth during the acquisition. Due to the large difference in the linear attenuation coefficients of bone, brain, soft-tissue and air (Table 1), small movements of the mouth may produce a bias in the attenuation correction applied to the brain region.

As it is clear from Fig. 1, the impact of mouth motion in the AC in the brain becomes more important when larger oblique angles are considered.

The quantitative accuracy of PET studies depends on a good AC. The combination of PET and Computerized Tomography (CT) in a single scanner provided a simple

Table 1 Linear Attenuation Coefficients (AC) for the annihilation gamma rays used in PET for different tissues

Tissue	AC for 511 keV (cm^{-1})
Air	8.7E-5
Brain (WM, GM)	0.096
Muscle	0.096
Bone	0.154

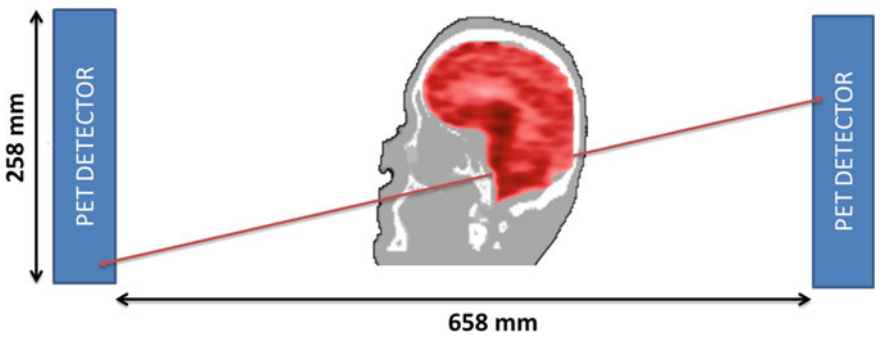

Fig. 1 Effect of the mouth motion in the attenuation of the gamma rays emitted from the brain in a neurological PET study

Table 2 Increase in the axial FOV in the different generations of Siemens Biograph PET scanners

Scanner	Axial FOV (cm)
True Point [9]	16.2
True Point TV [9] & mCT [1]	21.8
mMR [1]	25.8

way to obtain the AC for PET. The images of CT provide the information of the attenuation of X-rays in the different regions of the body, which can be extrapolated to the attenuation of the 511-keV gamma-rays used in PET [4]. In contrast to CT imaging, MRI does not provide direct information concerning tissue attenuation properties, and there is therefore no direct way to obtain the required information for PET AC purposes. Most of the approaches currently proposed in clinical PET/MR systems for PET AC are based on the combination of specific MR sequences (ultrashort echo time (UTE) sequences able to display tissues with very short T2* like bone) [5, 6] and/or subsequent image segmentation [7].

Motion correction methods in PET-CT imaging have been mainly focused in respiratory and cardiac motion [8]. To the best of our knowledge, the impact of the possible motion of the mouth in a neurological PET studies have not yet been considered. This is mainly caused by the fact that in PET acquisitions performed in 2D-mode [3] or 3D mode with low accepted oblique angle, the attenuation in the mouth region does not affect the brain region. Nevertheless, this effect can become a problem if larger axial FOV are going to be used in the future (Table 2).

2 Methods

Two MR volumes of the head (one with the mouth completely closed and the other with the jaw relaxed) were acquired on a General Electric Signa HDxt 3.0T MR scanner using the body coil for excitation and an 8-channel quadrature brain coil for reception. Imaging was performed using an isotropic 3D T1-weighted IR sequence with a TR = 10.024 ms, TE = 4.56 ms, TI = 600 ms, NEX = 1, acquisition matrix = 288 × 288, resolution = 1 × 1 × 1 mm, flip angle = 12. The different tissues (white matter, gray matter, cerebrospinal fluid, skull, muscle, fat, and skin) were segmented using the automatic segmentation pipeline proposed in [10]. This method estimates the skull using a CT multi-atlas and label-fusion based approach [11]. Figure 2 shows both acquisitions and their correspondent tissue segmentations. Each of the 7 materials in the segmented images was assigned a typical value of FDG-PET activity concentration and a linear attenuation coefficient (Table 1).

As we are mainly interested in the bias introduced by an inaccurate AC and not in the noise, we generated the acquisition sinograms as a projection of the activity image (i.e. without any Monte Carlo code), with a Siddon ray-tracer algorithm with

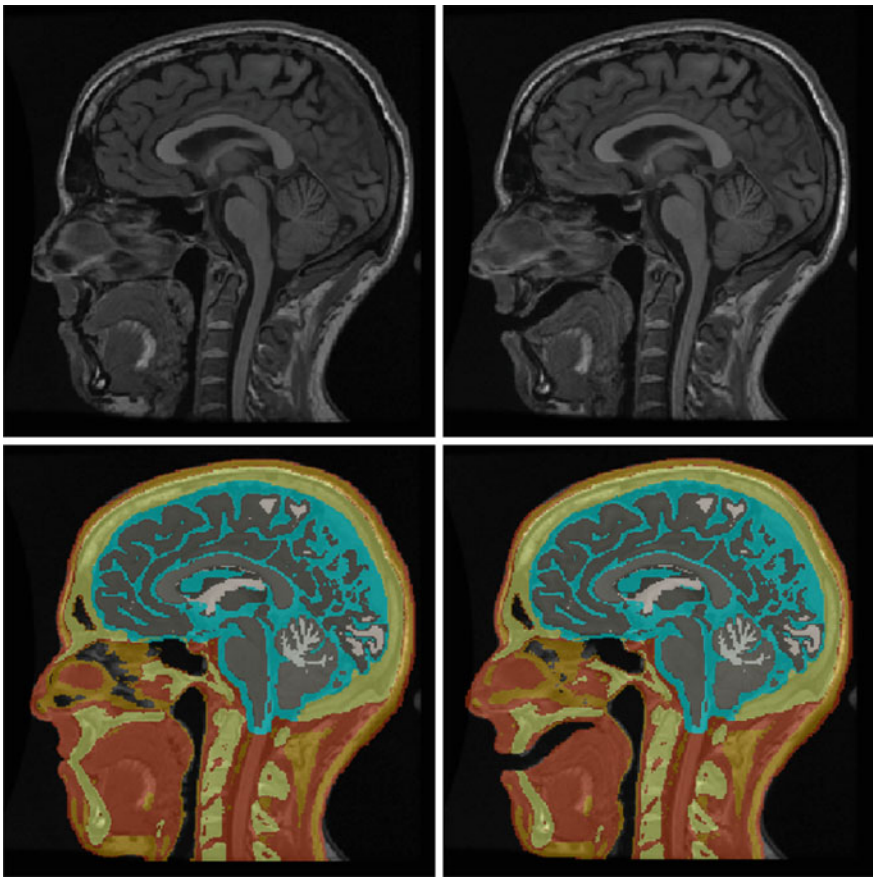

Fig. 2 MRI volumes of the head with the mouth completely closed and with the jaw relaxed (up) with their correspondent tissue segmentations. A slight relaxation introduces a notorious change in the mouth

a gaussian kernel (4 mm FWHM) to incorporate the blurring effects in PET (positron range, non-collinearity, pitch size). Isotropic images were reconstructed with resolution $= 2 \times 2 \times 2$ mm, FOV $= 400$ mm, Axial FOV$= 258$ mm. We assigned activities to the different tissues according to these relative values (GM: 2.7, WM and soft tissue: 1.0, CSF: 0.0, bone: 0.3) [12].

For the attenuation, we generated a sinogram for each of the two attenuation maps with the same projection code, in this case without any blurring. The “ideal" emission sinogram was “attenuated” using the image with the mouth completely closed and then it was corrected with an erroneous attenuation projection, obtained from the image with the mouth relaxed. This final sinogram was reconstructed with the OSEM algorithm (3 iterations 20 subsets) [13] and the differences between the

images reconstructed with the proper attenuation correction (which corresponds to the image obtained from the emissions sinogram) were studied.

This effect of an erroneous AC was studied for the mCT and the mMR scanners, which main properties are shown in Table 3 [1].

3 Results

An example of the images reconstructed is shown in Fig. 3(left). In this case it corresponds to the mMR scanner with a correct attenuation correction. The relative error between the reconstructed image obtained with the incorrect AC respect to the one with the correct AC for different tissues of interest is shown in Fig. 3(right). The maximum values in each region are shown.

Table 4 shows the maximum relative differences (in %) for the two hybrid modalities, PET/CT and PET/MR.

Table 3 Main parameters of the PET scanners considered in this work

	Biograph	
	mCT scanner (cm)	mMR scanner (cm)
Axial FOV	21.8	25.8
Maximum ring difference	49	60
Diameter of the scanner	84.2	65.6

Fig. 3 Example of the reconstructed image (*left*) and image of relative differences (in %) between the image reconstructed with the correct and the erroneous AC for the mMR scanner

Table 4 Maximum error in each region of interest for the two PET scanners considered, when an erroneous AC is used

	Biograph	
	mCT scanner (%)	mMR scanner (%)
Cerebellum	4	5
White matter	7	7
Gray matter	16	18

4 Discussion

As expected, the most significant impact of the use of an erroneous AC occurs in the region close to the mouth. Nevertheless, the reconstructed PET images are not only affected in that region. Errors up to 18 % are found in some voxels in the cerebellum, as well as in gray and white matter. This is caused by the propagation of the errors between regions during the reconstruction. The average error over large regions in the tissues of interest is around 1 % in all cases, but its effect in small local regions can be significant in some studies. It is clear that these effects will be even more important when the mouth is moved much more than what it was considered in this study. Furthermore, the effects will be more important in scanners with larger axial FOV and acceptance angles, as can be seen comparing our results from the mCT and the mMR scanners. In these cases, we propose to monitor the mouth motion with some specific fast MR acquisitions [12, 14, 15] to be able to properly correct them.

5 Conclusions

As PET scanners with larger axial FOV become available, the motion of the mouth should be considered to avoid possible errors in the quantification of neurological studies from the attenuation correction. The errors can be significant in a scanner such as the Biograph mMR.

Acknowledgments This project has been financially supported by the Comunidad de Madrid and the Madrid-MIT M+Visión Consortium.

References

1. Delso, G., Frst, S., Jakoby, B., Ladebeck, R., Ganter, C., Nekolla, S.G., Schwaiger, M., Ziegler, S.I.: Performance measurements of the Siemens mMR integrated whole-body PET/MR scanner. J. Nucl. Med. **52**(12), 1914–1922 (2011)
2. Poon, J.K., Dahlbom, M.L., Moses, W.W., Balakrishnan, K., Wang, W., Cherry, S.R., Badawi, R.D.: Optimal whole-body PET scanner configurations for different volumes of LSO scintillator: a simulation study. Phys. Med. Biol. **57**(13), 4077–4094 (2012)
3. MacDonald, L.R., Harrison, R.L., Alessio, A.M., Hunter, W.C.J., Lewellen, T.K., Kinahan, P.E.: Effective count rates for PET scanners with reduced and extended axial field of view. Phys. Med. Biol. **56**(12), 3629–3643 (2011)
4. Kinahan, P.E., Townsend, D.W., Beyer, T., Sashin, D.: Attenuation correction for a combined 3D PET/CT scanner. Med. Phys. **25**(10), 2046–2053 (1998)
5. Keereman, V., Fierens, Y., Broux, T., De Deene, Y., Lonneux, M., Vandenberghe, S.: MRI-based attenuation correction for PET/MRI using ultrashort echo time sequences. J. Nucl. Med. **51**, 812–818 (2010)
6. Johansson, A., Karlsson, M., Nyholm, T.: CT substitute derived from MRI sequences with ultrashort echo time. Med. Phys. **38**, 2708–2714 (2011)

7. Yang, Z., Choupan, J., Sepehrband, F., Reutens, D., Crozier, S.: Tissue classification for PET/MRI attenuation correction using conditional random field and image fusion. Int. J. Mach. Learn Comput. **3**(1), 87–92 (2013)
8. Petibon, Y., El Fakhri, G., Nezafat, R., Johnson, N., Brady, T., Ouyang, J.: Towards coronary plaque imaging using simultaneous PET-MR: a simulation study. Phys. Med. Biol. **59**(5), 1203–1222 (2014)
9. Jakoby, B.W., Bercier, Y., Watson, C.C., Bendriem, B., Townsend, D.W.: Performance characteristics of a new LSO PET/CT scanner with extended axial field-of-view and PSF reconstruction. IEEE Trans. Nucl. Sci. **56**(3), 633–639 (2009)
10. Torrado-Carvajal, A., Hernandez-Tamames, J.A., Herraiz, J.L., Eryaman, Y., Adalsteinsson, E., Wald, L.L., Malpica, N.: Automatic segmentation pipeline for patient-specific MRI tissue models. Int. Soc. Magn. Reson. Med. **2014**(22), 4906 (2014)
11. Torrado-Carvajal, A., Hernandez-Tamames, J.A., Herraiz, J.L., Eryaman, Y., Adalsteinsson, E., Wald, L.L., Malpica, N.: A multi-atlas and label fusion approach for patient-specific MRI based skull segmentation. Int. Soc. Magn. Reson. Med. **2014**(22), 1177 (2014)
12. Aitken, A.P., Giese, D., Tsoumpas, C., Schleyer, P., Kozerke, S., Prieto, C., Schaeffter, T.: Improved UTE-based attenuation correction for cranial PET-MR using dynamic magnetic field monitoring. Med. Phys. **41**(1), 012302 (2014)
13. Herraiz, J.L., Espaa, S., Cabido, R., Montemayor, A.S., Desco, M., Vaquero, J.J., Udas, J.M.: GPU-based fast iterative reconstruction of fully 3-D PET Sinograms. IEEE Trans. Nucl. Sci. **58**(5), 2257–2263 (2011)
14. Catana, C., Benner, T., van der Kouwe, A., Byars, L., Hamm, M., Chonde, D.B., Michel, C.J., El Fakhri, G., Schmand, M., Sorensen, A.G.: MRI-assisted PET motion correction for neurologic studies in an integrated MR-PET scanner. J. Nucl. Med. **52**(1), 154–161 (2011)
15. Chun, S.Y., Reese, T.G., Ouyang, J., Guerin, B., Catana, C., Zhu, X., Alpert, N.M., El Fakhri, G.: MRI-based nonrigid motion correction in simultaneous PET/MRI. J. Nucl. Med. **53**(8), 1284–1291 (2012)

Dual Estimation of Activity Maps and Kinetic Parameters for Dynamic PET Imaging

Jingjia Xu, Huafeng Liu, Pengcheng Shi and Fei Gao

Abstract Due to rapid adoption of dynamic PET, the dual estimations of the activity maps and kinetic parameters have been attracting a lot of attention. In this paper, we propose a novel approach to solve this problem by using Dual-Kalman Filter (DKF) based on state space framework. One Kalman Filter is adopted to reconstruct the activity maps and the other is to estimate the kinetic parameters, where each filter uses the estimation results from the other one as initialization, then the two filters are solved iteratively until convergence. In addition, this approach combines the compartmental model guided activity map reconstruction and the state space based kinetic parameter estimation. The simulation experiments are presented by both utilizing DKF and other methods based on fitting the compartmental model. The final results show the more robust and accurate performance using proposed method.

Keywords Positron emission tomography · Parameter estimation · Dynamic reconstruction · Compartmental model · Dual filter

1 Introduction

In nuclear medicine, PET (Positron Emission Tomography) is emerging as one of the leading modalities in the biomedical research and clinical diagnostic procedure. Dynamic PET imaging plays a more and more important role in research, which reveals the dynamic metabolism of specific organs and tissues through imaging the spatiotemporal distributions of injected radiotracers *in vivo*. The dynamic changes

J. Xu (✉) · P. Shi · F. Gao
Rochester Institute of Technology, Rochester, NY 14623, USA
e-mail: Xujingjia.zju@gmail.com

F. Gao
e-mail: Gaofei.rit@gmail.com

H. Liu
Zhejiang University, Hangzhou, China
e-mail: liuhf@zju.edu.cn

F. Gao et al. (eds.), *Computational Methods for Molecular Imaging*,
Lecture Notes in Computational Vision and Biomechanics 22,
DOI 10.1007/978-3-319-18431-9_8

of these spatiotemporal distributions reflect several complex events and can be represented by compartment models and kinetic parameters [3]. The compartmental model describes the tracer metabolism and is widely used in the dynamic PET research. The kinetic parameters are used to quantify the distribution of the radiotracer throughout the tissues or the organs.

The estimation methods for activity maps include conventional Expectation Maximization (EM) methods, accelerated Ordered Subset Expectation Maximization (OSEM), Maximum A Priori (MAP) and state space framework [1]. The estimation of kinetic parameters is more difficult [2, 5, 8]. Generally, the methods include indirect and direct methods. The indirect methods first reconstruct the activity maps and then fit the results to specific compartment models. These methods are simple and easy to implement, because activity reconstruction and kinetic modeling are performed in two separate steps. However, the noise distribution which should be spatially variant and object dependent is not modeled in the kinetic analysis, this will lead to suboptimal results. The direct methods estimate parametric images from dynamic PET sinograms directly, and theoretically they should be more efficient, however, the algorithms are often difficult to implement and are limited to the specific models.

In this paper, we proposed a novel method for dual estimation of activity maps and kinetic parameters for dynamic PET imaging. Formulating the two estimations by using DKF based on our state space frameworks which have inherent ability to deal with noise distribution, we set one Kalman Filter to reconstruct the activity maps from dynamic PET data and the other to estimate the kinetic parameters, where each filter uses the estimation results from the other one as initialization, then the two filters are solved iteratively until convergence. The DKF method combines the compartment model guided activity map reconstruction [7] and state space based kinetic parameter estimation, and the merits of this iterative estimation yield more robust and accurate estimation of both activity maps and kinetic parameters. Data sets from computer simulations are conducted for quantitative analysis and validation.

2 Methodology

2.1 Compartmental Model

In the PET tracer kinetic research, there are many models,such as none-compartmental model and compartmental model, proposed to describe the process of tracer distribution in the organs and tissues. Compartmental model is generally utilized to describe movement of tracer between different physically or chemically distinct state and compartments. In this paper, a two-tissue compartmental model, widely validated in many radioligand tracers, is the main algorithm in dynamic PET research. The two-tissue compartmental model use the the first-order ordinary differential equations to depicted the exchange of tracer between the compartments illustrate in Fig. 1 and

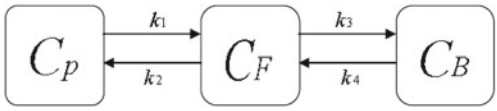

Fig. 1 The two-tissue compartmental model

Eqs. (1–3):

$$\begin{aligned} \frac{dC_{Fi}}{dt} &= k_{1i}C_P(t) + k_{4i}C_{Bi}(t) - (k_{2i} + k_{3i})C_{Fi}(t) \\ \frac{dC_{Bi}}{dt} &= k_{3i}C_{Fi}(t) - k_{4i}C_{Bi}(t) \\ C_{Mi}(t) &= C_{Fi}(t) + C_{Bi}(t) \end{aligned} \tag{1}$$

where the $C_P(t)$, $C_{Fi}(t)$ and $C_{Bi}(t)$ represent the tracer concentration in the plasma, the tracer concentration in the tissues and the metabolites of tracer concentration in the tissues, respectively. The model depends on the kinetic parameters k_1, k_2, k_3 and k_4, which specify tracer exchange rates between the compartments in the units of inverse minutes (min^{-1}), and C_{Mi} is the total tissue activity.

The other parameter $K_r = k_1k_3/(k_2 + k_3)$ is proportional to the regional cerebral metabolic rate for metabolized tracers and to the uptake of tracer, which is one of the main parameters used to evaluate the accuracy of our proposed method.

2.2 Compartment Model Guided Activity Map Estimation

The activity map estimation has been specifically interpreted in the [7], which puts forward the state space representation for the dynamic reconstruction where the compartmental model is guided as a continuous-time system equation and the image data is expressed in a measurement equation. The general form of the framework for the activity map reconstruction for voxel i as follows:

$$\begin{aligned} \dot{x_i}(t) &= a_i x_i(t) + b_i \widetilde{C_P}(t) + \nu(t) \\ Y &= DX(t) + e(t) \end{aligned} \tag{2}$$

where $X(t) = \{x_1(t), x_2(t), \ldots, x_n(t)\}$ describes all the pixels in one frame image, and each pixel is defined as $\dot{x}_i(t) = \begin{bmatrix} \dot{C_{Fi}}(t) \\ \dot{C_{Bi}}(t) \end{bmatrix}$, $a = \begin{bmatrix} -(k_{2i} + k_{3i}) & k_{4i} \\ k_{3i} & -k_{4i} \end{bmatrix}$ and $b = \begin{bmatrix} k_{4i} & 0 \end{bmatrix}$; and measurement matrix is $D = CT_r$, where C is the image matrix and T_r is the transformation matrix with the block diagonal; $\nu(t)$ and $e(t)$ are the process and measurement noise, respectively, which are Gaussian distribution with zero mean and the covariance matrix of the process and measurement Q and R, respectively.

2.3 State Space Formulation of Kinetic Parameter Estimation

State Space Formulation *The state equation*. As discussed in the previous Sect. 2.1, the parameters k_1, k_2, k_3 and k_4 represent tracer exchange rates between the compartments and the values of the parameters are assumed to be barely changed for one tracer in the same organ or tissue. The form of state equation of parameter estimation adopted in current study assumes a static, discrete-time linear function as follows:

$$\left[k_1\ k_2\ k_3\ k_4\right]_{(t)} = \left[k_1\ k_2\ k_3\ k_4\right]_{(t-1)} \tag{3}$$

Defining $T_i = \left[k_1\ k_2\ k_3\ k_4\right]_i^T$ and also introducing a system noise term $\widetilde{\nu}(t)$, the state equation for all voxels expresses as:

$$T(t) = T(t-1) + \widetilde{\nu}(t) \tag{4}$$

The measurement equation. By applying the compartmental model to all the voxels, the measurement equation for any voxel i is governed from the Eqs. (1) and (2) as:

$$\begin{bmatrix} \dot{C_{Fi}}(t) \\ \dot{C_{Bi}}(t) \end{bmatrix} = \begin{bmatrix} C_P(t) & -C_{Fi}(t) & -C_{Fi}(t) & C_{Bi}(t) \\ 0 & 0 & C_{Fi}(t) & -C_{Bi}(t) \end{bmatrix} \times T_i \tag{5}$$

With the subscript i denoting different voxel locations, the above measurement equation can be expressed in a compact notation as:

$$y(t) = D_i \cdot T_i(t) + \widetilde{\mu}(t) \tag{6}$$

where

$y(t) = \left[\ \dot{C_{Fi}}(t)\ \dot{C_{Bi}}(t)\ \right]^T$

$D_i = \begin{bmatrix} C_P(t) & -C_{Fi}(t) & -C_{Fi}(t) & C_{Bi}(t) \\ 0 & 0 & C_{Fi}(t) & -C_{Bi}(t) \end{bmatrix}$ and $\widetilde{\mu}(t)$ is the measurement noise.

Equations (7) and (9) have formed a standard state-space representation for estimating kinetic parameters, in which the parameters serve as static variable state equation and the reconstruction data convey the discrete sampling in the measurement equation.

Kalman Filter Solution The Kalman Filter (KF) strategy, which has been applied to solve the state space equations, estimates a process by using a form of feedback control: the filter estimates the state at some time and then obtains feedback in the form of measurement. Thus the equations for KF are divided into two groups: the time update equations and the measurement update equations [6]. The KF has been proved that can resolve the estimate problem in the state space principles for PET image reconstruction. KF uses the feedback control method to reach convergence and obtain the optimal solution, and the detail of this algorithm explains in the [4]. The specific equations for the time and measurement updates are presented as follows:

Time-update equations:

$$\mathbf{x}(t) = A\mathbf{x}(t^-) + B\mu \tag{7}$$

$$\mathbf{P}(t) = A\mathbf{P}(t^-)A^T + Q \tag{8}$$

Measurement-update equations:

$$\mathbf{x}(t) = \mathbf{x}(t^-) + K(y - D\mathbf{x}(t^-)) \tag{9}$$

$$\mathbf{P}(t) = (I - KD)\mathbf{P}(t^-) \tag{10}$$

$$K = PD(DPD + R)^{-1} \tag{11}$$

where the term $P(t)$ denotes the covariance of the estimation error and $P(t^-)$ denotes the covariance of the estimation error of $x(t^-)$. K is called the KF gain.

The above solutions are to estimate the state of a discrete-time controlled process that is governed by a discrete-time linear stochastic difference equation. However, the process to be estimated is continuous-time sometimes. In this case, the time and measurement update equations are required to do some transformations [6]:

$$\dot{\mathbf{x}} = A\mathbf{x}^- + Bu \tag{12}$$

$$\dot{P} = AP^- + P^-A^T + Q \tag{13}$$

$$K = PD^T R^{-1} \tag{14}$$

2.4 Dual Estimation Framework

The first Kalman Filter: the PET data as the observation $y(t)$ and kinetic parameters as the known variable, a KF estimate the activity map quantity X_f, where the f means the frame of the reconstruction images. In this process, this framework of the state-space, as Eq. (1), is a continuous-time system, and the compartmental model is the priori, so that the processing noise covariance matrix Q is very little.

The second Kalman Filter: estimate the kinetic parameters from the sequence of X_f. The set of Eqs. (7) and (8) defines the discrete-time state-space representation employed to estimate the kinetic parameters k_1, k_2, k_3 and k_4.

Hence, the process of DKF algorithm is expressed in Fig. 2. the first KF is to reconstruct the activity maps using the kinetic parameters as known parameters, while the other is to estimate the kinetic parameters using the estimation of activity maps as known parameter. Every iteration using the update activity maps and the update kinetic parameters as the known condition respectively to optimize the results until both of the estimations are convergence.

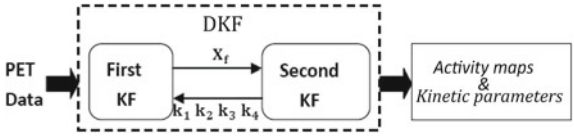

Fig. 2 The principle of the Dual Kalman Filter

3 Experiment and Result

3.1 Experiments with Zubal Phantom

The computer simulation experiments are used to evaluate the accuracy and robustness of the proposed method. Our simulation experiments are based on a Zubal Phamtom. Figure 3a shows a schematic representation of the Zubal Phamtom with three ROIs selected and a background, indicated ROI 1, 2, 3 respectively. The simulated tracer is 11C-acetate and the phantom is digitized at 96×96 pixels and forward parallel projection data is calculated at 96×96. Time frames of emission images are generated using two-tissue compartmental model and the plasma function, $C_P(t)$, is generated using the Feng Input function [1]:

$$C_P^{acetate}(t) = \left[1 - 0.88\left(1 - e^{-\left(\frac{2ln2}{15}t\right)}\right)\right] C_P^{FDG}(t) \tag{15}$$

$$C_P^{FDG}(t) = (A_1 t - A_2 - A_3)e^{-\lambda_1 t} + A_2 e^{-\lambda_2 t} + e^{-\lambda_3 t} \tag{16}$$

With $A_1 = 851.1225\,\mu\text{Ci/mL/min}$, $A_2 = 20.8113\,\mu\text{Ci/mL}$, $A_3 = 21.8798\,\mu\text{Ci/mL}$, $\lambda_1 = 4.133859\,\text{min}^{-1}$, $\lambda_2 = 0.01043449\,\text{min}^{-1}$, $\lambda_3 = 0.1190996\,\text{min}^{-1}$.

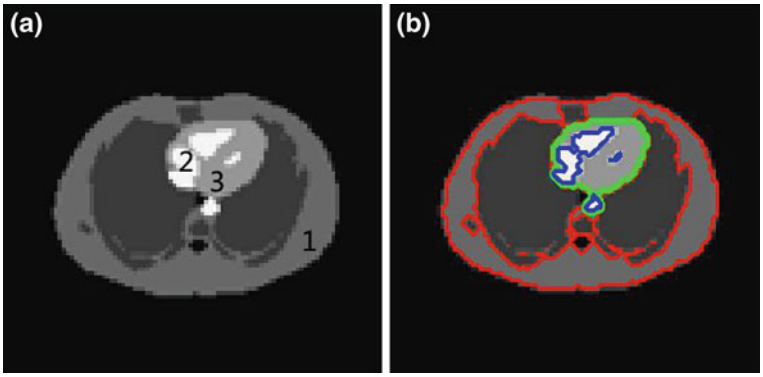

Fig. 3 The schematic representation of the experiments, **a** is Zubal Phantom. **b** is the segmentation of activity map

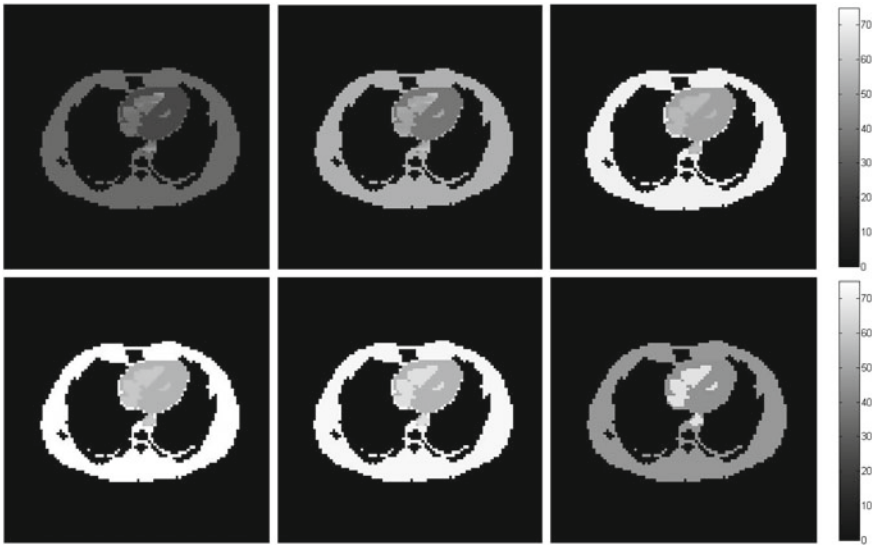

Fig. 4 The estimated activity maps including the 3rd, 7th, 11th, 15th, 20th, 25th time frame

28 frames of dynamic acquisition are performed as 7×0.2 min, 8×0.5 min, 5×1 min, 4×2 min and 4×5 min, total scan time is 40 min.

To evaluate the estimation performances, we take quantitative analysis on the results, by defining the error between the reconstruct result and ground truth as follow:

$$bias = \frac{1}{N_p} \sum_{i=1}^{N_p} \frac{|XR_i - XT_i|}{XT_i} \tag{17}$$

where N_p is the total number of pixels, XR_i is the final estimation result of pixel i, and XT_i is the true value of corresponding pixel i. Figure 4 shows the estimated activity maps from the dynamic PET data, at frame 3, 7, 11, 15, 20 and 25, and the Table 1 summarizes the calculated bias value of the reconstructed images from different time frames. The reconstructed images preserve the image quality at the same level as the results in [7].

Meanwhile, the parameters estimated are summarized in the Table 2. To reduce the calculation time during the experiment, we segment the activity maps as the Fig. 3b, and get the average value of the kinetic parameters via calculating the mean of each ROI.

Comparative study of parameter estimation was taken between existing techniques and our proposed method. The technique, we apply in the comparative study, is the LMWLS estimation algorithm from the COMKAT, which is a software package for compartmental modeling oriented for biomedical image quantification. It should be noted that, for fair comparison, in the fitting procedures, the activity maps from

Table 1 Statistical studies of activity maps

	*frame*3	*frame*7	*frame*11
bias	0.0282	0.0235	0.0124
	*frame*15	*frame*20	*frame*25
bias	0.0160	0.0155	0.0968

Table 2 The parameters estimation using DKF and the LMWLS, compared with the true value (TV)

ROI1	k_1	k_2	k_3	k_4	K_r
TV	0.6518	0.2276	0.0531	0.0388	0.1252
DKF	0.6484	0.2199	0.0526	0.2111	0.1233
LMWLS	0.8302	0.2705	0.0232	0.0009	0.0656
ROI2	k_1	k_2	k_3	k_4	K_r
TV	0.4504	0.2287	0.0725	0.0141	0.1085
DKF	0.4469	0.2172	0.0716	0.0200	0.1108
LMWLS	0.7491	0.3381	0.0044	0.9768	0.0096
ROI3	k_1	k_2	k_3	k_4	K_r
TV	0.7307	0.5369	0.1776	0.0143	0.1816
DKF	0.7252	0.5176	0.1672	0.0109	0.1771
LMWLS	0.9616	0.7192	0.1851	0.0789	0.1968

the our estimation framework are used as the input activity curves for the LMWLS algorithm to estimate the kinetic parameters.

The calculated bias values of the estimated parameters from two methods are demonstrated in the Table 3. Comparing with the variance calculation, it is demonstrate that the variance calculation has no priority to the bias calculation and at the same time it is limited by the four pages requirement, so in this paper, we don't display the variance calculation. The bias of k_1 from our method is about 0.01, but that from the LMWLS is more than 0.25. At the same time, k_2 estimation is 0.05 in our method while around 0.35 in the LMWLS. As we all known, in parameter estimations of 2 compartment model based problem, k_4 is the most difficult one to estimate. By our method, the bias of k_4 is less than 4.4, however, the biggest bias of the LMWLS reaches 66.515. Consequently, the parameter K_r is also adopted to evaluate the algorithm. To some extent it shows that our method can maintain higher accuracy in dual estimation of activity maps and kinetic parameters.

Table 3 Statistical studies of estimated parameters

ROI1	k_1	k_2	k_3	k_4	K_r
$bias_{DKF}$	0.0053	0.0341	0.0096	4.4379	0.0154
$bias_{LMW}$	0.2735	0.1882	0.5632	0.9768	0.4680
ROI2	k_1	k_2	k_3	k_4	K_r
$bias_{DKF}$	0.0079	0.0503	0.0128	0.4114	0.0212
$bias_{LMW}$	0.6630	0.4783	0.9393	66.515	0.9115
ROI3	k_1	k_2	k_3	k_4	K_r
$bias_{DKF}$	0.0076	0.0359	0.0583	0.9235	0.0248
$bias_{LMW}$	0.3159	0.3394	0.0422	4.5375	0.0837

4 Conclusions

Dual estimation of the activity maps and kinetic parameters for dynamic PET imaging is presented in this paper. The procedure is realized by DKF, where one KF is to reconstruct the dynamic images and the other is to estimate the kinetic parameters, and each one uses the results from the other one as initialization, finally, the two filters are solved iteratively until convergence. The simulated experiments indicate that DKF can estimate the activity maps and kinetic parameters robustly and accurately.

References

1. Gao, F., Liu, H., Jian, Y., Shi, P.: Dynamic dual-tracer pet reconstruction. In: Information Processing in Medical Imaging, IPMI09, pp. 38–49. Springer (2009)
2. Gao, F., Liu, H., Shi, P.: Efficient robust reconstruction of dynamic pet activity maps with radioisotope decay constraints. In: Medical Image Computing and Computer-Assisted Intervention-MICCAI 2010, pp. 571–578. Springer (2010)
3. Gao, F., Liu, H., Shi, P.: Robust estimation of kinetic parameters in dynamic PET imaging. In: Medical Image Computing and Computer-Assisted Intervention-MICCAI 2011, pp. 492–499. Springer (2011)
4. Liu, H., Tian, Y., Shi, P.: PET image reconstruction: a robust state space approach. In: Information Processing in Medical Imaging, pp. 197–209. Springer (2005)
5. Reader, A., Sureau, F., Comtat, C., Trébossen, R., Buvat, I.: Joint estimation of dynamic PET images and temporal basis functions using fully 4D ML-EM. Phys. Med. Biol. **51**, 5455 (2006)
6. Simon, D.: Optimal State Estimation: Kalman, H [Infinity] and Nonlinear Approaches. Wiley, New York (2006)
7. Tong, S., Shi, P.: Tracer kinetics guided dynamic PET reconstruction. In: Information Processing in Medical Imaging, IPMI07, pp. 421–433. Springer (2007)
8. Wang, G., Qi, J.: Generalized algorithms for direct reconstruction of parametric images from dynamic PET data. IEEE Trans. Med. Imaging **28**(11), 1717–1726 (2009)

Time-Activity Curve Based Sinogram Decomposition for Streak Artifacts Reduction in Dynamic PET Reconstruction

Xiaoyin Cheng, Jun Liu, Jakob Vogel, Zhen Liu, Nassir Navab, Sibylle Ziegler and Kuangyu Shi

Abstract This paper developed a novel dynamic PET reconstruction algorithm to reduce the severe streak artifacts due to the existence of overwhelmingly higher signals such as bladder than other areas. This is achieved by a clustering of temporal development into comparable signal levels and decomposition in projection space accordingly. The results show a significant improvement in quality of reconstructed images as well as an improvement in quantification compared with conventional FBP reconstruction.

Keywords Streak artifact reduction · FBP · Dynamic PET

FBP is considered to be the reconstruction method with low system bias and is thus popularly applied in physiological quantification, e.g. kinetic modeling, of dynamic PET (dPET) [1]. Although there may exist streak artifacts in FBP-reconstructed images for routine PET with a limited number of projections, these artifacts are typically far smaller than the normal signal and do not influence the quantitative analysis—and thus can generally be ignored. However, due to overwhelmingly high uptake in some organs—a situation often observed in practice—, these artifacts get amplified, thus suppressing and destroying the normal signal. For instance, the streak artifacts due to high activity in the bladder hamper the application of FBP in the abdomen area, and complicate the diagnosis of prostate or cervical cancer [2].

Streak artifacts have been extensively studied in CT, where they are caused mainly by metallic implants heavily attenuating the X-rays. Efforts have been focused on either linear/higher-order interpolations between two successive projections [3] or adding more constraints using modified iterative methods [4]. Although these

X. Cheng (✉) · Z. Liu · S. Ziegler · K. Shi
Department of Nuclear Medicine, Technical University Munich, Munich, Germany
e-mail: Xiaoyin.cheng@gmail.com

J. Liu
Statistical Analysis System (SAS) Institute Inc., Cary, USA

J. Vogel · N. Navab
Chair for Computer Aided Medical Procedures & Augmented Reality,
Technical University Munich, Munich, Germany

F. Gao et al. (eds.), *Computational Methods for Molecular Imaging*,
Lecture Notes in Computational Vision and Biomechanics 22,
DOI 10.1007/978-3-319-18431-9_9

methods generate promising results, their applications in PET are not straightforward, where acquisitions are measured via lines-of-response (LOR) for each detector pair. In addition, quantitative analysis with dPET is more sensitive to errors introduced by improper interpolation or constraints.

This paper proposes a novel method to automatically reduce streak artifacts for the FBP reconstruction of dPET images by decomposing the measured signal in the projection space. The feasibility of sinogram decomposition in projection space based on temporal information has been theoretically investigated in [5]. Concerning the strong artifacts due to the existence of incomparable signal levels, we developed a framework to extract the characteristic temporal course, i.e. time-activity curve (TAC), of each comparable signal level by clustering areas of similar tracer evolution in image space. The characteristic TACs serve as basis function for sinogram decomposition in the projection space, which enables the reduction of streak artifacts in the final reconstruction. The image quality and the quantitative accuracy of the new method were compared with conventional FBP and show a clear improvement.

1 Methods

The proposed algorithm consists of four steps as sketched in Fig. 1: 1. pre-reconstruction; 2. separation of TACs of comparable levels; 3. decomposition in projection space based on the separated characteristic TACs; 4. reconstruction from decomposed sinograms and reassembling.

1.1 Extraction of Characteristic TACs

Given dPET measurements contain in total L temporal frames. Conventional FBP is applied on each frame and the vector $\mathbf{x}'(t) \in \mathbb{R}^N$ represents the pre-reconstructed

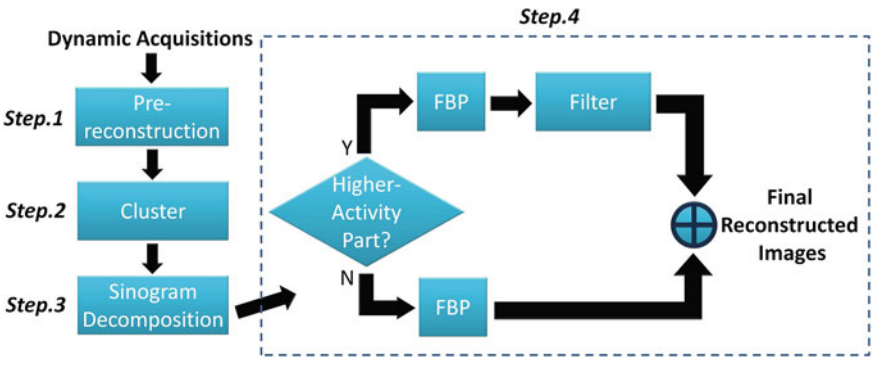

Fig. 1 The flow chart of the proposed algorithm

image of N voxels at the tth frame. Investigating the intensity of the ith voxel over time, $x_i'(t) = [x_i'(1), x_i'(2), \ldots, x_i'(L)]^T \in \mathbb{R}^L$ represents a TAC of length L. The whole dynamic image set $\mathbf{x}'$ consisting of L images (of N voxels each) can be also considered as a set of N TACs (of length L). The K-Mean algorithm with the Euclidean distance as similarity metrics is applied to separate these TACs $x_i'(t)$ into K clusters with the mean curve $\bar{c}_k(t)$ and variance σ_k of each cluster k ($k = 1, 2, \ldots, K$, $K \ll N$) with the condition:

$$\sigma_k \ll \sigma / K$$

where σ is the variance of $x_i'(t)$.

1.2 Decomposition in Projection Space

For 4D dPET, individual temporal courses are associated with spatial regions of specific physiological properties relating to distinct components in projection space. With the discrimination of TACs in the temporal domain, sinograms in the projection space can be distinguished [5].

Given dPET measurements at tth temporal frame in projection space $\mathbf{y}(t) \in \mathbb{R}^M$, where M is the number of LORs. Its relation to the reconstructed image $\mathbf{x}(t) \in \mathbb{R}^N$ can be written as $\mathbf{y}(t) = \mathbf{A}\mathbf{x}(t)$. $\mathbf{A} = (a_{j,i}) \in \mathbb{R}^{M \times N}$ is the system matrix and $a_{j,i}$ the probability of a photon originating from the ith voxel and being detected by the jth LOR.

For the dynamic image set, the characteristic TACs of each physiological region in image space are considered as temporal basis functions, and the sinogram in projection space can be decomposed into weightings of each basis function. Given a set of K characteristic TACs $\mathbf{c}(t) \in \mathbb{R}^K$, each TAC $c_k(t) = [c_k(1), c_k(2), \ldots, c_k(L)]$ corresponds to a physiological region, then sinogram $y(t)$ can be expressed as:

$$\mathbf{y}(t) = \mathbf{B}\mathbf{c}(t) \tag{1}$$

where $\mathbf{B} = (b_{j,k}) \in \mathbb{R}^{M \times K}$ and $b_{j,k}$ is the weighting for voxels detected by the jth LOR and meanwhile possessing the same kth characteristic TAC. Thus the matrix $\mathbf{B}$ contains the decomposed sinograms corresponding to each of the K TACs. To obtain a stable solution of $\mathbf{B}$ from (2), the ℓ_2-norm and regularization constant λ are added, leading to a minimization of the following term:

$$\arg\min_{\mathbf{B}}(\|\mathbf{y} - \mathbf{B}\mathbf{c}\|_2 + \lambda\|\mathbf{B}\|_2) \tag{2}$$

$$\mathbf{B}_{ik} = (\sum_t \mathbf{y}_{it}\mathbf{c}_{kt}^T) \times ((\sum_{kt} \mathbf{c}_{kt}\mathbf{c}_{kt}^T + \lambda))^{-1}; \tag{3}$$

The optimization of **B** are analytically calculated in Eq. 3. The inversion can be calculated using numerical algorithms such as singular value decomposition (SVD). The clustered mean curves $\bar{c}_k(t)$ in Sect. 1.1 are taken as characteristic TACs here for sinogram decomposition. Considering the incomparable signals usually appear after a few minutes when the radioactive tracer has metabolized for a while, the decomposition starts from the frame l_0 when obvious incomparable signals appear ($max(\bar{c}_{k,l_0})/min(\bar{c}_{k,l_0}) > \alpha$, α is a constant).

The decomposed sinograms are reconstructed individually using FBP with a ramp filter. The strong streak artifacts in the reconstructed images can be easily filtered out using standard algorithms such as clustering. The final images are reassembled from all the reconstructions of decomposed sinograms.

2 Results

2.1 Numerical Phantom and Simulations

A numerical abdomen phantom was constructed with realistic anatomical structures including bladder, prostate, rectum, bones, spine, fat and muscle as shown in Fig. 2. A ^{18}F-FDG dynamic PET for 60 minutes was simulated on this phantom [6], where the time course (TACs) of each tissue was calculated based on the physiological parameters taken from literatures. The phantom consists of 256 × 256 pixels and 43 frames (frame duration: 1 s–2.5 min) according to a real PET protocol. The tracer was continuously cleaned during the metabolism and accumulated in the bladder, leading to at least 30 times higher activity concentration than in other tissues in last 20 minutes. Each image slice was forward-projected and binned into a sinogram (128 bins, 64 projections). Poisson noise was generated in each LOR. In total, the simulated acquisition consisted of 43 frames and 128 × 64 LORs per frame.

The sinogram acquisition was pre-reconstructed into an image series (256 × 256 × 43) using conventional FBP. Here, the activity had two comparable levels (bladder and regular tissue). TACs of the reconstruction were clustered into two categories with two mean curves (Fig. 3a). The clustered TACs were taken as the basis function

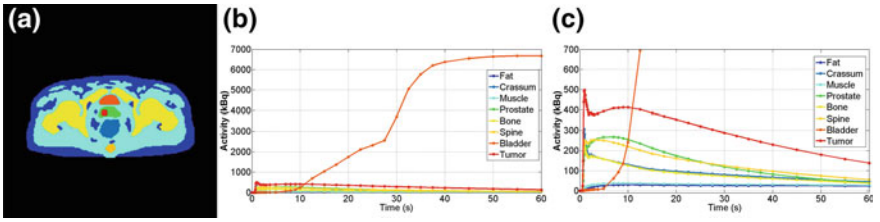

Fig. 2 **a** the abdomen phantom; **b** realistic TACs associated to each tissue; **c** zoom into the tissue TACs on low activity level

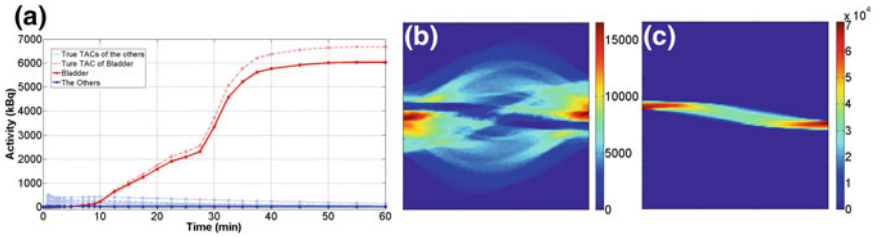

Fig. 3 **a** TACs assigned to tissues (*dash*) and extracted TACs by clustering (*solid*); A sinogram (34th frame) includes: **b** a normal activity part and **c** a high activity part

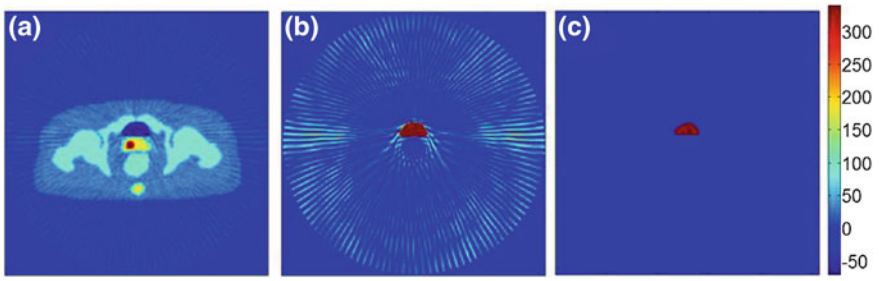

Fig. 4 FBP reconstruction of sinogram with: **a** normal activity; **b** high activity. **c** the segmented bladder area using cluster

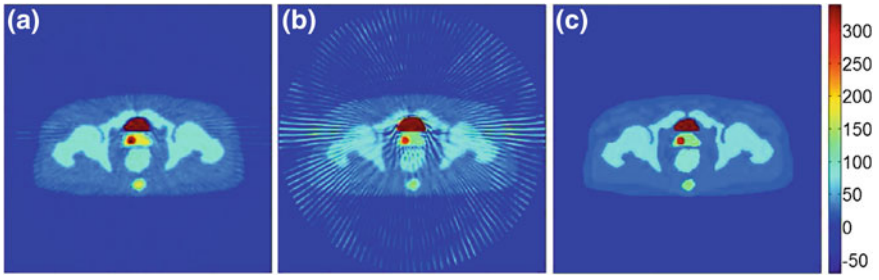

Fig. 5 An example image (34th frame) reconstructed by: **a** proposed algorithm; **b** FBP; **c** ground truth

for sinogram decomposition. Here $\alpha = 20$ is taken and leads to decomposition on frames from 28 to 43. The decomposed sinogram ($\lambda = 270$) includes a high activity concentration part (Fig. 3c) corresponding to the bladder and a normal activity concentration part (Fig. 3b) to rest tissues.

Decomposed sinograms were reconstructed using conventional FBP (Fig. 4a, b). The streak artifacts in reconstructed images of the high activity part were filtered out using a clustering algorithm (Fig. 4c). The cleaned bladder image was added to the reconstruction obtained from the normal intensities, yielding the final result. Figure 5a, b show a comparison of images using the proposed algorithm and

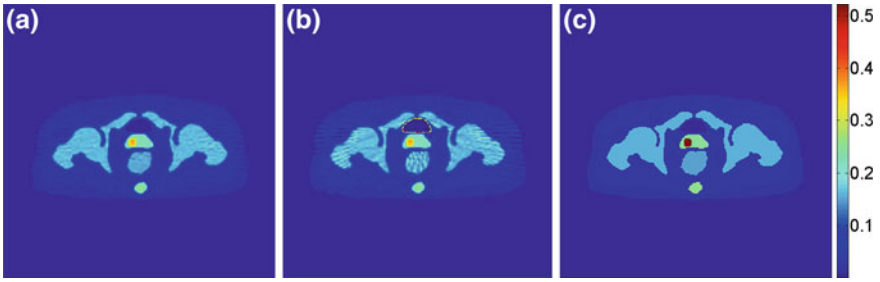

Fig. 6 K_1 image generated by: **a** proposed algorithm; **b** FBP; **c** ground truth

Table 1 RMSE of kinetic parameters and tracer activity concentration

	k_1			K_3			K_i			Activity distribution		
Projections	32	64	128	32	64	128	32	64	128	32	64	128
FBP	0.04	0.03	0.03	0.44	0.29	0.14	0.06	0.04	0.04	102.8	63.7	57.8
New Method	0.022	0.019	0.019	0.069	0.064	0.064	0.01	0.01	0.01	19.24	15.19	14.55
Improve (%)	43.6	40.6	36.7	84.1	78.2	54.6	90.5	84.2	82.9	81.3	76.2	74.8

conventional FBP. The ramp filter is used avoiding any loss of high frequency information [3]. The proposed method achieved a significant reduction of artifacts compared to FBP.

A typical irreversible two-tissue compartmental model is applied on the reconstructed images to assess the quantitative accuracy of different algorithms (Fig. 6). The resulting parametric images were compared with the ground truth in terms of RMSE as shown in Table 1 (K_1, k_3 and $K_i = \frac{K_1 k_3}{k_2+k_3}$ are presented.). Note that the bladder is not applicable for the two-tissue compartment model which is usually excluded from quantitative analysis. Thus we did not consider the bladder for RMSE. The quantitative accuracy such as the border of bladder in Fig. 6b is affected by the severe artifacts of conventional FBP, which is not noticeable for the new method. To study the influence of the number of projections, data sets with 32 or 128 projections were also simulated and reconstructed under the same condition for comparison. The result shows that the reconstruction using the new method has a better quantification accuracy than FBP that a 37 to 91 % improvement is gained.

The reconstructed image quality is assessed by comparing the tracer activity concentration in terms of RMSE, which is calculated from the difference between the reconstructed images with the ground truth. On the average of all frames a $77\,\% \pm 3\,\%$ improvement is obtained (Table 1). The improvement can be further confirmed by Fig. 7: the RMSEs at frames where the new method was applied (frame 28 to 43) is significantly lower compared with conventional FBP.

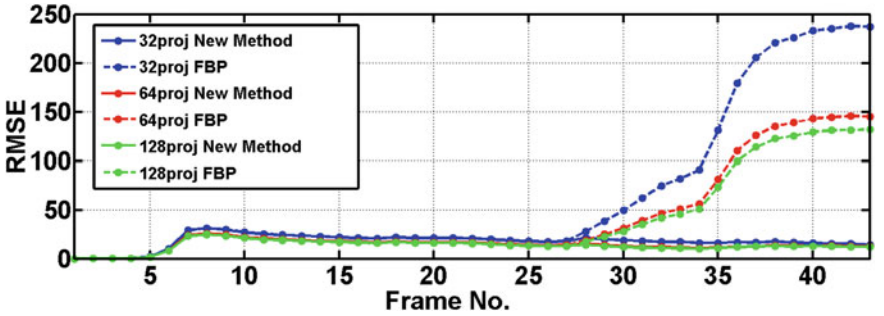

Fig. 7 RMSE of tracer activity concentration over time between the ground truth and FBP (*dash*) or the new method (*solid*)

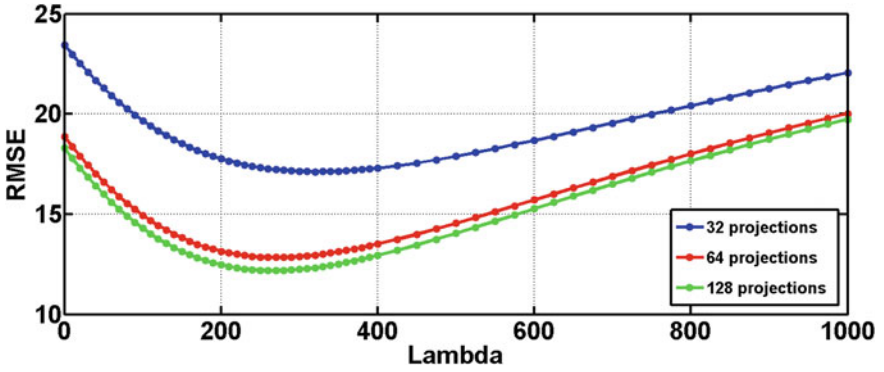

Fig. 8 Lambda versus RMSE of image quality

Note that the parameter λ in Eq. (2) is case-dependent. The accuracy of the reconstruction varies as λ changes (Fig. 8). Nevertheless an optimum can be usually found within a relatively wide range (220–330) and is almost independent of the number of projections, thus the selection of λ does not influence the result significantly. $\lambda = 270$ is chosen in this study to optimize the performance of the proposed method at 128 projections.

2.2 Physical Phantom and Real Measurements

To evaluate the algorithm in real measurements, a dynamic PET scan of a physical phantom was performed with a Siemens Inveon PET. The phantom consists of 7 holes for insertable eppendorf tubes which can be filled with ^{18}F-FDG tracer (Fig. 9a). The dynamic scan is made up by 35 static scans where tubes with different tracer concentration were imaged according to realistic TACs. In total, the dynamic scan

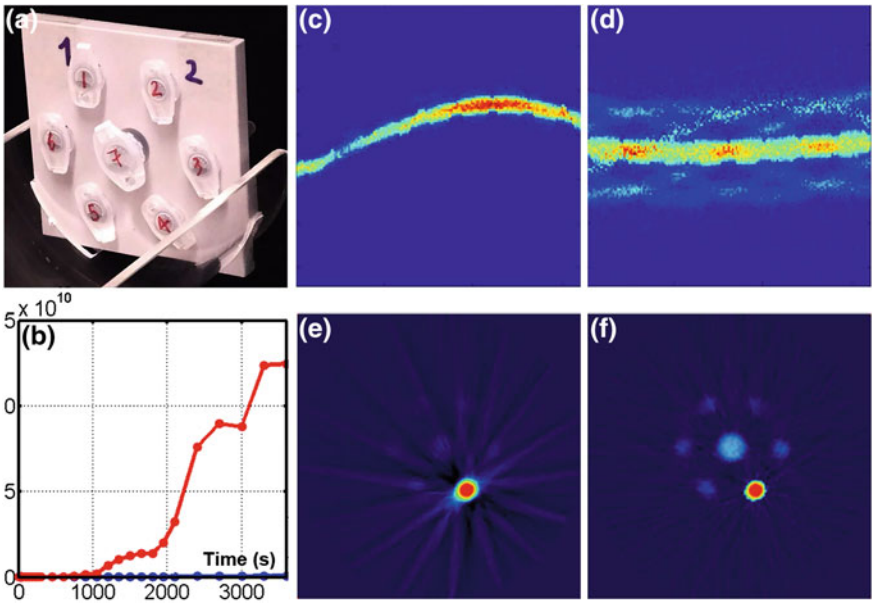

Fig. 9 **a** Phantom; **b** Clustering results; The separated sinogram (35th frame) corresponding to the high (**c**) and low (**d**) activity areas; The 35th slice of: **e** FBP; **f** proposed algorithm

contains 35 frames: 5 s for 8 frames, 10 s for 2 frames, 30 s for 8 frames, 150 s for 12 frames, and 300 s for 5 frames. The resulting acquisition consists of 128×160 LORs and 159 planes per frame. Data are corrected for decay to the starting time point of the experiment.

The reconstruction of this dynamic acquisition shows a clear improvement in image quality using the proposed method ($\alpha = 20$; $\lambda = 270$) in comparison with FBP (Fig. 9b, c). Due to technical problems of this complicated experiment, a small portion of data is missing and is completed by interpolation. A repeat experiment is scheduled.

3 Conclusion

This paper proposed a novel dynamic PET reconstruction algorithm to reduce streak artifacts of FBP while preserving the quantitative accuracy. Tests on realistic numerical simulations show a clear improvement in image quality as well as quantitative accuracy using the new algorithm. The evaluation on physical phantom further proves that better images can be achieved with the proposed method. For future work, this

method will be extended to 3D reconstruction, which has the potential to prompt dynamic 3D-FBP for practical use. Further evaluation needs to be done on clinical studies.

References

1. Herranz, E., Herraiz, J.L., Vicente, E., Espana, S., Desco, M., Vaquero, J.J., Udias, J.M.: Quantification limits of iterative PET reconstruction algorithms and improved estimation of kinetic constants. ISBI SA-PS1a.4 (2011)
2. Schiepers, C., Nuyts, J., Wu, H.M., Verma, R.: PET with 18F-fluoride: effects of interactive versus filtered backprojection reconstruction on kinetic modeling. IEEE Trans. Nucl. Sci. **44**(4), 3–1591 (1997)
3. Bruyant, P.P., Sau, J., Mallet, J.J.: Streak artifact reduction in filtered backprojection using a level line-based interpolation method. J. Nucl. Med. **41**, 9–1913 (2000)
4. Wang, G., Snyder, D., O'Sullivan, J., Vannier, M.: Iterative deblurring for CT metal artifact reduction. IEEE Trans. Med. Imaging **15**, 64–657 (1996)
5. Krestyannikov, E., Tohka, J., Ruotsalainen, U.: Segmentation of dynamic emission tomography data in projection space. CVAMIA **4241**, 108–119 (2006)
6. Saad, A., Smith, B., Hamarneh, G., Möller, T.: Simultaneous segmentation, kinetic parameter estimation, and uncertainty visualization of dynamic PET images. In: MICCAI 2007, vol. 4792, pp. 726–33 (2007)

Part II
Clinical Applications

4-D PET-MR with Volumetric Navigators and Compressed Sensing

Stefano Pedemonte, Ciprian Catana and Koen Van Leemput

Abstract Hybrid PET-MR scanners acquire multi-modal signals simultaneously, eliminating the requirement of software alignment between the MR and PET imaging data. However, the acquisition of high-resolution MR and PET images requires long scanning times, therefore movement of the subject during the acquisition deteriorates both the PET and the MR images. In this work we have developed an approach for tightly integrated PET-MR imaging, making use of volumetric MR navigators to inform, in real-time, both the MR acquisition and the PET reconstruction. The integrated imaging procedure that we describe exploits the simultaneity of MR and PET in hybrid PET-MR systems, producing inherently-aligned motion-free MR and PET images. We describe the system setup, the algorithm for motion-corrected reconstruction, an adaptive sinogram binning algorithm and software design decisions aimed at integrating tightly the MR and PET subsystems. Application of the integrated motion-corrected acquisition procedure to a phantom study and to a volunteer subject demonstrates the validity of the approach for a variety of motion patterns.

Keywords Unified PET-MR · 4-D Tomographic reconstruction · Motion aware imaging

1 Introduction

Hybrid PET-MR scanners acquire multi-modal signals simultaneously, eliminating the requirement of software alignment between the MR and PET imaging data.

S. Pedemonte (✉) · C. Catana · K. Van Leemput
Athinoula A. Martinos Center for Biomedical Imaging, MGH/Harvard, Charlestown, MA, USA
e-mail: spedemonte@mgh.harvard.edu

S. Pedemonte · K. Van Leemput
Department of Information and Computer Science, Aalto University, Espoo, Finland

K. Van Leemput
Department of Applied Mathematics and Computer Science, Technical University of Denmark, Copenhagen, Denmark

F. Gao et al. (eds.), *Computational Methods for Molecular Imaging*,
Lecture Notes in Computational Vision and Biomechanics 22,
DOI 10.1007/978-3-319-18431-9_10

However, the acquisition of high-resolution MR and PET images requires long scanning times. Movement of the subject during the acquisition determines a deterioration of both the PET and the MR images. In the context of neuro-imaging, recent advancements of MR technology have seen the development of *prospective* motion correction algorithms [1, 2] based on the insertion, in the MR sequences, of navigators designed to acquire information about the position of the head. In this work we have developed an approach for tightly integrated PET-MR imaging, making use of navigators to inform both the MR acquisition and the PET reconstruction. The integrated imaging procedure that we describe exploits the simultaneity of PET and MR, producing inherently-aligned motion-free PET and MR images. The methodology that we describe is based on a spatio-temporal model of PET imaging that enables the inclusion of sparsity constraints. We describe a reconstruction algorithm based on the Alternating Direction Method of Multipliers that enables the use of the non-smooth sparsity prior while incorporating efficiently the information from multiple time frames.

2 Method

2.1 Volumetric Navigators

High resolution tissue contrast images are acquired with the MEMPRAGE sequence, widely employed for morphometry studies. In order to acquire motion information, sampling of k-space is interleaved with the acquisition, during the dead time of each repetition (TR) of a volumetric navigator (vNav) [2]. The vNav consists of a 32^3 isotropic volume 3D-encoded with EPI, requiring 275 ms to acquire. Motion estimation is performed using the PACE [3] library to register each vNav's image to the reference vNav acquired in the first TR. Due to the low resolution of the vNav image, this is performed reliably in under 100 ms on current scanner hardware (Siemens Biograph mMR). The direction of the MR gradient for the acquisition of each new slice of k-space for the MEMPRAGE sequence is adjusted in real-time according to the pose estimate provided by the vNav, effectively acquiring all of k-space in the moving frame attached to the head of the subject.

2.2 Compressive Model-Based Motion Correction

The PET list-mode data is binned into N_t sinograms q_d^t, with $t = 1, 2, \ldots, N_t$ indexing the time frames and d indexing the lines-of-response (LOR) of the scanner. Let p_{vd} be the probability that a decay event at location X_v within the imaging volume of the scanner is detected in LOR d; let L^t be the $[4 \times 4]$ transformation

matrix that maps the coordinate system attached to the head of the patient to the coordinate system of the PET scanner and let $\widetilde{L}^t$ be the corresponding $[N_v \times N_v]$ resampling operator, with N_v voxels of the imaging volume. The model is framed in the probabilistic setting. In order to account for motion, in this first formulation, we introduce the assumption that the activity in the coordinate system attached to the head of the patient is constant: $\boldsymbol{\lambda} = \lambda_1, \ldots, \lambda_v, \ldots, \lambda_{N_v}$. Under this assumption, the conditional probability distribution associated to the number of counts in LOR d at time t is given by:

$$p(q_d^t|\boldsymbol{\lambda}, \widetilde{L}^t) = \mathcal{P}\left(\sum_v p_{vd}[\widetilde{L}^t\boldsymbol{\lambda}]_v; q_d^t\right) \tag{1}$$

We assume a sparsifying L1-norm prior probability distribution for the activity:

$$p(\boldsymbol{\lambda}) \propto e^{-\beta\|\boldsymbol{\lambda}\|_1} \tag{2}$$

2.3 Alternating Direction Method of Multipliers

The most commonly employed algorithm for PET reconstruction is Maximum Likelihood Expectation Maximization—MLEM (and its variant OSEM). Compared to other optimization algorithms, MLEM has the advantage of not requiring the selection of the step size, providing a simple and reliable solution. However MLEM is only applicable to the unconstrained reconstruction (see e.g. [4]). Although approximations of MLEM have been devised to include differentiable constraints, there use of a non-differentiable prior such as the sparsity prior (2) poses an additional challenge. Here, in order to include the sparsity prior, we adopt a data-augmentation method, the Alternating Direction Method of Multipliers (ADMM). As discussed in the review of ADMM presented in [5], in order to derive the ADMM update formula, for the maximum probability problem, we reformulate the problem as a constrained linear program with equality constraints:

$$\hat{\boldsymbol{\lambda}} = \arg\min -\sum_t \log p(q_d^t|\boldsymbol{\lambda}_t, \widetilde{L}^t) - \log p(\boldsymbol{\lambda}) \tag{3}$$

$$\text{subject to } \boldsymbol{\lambda}_t = \boldsymbol{\lambda}, \textit{ for each } t \tag{4}$$

The point is that the variables $\boldsymbol{\lambda}_i$ must ultimately equal each other, but they can temporarily be unequal while they separately try to satisfy different cost functions. This optimization problem corresponds to the maximization of the augmented Lagrangian:

$$L(\boldsymbol{\lambda}, \boldsymbol{\lambda}_1, \ldots, \boldsymbol{\lambda}_t, u_1, \ldots, u_t) = -\sum_t \log p(q_d^t|\boldsymbol{\lambda}_t, \widetilde{L}^t) - \log p(\boldsymbol{\lambda}) + \tag{5}$$

$$+ \sum_t u_t^T(\boldsymbol{\lambda} - \boldsymbol{\lambda}_t) + \frac{\rho}{2}\sum_t \|\boldsymbol{\lambda} - \boldsymbol{\lambda}_t\|_2^2, \tag{6}$$

where u_t are the Lagrange multipliers and $\frac{\rho}{2}\sum_t \|\boldsymbol{\lambda} - \boldsymbol{\lambda}_t\|_2^2$ is the augmentation term. Minimization of the augmented Lagrangian with dual descent yields the ADMM algorithm [5]:

$$\boldsymbol{\lambda}_t^{n+1} := \arg\min_v -\log p(q_d^t|v, \widetilde{L}^t) + \frac{\rho}{2}\|v + u_t^n - \boldsymbol{\lambda}^n\|_2^2 \tag{7}$$

$$\boldsymbol{\lambda}^{n+1} := S_{\frac{\rho}{\beta}}\left(\frac{1}{N_t}\sum_t \boldsymbol{\lambda}_t^{n+1} + \frac{1}{\rho N}\sum_t u_t^n\right) \tag{8}$$

$$u_t^{n+1} := u_t^n + \boldsymbol{\lambda}_t^{n+1} - \boldsymbol{\lambda}^{n+1}, \tag{9}$$

where $S_{\frac{\rho}{\beta}}$ is the soft-thresholding operator (see [5]). For the update of $\boldsymbol{\lambda}_t^{n+1}$ we adopt a single iteration of OSEM with warm start (i.e. initializing v at $\boldsymbol{\lambda}_t^n$) and with the One Step Late approximation proposed by Green [4]. In order to account for scatter and randoms, we adopt the Ordinary Poisson version, obtaining:

$$\lambda_{t,v}^{n+1} = \lambda_{t,v}^n [\widetilde{L}^t]^T \left[\frac{1}{\sum_{d\in\mathcal{D}^t} p_{vd} - \rho(\boldsymbol{\lambda}_t^n + u_t^n - \boldsymbol{\lambda}^n)} \sum_{d\in\mathcal{D}^t} \frac{p_{vd} q_d^t}{\sum_{v'} p_{v'd}[\widetilde{L}^t \lambda]_{v'} + r_d^t + s_d^t} \right],$$

where $\mathcal{D}^t$ are time-dependent subsets of the LORs of the scanner. In the experiments that follow, time-dependent randoms rates r_d^t are estimated from single crystal event rates obtained by instantiating singles sinograms for each time frame; the scatter estimates s_d^t are obtained by weighting, by the duration of the time frames, the scatter estimate obtained by single scatter simulation (SSS) [6] based on the static, non motion-corrected, reconstruction. The estimate of the attenuation map is derived from a radial-VIBE MR image acquired right before the first TR of the vNav MEMPRAGE sequence. As dictated by the model, projections and back-projections account for the attenuation by transforming the attenuation map by $\widetilde{L}^t$ at each time frame.

2.4 Extraction of the Motion Events

In order to optimize the computing resources, binning of the list-mode data into the 4-D sinogram q_d^t is performed adaptively. Let us index with $t' = 1, 2, \ldots$ the MR repetitions and denote by $M^{t'}$ the $[4 \times 4]$ transformation matrix that maps the vNav at time t' to the first vNav. After each vNav acquisition and registration, at time t', the

binning algorithm decides whether a motion event has occurred by setting a threshold on the extent of motion since the previous motion event t'^* (starting with $t'^* = 1$). As the measure of the extent of motion, we employ the mean voxel displacement in the imaging volume:

$$w^{t'} = \frac{1}{N_v} \sum_{v=1}^{N_v} \| M^{t'^*} X_v - M^{t'} X_v \| \tag{10}$$

Each time a motion event is detected, the PET time frame index t is increased; a new sinogram is instantiated and L^t is set to $L^t = M^{t'} M^{\mathrm{MR}\to\mathrm{PET}}$, where the calibration matrix $M^{\mathrm{MR}\to\mathrm{PET}}$ is computed initially according to the MR acquisition settings, the geometry of the system and the position of the bed of the scanner. In the current implementation, interaction events acquired during the period TR preceding each motion event are discarded.

2.5 Software Framework for 4-D Reconstruction

A considerable software design effort was necessary in order to implement the 4-D reconstruction algorithm that processes the list-mode data, synchronizing the MR and PET subsystems. Projection and back-projection algorithms based on ray-tracing have been designed with the aim of computing, without overhead, the spatial transformations required by the algorithm of Eq. (10). The projection and back-projection algorithms operate directly on compressed 4-D sinograms designed to enable storage of the full sequence on the memory of a single Graphics Processing Unit (GPU).

3 Experiments

Experiments were performed on a Siemens scanner Biograph mMR. TR was set to 2.5 s and the threshold of $w^{t'}$ was set to 0.5 mm.

Phantom study—A pineapple with attached a helicoidal capillary filled with 1.5 mCi of FDG was scanned for 400 s. The phantom was translated periodically by 12 mm along the axis of the scanner every 40 s. Figure 1a reports the motion estimates. Figure 1b-g display the reconstructions with and without motion correction and with and without sparsity constraint (sparsity parameter $\beta = 0.1$).

Healthy volunteer—A healthy volunteer was scanned for 400 s, 20 min post injection of 4.7 mCi of FDG. Figure 2 reports the motion estimates, the extent of motion, the motion events, and the unconstrained reconstructions without motion correction and

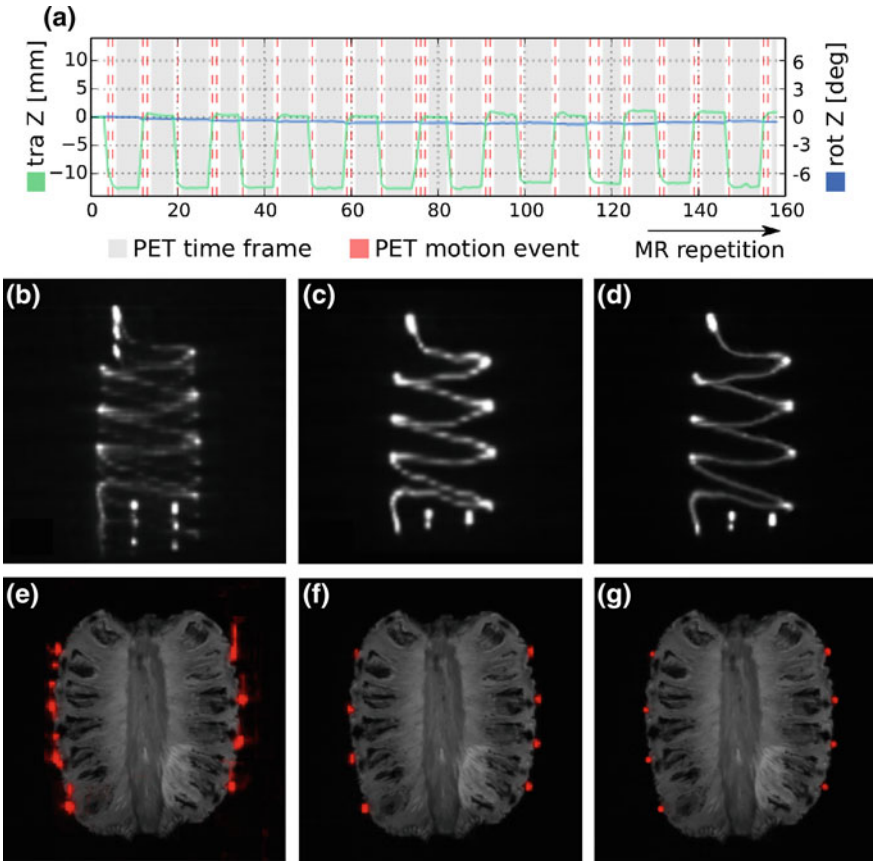

Fig. 1 Pineapple with helicoidal FDG capillary source. **a** Estimated motion profiles (tanslation along the axis of the scanner Z and rotation around Z). Each *gray box* corresponds to a sinogram. **b–d** Volume renderings of the PET reconstructions without motion correction (**b**), with motion correction (**c**), with motion correction and sparsity (**d**). **e–g** Representative slice of fused MR and PET images without motion correction (**e**), with motion correction (**f**), with motion correction and sparsity constraint (**g**)

the constrained motion corrected reconstruction. The subject was scanned again for 400 s after insertion of a 3 cm-thick latex pillow. Note that in case of continuous motion, as displayed in Fig. 3, the algorithm of paragraph 2.4 adapts the duration of the sinograms according to the rate of change of the extent of motion. Note, in Figs. 2 and 3, that the binning algorithm generated, in both experiments, 11 time frames. The reconstruction time, which scales linearly with the number of time frames, was 14 min.

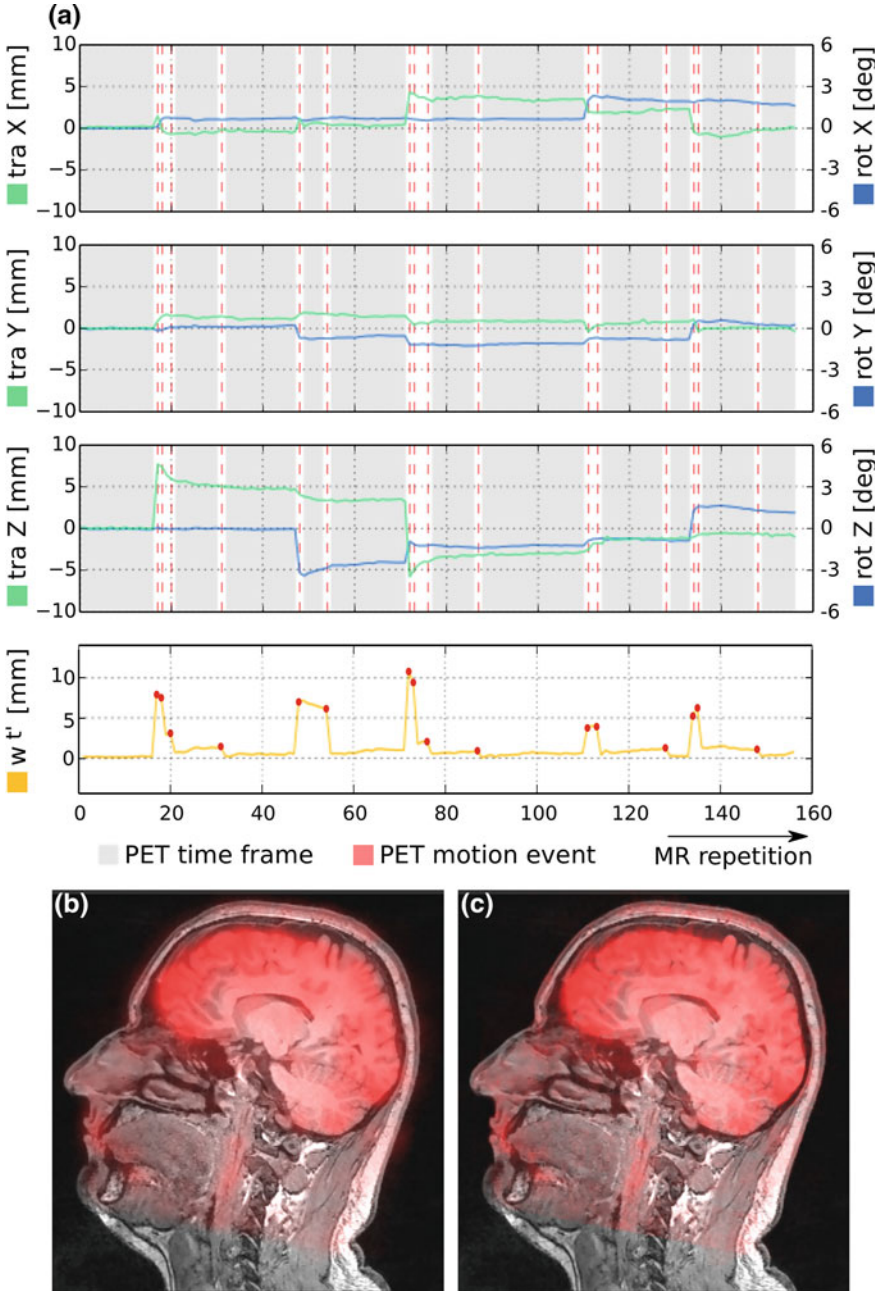

Fig. 2 Healthy volunteer. **a** Estimated motion profiles and extent of motion $w^{t'}$. **b, c** Representative slices of the fused MR and PET images without motion correction (**b**) and with motion correction and sparsity constraint (**c**)

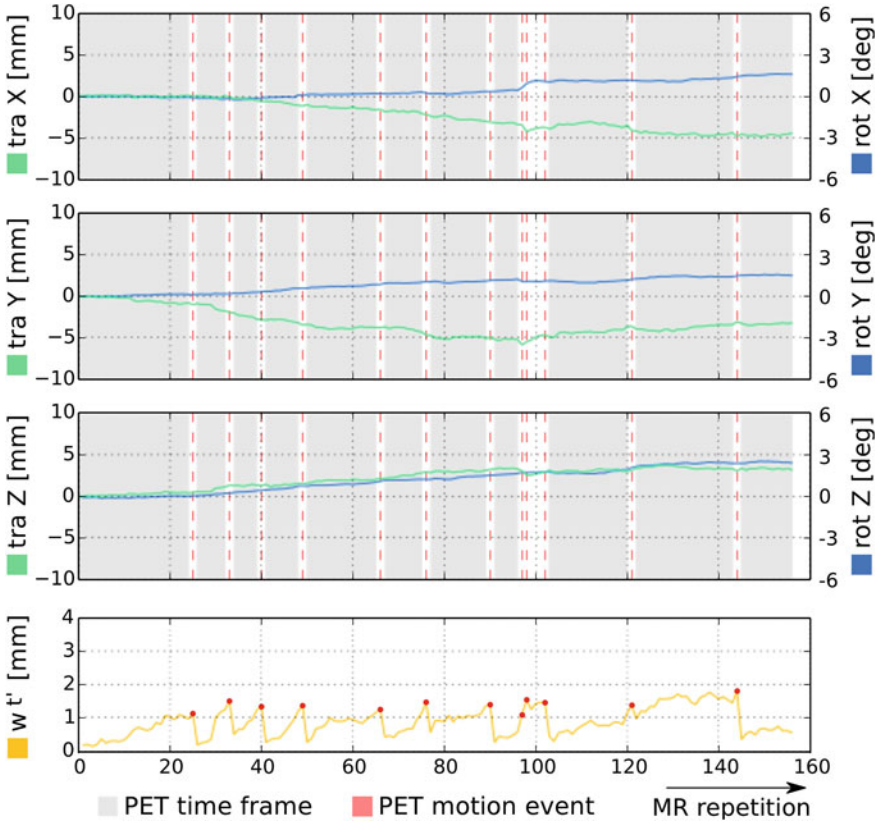

Fig. 3 Healthy volunteer on 3 cm-thick latex pillow. The adaptive binning algorithm produces sinograms with longer duration (*gray boxes*) when the pillow is fully compressed

4 Conclusion

We have developed an integrated approach to PET-MR that enables the reconstruction of motion-free PET and MR images in the same frame of reference. The model-based approach for PET reconstruction that we have described enables us to account for attenuation, randoms and scatter, while integrating motion information. The event-based methodology based on a relative measure of extent of motion enables the correction of large motion events and of slow drifts, adapting the demand of computing resources to the motion patterns. The optimization algorithm, based on the Alternating Direction Method of Multipliers, enables the inclusion of a sparsity constraint, which improves image quality. The GPU accelerated software implementation (http://niftyrec.scienceontheweb.net) enables reconstruction times comparable to static reconstruction. In future work we will explore the inclusion of

pharmacokinetics in the imaging model, the acquisition of multiple MR sequences with embedded volumetric navigators and non-rigid motion.

Acknowledgments This research was supported by the NIH NCRR (P41-RR14075), the NIH NIBIB (R01EB013565), and TEKES (ComBrain).

References

1. der Van Kouwe, A.J., et al.: Real-time rigid body motion correction and shimming using cloverleaf navigators. MRM **56**(5), 1019–1032 (2006)
2. Tisdall, M.D., et al.: Volumetric navigators for prospective motion correction and selective reacquisition in neuroanatomical MRI. MRM **68**(2), 389–399 (2012)
3. Thesen, S., et al.: Prospective acquisition correction for head motion with image-based tracking for real-time fMRI. Magn. Reson. Med. **44**(3), 457–465 (2000)
4. Green, P.J.: Bayesian reconstructions from emission tomography data using a modified EM algorithm. IEEE TMI **9**(1), 84–93 (1990)
5. Boyd, S., Parikh, N., Chu, E., Peleato, B., Eckstein, J.: Distributed optimization and statistical learning via the alternating direction method of multipliers. Found. Trends. Mach. Learn. **3**(1), 1–122 (2012)
6. Watson, et al.: A single scatter simulation technique for scatter correction in 3D PET. Three-Dimensional Image Reconstr. Radiol. Nucl. Med. **4**, 68–255 (1996)

Robust Feature Selection to Predict Lung Tumor Recurrence

Hongmei Mi, Caroline Petitjean, Pierre Vera and Su Ruan

Abstract The recurrence of cancer increases the risk of death. The ability to predict such recurrence could be beneficial to planning treatment. We aim to find a predictive feature subset from a series of spatiotemporal PET image characteristics, including SUV-based and texture features, in order to predict lung tumor recurrence one year after treatment. To overcome the small sample size, class imbalance problem, we propose a hierarchical forward selection algorithm to select the smallest feature subset that results in the best prediction performance. As the SUV-based features have been recognized as significant predictive factors for a patient's outcome, we propose incorporating this prior knowledge into the selection procedure to improve its robustness and accelerate its convergence. By fixing the first feature as one SUV parameter, the proposed hierarchical forward selection yields a small robust feature subset with promising prediction performance.

Keywords Hierarchical forward selection · Robustness · Prior knowledge · Tumor recurrence prediction · Small sample · PET

1 Introduction

A proportion of lung cancer patients, even when treated with curative intent, develop post-treatment recurrence, which increases the risk of death. The ability to predict such recurrence prior to or even during the treatment could be of clinical value with regard to determining a treatment strategy. Imaging can play a crucial role as it allows for a non-invasive following up the tumor. Indeed, functional

This work is partly supported by China Scholarship Council.

H. Mi (✉) · C. Petitjean · P. Vera · S. Ruan
QuantIF - LITIS (EA4108 - FR CNRS 3638), University of Rouen, 76000 Rouen, France
e-mail: hongmei_mi@hotmail.com

P. Vera
Centre Henri-Becquerel, 76038 Rouen, France

F. Gao et al. (eds.), *Computational Methods for Molecular Imaging*,
Lecture Notes in Computational Vision and Biomechanics 22,
DOI 10.1007/978-3-319-18431-9_11

information gathered by positron emission tomography (PET) using the radiotracer FDG has already shown its predictive value for tumor response to treatment in several cancers, including esophageal [10], lung [7], and cervix [8]. The well-explored FDG-PET imaging features include, but are not limited to, metabolic tumor volume (MTV), total lesion glycolysis (TLG), as functional indices describing metabolic tumor burden, and standardized uptake values (SUVs) describing FDG uptake within a region of interest (ROI), e.g. SUVmean, SUVpeak, or single pixel (SUVmax) [8, 10]. Characterization of PET images through analysis of texture [3, 11], tumor shape [3], and intensity volume histogram [3] may also have potential predictive value for treatment outcome, providing additional and complementary indices. However, there is no clear consensus regarding the optimum predictive factors. This study therefore aims at finding predictive PET image characteristics that accurately anticipate the lung tumor recurrence through feature selection techniques. It is indeed of practical importance to make a prognosis based on a small subset of features. Furthermore, our dataset, as often in the medical domain, is small and imbalanced: there are more recurrence cases than non-recurrence ones, for a total of a few dozen of samples.

Several feature selection algorithms have been proposed to overcome the small sample problem. Authors in [2] propose a feature ranking method called FAST (Feature Assessment by Sliding Thresholds) based on the area under the receiver operating characteristic which is generated by sliding threshold value in one dimensional feature space. However, univariate ranking methods like FAST overlook the interaction between features. Guyon and Elisseeff [4] have pointed out that features which are irrelevant on their own can be useful in conjunction with other features, and the combination of two highly correlated features can be more useful than either feature independently. Feature subset selection methods evaluate subsets of features together, as opposed to ranking features according to their individual discrimination power. Feature selection with kernel class separability (KCS) ranks feature subsets according to their class separability. KCS is claimed robust to small size samples and to the presence of noisy features [12]. However, as for other feature ranking methods, a threshold value or a number of features should be specified by users to obtain the final subset. Enlightened by the outstanding generalization performance of Support Vector Machines (SVM), Guyon et al. propose a method using SVM based on Recursive Feature Elimination, named SVMRFE [5]. Starting with the whole feature space, SVMRFE progressively eliminates the least promising one(s) whose removal minimizes the variations of feature weights, until a user-defined number of features remains, which yields nested feature subsets. SVMRFE still retains the risk of removing useful features as complementary to others. In addition to a good accuracy, robustness of feature selection is a desirable property. Robustness can be viewed as the property of an algorithm to produce a consistent feature subset under varying conditions such as perturbations of training data [13]. It is particularly difficult for a feature selection algorithm to obtain a robust feature subset dealing with small data sets.

In this paper, we are interested in selecting a minimum subset of features, thus we consider the forward selection for its good performance when the optimal subset is small. In such a search strategy, features are progressively incorporated into larger

and larger subsets until a certain criterion is satisfied. Forward selections thus produce nested feature subsets. To improve the probability of obtaining the most discriminant feature subset, we propose a feature selection algorithm that hierarchically forward searches for the smallest subset that produces the best prediction. The second point of our paper deals with prior information, which is often available in the medical field (e.g. organ shape, patient characteristics, ...). With respect to predictive factors for patient's outcome, many researches have shown that SUV-based features are of great significance [7, 8, 10]. The idea is that this prior knowledge should be incorporated into the feature selection procedure. We thus propose to incorporate this knowledge to the hierarchical forward selection, by fixing the first one feature as one of the SUV-based features, to obtain a robust feature subset more efficiently.

2 Methods

2.1 Feature Extraction

To follow up the tumor response to treatment, several PET scans, including baseline (PET_0) and two following-ups (PET_{1-2}) are performed. As seen in Fig. 1, PET uptake longitudinal distributions show great intra- and inter- class variability, which is challenging. The same ROI (semiautomatically delineated) is used on three scans. Five SUV-based features are extracted on each PET: SUVmax, SUVmean, SUV-peak (mean value inside $3\times3\times3$ neighborhood of SUVmax), MTV (defined by a thresholding of 40 % of SUVmax on PET_0), TLG (SUVmean $\times$ MTV). Complementary to these SUV-based features, texture analysis allows us to explore spatial uptake heterogeneity information. We use gray level size zone matrices (GLSZM) [11], which have shown good properties on PET image characterization, from which eight regional heterogeneity parameters can be computed (please see [11] for more details).

Considering that the longitudinal change of image characteristics may provide predictive value, we calculate temporal changes between baseline and follow-ups features. Let Y denote the final spatiotemporal feature set, of length $d = 52$. Features are rescaled to the range of [0,1] to make them comparable.

2.2 Hierarchical Forward Selection (HFS)

In the following, we describe the measure to evaluate the "goodness" $J(S)$ of a feature subset S, and the search strategy for our HFS wrapper feature selection algorithm. For the evaluation measure, we use the leave-one-out (LOO) gmean [6]:

$$\text{gmean} = \sqrt{\text{sensitivity} \times \text{specificity}}, \tag{1}$$

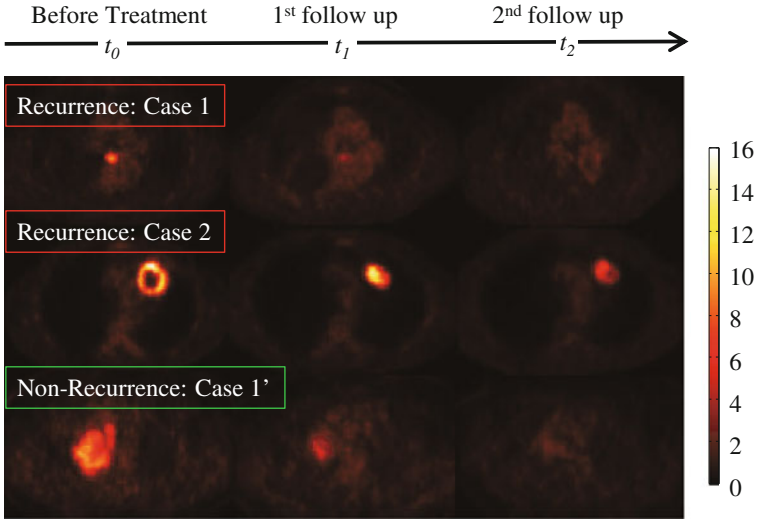

Fig. 1 Illustration of PET scans at baseline and following-ups for three patients with (*top two rows*) and without (*bottom row*) recurrence, shown with the same color scale

which is an accuracy measure balancing the classification between imbalanced classes. Under the small sample size assumption, the classification accuracy exhibits only a few possible values. While the subset feature space can easily be of the order of thousands ($2^d - 1$), there is a high probability that some feature subsets will produce the same classification accuracy, making it difficult to distinguish different feature subsets. To improve the possibility of finding the best feature subset, we propose to search the feature subsets hierarchically in an iterative manner.

In the kth iteration, denote $\mathcal{F}_k$ the set of the current candidate solutions, whose elements are feature subsets of the original feature set Y, and of the same size k. Define the operation $\mathcal{A}(X, T) = \{X \cup \{e\} | \forall e : e \in T\}$, which returns the set with each element of set T added to the set X. Denote J the gmean based evaluation function. Starting with the initial candidate solution $\mathcal{F}_0 = \{\emptyset\}$ and lowerbound value J_0^l and upperbound final value J^u, $k = 0$,

1. Generate successors $\mathcal{G}_{k+1}$ of $\mathcal{F}_k$: $\mathcal{G}_{k+1} = \{\mathcal{A}(E, \mathrm{Y} \backslash E) | \forall E : E \in \mathcal{F}_k\}$.
2. Select the feature subset E in $\mathcal{G}_{k+1}$ that outperforms the best feature subset of the preceding kth iteration, i.e. $\mathcal{F}_{k+1} = \{E \in \mathcal{G}_{k+1} | \forall E : J(E) > J_k^l\}$.
3. If $\mathcal{F}_{k+1} = \emptyset$, then go to 6; else go to 4.
4. Update:
   a. $k = k + 1$;
   b. $J_k^l = \max_{E \in \mathcal{F}_k} J(E)$.
5. If $J_k^l \geq J^u \vee J_k = 100\,\%$, then go to 6; else go to 1.
6. Stop and return $\mathcal{F}_k$.

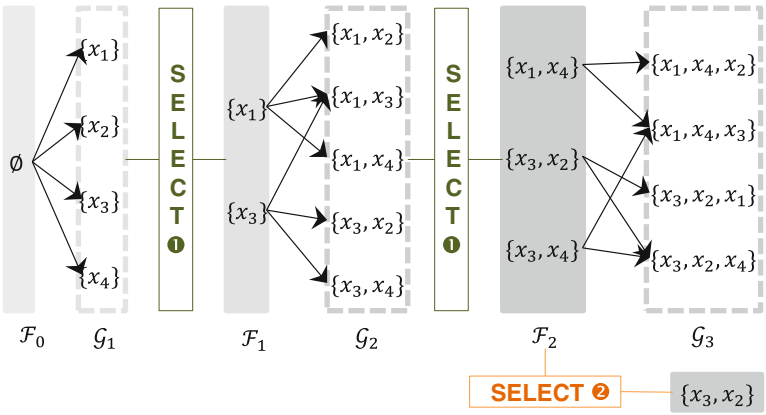

Fig. 2 An example of hierarchical forward selection from an original feature set $Y = \{x_1, x_2, x_3, x_4\}$ of length 4. Feature subsets are input into the selector ❶, and those yielding better LOOCV accuracy than preceding iteration are retained. As a result, the size of subsets of features obtained progressively increases and the accuracy of the retained subsets increases as well. The forward search stops when the accuracy stops increasing, i.e., at the 3rd iteration in this example. More than one subset of features are retained in $\mathcal{F}_2$. A unique subset of features is then selected by selector ❷, where the extremal margin is the selection criterion

Figure 2 illustrates the proposed HFS algorithm via an example, from where we can see that the structure of iterative candidate solutions is hierarchical. In fact, sequential forward selection can be considered as a special case of our HFS method: linear hierarchy, in which the maximum branching degree of any item is 1. While items in ours can have a branching degree of 1, 2 or more, so that the possibility of finding the optimal solution is greater.

We define the stopping criterion as follows (step 5): the value of J does not increase from one iteration to another, or it surpassed a prefixed upperbound value J^u, or it achieves 100 %. As several feature subsets may provide the same J value at the final iteration, we propose an auxiliary criterion to produce a unique solution when the stopping criterion is met, based on the output extremal margin (EM) of the SVM classifier:

$$\mathrm{EM} = \min_{i \in 1, \cdots, s} D_f(\mathbf{x}_i) \cdot y_i \tag{2}$$

where D_f is the decision function, $\mathbf{x}$ are support vectors, and y corresponding labels. It is the minimum distance between the outputs of support vectors and decision surface. Notice that an extremal margin may be computed on each LOO training set. A mean value may then be used as the final criterion.

2.2.1 Prior Knowledge

As the SUV-based features are known for their significant values to predict patient's treatment outcome [7, 8, 10], we propose incorporating this prior knowledge into the feature selection algorithm to improve the robustness. Among the 20 temporal SUV-based features, the feature with the maximum distance of sample mean of two classes is fixed as the first one feature, denoted by $f_{(1)}$, in the feature selection algorithm. This prior-based version of hierarchical forward selection (pHFS) starts thus from an initial solution $\mathcal{F}_1 = \{f_{(1)}\}$ and $J_1^l = J(f_{(1)})$.

3 Experimental Results

In the following, we assess our HFS algorithm on a real-world data set, as well its prior-based version pHFS, and compare it to state-of-the-art feature selection techniques.

3.1 Data

Twenty-five patients with stage II–III non small cell lung cancer treated with curative intent chemo-radiotherapy are considered in this study. The patients are treated with chemotherapy, then radiotherapy (of total dose at 60–70 Gy delivered in daily fractions of 2 Gy, 5 days a week) with possible concomitant chemotherapy. Baseline and following-up FDG-PETs at different time points are performed: PET_1 before the treatment, PET_2 after chemotherapy, and PET_3 during radiotherapy at about 45 Gy dose radiation. The images are 4.06 mm $\times$ 4.06 mm pixel size and 2 mm slice spacing. Each patient's following-up scans are manually registered to the baseline scan, with nearest-neighbor interpolation. For longitudinal analysis, all PET scans are converted into SUV which is a standardized decay-corrected value of FDG activity per unit volume of body weight (MBq/kg). Our definition of recurrence at one year after the treatment is primarily clinical, based on the evaluation by the clinician, with biopsy and PET/CT. Local or distant recurrence is diagnosed on 19 patients, and no recurrence is reported on the remaining 6 patients (Fig. 1).

3.2 Results

The numerical experiments are implemented using Matlab 7.8, whose embedded SVM package is used for training and classification. In the feature selection process, gaussian kernel SVM with sigma = 1 and C = 1 (the box constraint value for the soft margin) is chosen empirically as the classifier. For the data base under investigation,

Table 1 Prediction accuracy (%) of different methods using leave-one-out cross-validation

Methods	Sensitivity	Specificity	Gmean	Accuracy
No selection	**100**	0	0	76
FAST	74	83	78	76
KCS	84	**100**	92	88
SVMRFE	95	83	89	92
HFS	**100**	**100**	**100**	**100**

the lowerbound initial value J_0^l is set to 80 %, and the upperbound final value J^u for the stopping criterion is set to 100 %. The proposed HFS is compared to three other feature selection techniques, including FAST [2], KCS [12] and SVMRFE [5] (using the toolbox released by [1]). For these three methods, the user has to fix a cutoff value either on ranking scores or subset size to get the final subset. In our case, the cutoff values are found through a rough grid search. Experiments with all features are also carried out as baseline results.

3.2.1 Prediction Performance

The predictive value of a feature subset can be evaluated through its classification performance on test data. Because of the small sample size, we use LOO cross-validation to evaluate the prediction performance. The same classifier as in feature selection process is then used to compute the prediction performance on the unseen patient. The metrics include sensitivity, specificity, gmean, and accuracy, in which recurrence is labeled positive and non-recurrence negative. The prediction results of the proposed HFS, as well as the best performance of the other three, are reported in Table 1. The poor results produced with all features make it very clear that feature selection is necessary. Without any selection, a classifier tends to classify all samples into the majority class. The proposed HFS produces promising results: 100 % of sensitivity and specificity. KCS yields 100 % specificity, while 84 % sensitivity. SVMRFE achieves 95 % sensitivity; however, the sensitivity is only 83 %.

3.2.2 Prior Knowledge and Robustness

To investigate the role that prior knowledge can play, we carry out experiments in which the prior knowledge is incorporated into HFS, and the other three feature selection methods. It turns out that, among all, prior-based version of HFS (pHFS) and SVMRFE (pSVMRFE) benefit the most from this prior knowledge. This benefit can be well measured in terms of robustness. The robustness is measured using the *relative weighted consistency* from [9]. It allows the comparison of different sized subsets, based on feature occurrence (frequency) statistics, originating from the different folds

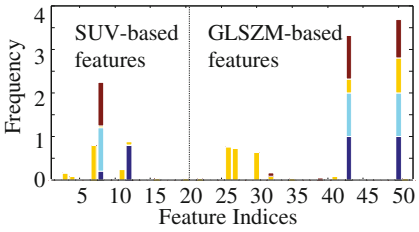

Methods	Robustness	Subset Size
HFS	89%	3
pHFS	**100%**	3
SVMRFE	56%	5
pSVMRFE	**92%**	3

Fig. 3 Normalized frequencies of each feature after LOO feature selection (*left*) and robustness and subset sizes for HFS and SVMRFE with and without prior knowledge (*right*). The robustness is improved for both methods when prior knowledge is incorporated

of the LOO. Its values range from 0 to 100 %, with 0 % indicating empty intersection between all subsets and 100 % indicating that all subsets are identical. pHFS not only predicts accurately with 100 %, also the robustness is improved, moving from 89 to 100 %. For pSVMRFE, the specificity improves from 83 to 100 %, and the robustness from 56 to 92 %. Figure 3 shows the frequency statistics, which reveals the improvement of robustness. It is of great interest that the optimal feature subsets for pHFS and pSVMRFE correspond very well.

3.2.3 Selected Features

The first fixed feature, as the prior knowledge, turns out to be the SUVmax extracted from PET_2 during radiotherapy (#8 in Fig. 3). This SUV parameter is widely used in clinic, where doctors usually apply a threshold based on this value, to help them make the decision. However, this only parameter is not sufficient, given that it yields 84 % sensitivity and 83 % specificity as prediction results on our data set. It is thus necessary to find other features combined with SUVmax so as to better predict tumor recurrence. Our method selects two other features based on GLSZM. The feature indexed as #43 is the temporal change between PET_2 and PET_0 of gray-level-non-uniformity, which is used to calculate the variability of gray level homogenous zones. The other texture feature indexed as #50 is the temporal change between PET_1 and PET_0 of zone-percentage, which is the ratio of the number of homogeneous zones to overall ROI size. These parameters corresponding to variability in the intensity or size of homogeneous areas, combined with SUVmax on PET_2, show good potential for differentiating patients in terms of tumor recurrence. Doctors who provided us with the dataset have confirmed the results.

3.2.4 Computational Cost

The average computational times on one LOO training set, for FAST, KCS, SVM-RFE, HFS are all in the order of one minute, on an Intel i5 PC (3.3 GHz CPU, 8 GB RAM). More precisely, the computational cost for HFS has been empirically compared to that of the exhaustive search. Three features are selected by our methods. Compared to exhaustive search in feature subset spaces of size 1–3, i.e. $\sum_{k=1}^{3} \binom{d}{k}$, HFS searches only in a subspace of 4.1 %, and pHFS 2.5 %. pHFS accelerates the convergence of the process.

4 Conclusion

In this paper, we aim to find the minimum features for tumor recurrence prediction. We propose a hierarchical forward selection based on SVM, which selects the smallest subset with the best prediction performance. We also propose to incorporate prior knowledge into feature selection algorithms to improve the robustness. We will next include a larger data set to further investigate our method.

References

1. Canu, S., Grandvalet, Y., Guigue, V., Rakotomamonjy, A.: SVM and kernel methods Matlab toolbox. Perception Systèmes et Information, INSA de Rouen, Rouen, France (2005)
2. Chen, Xw, Wasikowski, M.: FAST: A roc-based feature selection metric for small samples and imbalanced data classification problems. In: ACM SIGKDD, KDD'08, pp. 124–132. ACM, New York (2008). doi:10.1145/1401890.1401910
3. El Naqa, I., Grigsby, P., Apte, A., Kidd, E., Donnelly, E., Khullar, D., Chaudhari, S., Yang, D., Schmitt, M., Laforest, R., et al.: Exploring feature-based approaches in pet images for predicting cancer treatment outcomes. Pattern Recognit. **42**(6), 1162–1171 (2009)
4. Guyon, I., Elisseeff, A.: An introduction to variable and feature selection. JMLR **3**, 1157–1182 (2003)
5. Guyon, I., Weston, J., Barnhill, S., Vapnik, V.: Gene selection for cancer classification using support vector machines. Mach. Learn. **46**(1–3), 389–422 (2002)
6. He, H., Garcia, E.: Learning from imbalanced data. IEEE Trans. Knowl. Data Eng. **21**(9), 1263–1284 (2009)
7. Mi, H., Petitjean, C., Dubray, B., Vera, P., Ruan, S.: Prediction of lung tumor evolution during radiotherapy in individual patients with PET. IEEE Trans. Med. Image **33**(4), 995–1003 (2014)
8. Roman-Jimenez, G., Leseur, J., Devillers, A., David, J.: Segmentation and characterization of tumors in 18F-FDG PET-CT for outcome prediction in cervical cancer radio-chemotherapy. Image-Guidance and Multimodal Dose Planning in Radiation Therapy, p. 17 (2012)
9. Somol, P., Novovicova, J.: Evaluating stability and comparing output of feature selectors that optimize feature subset cardinality. IEEE Trans. Pattern Anal. Mach. Intell. **32**(11), 1921–1939 (2010)
10. Tan, S., Kligerman, S., Chen, W., Lu, M., Kim, G., Feigenberg, S., D'Souza, W.D., Suntharalingam, M., Lu, W.: Spatial-temporal [18F] FDG-PET features for predicting pathologic response of esophageal cancer to neoadjuvant chemoradiation therapy. Int. J. Radiat. Oncol.* Biol.* Phys. **85**(5), 1375–1382 (2013)

11. Tixier, F., Hatt, M., Le Rest, C.C., Le Pogam, A., Corcos, L., Visvikis, D.: Reproducibility of tumor uptake heterogeneity characterization through textural feature analysis in 18F-FDG PET. J. Nucl. Med. **53**(5), 693–700 (2012)
12. Wang, L.: Feature selection with kernel class separability. IEEE Trans. Pattern Anal. Mach. Intell. **30**(9), 1534–1546 (2008)
13. Yang, F., Mao, K.: Robust feature selection for microarray data based on multicriterion fusion. IEEE/ACM TCBB **8**(4), 1080–1092 (2011)

Region-Based Data-Driven Intensity Normalization for Group Comparison of Functional Brain Images

Zhiyong Xie, Aijun Zhu, Laigao Chen and Timothy McCarthy

Abstract Intensity normalization is widely used to remove the confounding effect of global change exhibited in PET or SPECT brain images such that the local activity can be detected. Improper estimate of global change may induce a biased normalization. To separate the global change from local measurements, an iterative method is proposed to identify reference regions that are not affected by the local activity. From more than one hundred predefined anatomical regions, the reference regions are selected based on their intensity similarity between two groups. Weighted least squares regression is used to compute linear intensity transformations to align intensities of corresponding reference regions across all subjects. Studies with simulated data demonstrated that the proposed method performed better in recovering real intensity change comparing with global mean normalization and with Andersson's data-driven method.

Keywords Brain imaging · Glucose metabolism · Intensity normalization · PET · SPECT

1 Introduction

Positron emission tomography (PET) and single photon emission computed tomography (SPECT) has been used to assess cerebral blood flow or metabolic activity at voxel level. With images acquired at different experimental conditions, statistical comparison can be performed between groups to discover their functional difference voxel-wisely or over a region of interest [1, 5, 9]. In a PET or SPECT image, the functional activity measured at each voxel is the confounding effect of a local activity and a global change. The global change is regional independent and always exhibits

Z. Xie (✉) · L. Chen · T. McCarthy
Pfizer Inc., Cambridge, MA, USA
e-mail: Zhiyong.Xie@pfizer.com

A. Zhu
Massachusetts General Hospital, Cambridge, MA, USA

F. Gao et al. (eds.), *Computational Methods for Molecular Imaging*,
Lecture Notes in Computational Vision and Biomechanics 22,
DOI 10.1007/978-3-319-18431-9_12

large inter- and intra-subject variation. To localize and quantify the regional activity, the global change needs to be removed to increase the statistical power of the group comparison. The global change can be estimated based on a predefined reference region which is assumed to have no local activity [4, 13]. However, selecting an appropriate reference region is very challenging in some studies. Using different brain regions may lead to different or even conflicting results [10, 12].

Besides the reference-based estimation, the average of all intracerebral voxels may be used as a measurement of the global change. In the widely used global mean normalization (GMN), the global effect is eliminated by dividing the local measurements by the whole-brain average [8]. This method works well in studies where a few small regions are activated by a task or cognitive challenge. In these kinds of studies, the magnitude of the activation is moderate and the whole-brain average is not affected by the local change. In studies with a pharmacological challenge however, a relatively large region may be activated and the local change may alter the whole-brain average. In this case, the GMN proportionally reduces the magnitude of the true activation and induces a bias in the opposite direction, thus decreasing the sensitivity and specificity in detecting the real functional change.

To address this issue, Andersson proposed an iterative method to identify voxels that are not affected by local activity and normalize images with the average intensity of identified voxels [2]. The method uses the GMN as an initial step. Then a voxel-wise comparison is performed between groups and all voxels with $p > 0.05$ are used to normalize the image. This procedure is repeated until there is no further change in the global estimate. Th Andersson method reduced the biased global estimate comparing to the GMN. However, in a study with a large inter-subject variation, voxels with moderate activation may be included in the global estimate due to the initial step of GMN and the insufficient criterion of $p > 0.05$. If the region with moderate activity is large enough, it will change the global estimate thus leads to a biased normalization in the similar way as the GMN. Such issue had been observed in a comparative study performed by Borghammer et al. [3]. Yakushev et al. proposed a non-iterative two-step method where the global change was estimated by only including "hypermetabolic" voxels [3]. This method only works for studies where the intensities of all activated regions change in a same pre-known direction. Moreover, the result of this method is very sensitive to the selection of the threshold of "hypermetabolic" voxels. Global change can be easily over or under estimated if the threshold is inappropriate [3].

In this paper, an automated region-based method is proposed by improving upon several drawbacks of the Andersson method: first, the proposed method removes the initial step of the GMN. Second, anatomical regions instead of individual voxels are identified for intensity normalization. Third, both p-value and percentage difference are used in indentifying the reference regions. Forth, the proposed method employs linear model to align the intensities of corresponding regions rather than using ratio only. Finally, linear transformations are computed using weighted least squares regression where the contribution of each identified region is determined based on its size and the intensity similarity between groups. To compare the proposed method with the GMN and the Andersson method, FDG-PET images from

normal rats were divided into two groups. Artificial intensity change was added in one group of images while the other group was used as the control. All images were normalized using three methods to test their capabilities of recovering the real intensity change in statistical comparisons.

2 Materials and Methods

2.1 Image Acquisition and Data Simulation

Twenty two male Sprague-Dawley rats were scanned using a Focus-220 PET scanner (Siemens Medical Solutions). Images were reconstructed into a $128 \times 128 \times 95$ volume with in-plane resolution of 0.6 mm and slice thickness of 0.8 mm with corrections for detector normalization, decay, attenuation, and scatter. The SUV (Standard Uptake Value) of FDG uptake was calculated and used for group comparison. All animal usage and experimental procedures were reviewed and approved by local Animal Usage Committee (IACUC).

All SUV images were evenly assigned into two groups so that the difference of their whole-brain average between groups was minimized (the difference was less than 1 % with p-value of 0.89 in a two tailed t-test). One group was used as control while images of another group were multiplied with a predefined scale image. In the first simulation, the SUV was increased by up to twenty percent in cortical regions. Figure 1 shows a representative slice of the scale image overlaid on a MRI template.

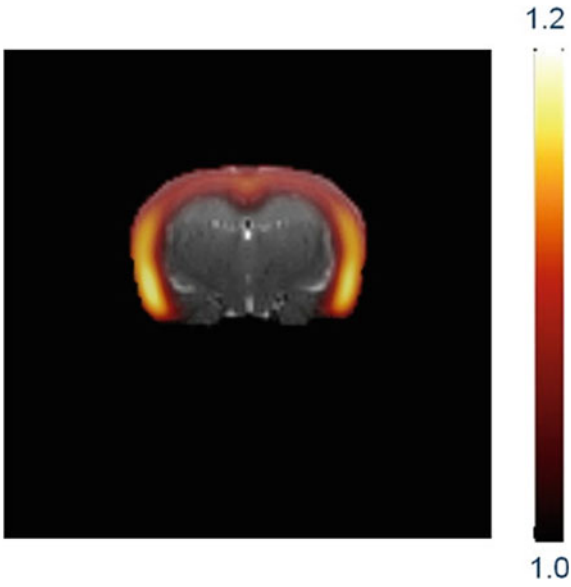

Fig. 1 A representative slice of the predefined scale image. The *color bar* represents the scale of intensity increase. The scale image is served as the ground truth in the evaluation of different normalization methods

After the data manipulation, the whole-brain average of the manipulated group was 3.93 % higher than the control group (p = 0.27 in a two tailed t-test).

In the second simulation study, SUV in cerebellum was increased 7 % in the manipulated group besides the SUV increase in cortical regions. This simulation was designed to assess the performance of different intensity normalization methods when there was a moderate signal change in a relatively large region. With the data manipulation, the difference of the whole-brain average between the two groups was 4.59 % with p-value of 0.21 in a two tailed t-test.

2.2 Normalization Method

All images were spatially aligned to a template on which more than one hundred anatomical regions had been delineated. The mean image G was computed by averaging all aligned images. Denotes the mean intensity of ith region on the G as G_i. The proposed algorithm is summarized as follows:

1. At every voxel of the brain, compute the absolute percentage difference between the two groups. The median percentage difference (denotes as Δ) is used as the threshold of percentage difference in step 3b.
2. For each anatomical region i = 1:m,
   a. Compute the mean intensity F_{ij} for each image j = 1:n,
   b. Compare the intensity difference between the two groups.
   c. Get p-value and percentage difference of intensity between groups.
3. The unaffected regions (denotes as Ω) are selected based on following criteria,
   a. The p-value of the region is greater than 0.1.
   b. The percentage difference of the regional intensity is less than the Δ defined in step 1.
4. For jth image F_j,
   a. Compute α_j and β_j by minimizing

$$\sum_{i \in \Omega} w_i (\alpha_j + \beta_j F_{ij} - G_i)^2$$

   Where the $w_i = s_i * p_i$ are weights defined by the size (s_i) and p-value (p_i) of the ith region.
   b. Update the intensity of image F_j by $F_j = \alpha_j + \beta_j F_j$.
5. Repeat step 1 to step 4 until $|\beta_j - 1| < 0.01$ and $|\alpha_j| < \theta_j$ for all images. θ_j is defined as one percent of the whole-brain average.
   For simplicity, this method is refered as ReDIN (**Re**gion-based **D**ata-driven **I**ntensity **N**ormalization) in the rest of the paper.

2.3 Image Analysis

After being aligned to the template, the intensities of all SUV images were normalized using the GMN, the Andersson, and the ReDIN separately. Statistical comparisons were performed on normalized images to detect the difference between the two groups at voxel level or over the anatomical region of interest (ROI). The Voxel-wise comparison was carried out using the software package AFNI (Analysis of Functional NeuroImages, http://afni.nimh.nih.gov) where two-tailed t-test was performed after all images were smoothed with a Gaussian filter (FWHM = 1.5 mm). The family-wise error rate was controlled to 0.05 when detecting clusters with significant metabolic differences.

In ROI analysis, the mean SUV of each ROI was computed on normalized images and compared between groups. The percentage differences and p-value of corresponding ROI were reported. The percentage differences recovered from different normalization methods were compared with the real change of the manipulation.

3 Results

3.1 Simulation I Study

The results of voxel-wise analysis is displayed in Fig. 2 where the detected clusters are highlighted by color. The red color represents the SUV increase of the manipulated group compared to the control group and the blue color shows the SUV decrease. Color bars indicate the percentage difference. After the GMN, only a part of SUV increase can be detected and an artificial SUV decrease was found in a large region

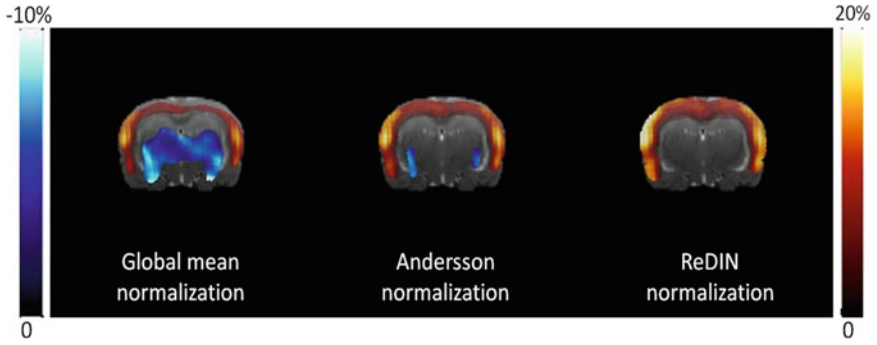

Fig. 2 The influence of different normalization methods on voxel-wise comparison in simulation I. The identified clusters were highlighted by colors that represented the detected percentage change of the manipulated group over the control group. *Red color* shows the regions with SUV increase and *blue color* indicates the SUV decrease

(left panel). The Andersson method improved the GMN method by recovering more regions with real SUV increase and inducing smaller region with the artificial SUV decrease (middle panel). ReDIN recovered most regions with SUV increase without inducing SUV decrease (right panel).

With ROI analysis, the influence of different normalization methods can be compared quantitatively. Table 1 shows the percentage difference and p-value between the two groups after normalizing data with different methods. The true change is the real percentage change applied to images of the manipulated group. With the GMN, the magnitude of SUV increase was reduced and around 5 % artificial signal decrease was induced in hippocampus and thalamus. With Andersson and ReDIN methods, the results were close to the real change.

3.2 Simulation II Study

In the second simulation study, a moderate SUV increase was introduced in cerebellum. Because the whole-brain average of the manipulated group is 4.59 % higher than the control group, the GMN reduced the intensity increase of the manipulated group and made the intensity change in cerebellum undetectable. In the Andersson normalization, cerebellum may be included in the global estimate after the initial step of the GMN. Considering the size of cerebellum, the global change was overestimated, therefore pushing the intensity of all voxels to an opposite direction of the real SUV change. Such influence is demonstrated by Fig. 3 and Table 2. Both GMN and Andersson method recovered only a part of real SUV increase and induced a large artificial SUV decrease. ReDIN did not suffer such issue.

4 Discussion

We presented an image normalization method and compared the proposed method with the GMN and the Andersson method. Simulation studies demonstrated that the proposed method yielded the best result in recovering the real metabolic change. The GMN suffered problems when the whole-brain average was affected by the local activities. The performance of the Andersson method is somewhere in between the GMN and the proposed method.

The propose method identifies anatomical regions instead of individual voxels for intensity normalization. The region-based method has two benefits: it reduced the computational cost by reducing the least squares regression from more than ten thousand voxels to less than a hundred of regions. Secondly, we can report the name of anatomical regions instead of using pictures to illustrate the region used for normalization. When preferred, some regions can be excluded based on prior knowledge.

Table 1 Quantitative comparison of different normalization methods in simulation study I

ROI	True change (%)	Global mean		Andersson		ReDIN	
		Percentage	P-value	Percentage	P-value	Percentage	P-value
CUL	1.05	−4.03	0.0508	−1.56	0.4352	0.95	0.5879
AINS	15.44	13.55	0.0007	16.58	0.0002	17.24	0.0002
AUD	12.13	10.79	<0.0001	13.67	<0.0001	13.58	<0.0001
MOp	9.77	6.43	0.0028	9.20	0.0002	9.34	<0.0001
MOs	8.37	4.15	0.0884	6.86	0.0082	7.51	0.0035
PIR	12.61	7.75	0.0127	10.60	0.0020	12.13	0.0011
RSP	7.40	4.19	<0.0001	6.90	<0.0001	7.34	<0.0001
SSp	9.88	7.15	<0.0001	9.93	<0.0001	10.00	<0.0001
SSs	12.83	8.95	0.0006	11.80	0.0001	11.79	0.0001
TE	12.30	6.41	0.0006	9.18	0.0003	9.83	0.0002
VIS	8.23	6.18	0.0678	8.89	0.013	9.44	0.0069
DG	1.06	−4.45	0.0011	−1.96	0.118	−0.36	0.7589
TH	0.13	−4.45	0.0008	−1.97	0.1109	−1.54	0.0946

CENT-central lobule cerebellum, SIM-simple lobule cerebellum, CUL-culmen cerebellum, AINS-agranular insular ctx, AUD-auditory ctx, MOp-motor ctx primary, MOs-motor secondary ctx, PIR-piriform ctx, RSP-retrosplenial ctx, SSp-somatosensory ctx primary, SSs-somaotsensory ctx secondary, TE-temporal ctx, VIS-visual ctx, DG-dentate gyrus hippocampus, TH-thalamus

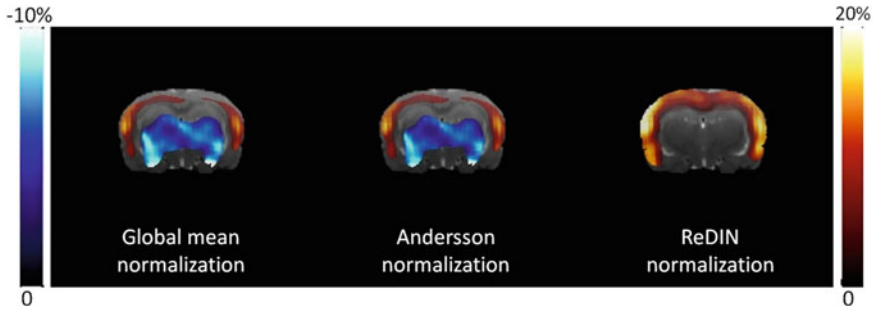

Fig. 3 In simulation II, moderate signal increase was added to some regions of cerebellum. Both the Andersson's method and the GMN created large areas of false SUV decrease (showed in *blue color*) where ReDIN method was not affected

Besides the applications in functional image analysis, the proposed method can be used in anatomical MRI analysis as well. For example, in tensor-base morphometry, Jacobian determinant is used to characterize the structural difference between groups at voxel level. To reduce the inter-subject variation, some studies calculated the Jacobian determinant only based on the deformation field and ignored the structural difference captured in affine registration. In Alzheimer's disease (AD) research, Affine transformation needs to be included in Jacobian determinant because there may be a whole brain atrophy in AD patients. In this case, the proposed method can be used to reduce the inter-subject variation in group comparison.

Although ReDIN normalization is developed based on preclinical data, it is straightforward to extend this method to clinical applications. In presented studies, a rigid body registration was used for spatial normalization due to the low resolution of PET image relative to the brain size of the rat. In clinical studies, more accurate deformable registration may be used if anatomical MRI of same subject is available. Software packages have been developed by different groups and were evaluated by Klein et al. [11].

Table 2 Quantitative comparison of different normalization methods in simulation study II

ROI	True change (%)	Global mean		Andersson		ReDIN	
		Percentage	P-value	Percentage	P-value	Percentage	P-value
CENT	7.17	3.04	0.0756	3.50	0.04170	7.25	0.0001
CUL	7.58	1.92	0.3548	2.36	0.2505	7.81	0.0081
SIM	8.56	1.32	0.6346	1.75	0.5241	7.96	0.0372
AINS	15.44	12.75	0.0012	13.28	0.0010	18.07	<0.0001
AUD	12.13	10.01	<0.0001	10.50	<0.0001	14.08	<0.0001
MOp	9.77	5.67	0.0069	6.14	0.0046	9.80	<0.0001
MOs	8.37	3.41	0.1556	3.87	0.1061	8.02	0.0025
PIR	12.61	6.99	0.0225	7.48	0.0170	13.06	0.0002
RSP	7.40	3.45	<0.0001	3.91	<0.0001	7.76	<0.0001
SSp	9.88	6.39	0.0003	6.85	0.0003	10.42	<0.0001
SSs	12.83	8.18	0.0013	8.69	0.0012	12.29	<0.0001
TE	12.30	5.66	0.0133	6.12	0.0073	10.37	0.0002
VIS	8.23	5.43	0.1038	5.86	0.0785	9.85	0.0075
DG	1.06	−5.12	0.0003	−4.70	0.0011	0.14	0.8973
TH	0.13	−5.12	0.0002	−4.70	0.0009	−1.25	0.1597

References

1. Aanerud, J., Borghammer, P., et al.: Brain energy metabolism and blood flow differences in healthy aging. J. Cereb. Blood Flow Metab. **32**(7), 87–1177 (2012)
2. Andersson, J.L.: How to estimate global activity independent of changes in local activity. Neuroimage **6**(4), 237–44 (1997)
3. Borghammer, P., Aanerud, J., et al.: Data-driven intensity normalization of PET group comparison studies is superior to global mean normalization. Neuroimage **46**(4), 981–8 (2009)
4. Boussion, N., Ryvlin, P., et al.: Towards an optimal reference region in single-photon emission tomography difference images in epilepsy. Eur. J. Nucl. Med. **27**(2), 60–155 (2000)
5. Camargo, E.E.: Brain SPECT in neurology and psychiatry. J. Nucl. Med. **42**(4), 23–611 (2001)
6. Cohen, B.D., Rosenbaum, G., et al.: Comparison of phencyclidine hydrochloride (Sernyl) with other drugs. Simulation of schizophrenic performance with phencyclidine hydrochloride (Sernyl), lysergic acid diethylamide (LSD-25), and amobarbital (Amytal) sodium; II. Symbolic and sequential thinking. Arch. Gen. Psychiatry **6**, 395–401 (1962)
7. Duncan, G.E., Miyamoto, S., et al.: Comparison of brain metabolic activity patterns induced by ketamine, MK-801 and amphetamine in rats: support for NMDA receptor involvement in responses to subanesthetic dose of ketamine. Brain Res. **843**(1–2), 83–171 (1999)
8. Fox, P.T., Mintun, M.A., et al.: Enhanced detection of focal brain responses using intersubject averaging and change-distribution analysis of subtracted PET images. J. Cereb. Blood Flow Metab. **8**(5), 53–642 (1988)
9. Friston, K.J., Frith, C.D., et al.: Comparing functional (PET) images: the assessment of significant change. J. Cereb. Blood Flow Metab. **11**(4), 9–690 (1991)
10. Gracia Marco, R., Aguilar Garcia-Iturrospe, E.J., et al.: Hypofrontality in schizophrenia: influence of normalization methods. Prog. Neuropsychopharmacol. Biol. Psychiatry **21**(8), 56–1239 (1997)
11. Klein, A., Andersson, J., et al.: Evaluation of 14 nonlinear deformation algorithms applied to human brain MRI registration. Neuroimage **46**(3), 786–802 (2009)
12. Lee, S.J., Lee, W.Y., et al.: Apparent relative hypermetabolism of selective brain areas in Huntington disease and importance of reference region for analysis. Clin. Nucl. Med. **37**(7), 8–663 (2012)
13. Talbot, P.R., Lloyd, J.J., et al.: Choice of reference region in the quantification of single-photon emission tomography in primary degenerative dementia. Eur. J. Nucl. Med. **21**(6), 8–503 (1994)
14. Yakushev, I., Hammers, A., et al.: SPM-based count normalization provides excellent discrimination of mild Alzheimer's disease and amnestic mild cognitive impairment from healthy aging. Neuroimage **44**(1), 43–50 (2009)

A Reaction-Diffusion Simulation Model of [^{18}F]FDG PET Imaging for the Quantitative Interpretation of Tumor Glucose Metabolism

Qian Wang, Zhen Liu, Sibylle I. Ziegler and Kuangyu Shi

Abstract Positron emission tomography (PET) using ^{18}F-fludeoxyglucose ([^{18}F]FDG) improves the cancer diagnosis by visualizing the pathological pathway of Warburg effect. As an analog of glucose, FDG uptake is mediated by glucose transporter (GLUT) and hexokinase (HK), which can be overexpressed under tumor hypoxia conditions. Quantitative interpretation of the images to the feature of tumor microenvironment is important to improve tumor staging and localization. However, it is usually difficult for such kind of quantitative analysis due to the complex metabolic procedure of multi-substance system within tumor. This study proposes a novel reaction-diffusion model to simulate the procedures of FDG: transported into tumor cells, catalyzed by GLUT and phosphorylated by HK leading to the production of FDG-6-phosphate (FDG6P) similar to glucose-6-phosphate (G6P). Hypoxia induced factor-1 (HIF-1) is incorporated to control the upregulations of GLUT and HK. The simulation results are compared with dynamic PET scans of nude mice with lymphoma xenograft tumors, which confirmed that the simulation can approach to real measurements. With this quantitative simulation model, the interaction of FDG to the substances, oxygen, HIF-1, glucose, G6P, and FDG6P within the tumor microenvironment is investigated under various vascularizations. By controlling the expression factor of GLUT and HK, their influences on FDG uptake is further assessed. The preliminary results of the simulation model have shown a potential to improve the quantification of FDG PET image and to assist cancer diagnosis and therapy prognosis.

Keywords Mathematical modeling of tumor microenvironment · Glucose metabolism · FDG PET imaging · Reaction-diffusion model

Q. Wang (✉) · Z. Liu · S.I. Ziegler · K. Shi
Department of Nuclear Medicine, Technical University Munich, Munich, Germany
e-mail: wang@lrz.tum.de

F. Gao et al. (eds.), *Computational Methods for Molecular Imaging*,
Lecture Notes in Computational Vision and Biomechanics 22,
DOI 10.1007/978-3-319-18431-9_13

1 Introduction

^{18}F-fluorodeoxyglucose ([^{18}F]FDG), the most commonly used tracer for clinic and pre-clinic applications of positron emission tomography (PET), is essentially a kind of glucose analog and as a result, its uptake and intracellular metabolism are similar with those of glucose. FDG and glucose are both imported into tumor cells with the help of GLUTs, among which GLUT1 has been documented elevating its expression in most cancers [1] and a more than 2-fold increase of FDG uptake due to GLUT upregulation was observed [2]. After being transported inside cells, FDG and glucose are subsequently metabolized in reactions mediated by enzyme HK and get phosphorylated, producing FDG-6-phosphate (FDG6P) and glucose-6-phosphate (G6P) [3]. G6P serves as the intermediate product of tumor respiration and glycolysis, while FDG6P undergoes very slow degradation compared in the time frame of PET imaging. HKI and II belonging to HK family are especially involved in tumor metabolisms and they have different kinetic properties. HKII is quite sensitive to oxygenations and its expression will be promoted almost 3-fold under hypoxic conditions [4].

The tumor microenvironment is spatiotemporally heterogeneous due to limited metabolite diffusion, perfusion, local consumption and transportation, etc. [5, 6]. Tumor hypoxia is the typical feature of tumor heterogeneity and encourages the overexpression of many proteins enhancing the proliferation of tumors, such as hypoxia induce factor-1 (HIF-1), vascular endothelial growth factor (VEGF), glucose transporter (GLUT), hexokinase (HK), etc. [7–13].

One of the factors responsible for the upregulation of GLUT1 and HK in tumor cells is HIF-1. The transcription factor HIF-1 is a key regulator for the induction of genes facilitating adaptation and survival of tumor cells [8]. The immunohistochemical analyses have demonstrated the detectable levels of HIF-1α in benign tumors and elevated HIF-1α levels in malignant tumors, in contrast to its absence in normal tissue [7, 8]. HIF-1 is exclusive with regards to oxygen availability and is stabilized by hypoxic conditions [7]. It upregulates many gene products which include GLUT1, HKI, HKII involved in tumor glucose metabolism [8, 14]. The inhibition of HIF-1 activity has marked effects on tumor growth [8].

Although FDG is widely applied in clinic oncology, the quantitative interpretation of FDG accumulation to the underlying pathophysiological understanding is still elusive. To overcome this, a mathematical model of FDG metabolism is proposed in this study. This model integrates the tumor microenvironment heterogeneity and the procedures of transportation and consumption of FDG and glucose in the mediation of GLUT and HK. The over-expressions of GLUT and HK driven by HIF-1 are also encompassed. The modeled time activity curve (TAC) is compared with experimental TAC from mice FDG scans. The correlations among involving substrates were evaluated. This modeling has the potential to bridge the gap between FDG imaging and tumor phenotypes.

2 Model

In order to have an in-depth understanding of the pathophysiology of FDG uptake by tumor cells, a two dimensional (2D) HIF-driven FDG model is established as shown in Fig. 1. In the model, glucose and FDG supplied by tumor microvessels are imported by GLUT. After the import, glucose and FDG are phosphorylated with the catalyzation of HK and transformed into glucose-6-phosphate (G6P) and FDG-6-phosphate (FDG6P) in tumor cells, respectively. Unlike G6P, FDG6P cannot be metabolized for further glycolysis or other usages due to the absence of 2′ hydroxyl group (-OH) and therefore trapped in cells. Because of the limited availability of GLUT and HK, FDG will compete with glucose for them during the cellular uptake. The expression levels of GLUT and HK are regulated by HIF-1 concentrations. As these exists more HIF-1 in hypoxic regions, the expressions of GLUT and HK are promoted, which leads to higher rates of FDG and glucose uptake (transport and metabolism). The model implementation steps are presented in Fig. 2, each of which will be illustrated in the following sections.

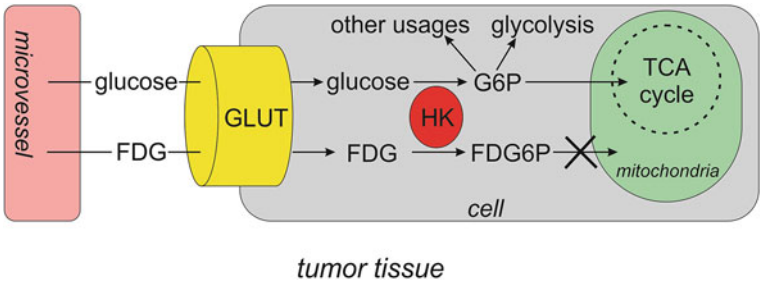

Fig. 1 Schematic presentation of the physiological processes of FDG and glucose uptake by tumor cells

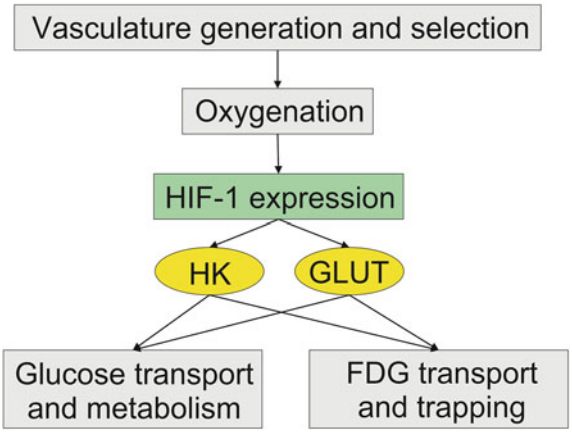

Fig. 2 Flow chart of the model implementation. Glucose and FDG compete for the mediators: GLUT and HK for their uptake. The expressions of GLUT and HK are regulated by HIF-1 level, which is determined by local oxygen concentrations

2.1 Microvasculature

As the origin site of nutrients and oxygen, the tumor vasculature is premature and chaotic. Its geometrical characteristics have been estimated by means of quantitative microvascular casting [15, 16]. With consideration of the microvessel diameter and intervascular distance ranges reporte, the 2D microvasculature is formed based on the assumption of log-normal distributed intervascular distances and uniform microvessel diameter, which are consistent with the previous articles [17, 18]. For further selection of the microvasculature satisfying the log-normal distribution, the Kolmogorov-Smirnov test is adopted to test the vascular map generated.

2.2 Oxygenation

The oxygen distribution in solid tumors is highly heterogeneous. Some areas distant from the microvessels are deprived of oxygen due to limited oxygen diffusion and local consumption. A region with oxygen tension less than 2.5 mmHg is known as the hypoxic region [17]. The spatio-temporal distribution of oxygen can be described by a reaction-diffusion equation [17–22], in which the convective oxygen transport in the tumor microenvironment is not considered and a constant diffusivity is used for the field of interest. Oxygen can traverse cell membrane, vessel membrane freely because of low molecular mass, dimension and tumor vessel leakage. The oxygen concentration $[O^2] = [O^2](x, y, t)$ is therefore described as

$$\frac{\partial [O_2]}{\partial t} = D_{O_2} \nabla^2 [O_2] - P([O_2]) \tag{1}$$

where D_{O_2} denotes the oxygen diffusivity. $P([O_2])$ represents the oxygen consumption rate, as well as a Michaelis-Menten term. It is determined by local oxygen concentration, maximum oxygen consumption rate $V_{\max, O_2}$ and Michaelis-Menten constant K_{m,o_2}.

$$P([O_2]) = V_{\max, O_2} [O_2] / ([O_2] + K_{m, o_2}) \tag{2}$$

2.3 HIF-1 Expression

Tumor cells shift a large part of their metabolisms toward glycolysis, some of which are regulated by HIF-1. HIF-1 acts as a critical intermediator between tissue oxygenation and stimulation factors (e.g. metabolic enzymes and transporters, signal factors) [14, 23, 24]. The oxygen content is a factor influencing the HIF-1 expressions and a negative correlation between them have been reported [25]. HIF-1 affects tumor metabolisms by regulating the expressions of transports and enzymes. In particular, GLUT and HK, the mediators of glucose metabolism, are regulated by HIF-1 in a

positive manner. To explore HIF-1 effect on tumor metabolism, it is introduced in the proposed model. Production of cellular HIF-1 is dependent on both the intrinsic capability to synthesis, which is assumed constant, and the degradation due to oxygen existence [26, 27]

$$\frac{d[\mathrm{HIF}]}{dt} = r_{\mathrm{H}} - V_{\mathrm{max,\,HIF}} \left(\frac{[\mathrm{O_2}]}{[\mathrm{O_2}] + K_{\mathrm{m,\,HIF}}} \right) [\mathrm{HIF}] \tag{3}$$

where [HIF] is the cellular HIF-1 concentration. r_{H} is the HIF synthesizing rate. $V_{\mathrm{max,\,HIF}}$ and $K_{\mathrm{m,\,HIF}}$ indicate the maximum HIF-1 degradation rate and the HIF concentration at which the degradation rate is half-maximal. The equilibrium HIF-1 distribution can be acquired when $\frac{d[\mathrm{HIF}]}{dt} = 0$. In the model implementation, the spatial-varying [HIF] is normalized by the maximum value in the field of interest.

2.4 Glucose Transport and Metabolism

Cellular glucose uptake is facilitated by the transporter GLUT. Subsequently, intracellular glucose is metabolized with catalyzation by HK and then transformed into glucose-6-phosphate (G6P) before being metabolized. In this model, glucose is divided into three physiological compartments: extracellular, intracellular and metabolized glucoses. The spatio-temporal evolutions of their concentrations are described by [28]:

$$\frac{\partial[\mathrm{G_{ex}}]}{\partial t} = D_{\mathrm{G}} \nabla^2 [\mathrm{G_{ex}}] - T([\mathrm{G_{ex}}] - [\mathrm{G_{in}}]) \tag{4}$$

$$\frac{\partial[\mathrm{G_{in}}]}{\partial t} = T([\mathrm{G_{ex}}] - [\mathrm{G_{in}}]) - P([\mathrm{G_{in}}]) \tag{5}$$

$$\frac{\partial[\mathrm{G_{me}}]}{\partial t} = P([\mathrm{G_{in}}]) \tag{6}$$

where $[\mathrm{G_{ex}}]$, $[\mathrm{G_{in}}]$, and $[\mathrm{G_{me}}]$ are the concentrations of extracellular, intracellular and metabolized glucose, respectively. $\mathrm{T}([\mathrm{G_{ex}}] - [\mathrm{G_{in}}])$ and $\mathrm{P}([\mathrm{G_{in}}])$ represent the transmembrane transport rate and the intracellular metabolic rate of glucose. $\mathrm{T}([\mathrm{G_{ex}}] - [\mathrm{G_{in}}])$ is determined by the concentration difference and kinetic parameters of GLUT and is regulated by HIF-1 levels.

$$T([\mathrm{G_{ex}}] - [\mathrm{G_{in}}]) = \frac{V_{\mathrm{max,\,GLUT}} K_{\mathrm{m,\,GLUT}} ([\mathrm{G_{ex}}] - [\mathrm{G_{in}}])}{\left(K_{\mathrm{m,\,GLUT}} + [\mathrm{G_{ex}}]\right)\left(K_{\mathrm{m,\,GLUT}} + [\mathrm{G_{in}}]\right)} (1 + k_{\mathrm{GLUT}}[\mathrm{HIF}]) \tag{7}$$

where $V_{\mathrm{max,\,GLUT}}$ and $K_{\mathrm{m,\,GLUT}}$ are the maximum transport rate and Michaelis-Menten constant of GLUT for glucose transport. It is assumed that GLUT have identical kinetic parameters at both sides of the cell membranes based on the

consideration that the transmembrane transport of glucose uses facilitated diffusion in most tumors rather than active (ATP-dependent) transport [29–31]. The HIF-1 regulation on glucose transport and metabolism is integrated by $(1 + k_{\mathrm{GLUT}}[\mathrm{HIF}])$ [27]. k_{GLUT}, named as the overexpression factor of GLUT, is a factor indicating the maximum fold that HIF-1 can upregulate the GLUT expression in hypoxic condition.

The metabolic rate $\mathrm{P}[\mathrm{G_{in}}]$ is represented by a Michaelis-Menten term:

$$P([\mathrm{G_{in}}]) = \frac{V_{\mathrm{max,\,HK}}\,[\mathrm{G_{in}}]}{K_{\mathrm{m,\,HK}} + [\mathrm{G_{in}}]}(1 + k_{\mathrm{GLUT}}[\mathrm{HIF}]) \tag{8}$$

where $V_{\mathrm{max,\,HK}}$ and $K_{\mathrm{m,\,HK}}$ are the maximum transport rate and Michaelis-Menten constant of HK for glucose phosphorylation. Similar with GLUT, the influence of HK overexpression is introduced by multiplying $(1+k_{\mathrm{HK}}[\mathrm{HIF}])$. The overexpression factor k_{HK} indicates the maximum fold that HK can get overexpressed due to highest HIF-1 level.

2.5 FDG Uptake

As an analog of glucose, FDG have similar metabolic characteristics with glucose except that it cannot be further metabolized after the phosphorylation. To simulate its uptake procedure, FDG is divided into extra- and intra-cellular FDG and trapped (or phosphorylated) FDG (FDG6P), whose concentrations are $[\mathrm{FDG_{ex}}]$, $[\mathrm{FDG_{in}}]$ and $[\mathrm{FDG_{tr}}]$, respectively. The FDG competition with glucose for GLUT and HK is considered (glucose is almost not influenced by the addition of FDG since its concentration is normally several orders higher than FDG concentration) [29]. The evolutions of extra- and intra-cellular FDG and trapped FDG satisfy:

$$\frac{\partial[\mathrm{FDG_{ex}}]}{\partial t} = D_{\mathrm{FDG}}\nabla^2\,[\mathrm{FDG_{ex}}] - T([\mathrm{FDG_{ex}}] - [\mathrm{FDG_{in}}]) \tag{9}$$

$$\frac{\partial[\mathrm{FDG_{in}}]}{\partial t} = T([\mathrm{FDG_{ex}}] - [\mathrm{FDG_{in}}]) - P([\mathrm{FDG_{in}}]) \tag{10}$$

$$\frac{\partial[\mathrm{FDG_{tr}}]}{\partial t} = P([\mathrm{FDG_{in}}]) \tag{11}$$

where $T([\mathrm{FDG_{ex}}] - [\mathrm{FDG_{in}}])$ and $P([\mathrm{FDG_{in}}])$ are the transport and metabolic rate of FDG with consideration of its competition with glucose. $T([\mathrm{FDG_{ex}}] - [\mathrm{FDG_{in}}])$ is determined by the difference between T_{cis} (import rate) T_{trans} and (export rate).

$$T([\mathrm{FDG_{ex}}] - [\mathrm{FDG_{in}}]) = (T_{cis} - T_{trans})(1 + k^{\mathrm{F}}_{\mathrm{GLUT}}[\mathrm{HIF}]) \tag{12}$$

$$T_{cis} = \frac{K_{\mathrm{m,\,GLUT}} V^{\mathrm{F}}_{\mathrm{max,\,GLUT}} [\mathrm{FDG_{ex}}]}{K_{\mathrm{m,\,GLUT}} [\mathrm{FDG_{ex}}] + K^{\mathrm{F}}_{\mathrm{m,\,GLUT}} [\mathrm{G_{ex}}] + K_{\mathrm{m,\,GLUT}} K^{\mathrm{F}}_{\mathrm{m,\,GLUT}}} \tag{13}$$

$$T_{trans} = \frac{K_{\mathrm{m,\,GLUT}} V^{\mathrm{F}}_{\mathrm{max,\,GLUT}} [\mathrm{FDG_{in}}]}{K_{\mathrm{m,\,GLUT}} [\mathrm{FDG_{in}}] + K^{\mathrm{F}}_{\mathrm{m,\,GLUT}} [\mathrm{G_{in}}] + K_{\mathrm{m,\,GLUT}} K^{\mathrm{F}}_{\mathrm{m,\,GLUT}}} \tag{14}$$

where $V^{\mathrm{F}}_{\mathrm{max,\,GLUT}}$ and $K^{\mathrm{F}}_{\mathrm{m,\,GLUT}}$ are the maximum transport rate and the Michaelis-Menten constant for FDG transport, respectively. The term implying the HIF-1 upregulation $(1 + K^{\mathrm{F}}_{\mathrm{GLUT}}[\mathrm{HIF}])$ is also applied on the FDG transport term with overexpression factor $K^{\mathrm{F}}_{\mathrm{GLUT}}$.

$P([\mathrm{FDG_{in}}])$ with HIF-1 regulation is given by

$$P([\mathrm{FDG_{in}}]) = \frac{K_{\mathrm{m,\,HK}} V^{\mathrm{F}}_{\mathrm{max,\,HK}} [\mathrm{FDG_{in}}]}{K_{\mathrm{m,\,HK}} [\mathrm{FDG_{in}}] + K^{\mathrm{F}}_{\mathrm{m,\,HK}} [\mathrm{G_{in}}] + K_{\mathrm{m,\,HK}} K^{\mathrm{F}}_{\mathrm{m,\,HK}}} (1 + k^{\mathrm{F}}_{\mathrm{HK}} [\mathrm{HIF}]) \tag{15}$$

$V^{\mathrm{F}}_{\mathrm{max,\,HK}}$ and $K^{\mathrm{F}}_{\mathrm{m,\,GLUT}}$ are maximum phosphorylation rate and Michaelis-Menten constant of FDG, respectively. $K^{\mathrm{F}}_{\mathrm{HK}}$ is the HK overexpression factor for FDG phosphorylation.

3 Methods

All simulations are programmed in C++ (Microsoft Visual Studio 2008) and the reaction-diffusion equations are solved using finite-difference methods (FDM). The region of interest is a 1 mm × 1 mm micro-tissue-phantom, which is tessellated into 100 × 100 elements with a grid size of 10 μm. The temporal iteration step size was set to 1 ms. The partial differential equations are iteratively solved up to the system equilibrium.

The no-flux boundary condition is applied on the edge of the region of the simulated domain. The vessel walls serve as barriers for glucose and FDG entering tumor tissue. Therefore the Neumann boundary condition is applied on the microvessels. The Neumann boundary condition for a neutral substance S on a blood vessel can be written as follows [32, 33]:

$$\vec{n_{\mathrm{s}}} D_{\mathrm{s}} \nabla [\mathrm{S}] = \mu_{\mathrm{s}} ([\mathrm{S}]_v - [\mathrm{S}]) \tag{16}$$

where $[\mathrm{S}]_v$ and $[\mathrm{S}]$ are the substance concentration in the blood and the substance concentration in the element immediately adjacent to the vessel, $\vec{n_{\mathrm{s}}}$ is the outward unit normal vector to the vessel surface. μ_{s} represents the permeability of substance S.

The parameters used in the simulation are listed in Table 1. The FDG plasma input functions are extracted from left ventricle with partial volume correction and spillover

Table 1 Parameters used in the simulation

Symbol	Parameter	Value	References
C_{O_2}	Plasma O_2 concentration	6.8×10^{-2} mM	[17]
C_G	Plasma glucose concentration	5.5 mM	[33]
D_{O_2}	O_2 diffusivity	2×10^{-5} cm^2/s	[18]
D_G	Glucose diffusivity	5.5×10^{-7} cm^2/s	[34]
D_{FDG}	FDG diffusivity	5.5×10^{-7} cm^2/s	[34]
μ_G	Glucose permeability	3×10^{-5} cm/s	[32]
μ_{FDG}	FDG permeability	3×10^{-5} cm/s	[32]
K_{m,O_2}	Michaelis-Menten constant for O_2 consumption	2.5 mmHg	[18]
$V_{max,\,O_2}$	Max. consumption rate of O_2	15 mmHg/s	[18]
$K_{m,\,GLUT}$	Michaelis-Menten constant of glucose transport via GLUT	26.2 mM	[35]
$K_{m,\,HK}$	Michaelis-Menten constant for glycolysis catalyzed by HK	0.13 mM	[3]
$K^F_{m,\,GLUT}$	Michaelis-Menten constant of FDG transport via GLUT	26.2 mM	[35]
$K^F_{m,\,HK}$	Michaelis-Menten constant for FDG phosphorylation catalyzed by HK	0.17 mM	[3]
$V_{max,\,GLUT}$	Max. glucose transport rate by GLUT	6 μM/s	[36–38]
$V_{max,\,HK}$	Max. glucose glycolytic rate by HK	4.3 μM/s	[37, 39]
$V^F_{max,\,GLUT}$	Max. FDG transport rate by GLUT	6 μM/s	[36–38]
$V^F_{max,\,HK}$	Max. FDG phosphorylation rate by HK	2.6 μM/s	[3, 37, 39]
r_H	HIF-1 synthesis rate	1.2×10^{-4} s^{-1}	[27]
$V_{max,\,HIF}$	Max. HIF-1 degradation rate	2.3×10^{-3} s^{-1}	[27]
$K_{m,\,HIF}$	Michaelis-Menten constant for FDG degradation	2.5 mmHg	[18, 27]

correction using addition blood samples. The tissue-to-blood ratio indicating the FDG retention in tumor tissues, is defined as the FDG tissue activities (the summation between extracellular, intracellular and trapped FDG over temporal span of plasma input function) normalized by the plasma input of FDG activity at the last sampling point.

The subtypes of GLUT and HK are not specified in this study to broaden model applicability. GLUT and HK are both documented sensitive to oxygen contents and HIF-1 levels, and have elevated expressions and/or activities in most cancers [1, 3, 4]. It is found that the transport rate is raised 2.53 ± 0.79 folds under hypoxia for human breast carcinoma cell line MCF7 and this is postulated to the [2]. By evaluating the mRNA and protein levels, HKI and HKII overexpress 1.5- and 5.5-fold respectively in human glioblastoma multiforme (GBM) center and 0.9- and 1.2-fold respectively in GBM periphery [13]. HKII expression increases 1.5 and 10 folds for hepatocellular carcinoma and metastatic liver cancer [11]. To investigate the influences of HIF-dependent protein expression/activity on the tumor metabolism, the overexpression factors of GLUT and HK are adapted from 1 to 10, which fall in the ranges of data reported in the literature. In addition, the vascular density is adapted from 20 to 200 vessels/mm^2 within the range of empirical tumor vascular densities in the literature, to assess its influence on the glucose and FDG uptake [15, 16].

In order to quantify the influence of physiological factors on tumor glucose metabolism, the response rate is proposed, which represents the glucose and FDG concentration/activity adaptions in responses to the unit change of overexpression factors. As an alternative parameter, the response rate can be normalized by mediator (i.e. GLUT and HK) expression levels for the estimation of substrate sensitivity to the mediator level variations [28]. The mediator expression is characterized by both maximum protein-facilitated transport or catalyzing rate ($V_{\max}$) and the overexpression factor in the proposed model.

4 Model Implementation and Results

The model is implemented on tumor tissue phantoms with different microvessel densities, and expressions of GLUT and HK. An example of model implementation is shown in Fig. 3, where the phantom has a microvessel density of 40 vessels/mm^2 and 3-fold maximum overexpressions for both GLUT and HK ($k_{\mathrm{GLUT}} = k_{\mathrm{HK}} = 3$). Figures (a) and (b) are the maps of oxygen (unit: mmHg) and normalized HIF-1 distributions, respectively. Figures (c)–(e) present the distributions of extra-, intracellular glucose (unit: mM) and glucose metabolic rate (unit: μM/s), respectively. The corresponding extra-, intra-cellular FDG (unit: mM) and FDG trapping rate (unit: μM/s) are exhibited in figures (f)–(h), respectively.

The average oxygen tension over the selected phantom is 3.5 mmHg, which fall in the range of published tumor pO2 values (Eppendorf data): 0–60 mmHg [40, 41]. Based on the proposed model, the average oxygen tensions simulated in different

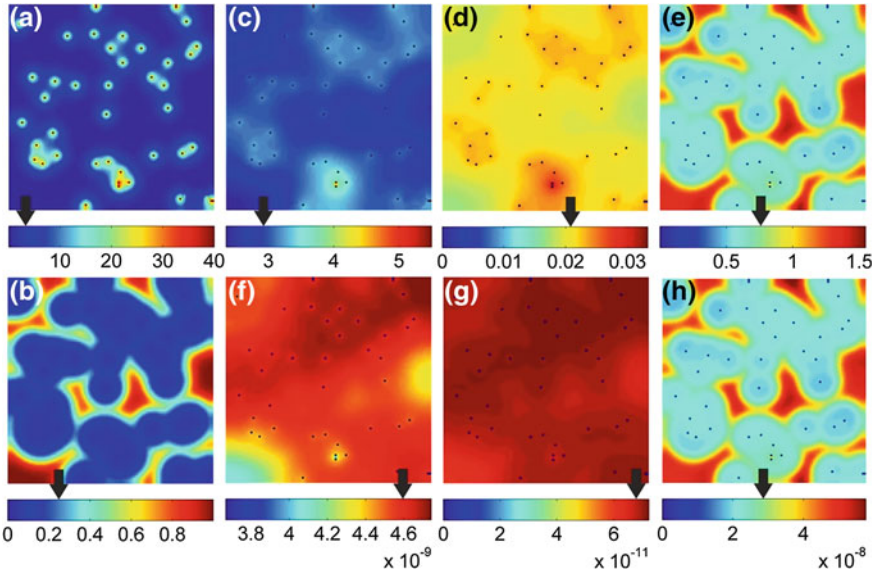

Fig. 3 Substrate concentration maps. Figures **a** and **b** are the 2D oxygen (mmHg) and normalized HIF-1 distributions. Figures **c**–**h** present the 2D distributions of extra-, intra-cellular glucose (mM) and glucose metabolic rate (μM/s), and extra-, intra-cellular FDG (mM) and FDG trapping rate (μM/s), respectively. The average values of these parameters are marked by *black arrows* pointing to the colorbars of each map

pathophysiological conditions vary from 1.6 to 23.5 mmHg, which also falls into the range of Eppendorf data. The average extracellular glucose concentration is 2.9 mM, which is much higher than the intracellular glucose concentration (0.02 mM on average). The extracellular glucose in tumor tissue has been reported within the range of 0.5–3.7 mM for several types of tumor cells [6].

In addition, the average values for normalized HIF-1, glucose metabolic rate, extra- and intra-cellular FDG concentration and FDG trapping rate are 0.26, 0.75 μM/s, 4.6×10^{-9} mM, 7.0×10^{-11} mM and 2.8×10^{-8} μM/s, respectively. They are marked by black arrows pointing to the colorbars of each map in Fig. 3.

Figure 4a shows the simulated TACs (blue curves) of tumor tissue phantoms with different vascular densities (20–200 vessels/mm^2). They are compared with the measured one (red curve), which shares the same plasma input function displayed in Fig. 4b. The tissue-to-blood (T/B) ratios for simulated TACs change from 1.4 to 4.6 as compared to 4.4 for measured TAC. Using other parameters (such as higher vascular density) promoting the FDG retention, the T/B can reach 6.5 in this model. The T/B measured in clinical and preclinical studies have been reported within the range of 1.3–17.2 for different types of tumors [42, 43].

The influences of GLUT and HK overexpressions in terms of overexpression factor adaptions on the glucose concentration and FDG activities are investigated using the tumor tissue phantoms containing different vascular densities as shown in Fig. 5.

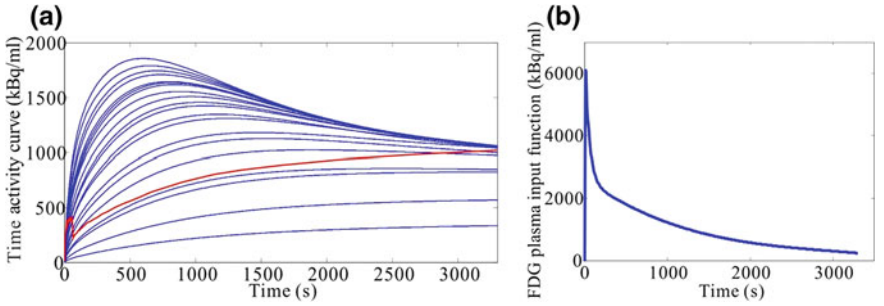

Fig. 4 **a** Simulated TACs (*blue curve*) under different vascular densities (20–200 vessels/mm^2) as a comparison with measured TAC (*red curve*) using the plasma input function displayed in figure (**b**)

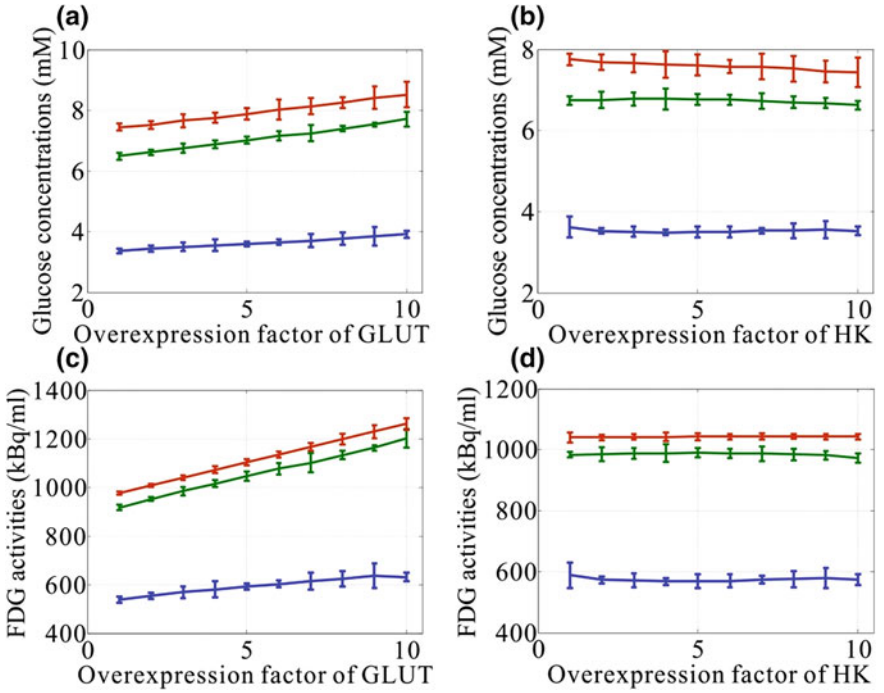

Fig. 5 Glucose concentrations as the functions of GLUT (figure (**a**)) and HK (figure (**b**)) overexpression factors, and FDG activities as the functions of GLUT (figure (**c**)) and HK (figure (**d**)) overexpression factors. The curves are plotted in different vascular densities (*blue curves* 20 vessels/mm^2; *green curves* 60 vessels/mm^2; *red curves* 100 vessels/mm^2). The *error bars* for each data point are added on each curve

Table 2 The response rates of glucose and FDG with respect to the GLUT and HK upregulations in terms of overexpression factors (OF) under different vascular densities

	Glucose			FDG		
Vascular density (vessels/mm^2)	20	60	100	20	60	100
Response rate to GLUT OF (mM)	0.06	0.12	0.13	11.2	30.0	31.6
Response rate to HK OF (kBq/ml)	0.003	−0.01	−0.03	0.48	−0.71	−0.51

The FDG activity indicates the tissue activity that can be imaged by PET and contains the extra- and intra-cellular FDG activities and FDG activity that are accumulated in tumor cells over the time span of plasma input function (3300 s). Similar with FDG, the glucose concentration encompasses the extra- and intra-cellular glucose concentrations and the integral concentration of glucose that are metabolized during the past 3300 s. Each curve point takes the average of 20 repeated simulations to decrease the heterogeneity of microvasculature. The error-bars are added on each data point in the figures. The glucose concentrations and FDG activities as the functions of the overexpression factors are presented in the conditions of low, medium and high vascular densities: 20 (blue curve), 60 (green curve) and 100 (red curve) vessels/mm^2

Both glucose concentration and FDG tissue activity show more activated responses to the altered overexpression factors of GLUT than that of HK. HK upregulation exerts little influence on glucose and FDG uptake using the current pathophysiological parameters. The response rates (the glucose and FDG concentration/activity adaptions in responses to the unit change of overexpression factors) are presented in Table 2. They are also associated with vascular densities. In particular for GLUT, higher response rate is found for phantoms with higher vascular densities.

As the transport and metabolic kinetics of glucose and FDG are very similar in tumors, we evaluate the correlations between glucose metabolism and FDG uptake to validate the efficacy of FDG PET images in reflecting the glucose metabolism. The correlation coefficient between FDG tissue activity and glucose concentration that are accumulated over a same period is 0.97 ($P \ll 0.05$) with consideration of various pathophysiological conditions (such as different GLUT and HK upregulating levels, and vascular distributions).

5 Discussions

A tumor pathophysiological model, which simulates the glucose and FDG uptake procedures, is proposed in this study. The oxygen-dependent HIF-1 is especially introduced to regulate the expressions of GLUT and HK. With the mediation of GLUT

and HK, extra- and intra-cellular and phosphorylated glucose and FDG distributions in tumors are emulated simultaneously. We validate the model by comparing the simulated substrate concentrations, FDG T/B and TAC curve with the experimental data. This model bridges the discrepancies between pathophysiological factors and tumor metabolisms, and enables the quantitative interpretation of glucose turnover and FDG accumulation in terms of pathophysiological understanding.

The cellular HIF-1 evolution is described by a reaction equation, which encompasses a constant synthesis rate (without consideration of the effect of HIF-1 synthesis saturation) and an oxygen-dependent degradation rate [26], therefore the HIF-1 level only depends on the local oxygen content in the proposed model. It has been reported that the HIF-1 levels change exponentially over a physiologically relevant range of oxygen tension in human cervical carcinoma HeLa cells [25]. Although the existence of such relationship, it is constrained to a specific tumor cell line. Thus, the equation-driven HIF-1 distribution is applied in the current model. By adjusting the parameters, the simulated HIF-1 distribution can approach the experimental distributions in different physiological situations. As to HIF-1 regulation on glucose and FDG uptake, the transport and metabolic rates are both assumed linearly correlated with HIF-1 levels. This simplified and analytic relationship can reflect the basic tendency of HK and GLUT expressions in response to the HIF-1 regulation and has been adopted by other modeling studies [27]. Moreover the experimental correlations are still elusive or not straight forward to the best of our knowledge. Therefore the linear relationship between HIF-1 levels and mediator expressions is utilized. The more sophisticated HIF-1 regulation function with physiological indications will be further explored.

The simulation results indicate that GLUT is more influential on the glucose and FDG uptake than HK. GLUT function is a critical factor in cellular glucose supply before the intracellular breakdown of glucose occurs. It can influence the further reactions during glucose metabolism and may form a bottleneck for the downstream metabolic steps. As an upstream factor of the HK-involved metabolisms, GLUT is therefore more determinate on the glucose and FDG concentrations. The relatively constant responses of glucose and FDG to HK upregulations may result from the counteraction between the enhanced metabolic rates and decreased intracellular glucose/FDG concentrations (refer to Eqs. (8) and (15)).

The model is validated by comparing (1) the simulated substrate concentrations with empirical data in the literature, and (2) the simulated TACs with measured TAC using the same blood input function. They are not completely direct validations. The direct validation indicates the comparison between simulated and measured metabolisms originated from the same set of pathophysiological factors extracted by immunohistochemical approaches. This study cannot achieve a complete direct validation due to the bottleneck of co-registration between macroscopic molecular imaging and microscopic tumor imaging [28]. Nevertheless, we try our best to verify that most simulated substrate concentrations fall in the range of experimental data reported in the literature, although not all the investigated properties has quantitative values due to the limited availability of literature data

6 Conclusion

We developed a realistic model to simulate FDG uptake in tumor microenvironment, which could assist the quantitative interpretation of PET imaging to oncologic metabolisms of substance and offers the potential to improve the clinic diagnosis. The preliminary results show that the simulation can approach to measurement and further validations will be carried out in the following up studies.

References

1. Ganapathy, V., Thangaraju, M., Prasad, P.D.: Nutrient transporters in cancer: relevance to Warburg hypothesis and beyond. Pharmacol. Ther. **121**(1), 29–40 (2009)
2. Burgman, P., et al.: Hypoxia-induced increase in FDG uptake in MCF7 cells. J. Nucl. Med. **42**(1), 170–175 (2001)
3. Muzi, M., et al.: Kinetic characterization of hexokinase isoenzymes from glioma cells: implications for FDG imaging of human brain tumors. Nucl. Med. Biol. **28**(2), 107–116 (2001)
4. Mathupala, S., Ko, Y.A., Pedersen, P.: Hexokinase II: cancer's double-edged sword acting as both facilitator and gatekeeper of malignancy when bound to mitochondria. Oncogene **25**(34), 4777–4786 (2006)
5. Vaupel, P., Kallinowski, F., Okunieff, P.: Blood flow, oxygen and nutrient supply, and metabolic microenvironment of human tumors: a review. Cancer Res. **49**(23), 6449–6465 (1989)
6. Vaupel, P.: Tumor microenvironmental physiology and its implications for radiation oncology. Semin. Radiat. Oncol. **14**(3), 198–206 (2004)
7. Semenza, G.L.: HIF-1: mediator of physiological and pathophysiological responses to hypoxia. J. Appl. Physiol. **88**(4), 1474–1480 (2000)
8. Semenza, G.L.: Targeting HIF-1 for cancer therapy. Nat. Rev. Cancer **3**(10), 721–732 (2003)
9. Airley, R., et al.: Glucose transporter glut-1 expression correlates with tumor hypoxia and predicts metastasis-free survival in advanced carcinoma of the cervix. Clin. Cancer Res. **7**(4), 928–934 (2001)
10. Zhang, J.-Z., Behrooz, A., Ismail-Beigi, F.: Regulation of glucose transport by hypoxia. Am. J. Kidney Dis. **34**(1), 189–202 (1999)
11. Yasuda, S., et al.: Hexokinase II and VEGF expression in liver tumors: correlation with hypoxia-inducible factor-1α and its significance. J. Hepatol. **40**(1), 117–123 (2004)
12. Natsuizaka, M., et al.: Synergistic up-regulation of Hexokinase-2, glucose transporters and angiogenic factors in pancreatic cancer cells by glucose deprivation and hypoxia. Exp. Cell Res. **313**(15), 3337–3348 (2007)
13. Wolf, A., et al.: Hexokinase 2 is a key mediator of aerobic glycolysis and promotes tumor growth in human glioblastoma multiforme. J. Exp. Med. **208**(2), 313–326 (2011)
14. Chen, C., et al.: Regulation of glut1 mRNA by hypoxia-inducible factor-1 interaction between H-ras and hypoxia. J. Biol. Chem. **276**(12), 9519–9525 (2001)
15. Konerding, M., et al.: Evidence for characteristic vascular patterns in solid tumours: quantitative studies using corrosion casts. Br. J. Cancer **80**(5–6), 724 (1999)
16. Konerding, M., Fait, E., Gaumann, A.: 3D microvascular architecture of pre-cancerous lesions and invasive carcinomas of the colon. Br. J. Cancer **84**(10), 1354 (2001)
17. Daşu, A., Toma-Daşu, I., Karlsson, M.: Theoretical simulation of tumour oxygenation and results from acute and chronic hypoxia. Phys. Med. Biol. **48**(17), 2829 (2003)
18. Kelly, C.J., Brady, M.: A model to simulate tumour oxygenation and dynamic [18F]-Fmiso PET data. Phys. Med. Biol. **51**(22), 5859 (2006)
19. Dalah, E., Bradley, D., Nisbet, A.: Simulation of tissue activity curves of 64Cu-ATSM for sub-target volume delineation in radiotherapy. Phys. Med. Biol. **55**(3), 681 (2010)

20. Petit, S.F., et al.: Intra-voxel heterogeneity influences the dose prescription for dose-painting with radiotherapy: a modelling study. Phys. Med. Biol. **54**(7), 2179 (2009)
21. David, M., et al.: Modelling and simulation of [18F] fluoromisonidazole dynamics based on histology-derived microvessel maps. Phys. Med. Biol. **56**(7), 2045 (2011)
22. Mönnich, D., et al.: Modelling and simulation of the influence of acute and chronic hypoxia on [18F] fluoromisonidazole PET imaging. Phys. Med. Biol. **57**(6), 1675 (2012)
23. Ullah, M.S., Davies, A.J., Halestrap, A.P.: The plasma membrane lactate transporter MCT4, but not MCT1, is up-regulated by hypoxia through a HIF-1α-dependent mechanism. J. Biol. Chem. **281**(14), 9030–9037 (2006)
24. Wada, H., et al.: Expression pattern of angiogenic factors and prognosis after hepatic resection in hepatocellular carcinoma: importance of angiopoietin-2 and hypoxia-induced factor-1a. Liver Int. **26**(4), 414–423 (2006)
25. Jiang, B.-H., et al.: Hypoxia-inducible factor 1 levels vary exponentially over a physiologically relevant range of O2 tension. Am. J. Physiol.-Cell Physiol. **271**(4), C1172–C1180 (1996)
26. Leedale, J., et al.: Modeling the dynamics of hypoxia inducible factor-1α (HIF-1α) within single cells and 3D cell culture systems. Math. Biosci. **258**, 33–43 (2014)
27. Kelly, C., Smallbone, K., Brady, M.: Tumour glycolysis: the many faces of HIF. J. Theor. Biol. **254**(2), 508–513 (2008)
28. Qian, W., et al.: Exploring the quantitative relationship between metabolism and enzymatic phenotype by physiological modeling of glucose metabolism and lactate oxidation in solid tumors. Phys. Med. Biol. **60**(6), 2547 (2015)
29. Bisswanger, H.: Enzyme kinetics: Section 2.6–2.12. Enzyme Kinetics, pp. 124–193. Wiley-VCH Verlag GmbH & Co. KGaA (2008)
30. Vinnakota, K.C., Beard, D.A.: Kinetic analysis and design of experiments to identify the catalytic mechanism of the monocarboxylate transporter isoforms 4 and 1. Biophys. J. **100**(2), 369–380 (2011)
31. Mueckler, M.: Facilitative glucose transporters. Eur. J. Biochem. **219**(3), 713–725 (1994)
32. Molavian, H.R., et al.: Fingerprint of cell metabolism in the experimentally observed interstitial pH and pO2 in solid tumors. Cancer Res. **69**(23), 9141–9147 (2009)
33. Casciari, J., Sotirchos, S., Sutherland, R.: Mathematical modelling of microenvironment and growth in EMT6/Ro multicellular tumour spheroids. Cell Prolif. **25**(1), 1–22 (1992)
34. Casciari, J.J., Sotirchos, S.V., Sutherland, R.M.: Glucose diffusivity in multicellular tumor spheroids. Cancer Res. **48**(14), 3905–3909 (1988)
35. Nishimura, H., et al.: Kinetics of GLUT1 and GLUT4 glucose transporters expressed in Xenopus oocytes. J. Biol. Chem. **268**(12), 8514–8520 (1993)
36. Rivenzon-Segal, D., et al.: Glucose transporters and transport kinetics in retinoic acid-differentiated T47D human breast cancer cells. Am. J. Physiol.-Endocrinol. Metab. **279**(3), E508–E519 (2000)
37. Rodríguez-Enríquez, S., et al.: Kinetics of transport and phosphorylation of glucose in cancer cells. J. Cell. Physiol. **221**(3), 552–559 (2009)
38. Smith, T.A., et al.: Decreased [18F] fluoro-2-deoxy-d-glucose incorporation and increased glucose transport are associated with resistance to 5FU in MCF7 cells in vitro. Nucl. Med. Biol. **34**(8), 955–960 (2007)
39. Marín-Hernández, A., et al.: Determining and understanding the control of glycolysis in fast-growth tumor cells. FEBS J. **273**(9), 1975–1988 (2006)
40. Höckel, M., et al.: Oxygenation of carcinomas of the uterine cervix: evaluation by computerized O2 tension measurements. Cancer Res. **51**(22), 6098–6102 (1991)
41. Vaupel, P., et al.: Oxygenation of human tumors: evaluation of tissue oxygen distribution in breast cancers by computerized O2 tension measurements. Cancer Res. **51**(12), 3316–3322 (1991)
42. Lee, T.S., et al.: Comparison of 18 F-FDG, 18 F-FET and 18 F-FLT for differentiation between tumor and inflammation in rats. Nucl. Med. Biol. **36**(6), 681–686 (2009)
43. Piert, M., et al.: Positron detection for the intraoperative localisation of cancer deposits. Eur. J. Nucl. Med. Mol. Imaging **34**(10), 1534–1544 (2007)

Generation of MR-Based Attenuation Correction Map of PET Images in the Brain Employing Joint Segmentation of Skull and Soft-Tissue from Single Short-TE MR Imaging Modality

Anahita Fathi Kazerooni, Mohammad Hadi A'arabi, Mohammadreza Ay and Hamidreza Saligheh Rad

Abstract Recently introduced PET/MRI scanners present significant advantages in comparison with PET/CT, including better soft-tissue contrast, lower radiation dose, and truly simultaneous imaging capabilities. However, the lack of an accurate method for generation of MR-based attenuation map (μ-map) at 511 keV is hampering further development and wider acceptance of this technology. Here, we present a new method for the MR-based attenuation correction map (μ-map), employing a proposed short echo-time (STE) MR imaging technique along with the nearly automatic segmentation. This method repeatedly applies active contours inhomogeneity correction, multi-class spatial fuzzy clustering (SFCM), followed by shape analysis, to classify the images into cortical bone, air, and soft tissue classes. The proposed segmentation method returned sensitivity of 81 % for cortical bone and above 90 % for soft tissue and air. These results suggest that this technique is accurate, efficient, and robust for discriminating bony structures from the neighboring air and soft tissue in STE-MR images, which is suitable for generating MR-based μ-maps.

Keywords PET/MRI · Short echo-time (STE) MRI · Attenuation correction · Inhomogeneity correction · Shape analysis · Spatial fuzzy clustering

A.F. Kazerooni · M.H. A'arabi · H.S. Rad (✉)
Quantitative MR Imaging and Spectroscopy Group,
Research Center for Cellular and Molecular Imaging,
Tehran University of Medical Sciences, Tehran, Iran
e-mail: h-salighehrad@tums.ac.ir

M. Ay
Medical Imaging Systems Group, Research Center for Cellular and Molecular Imaging,
Tehran University of Medical Sciences, Tehran, Iran
e-mail: mohammadreza_ay@tums.ac.ir

A.F. Kazerooni · M.H. A'arabi · M. Ay · H.S. Rad
Department of Medical Physics and Biomedical Engineering, School of Medicine,
Tehran University of Medical Sciences, Tehran, Iran

F. Gao et al. (eds.), *Computational Methods for Molecular Imaging*,
Lecture Notes in Computational Vision and Biomechanics 22,
DOI 10.1007/978-3-319-18431-9_14

1 Introduction

Attenuation correction plays an important role in providing accurate and quantitative reconstruction of positron emission tomographic (PET). In this light, deriving an attenuation correction map (μ-map) from magnetic resonance (MR) volumes has become an important problem in hybrid PET/MR imaging [1].

Due to short T2 relaxation times, a major problem with MR-based μ-map generation arises due to the weak signal of bone, close to the signal intensity of its proximal air in conventional MR images, which makes it almost impossible to differentiate the bone from air. As air and bone manifest different attenuation properties and misclassification of bone tissue leads to significant errors in PET images quantification, correct segmentation of these tissue types is important [2]. Recently, ultra-short echo-time (UTE) MRI sequences have been developed, which facilitate the separation of the cortical bone and air [3]. UTE sequences are capable of capturing cortical bone signals before decaying; thus, they can be used to derive μ-map for MR attenuation correction (MRAC) of head and neck PET images. Unfortunately, sequential application of these sequences is time-consuming, complicates image registration and hence is not plausible in routine clinical practice. Besides, the prediction at the bone/air or soft-tissue/air interfaces occurring in the sinuses is challenging in UTE MR-based μ-maps.

Recently, development of short echo-time (STE) MR imaging sequences, has shown promise in differentiating cortical bone from air [4, 5]. On STE-MR images, cortical bone appears with adequate signal to facilitate its differentiation from air, but with discontinuous boundaries. Therefore, techniques based on segmentation, such as thresholding [4] or fuzzy C-means [5], fail to homogeneously delineate bone boundaries. The performance of these methods become further complicated in the presence of intrinsic noise and intensity inhomogeneity artifacts. Methods that predict attenuation coefficients, on a continuous scale usually either register an atlas of CT or a PET transmission scan template or use techniques from machine learning, which may be time-consuming, and the robustness of these methods to anatomical variability must be carefully evaluated. On the other hand, methods that perform segmentation based on MR voxel intensity are relatively robust and do not require external sources of information apart from MRI data, if the appropriate MR sequences are used. They are generally computationally efficient and easy to implement in the clinical workflow, but they may lack quantification accuracy in brain imaging.

The mentioned issues have been our main motivation to design and implement a clinically-efficient pulse sequence, namely "short echo-time (STE) MRI", which is capable of acquiring short $T2^*$ of the bone, in combination with a spatial fuzzy C-means (SFCM) segmentation approach to differentiate the tissue classes. SFCM algorithm relies on the assumption of intensity inhomogeneity within a specific tissue class. This assumption becomes essentially invalid in the presence of intensity inhomogeneity. To overcome this problem, we incorporated an intensity inhomogeneity correction and shape analysis in our segmentation framework.

2 Materials and Methods

Here, the acquired STE-MR images were employed to derive a relevant μ-map of the area under imaging at 511 keV using the combined imaging and automatic segmentation approach. The overall flow diagram of the proposed method is shown in Fig. 1, which is described in more details as follow:

2.1 MRI Data Acquisition

Short TE (STE)-MR images of five normal volunteers were acquired on a clinical 1.5T MRI System, MAGNETOM Avanto (Siemens Medical Solution, Erlangen,

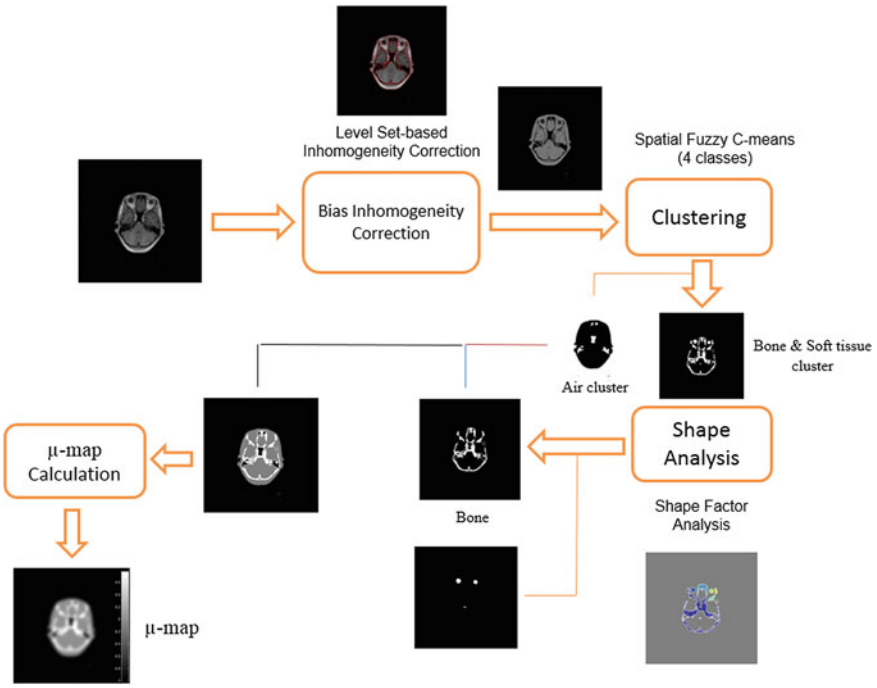

Fig. 1 The overall flow diagram of MR-based attenuation map correction, which is composed of four main steps: (1) intensity inhomogeneity correction by a level set-based intensity correction technique; (2) SFCM segmentation to classify the images into four clusters (air, a part of soft tissue and bone, and two other soft tissue classes); (3) shape factor analysis to remove the eyes, that show close signal intensity to that of bone; and (4) μ-map generation by downsampling and assigning attenuation coefficients to the corresponding segmented tissues

Germany), using a FLASH 3D pulse sequence with TE = 1.1 ms, TR = 12 ms, flip angle = 18°, voxel size = 1.2 × 1.2 × 2 mm^3, and an overall acquisition time of 7:42 min.

2.2 Intensity Inhomogeneity Correction

Magnetic resonance images are commonly deteriorated by intensity inhomogeneities, resulting in erroneous quantification outcomes. Most of the automatic segmentation methods, such as clustering- and region-based methods, rely on the assumption that a given tissue is represented by similar voxel intensities throughout the image. Consequently, any estimated parameter from inhomogeneous data will be highly affected by the presence of this artifact. In order to diminish the effect of this phenomena, here, we employed the method proposed in [6], which uses a clustering-based level set approach for modeling and correcting the intensity inhomogeneity over consequent iterations of level-set evolution. In this technique, k-means clustering is applied to estimate the intensity properties of each region for bias field correction simultaneously with the level-set segmentation. This algorithm incorporates both intensity and spatial information to define continuous boundaries. This is an essential step to help separate air and bone in the regions with high inhomogeneity, like the nasal areas.

2.3 Spatial Fuzzy Clustering

The main challenges with STE-MR segmentation are the ambiguous boundary between air and soft tissue in sinuses, unclear border between soft tissue and bone, and similar intensity values of air and bone in ear area. Fuzzy C means (FCM) is an unsupervised clustering method widely utilized in medical image segmentation, which can account for inherent fuzzy boundaries in the STE-MR images. Nonetheless, FCM technique merely relies on image intensity information and is highly sensitive to noise. In this light, spatial FCM (SFCM) technique has been developed, by incorporating the spatial neighborhood information into the standard FCM clustering algorithm.

Here, SFCM was applied to segment the images into four clusters including air, a part of soft tissue and bone, and two other soft tissue classes. Upon this step, the air cluster would be accurately separated (Fig. 1); this is possible as STE-MR imaging has captured bone signal, which could be discriminated from air with no signal through intensity clustering.

2.4 Shape Analysis

In the next step, the bone class which includes some parts of soft tissue (eyes with close signal intensity to that of bone) should be further processed, so the misclassified tissue could be assigned to its correct class. Here, shape factor analysis was applied as a filter, to eliminate the eyes from bone class. The shape factor (SF) is a measure of circularity or compactness of a shape, represented by:

$$SF = \frac{4\pi A}{P^2} \tag{1}$$

where A is the area and P is the perimeter of the shape. Here, the SF analysis can remove the water in the eye area (that manifests close signal intensity to that of bone) and allocate it to the soft tissue class (Fig. 1).

2.5 Smoothing and Down-Sampling

As the final step, in order to create a suitable μ-map, which is compatible with image resolution and matrix size of Discovery 690 PET/CT scanner (GE Healthcare Technologies, WI, USA), the segmented image was down-sampled to 128 × 128 matrix size and smoothed using a Gaussian filter with 6 mm full width at half maximum.

2.6 Validation

We assessed sensitivity and specificity of the proposed combined imaging and segmentation approach, by comparing the results of STE-MRI segmentation of each region, i.e. bone, air and soft tissue, with the respective regions in CT images of each subject. For this purpose, CT images of the same volunteers were acquired on a multi-slice CT scanner, with no gantry tilt, kVp = 80 kV, tube current = 10 mA and rotation time = 0.5 s. The CT images of each subject were co-registered with their corresponding STE-MR images using FLIRT 3D registration method [7], with affine transformation model and normalized mutual information similarity measure.

3 Results

The results of the proposed segmentation technique for categorizing the brain image into the three comprising tissue classes, i.e. bone, air and soft tissue, are illustrated in Fig. 2. In the left column, three selected slices of CT images of a subject are shown, along with their corresponding STE-MR images in the middle column and the

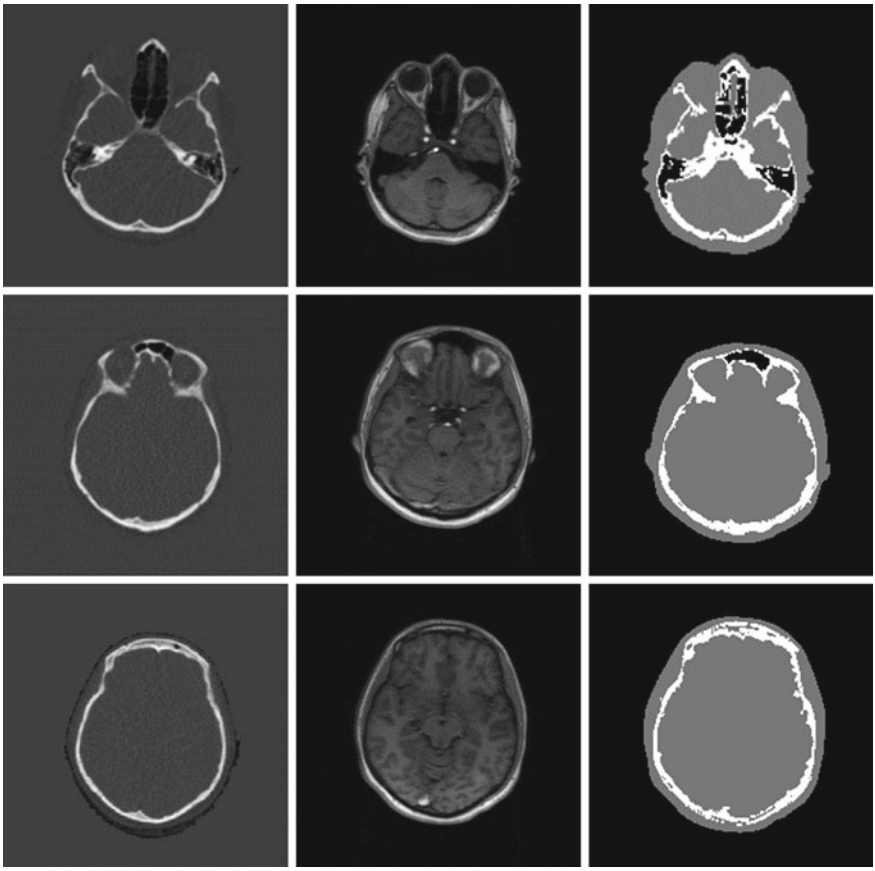

Fig. 2 The results of segmentation of STE-MR images in three selected slices of a subject: (*left column*) CT images, (*middle column*) the corresponding STE-MR image, (*right column*) the result of segmentation of STE-MR image into three classes: air (*black*), bone (*white*) and soft tissue (*gray*)

segmentation results on the STE-MR images using the proposed technique. Quantitative evaluation indicated sensitivity of more than 95 % for air and soft tissue and about 81 % in the bony region, and specificity of over 95 % for all tissue classes, in all of the subjects.

The results of constructed MR-based attenuation maps (μ-map) from the segmented tissue classes are demonstrated in Fig. 3.

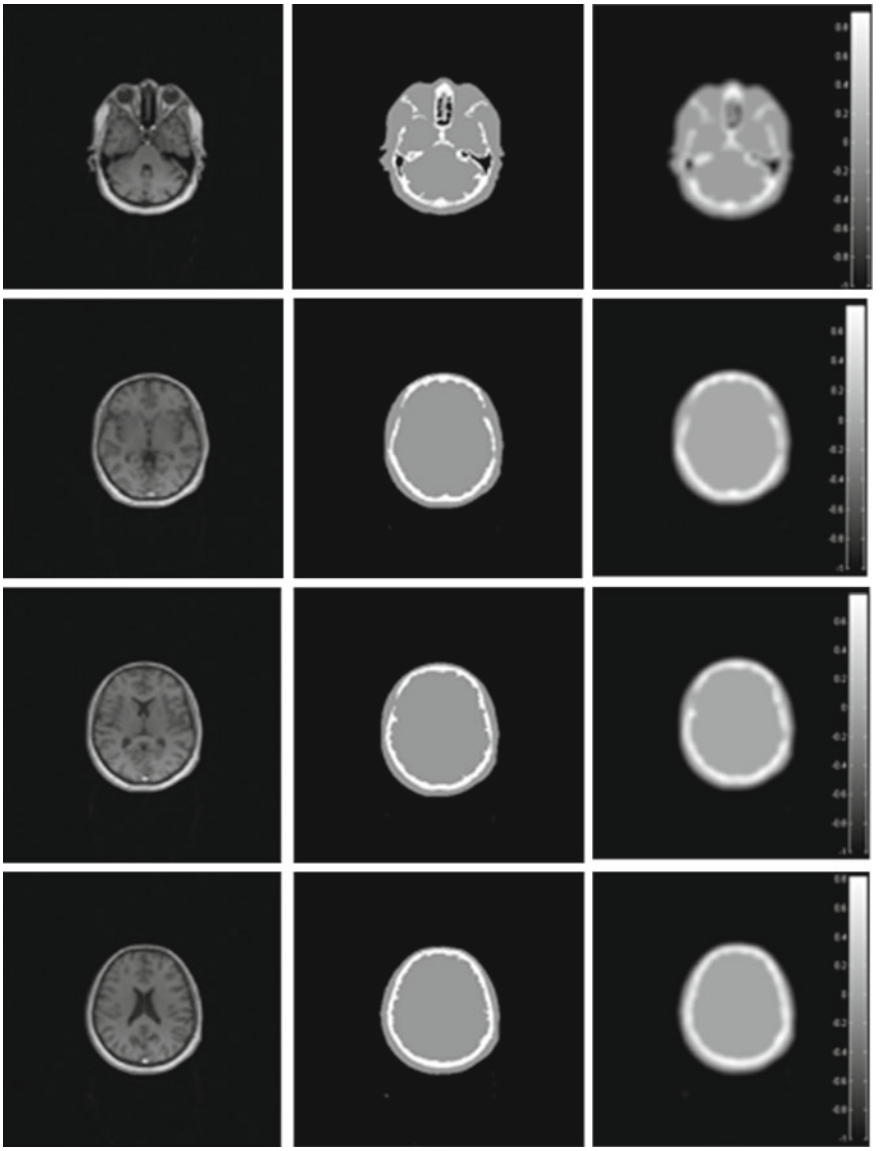

Fig. 3 MR-based attenuation map correction using the proposed method: (*left column*) the acquired STE image which has been acquired with STE pulse sequence, (*middle column*) the result of STE-MR image segmentation based on the suggested approach; and (*right column*) the constructed μ-map, which has been derived from the STE-MR images

4 Discussions

Generating MR-based attenuation correction map (μ-map) for quantitative reconstruction of PET images still remains a challenge in hybrid PET/MRI systems. The issue is mainly due to the fact that in conventional MR images, cortical bone structures are indistinguishable from proximal air cavities, e.g. in facial sinuses in the head images [1]. To overcome this problem, several segmentation approaches have been proposed, such as a combination of consequent thresholding and mathematical morphological operations [8] or CT-derived model-based segmentation algorithms [9]. However, due to close signal intensity of cortical bone to that of air, these methods fail to robustly separate bony structures from proximal air cavities. In recent years, ultrashort echo-time (UTE) MRI acquisition techniques have been developed for head segmentation, which are capable of imaging the tissues with short T2* relaxation time [3]. Nonetheless, UTE-MRI techniques are costly and time-consuming, and hence not plausible in routine clinical practice.

To overcome the mentioned problems, in the present study, we introduced a new fully automatic and reproducible STE-MR segmentation approach exploiting a single short TE (STE)-MR imaging technique along with an efficient automatic segmentation approach, exploiting spatial fuzzy C-means (SFCM) algorithm and shape factor analysis to reliably segment the bone from soft tissue and air.

Considering the limitations of employing UTE-MRI in whole-body imaging, the proposed combined imaging and processing method seems to be used as a substitute for UTE-based PET attenuation correction.

One of the problems with UTE-based methods is misclassification of water and eye tissue as bone, due to their proximal signal intensity to that of bone. This issue was also present in STE-based imaging method, which was overcome by applying a measure of circularity for eliminating the eyes. The accuracy of cortical bone segmentation was about 88 % in the air and bone interface region, where susceptibility artifact exists.

This work has some limitations that need to be refined in future. As shown in Fig. 3, some parts of bone appear with discontinuity. This is the reason that the sensitivity of bone segmentation is about 81 %. This issue calls for further investigation of segmentation and intensity correction methods to achieve optimal performance of the technique in cortical bone discrimination and accurate μ-map generation. Nevertheless, this approach should be assessed on a larger population to confirm its potentials. Moreover, the generated attenuation map must be evaluated in comparison with the state-of-the-art techniques for constructing μ-map in hybrid PET/MR systems.

From visual inspection of the segmentation results and the quantitative assessment outcomes, it can be concluded that the proposed STE-MR imaging in combination with the segmentation technique can provide reliable segmentation of human brain skull and soft tissue from a single clinical MR imaging modality. Hence, this method can be used efficiently to generate accurate MR-based attenuation correction maps.

References

1. Navalpakkam, B.K., Braun, H., Kuwert, T., Quick, H.H.: Magnetic resonance—based attenuation correction for PET/MR hybrid imaging using continuous valued attenuation maps. Invest. Radiol. **48**(5), 323–332 (2013)
2. Zaidi, H., Del Guerra, A.: An outlook on future design of hybrid PET/MRI systems. Int. J. Med. Phys. Res. Pract. **38**(10), 5667–5689 (2011)
3. Catana, C., et al.: Toward implementing an MRI-based PET attenuation-correction method for neurologic studies on the MR-PET brain prototype. J. Nucl. Med. **51**(9), 1431–1438 (2010)
4. Khateri, P., et al.: Generation of attenuation map for MR-based attenuation correction of PET data in the head area employing 3D short echo time MR imaging. Nucl. Instrum. Methods Phys. Res. Sect. A: Accel. Spectrom. Detect. Assoc. Equip. **702**, 133–136 (2013)
5. Khateri, P., et al.: A novel segmentation approach for implementation of MRAC in head PET/MRI employing short-TE MRI and 2-point Dixon method in a fuzzy C-means framework. Nucl. Instrum. Methods Phys. Res. Sect. A: Accel. Spectrom. Detect. Assoc. Equip. **734**, 171–174 (2014)
6. Li, C., et al.: A level set method for image segmentation in the presence of intensity inhomogeneities with application to MRI. IEEE Trans. Image Process. **20**(7), 2007–2016 (2011)
7. http://fsl.fmrib.ox.ac.uk/fsl/fslwiki/FLIRT
8. Dogdas, B., Shattuck, D.W., Leahy, R.M.: Segmentation of skull and scalp in 3-D human MRI using mathematical morphology. Hum. Brain Mapp. **26**(4), 273–285 (2005)
9. Wang, D., Shi, L., Chu, W.C., Cheng, J.C., Heng, P.A.: Segmentation of human skull in MRI using statistical shape information from CT data. J. Magn. Reson. Imaging **30**(3), 490–498 (2009)

Query by Image of Brain SPECT Database

David S. Wack, Feyza Erenler and Robert Miletich

Abstract In contrast to search engines for medical image databases that use age, gender, or disease classification, Query by Image search allows an *image* to be presented as input to the search engine. Images together with clinical reports are returned that best match the presenting image. Work on query by image systems have been ongoing for more than two decades, predominately in fields outside of medical imaging. In these fields, features are often identified and used in the search for similar images. Corresponding strategies have been taken in medical imaging, especially MRI where it is reasonable to match based on a feature. However, in brain SPECT imaging, clinicians are often interested in the global pattern of brain activity for making diagnoses such as Small Vessel Disease, Mild Cognitive Impairment, Parkinson's or Alzheimer's Disease, which have some commonalities as "Global Brain Impairment" patterns. By utilizing robust spatial normalization methods to transform images to a common stereo-tactic space, we are able to use simple methods for measuring and ranking the closeness between the presenting image and images in the database. Our decomposition of the Brain SPECT dataset shows that images within the dataset have very high similarity. However, subtle differences can be reliably utilized for selecting best image matches. Throughout testing, highly relevant cases were consistently returned for our image queries. Our method is fast, robust, intuitive for users, and practical.

Keywords Query by image · Brain SPECT database · Data-mining · SVD

1 Introduction

An ultimate goal of many researchers working within medical imaging informatics is to provide automated diagnosis from medical images. This is a grand challenge that can lead to complicated approaches. Our goal here is to present a simple query

D.S. Wack (✉) · F. Erenler · R. Miletich
Department of Nuclear Medicine, Center for Positron Emission Tomography,
SUNY at Buffalo, 105 Parker Hall, 3435 Main St., Buffalo, NY 14214, USA
e-mail: dswack@buffalo.edu

F. Gao et al. (eds.), *Computational Methods for Molecular Imaging*,
Lecture Notes in Computational Vision and Biomechanics 22,
DOI 10.1007/978-3-319-18431-9_15

by image search engine that we believe is a strong mid-point goal, between an unassisted human expert reading of the image and that of a fully algorithmic approach. There have been several previous methods that have explored query by image search across many disciplines. In finding matching images, the fundamental question is "are two images close". For example, if one was trying to find similar photographs to a presenting picture, one method might try to match faces, whereas another might look for similar colors, etc. For our application, we use query by image to match global features of SPECT images. Characteristics of brain SPECT image datasets allow us to take a simple robust approach for a solution.

Query by Image Content (QBIC) methods originated over two decades ago [1–3]. Following this work, Cheng et al. [4] developed the system SMIRE (similar Medical Image Retrieval Engine). Image similarity values were calculated using the histograms after some preprocessing. Furthermore, for 2 D images there is the free and openly available "GNU Image Finding Tool" (www.gnu.org/software/gift). These methods also use user feedback to improve search results. Other methods became known as "Content based medical image retreival" methods, and are seen as part of medical image data-mining efforts [5, 6]. Finally, there is a large amount of work in facial recognition, and object identification in other fields.

Fundamentally, in developing a search engine to match images based on global pattern of activity of SPECT images, we need to be able to measure the distance between two images. This measure should be robust and invariant to global differences in dose and global uptake, and most dependent on the overall pattern of the images. While we will use singular value decomposition to form "eigen-images" of the data set to explore the overall patterns of activity across the set of images, a simple similarity value between two images is Spearman linear correlation, such that image pairs with higher correlation are judged to be closer. We choose to use correlation over, say, Euclidean distance as a straightforward way to compare images because it automatically accounts for global dosing differences.

We believe that the scans within the database have clear patterns relating to disease states. We believe that linear correlation can be utilized to provide ranking of images in a database such that images with the highest correlations will have similar diagnoses.

2 Methods

Clinical data was collected from a double head ADAC Atlas SPECT scanner using Neurolite tracer. Patient images and reports were linked together and then anonymized. This analysis project was approved by the University at Buffalo, Health Sciences IRB. Multiple frames were summed to provide activity between 0 and 40 min. These volumes were spatially normalized using SPM8 to an in house SPECT template in the Montreal Neurological Institute (MNI) coordinate system. Resulting spatially normalized images had voxel size of $2 \times 2 \times 2$ mm and X, Y, Z dimensions of 79, 95, 68 voxels. 2198 patient scans and matching reports were used to form

the database. These patients represented a full cross section of the clinic's patient population. The clinical diagnosis included patients with Small Vessel Disease, Hydrocephalus, Parkinson's, and Alzheimer's Disease.

Singular Value Decomposition: By representing each image volume as a 1-d vector, the 2198 scans with dimensions $79 \times 95 \times 68$, were represented as a single matrix, M, with dimensions 510340×2198. Matlab (Natick, MA) was used to calculate the singular value decomposition of M, as [U S V] = svd(M,0). The 0 parameter selects the "economy size" decomposition and limits the number of columns calculated for U to 2198. Resulting "eigen-images" were formed from reshaping the columns of U to the image volume dimensions, eigenvalues from the diagonal of S, and image coefficients from the columns of V. The relative size of the first eigen-values to the remaining values gives an indication of the overall similarity of images across the data set. The eigen-images show commonalities in the differences found between images. The image coefficients provide information based on how they cluster when plotted, and give an indication of whether there are distinct subsets of images or if the images represent more of a continuum of disease states.

Queries by Image: The Spearman correlation was used to determine the similarity between the input image and the database images. For the Input, Best Match (database case whose image has the highest correlation to the input image), and Median Match (database case whose image has the 1099th highest correlation to the input image), the highlights of the clinical reports were recorded. Twenty image queries were performed, and the report findings of the input image were compared with the findings from the closest match, and the image/report from the median match (to provide a control). The belief is that the best match image/report will share stronger similarities with the input image/report than that of from the median match.

3 Results

The min/mean/max of the twenty queries of the best matching case was 0.933/0.974/0.985. The min/mean/max of the twenty queries of the median matching case was 0.861/0.947/0.968. Across the entire data set the mean correlation tested between all pairs of images was 0.94, and over 64 % of image pair correlations were above 0.95. These high correlation values were consistent with the eigen-values given in Fig. 1, which demonstrates that the first eigen-value was considerably larger than the rest. Despite the much lower values for the second and above eigen-values, the corresponding eigen-images formed showed clear structure well past the first 10 components. The first four eigen-images are shown in Fig. 2. Only mild clustering sets can be observed from the image coefficients (columns of V) indicating that images likely provide a continuum of disease states, Fig. 3.

In all cases, the associated case reports from the best image match had stronger similarities with the report associated with input image than the median match. All best matches were judged to have at least good relevance to the input image, and all

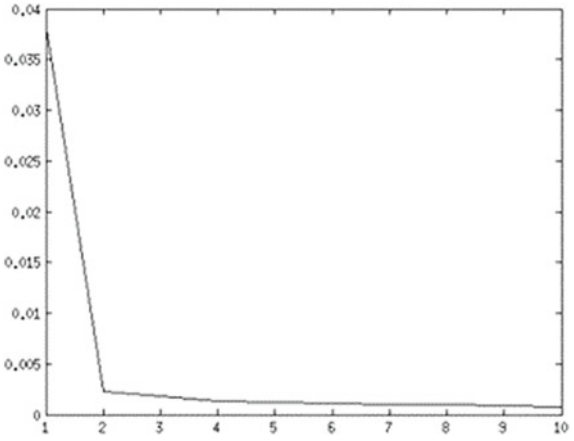

Fig. 1 Magnitude of the first ten eigen-values from SVD of 2198 brain SPECT image dataset

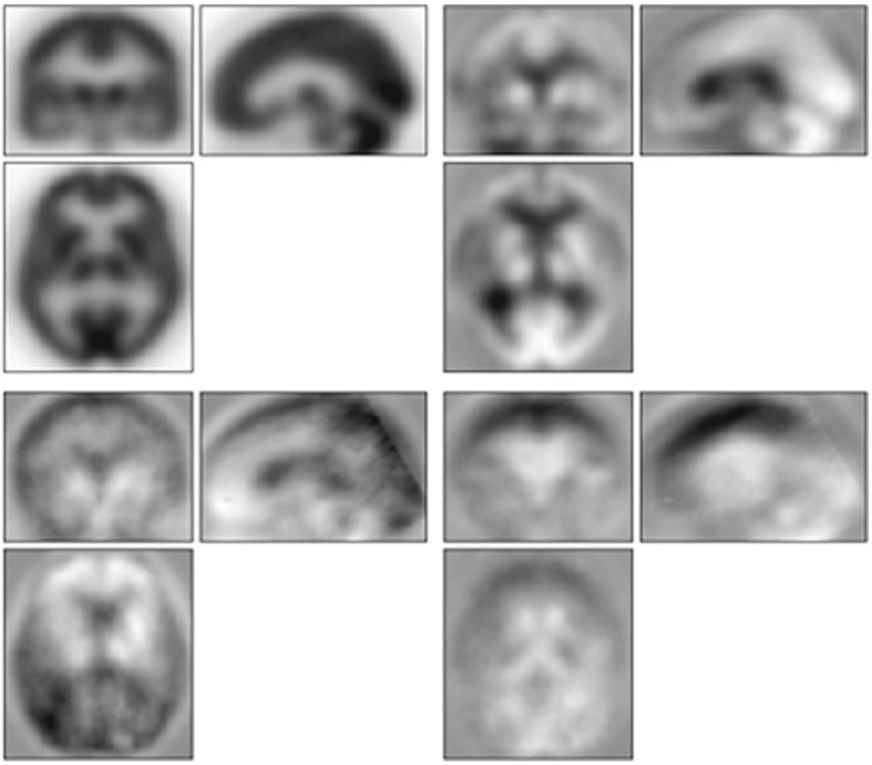

Fig. 2 First four eigen-images from singular values decomposition of brain SPECT dataset

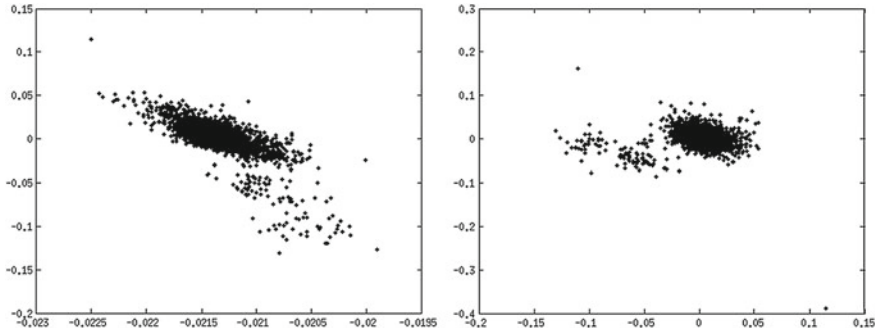

Fig. 3 Image coefficients of the 2198 brain SPECTs. *First graph* coefficient of the 1st component versus the 2nd component (first two columns of matrix V). *Second graph* Coefficients of the 2nd component versus the 3rd

had better relevance than the median match image. Because this is a clinical data set, even the median match image could have relevance with the input image. For example, many of the images were clinically judged to show at least possible signs of Small Vessel Disease. Highlights of the input, best, and median case reports for the first five queries are provided in Table 1, together with the correlation values. The spatially normalized input, best match, and median match images for the first query are shown in Fig. 4. A query took approximately 1 s to determine the best match.

4 Discussion

We were successful in demonstrating a straightforward approach, which uses linear correlation between spatially normalized images, to implement a query by image system for brain SPECT scans. This despite the very small separation between images, such that the mean correlation between two images was over 0.94, and over 65 % of correlations had a better than 0.95 correlation. A significant advantage of our problem set is that spatial normalization for SPECT images is very robust. We choose correlation over a voxel-wise distance, such as sum of squares, to provide a natural means of accounting for global dose differences. We used linear correlation as a means to provide a simple bench mark, so that future, and likely more complex methods, can be compared to this straightforward, and well performing standard.

Singular Value Decomposition: The first eigen-image is equivalent to finding the mean of the set of images and because of the relative size of the first eigen-value this represents an overwhelming commonality between images, which is consistent with the high overall correlation between images. Another way to view this is that to an untrained eye, the difference between a healthy normal subject and subject with impairment may be too subtle to be reliably observed. We believe the second and third eigen-images (Fig. 2), which display frontal and striatal patterns,

Table 1 First five reports of input, best and median match reports from image search

Query number	Image class	Corr.	Clinical report highlights
1	Input	1	Suspicion of Lewy body disease
			Moderate hypo-perfusion consistent with SVD
	Best	0.970	Suggestive of diffuse Lewy body disease
			hypo-perfusion consistent with SVD
	Median	0.949	Suspicion of SVD
2	Input	1	Frontal hypo-perfusion
			WM hypo-perfusion consistent with SVD
	Best	0.932	Frontal hypo-perfusion
			WM hypo-perfusion consistent with SVD
	Median	0.867	Hypo perfusion left anterior temporal lobe
			Possible very mild SVD
3	Input	1	Hydrocephalus present
			Hypo-perfusion seen in GM supratentorially
	Best	0.977	Hydrocephalus present
			Hypo-perfusion seen in WM
	Median	0.955	Findings suggestive of neurodegenerative disease and consistent with Alzheimer disease
			Hypo-perfusion in WM consistent with SVD
4	Input	1	Moderate pattern of multifocal WM hypo-perfusion consistent with SVD
	Best	0.978	At worst moderate SVD seen within WM
	Median	0.962	Severe extensive pattern of WM hypo-perfusion. Most consistent with neurodegenerative disease and vascular disease
5	Input	1	Cortical changes suggestive of Alzheimer's disease. Widespread cerebral atrophy
			WM hypo-perfusion consistent with SVD
	Best	0.980	Cortical changes suggestive of Alzheimer's disease. WM hypo-perfusion consistent with SVD
	Median	0.960	Likely Lewy body disease
			WM hypoperfusion consistent with SVD

Abbreviations Small Vessel Disease (SVD), White Matter (WM)

are particularly interesting, and believe that they provide insight to global brain impairment diseases [7]. As these components explain differences between images beyond scaling the mean, we believe these eigen-image patterns can be eventually used to represent the image patterns associated with different diseases, and ultimately lead to a more sophisticated distance index. As there is not a relevant temporal ordering to the images, we did not use complex singular values decomposition, as we have previously [8].

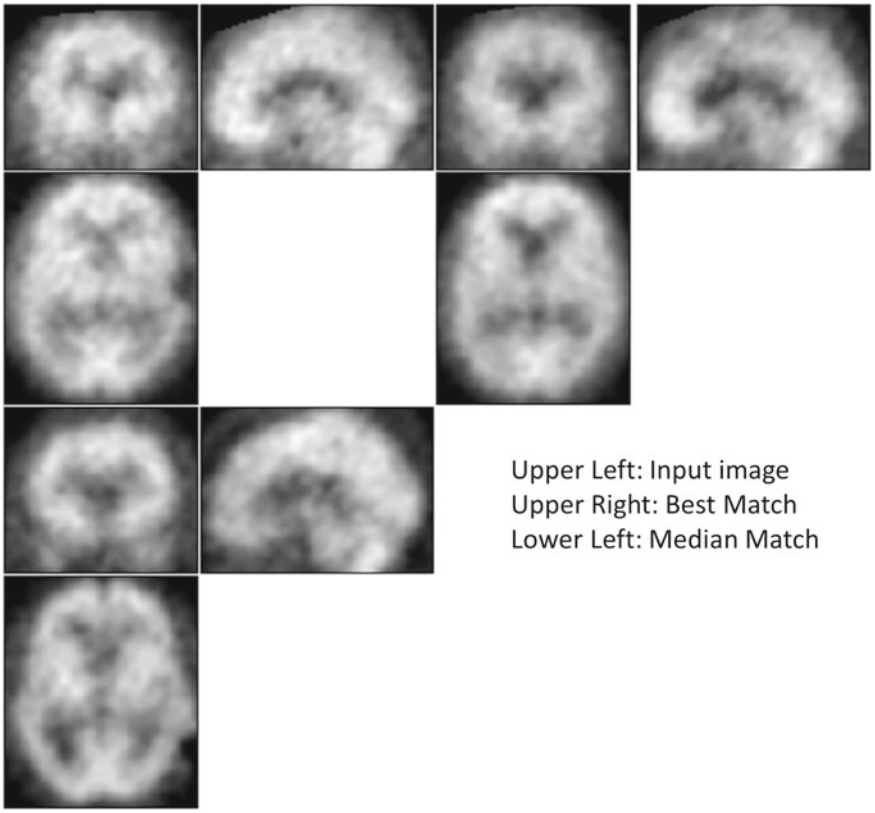

Fig. 4 Notice similar frontal pattern between input and best match images. All show decrease WM activation, but this is predominate on median match image

Query by Image: Our method of comparing the best and median match images demonstrated that many images in our database not only appear similar (Fig. 4), but they also have similar diagnostic reports (Table 1). This should not be surprising, and simply demonstrates that we have a very fine covering of images for more common disease states, while other disease states/images are rarer. This is also shown by a range of correlation values for the median match image as well as the few sparse clusters seen in Fig. 3. Our overall approach has obvious similarities with nearest neighbor pattern recognition methods. Indeed, we believe future methods could rely on classification measures internally used in various pattern recognition methods such as Stochastic Discrimination [9, 10].

We used a similar number of query trials as Cheng et al. [1], however we made use of a control image findings by listing the highlights of the clinical report of the median image, whereas Cheng et al. used raters to rate the findings as relevant or not. Given the tight clustering of most images (Fig. 3), and the high mean correlation of images, a similar approach would be unfairly lenient because there are many common

elements within a large fraction of the image database—such as the many reports that are consistent with Small Vessel Disease (Table 1). Our approach instead used a control by reporting the findings of the clinical report of the median match image. The commonalities of both the best and median match images allow the reader to see how some image traits are more prevalent than others. For example in our first query (Table 1), we see that Lewy Body Disease was in common between the best match and input image (but not the median match image), but all three reports had mention of small vessel disease.

Future Directions: Our approach gives a straight forward way to better utilize our database of SPECT images by opening a new line of searching for commonalities between scans. We believe that weighted correlations and correlations limited to specific regions represent promising next steps, along with more complicated metrics that can be borrowed from pattern recognition approaches. Regardless of the specifics of a next approach, the linear correlation approach described here provides an easy to implement benchmark that new approaches can be tested against.

References

1. Faloutsos, C., Barber, R., Flickner, M., Hafner, J., Niblack, W., et al.: Efficient and effective querying by image content. J. Intell. Inf. Syst. **3**, 231–262 (1994)
2. Flickner, M., Sawhney, H., Niblack, W., Ashley, J., Huang, Q., et al.: Query by image and video content: the QBIC system. Computer **28**, 23–32 (1995)
3. Niblack, C.W., Barber, R., Equitz, W., Flickner, M.D., Glasman, E.H., et al.: QBIC project: querying images by content, using color, texture, and shape. In: International Society for Optics and Photonics, pp. 173–187 (1993)
4. Cheng, P.-C., Chien, B.-C., Ke, H.-R., Yang, W.-P.: SMIRE: Similar medical image retrieval engine. Multilingual Information Access for Text, Speech and Images. Springer, Berlin (2005)
5. Lehmann, T.M., Güld, M.O., Deselaers, T., Keysers, D., Schubert, H., et al.: Automatic categorization of medical images for content-based retrieval and data mining. Comput. Medi. Imaging Graph. **29**, 143–155 (2005)
6. Ramamurthy, B., Chandran, K.: CBMIR: shape-based image retrieval using canny edge detection and k-means clustering algorithms for medical images. Int. J. Eng. Sci. Technol. **3**, 209–212 (2011)
7. Miletich, R.S.: Positron emission tomography for neurologists. Neurol. Clin. **27**, 61–88 (2009)
8. Wack, D.S., Badgaiyan, R.D.: Complex singular value decomposition based noise reduction of dynamic PET images. Curr. Med. Imaging Rev. **7**, 113–117 (2011)
9. Kleinberg, E.M.: On the algorithmic implementation of stochastic discrimination. IEEE Trans. Pattern Anal. Mach. Intell. **22**, 473–490 (2000)
10. Wack, D., Dwyer, M., Hussein, S., Caiola, C., Hojczyk. P., et al.: Automated lesion discrimination and outlining, p. 1540 (2008)

Age-Related Glucose Metabolism Changes in Brain

Xiaoyan Shen, Zhiliang Liu, Zhenghui Hu and Huafeng Liu

Abstract Normal aging is associated with a progressive decline in cognitive performance, including perception, attention, language and memory. Cerebral glucose metabolism is a reliable index of neural activity and may provide evidence for brain function in healthy adults. To explore the metabolic topography of brain with normal aging, we studied the correlation between cerebral glucose metabolism and age under the resting-state in male and female groups respectively with position emission tomography (PET). In addition, many studies about brain network have suggested that normal aging is associated with alterations in coordinated patterns of the large-scale brain functional and structural systems. However, age-related changes in functional networks constructed via PET data are still barely understood. Here, large-scale functional networks in younger and older age groups were constructed by computing the partial correlation matrices of the regional mean intensity values from PET data to investigate the brain functional topological properties.

Keywords Brain · Normal aging · Glucose metabolism · Functional network · Correlation · Small world topology

X. Shen (✉)
Zhejiang University of Technology, Zhejiang, China
e-mail: shenxiaoyan@zjut.edu.cn

Z. Liu · Z. Hu · H. Liu
Zhejiang University, Zhejiang, China
e-mail: liuzhiliang@zju.edu.cn

Z. Hu
e-mail: zhenghui@zju.edu.cn

H. Liu
e-mail: liuhf@zju.edu.cn

F. Gao et al. (eds.), *Computational Methods for Molecular Imaging*,
Lecture Notes in Computational Vision and Biomechanics 22,
DOI 10.1007/978-3-319-18431-9_16

1 The Metabolic Topography of Normal Aging

It is now well established that normal aging is associated with a progressive decline in cognitive performance, including perception, attention, language and memory [1–4]. Although the causes of age-related cognitive decline remain elusive, many studies point out that the normal aging is accomplished by a decline of synaptic activity, which may impact the cognitive functions [5–9]. Parkin et al. [7] and Miller et al. [5] found that age-related memory deficits were associated with a decreased neuronal activity in frontal and temporal lobes, and the influences of hippocampal synaptic activity on memory impairment had also been observed by Geinisman et al. [9]. Moreover, Pardo et al. [6] reported a positive correlation between the neuron activity in the prefrontal lobe and semantic fluency. Therefore, understanding age-related brain activity changes is essential for assessing the elderly presenting with cognitive complaints and preventing potential cognitive impairment with aging.

In the resting state, the level of cerebral glucose metabolism is considered as a reliable index of neural activity [10]. Synapses are the key sites for information transfer between neurons in the brain. Phelps et al. [11] studied the cerebral metabolic rate of glucose in resting state and found that up to 75 % of the glucose consumption in the brain was used to maintain a baseline synaptic activity. Therefore, measuring the resting cerebral glucose metabolic with PET is available for detecting age-related brain activity changes. In the past few years, considerable efforts have been done in studying the age-related brain activity changes by measuring the resting cerebral metabolic rate of glucose with [^{18}F] fluoro-2-deoxyglucose (FDG)-PET and an age-related glucose metabolism decline prominently appears in the frontal lobe [6, 10, 12–15].

However, previous reports about the relationship between the regional cerebral glucose metabolism and age are discrepant in a number of brain areas, sometimes conflicting. For example, one study indicated a decreased glucose metabolism with age in the thalamus [6], while Willis et al. reported an increased glucose metabolism in the same region [15]. The divergence in results may be due to the different methodologies, screen criteria and range of subject ages, especially the sample size which is one of the key issues to obtain consistent, statistical results. On the other hand, most early studies on age-related glucose metabolism use region of interest (ROI) analysis [14, 16–23]. In recent years, voxel-based quantitative analysis methods such as statistical parametric mapping (SPM) have been widely used [6, 10, 15]. SPM offers a statistical mapping of whole brain by an automated and voxel-based analysis, which helps to detect the areas missed in region of interest (ROI) analysis and avoid subjectivity variation. Here, we used resting state FDG-PET data from a large sample of health adults (in total 234 subjects) across a wide range of age, analyzed by SPM to identify the correlation of the regional cerebral glucose metabolism changed with normal aging. As various studies have reported the sex differences in brain function [4, 17, 24], it is reasonable to analyze the age effects on regional cerebral glucose metabolism for females and males separately. We expect to find a consistency effect of aging on the regional brain activities.

1.1 Materials and Methods

1.1.1 Subjects

We studied 234 consecutive subjects from a clinical database, and all subjects were gave written informed consent for their information to be used for the future research. The study was reviewed and approved by the ethics committee of Zhejiang University and the experiments were conducted according to the Declaration of Helsinki. The subjects consisted of 108 females aged from 26 to 71 years (mean ± S.D. = 45 ± 10 years) and 126 males aged from 28 to 77 years (mean ± S.D. = 49 ± 11 years). All subjects had a normal physical examination before imaging. The subjects were selected according to the following criteria: no significant acute or chronic disease was found at the time of the study. Subjects reported no history of brain injury, neurological illness or clinical evidence of significant cognitive decline beyond the expected for normal aging.

1.1.2 PET Imaging

All PET investigations were performed at the Medical PET Center of Zhejiang University. PET images were acquired with Hamamatsu SHR 22000 whole-body PET scanner in two-dimensional mode. The scanner has a 600 mm patient aperture and an axial field-of-view of 225 mm, which can cover the whole human head. The spatial resolution of the scanner is 3.2 mm full width at half maximum (FWHM) in axial plane and 3.5 mm FWHM in sagittal or coronal plane. A 10-min transmission scan was performed before the emission scan using a ^{68}Ge source for attenuation correction. All subjects rested in a quiet, dark room with eyes closed and ears open for 40 min after 333–444 MBq (9–12 mCi) FDG was injected intravenously. Then emission scans were acquired under the resting state (lying quietly with eyes closed) for 8 min. PET images were reconstructed with a ramp filter to the Nyquist frequency, using the maximum-likelihood expectation maximization (MLEM) algorithm.

1.1.3 Data Analysis

The tissue concentration of FDG can be calculated from the pixel intensity values of the PET images as described by Kumar et al. [25] The regional cerebral metabolic rates for glucose were derived form the relationship between the tissue concentration and the integrated plasma levels of FDG by using a modified Sokoloff equation [26]. Therefor, the regional cerebral metabolic rates for glucose can be represented by pixel intensity values of the PET images, which can be quantitatively used for statistical analysis. PET images were analyzed using matlab 6.5 (MathWorks Inc., Notich, MA, USA) and Statistical Parametric Mapping (SPM5, Wellcome Department of Cognitive Neurology, London, UK) software. Prior to statistical analysis, raw PET data were converted into Analyze format using ImageJ (Wayne Rasband, National Institute of Mental Health, USA) and MRIcro software (www.mricro.com).

All PET images were spatially normalized into the Montreal Neurological Institute (MNI, McGill University, Montreal, Canada) standard template using SPM5. After normalization, spatial smoothing was performed by convolution, using an isotropic Gaussian kernel with 12 mm FWHM to increase the signal-to-noise ratio. All subjects were separated into two groups (the female group and the male group) and analyzed respectively. Statistical test of age effect on cerebral glucose metabolism was performed through voxel-based analysis using a general liner model (GLM). In the GLM analysis, age was a covariate to study the relationship between glucose uptake and normal aging. T-test was used to examine the regression coefficient. Global nuisance effects were eliminated by including the global covariate in the general linear model. In SPM maps, we searched the brain areas with a significant correlation using a statistical threshold of $p < 0.05$, family wise error (FWE)-corrected for the problem of multiple comparisons, with an extent threshold of 100 voxels. For the whole brain of 228 resels, the uncorrected p values were 2.19e−4. The significant areas were overlaid on a T1-weighted MRI image slice by slice. The MNI coordinates were converted to the Talairach coordinates, and the Talairach Client was used for localization. In order to measure the effect of age on regional cerebral glucose metabolism quantitatively, correlation analysis were obtained by calculating the Pearson correlation coefficient (r) for each significant cluster. Scatter plotted using local maximum activity of each cluster versus age.

1.2 Results

1.2.1 Effects of Aging on Glucose Metabolism in the Female Group

The result of one-sample t-test of correlation between glucose metabolism and age in the female group was shown in Fig. 1. The map illustrated the regions of negative correlation with a statistical threshold of $p < 0.05$ FWE-corrected and an extend threshold of 100 voxels. Three clusters in the frontal lobe and the temporal lobe showed the significant negative correlations: the left medial frontal gyrus (BA 9, $p < 0.001$ FWE-corrected, $r = 0.4837$), the left inferior frontal gyrus (BA 47, $p = 0.0038$ FWE-corrected, $r = -0.4599$) and the right superior temporal gyrus (BA 38, $p = 0.0044$ FWE-corrected, $r = -0.4573$). More detailed information was listed in Table 1.

Figure 2 showed the scatterplots of glucose metabolism in local maximum of each cluster versus age, and a quadratic polynomial fitting was used to express a trend of decreased glucose uptake with aging. For the left medial frontal gyrus and the left inferior frontal gyrus, the curves were nearly horizontal before 40 years of age, and after that the curve appears an accelerated declining trend. For the right superior temporal gyrus, the curve remained an almost constant non-zero curvature and slow downward trend.

In the female group, regions of positive correlation between glucose metabolism and age were not found.

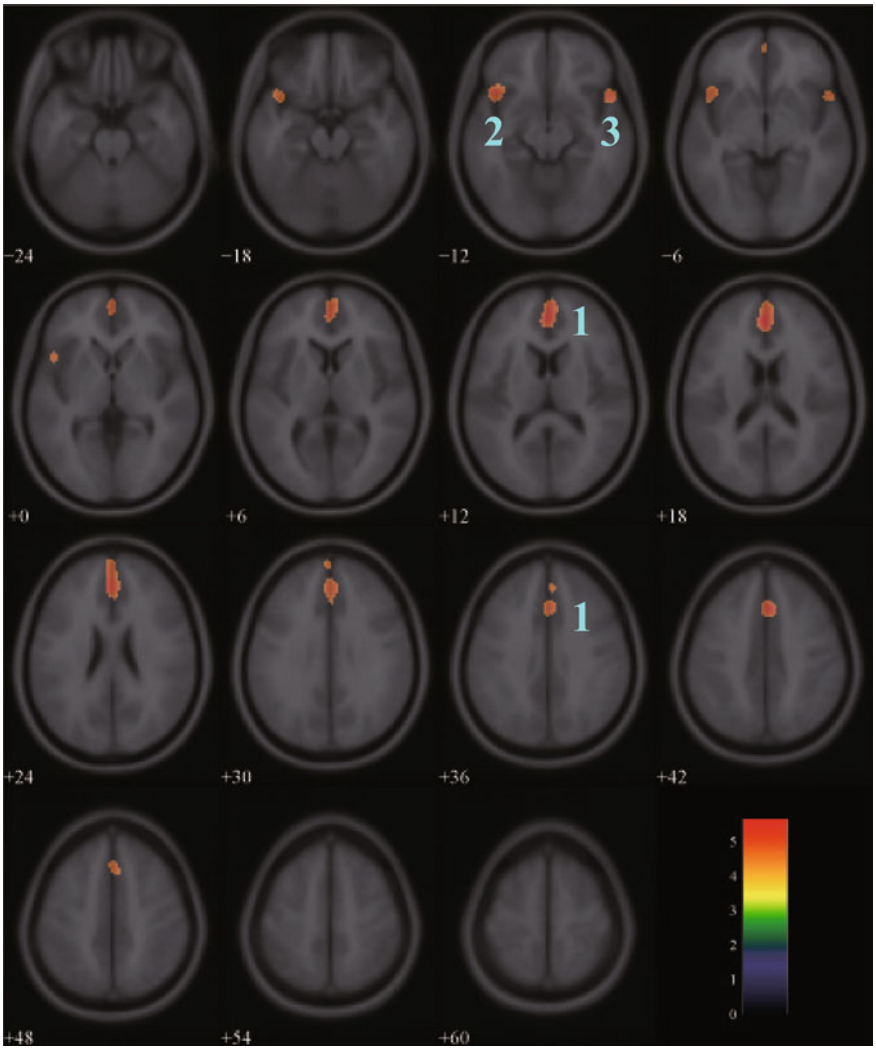

Fig. 1 Areas of negative correlation between glucose metabolism and age in the female group. The significant areas overlaid on a T1-weighted MRI image are displayed with a statistical threshold of $p < 0.05$ FWE-corrected and an extend threshold of 100 voxels. The number of slices correspond to the z values in Talairach coordinate system which defined form inferior to superior. Clusters 1–3 represent the left medial frontal gyrus/right cingulate gyrus, the left inferior frontal gyrus and the right superior temporal gyrus respectively. *Color scale* denotes t value

Table 1 Clusters of glucose metabolism decrease with normal aging in the female group

Cluster	Region name	BA	Talairach coordinates *x y z* (mm mm mm)			*p* FWE-corr	*r*	Voxels
1	Medial frontal gyrus (L)	9	0	43	13	<0.001	−0.4837	1263
	Cingulate gyrus (R)	32	4	23	36	0.0016	−0.4751	
2	Inferior frontal gyrus (L)	47	−42	17	−11	0.0038	−0.4599	282
3	Superior temporal gyrus (R)	38	51	13	−11	0.0044	−0.4573	132

BA: Brodmann area; (x, y, z), local maximum activity of cluster in Talairach coordinate system; *p*: significance level; *r*: Pearson correlation; Voxels: number of voxels within cluster; L: left; R, right

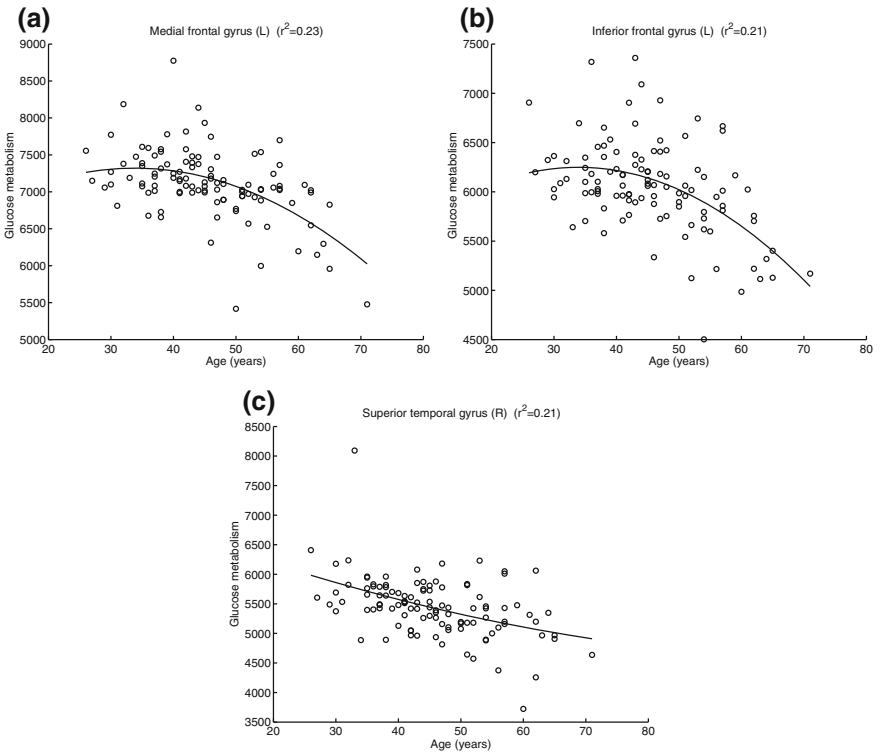

Fig. 2 Scatterplots of glucose metabolism in local maximum of each cluster versus age in the female group. A quadratic polynomial fitting is used to express the relationship between glucose uptake and age. **a** Left medial frontal gyrus, $r^2 = 0.23$; **b** Left inferior frontal gyrus, $r^2 = 0.21$; **c** Right superior gyrus, $r^2 = 0.21$

1.2.2 Effects of Aging on Glucose Metabolism in the Male Group

Figure 3 showed the areas of negative correlation between glucose metabolism and age in the male group with the same threshold set as above. Areas of relative decreased

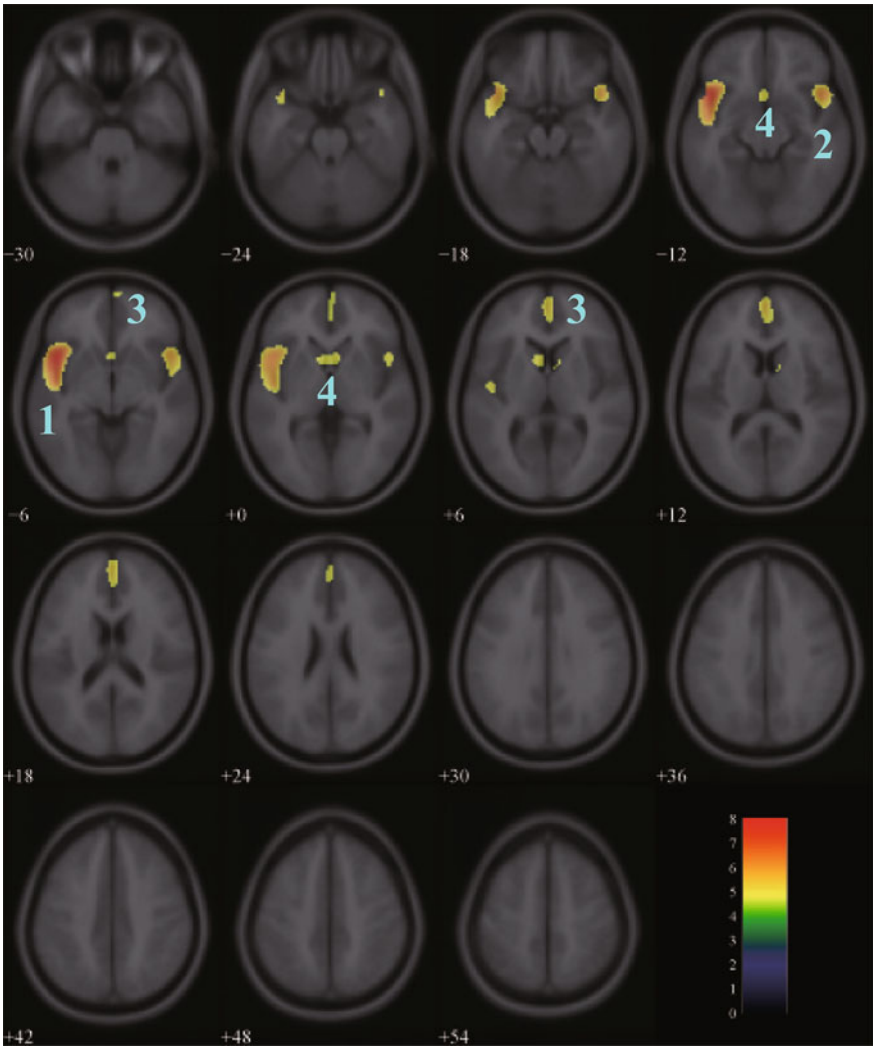

Fig. 3 Areas of negative correlation between glucose metabolism and age in the male group. The significant areas overlaid on a T1-weighted MRI image are displayed with a statistical threshold of $p < 0.05$ FWE-corrected and an extend threshold of 100 voxels. The number of slices correspond to the z values in Talairach coordinate system which defined form inferior to superior. Clusters 1–4 represent the left superior temporal gyrus, the right superior temporal gyrus, the medial frontal gyrus, and the caudate/left subcallosal gyrus respectively. *Color scale* denotes t value

Table 2 Regions of glucose metabolism decrease with normal aging in the male group

Cluster	Region name	BA	Talairach coordinates *x y z* (mm mm mm)			*p* FWE-corr	*r*	Voxels
1	Superior temporal gyrus (L)	38	−46	11	−7	<0.0000001	−0.5880	1682
2	Superior temporal gyrus (R)	38	48	13	−11	<0.0001	−0.4998	566
3	Medial frontal gyrus (L)	10	0	53	8	0.0021	−0.4419	531
	Medial frontal gyrus (R)	10	4	64	−8	0.0189	−0.4033	
4	Caudate (L)		−8	10	3	0.0090	−0.4170	282
	Subcallosal gyrus (L)	25	−2	13	−11	0.0110	−0.4134	
	Caudate (R)		6	12	1	0.0121	−0.4116	

BA: Brodmann area; (x, y, z), local maximum activity of cluster in Talairach coordinate system; *p*: significance level; *r*: Pearson correlation; Voxels: number of voxels within cluster; L: left; R, right

glucose uptake with age emerged bilaterally in the superior temporal gyrus (BA 38, $p < 0.001$ FWE-corrected, $r = -0.5880$ for the left and $r = -0.4998$ for the right), the medial frontal gyrus (BA 10, $p = 0.0021$ FWE-corrected, $r = -0.4419$ for the left; $p = 0.0189$ FWE-corrected, $r = -0.4033$ for the right) and the caudate ($p = 0.0090$ FWE-corrected, $r = -0.4170$ for the left; $p = 0.0121$ FWE-corrected, $r = -0.4116$ for the right) and in the left subcallosal gyrus (BA 25, $p = 0.0011$ FWE-corrected, $r = -0.4134$). Table 2 listed the detailed information for each cluster.

In Fig. 4, scatterplots of glucose metabolism in local maximum of each cluster versus age were fitted with quadratic polynomial method. As shown in Fig. 4a, b, the decline with aging in the left superior temporal gyrus was steeper than in the right superior temporal gyrus. For each of the four clusters, the curvature of curve increased with aging.

In the male group, significant age-related increasing in glucose metabolism was evident in the lentiform nucleus in the right sub-lobar ($p < 0.00001$ FWE-corrected, $r = 0.5378$) (Fig. 5, Table 3). The positive correlations were also found in the left thalamus, the left paracentral lobule (BA 5), the right middle frontal gyrus (BA 10) and the right precuneus (BA 7). Figure 6 showed scatterplots of glucose metabolism versus age in the brain area with positive correlation.

1.3 Discussion

Age related gyral narrowing and sulcal widening can cause artifacts in glucose metabolism. Some studies found that a decline glucose uptake with normal aging

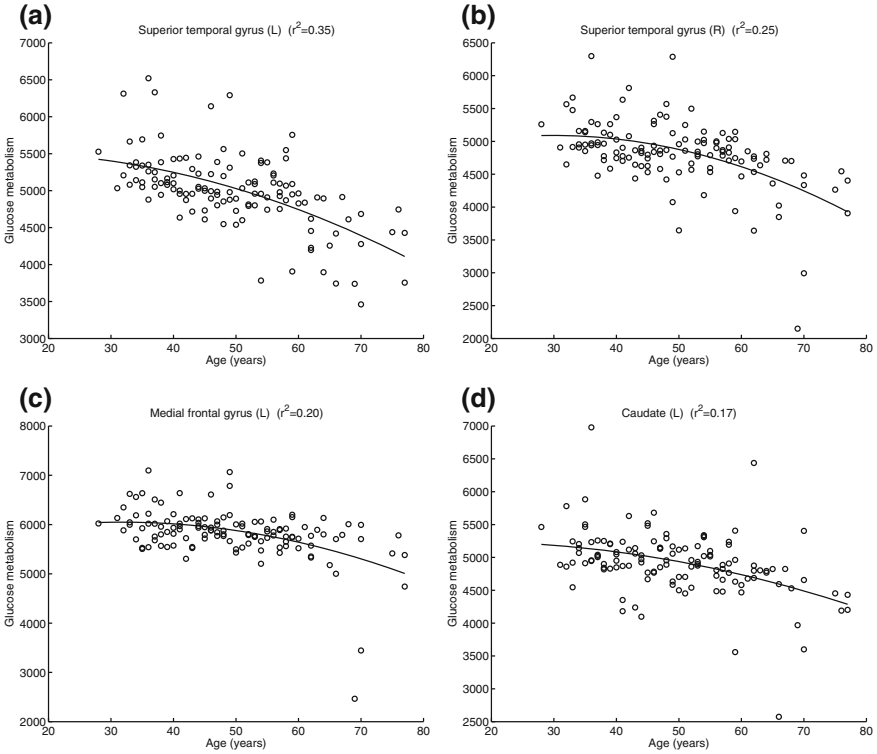

Fig. 4 Scatterplots of glucose metabolism in local maximum of each cluster versus age in the male group (negative correlation). A quadratic polynomial fitting is used to express the relationship between glucose uptake and age. **a** Left superior temporal gyrus, $r^2 = 0.35$; **b** Right superior temporal gyrus, $r^2 = 0.25$; **c** Left medial frontal gyrus, $r^2 = 0.20$; **d** Left caudate, $r^2 = 0.17$

becomes insignificant after taking the partial volume effects into account [27, 28]. However, the structure atrophy is not able to fully explain the age related declines in glucose metabolism. First, studies that investigated the cortical changes across the life span showed a prominent atrophy in the prefrontal cortex, while the cortical thinning in the temporal cortex was noted to a less extent [29, 30]. Furthermore, in the frontal cortex, the age effects on structural atrophy [29] showed a different pattern from the age effects on hypometabolism in our study (Figs. 2 and 4). With increasing age, gray matter intensity declines quickly before 40 years of age and then remains relatively stable [29], while in our study the glucose metabolism keep stable before age 40 and then acceleration decrease. This suggests that the results we reported at least partially reflect the declines in glucose metabolism.

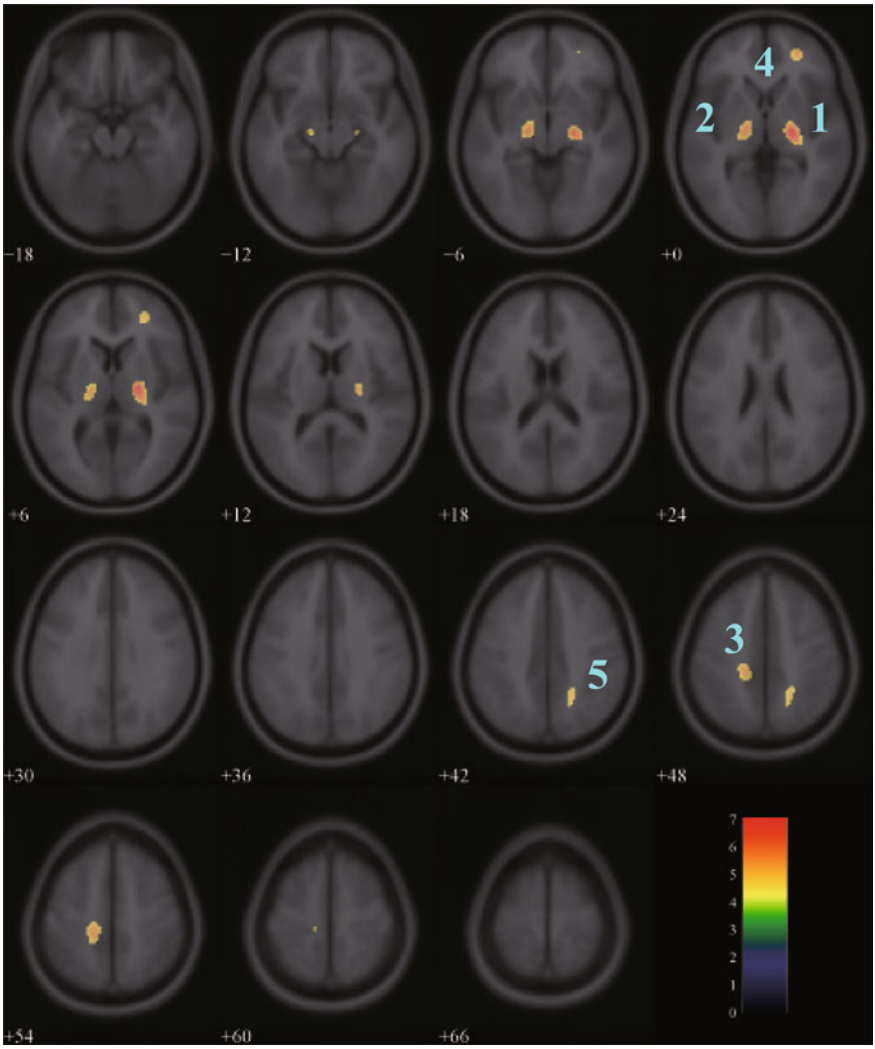

Fig. 5 Areas of positive correlation between glucose metabolism and age in the male group. The significant areas overlaid on a T1-weighted MRI image are displayed with a statistical threshold of $p < 0.05$ FWE-corrected and an extend threshold of 100 voxels. The number of slices correspond to the z values in Talairach coordinate system which defined form inferior to superior. Clusters 1–5 represent the right lentiform nucleus, the left thalamus, the left paracentral lobule, the right middle frontal gyrus and the right precuneus respectively. *Color scale* denotes t value

In our analysis of the resting-state PET images, the glucose metabolism in the frontal lobe declines with normal aging in both the female and the male groups. It is consistent with the results of prior studies which have also used a voxel-based analysis [6, 13, 15]. The frontal lobe plays a key role in reasoning, planning, language,

Table 3 Regions of glucose metabolism increase with normal aging in the male group

Cluster	Region name	BA	Talairach coordinates *x y z* (mm mm mm)			*p* FWE-corr	*r*	Voxels
1	Lentiform nucleus (R)		22	−15	3	<0.00001	0.5378	460
2	Thalamus (L)		−16	−14	−1	<0.001	0.4802	289
3	Paracentral lobule (L)	5	−16	−29	47	<0.001	0.4738	222
4	Middle frontal gyrus (R)	10	28	47	−2	<0.001	0.4594	131
5	Precuneus (R)	7	20	−46	43	0.0055	0.4257	110

BA: Brodmann area; (x, y, z), local maximum activity of cluster in Talairach coordinate system; *p*: significance level; *r*: Pearson correlation; Voxels: number of voxels within cluster; L: left; R, right

attention, emotions and movement [6, 31, 32]. The decline of glucose metabolism with normal aging in the frontal lobe may explain why the mental efficiency reduces in the elderly.

The decline of glucose metabolism in the superior temporal gyrus with aging is significant in both sexes. Willis et al. [15] reported a similar correlation in cerebral glucose uptake with aging. Comparing the Fig. 2c with Fig. 4c, d, we find the decline trend of glucose metabolism in the male group is faster than in the female group in the temporal lobe. In prior MRI studies, Murphy et al. [17] and Gur et al. [33] reported that the age-related brain atrophy in men is greater than in women, which may explain the result obtained in our statistical analysis. Another interpretation for this sex-related variance is that men tend to be more prone to age-related cognitive decline than women. However, more experiments are needed to further clarify this conclusion.

Another observed phenomenon from this study is the asymmetry of the metabolism decline in frontal and temporal lobes, which is predominant in the male group. As described in Figs. 1 and 3, the metabolism decline with normal aging in the left cerebrum shows greater significance and larger range compared with the right cerebrum. This result may provide additional evidences to support the model of HAROLD (hemispheric asymmetry reduction in older adults) [34, 35]. HAROLD model states that younger adults show a prominent lateralization of cerebral function in the frontal lobe, but the activity during cognitive performance trends to be more bilateral in older adults, which also happens in the temporal and parietal lobes [36]. According to the research by Reuter-Lorenz et al. [37], the elders who displayed a bilateral pattern of activity had a better performance in the verbal working memory task.

A negative correlation between glucose metabolism and age in the caudate is observed in the male group with a less significance relatively. It has been reported by Kawachi et al. [38] in females, however, not in males. The caudate nucleus is a small structure that is located in the subcortical region of the brain. A moderate age-related atrophy of the caudate was studied by [24] using MRI images. The decrease

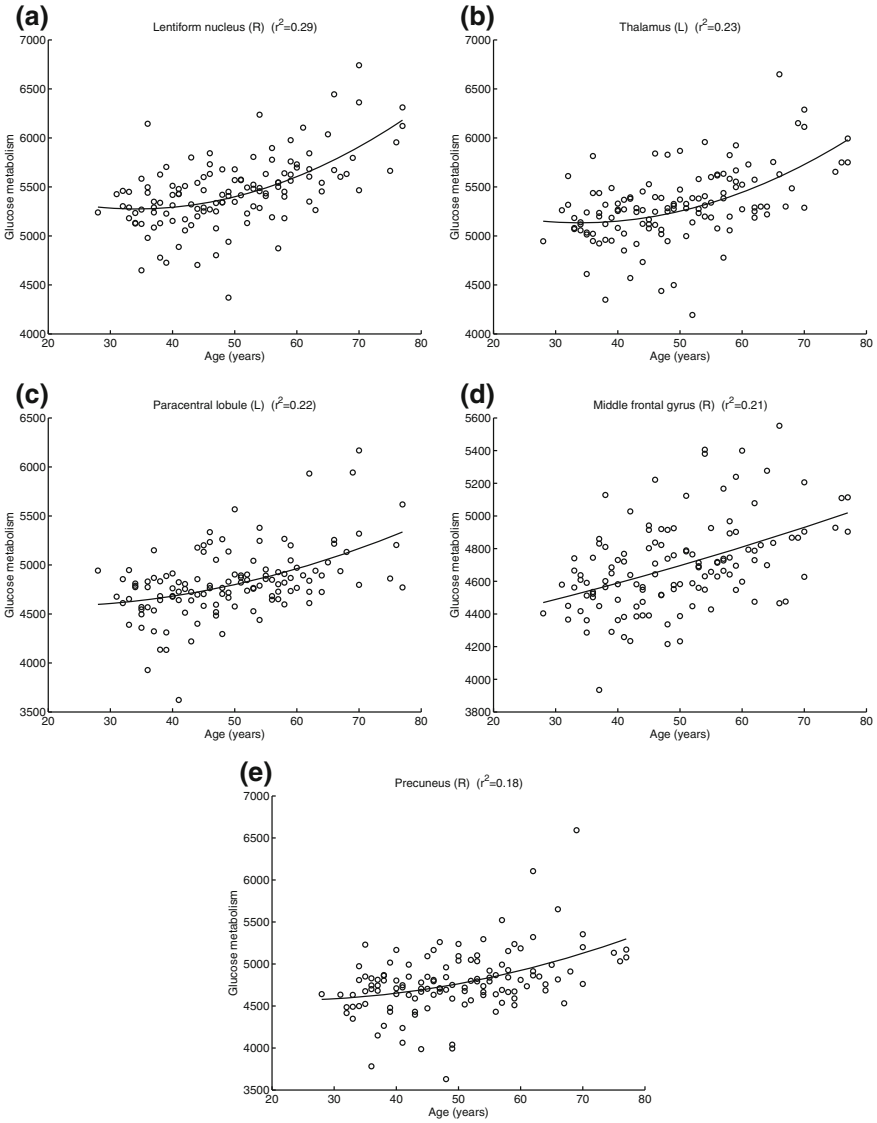

Fig. 6 Scatterplots of glucose metabolism in local maximum of each cluster versus age in the male group (positive correlation). A quadratic polynomial fitting is used to express the relationship between glucose uptake and age. **a** Right lentiform nucleus, $r^2 = 0.29$; **b** Left thalamus, $r^2 = 0.23$; **c** Left paracentral lobule, $r^2 = 0.22$; **d** Right middle frontal gyrus, $r^2 = 0.21$; **e** Right precuneus, $r^2 = 0.18$

of glucose metabolism with age in the caudate will be resulted by partial volume effects of PET due to the limited spatial resolution.

In the male group, the regions of the lentiform nucleus, thalamus, paracentral lobule, middle frontal gyrus and precuneus show the positive correlation between glucose uptake and age from our studies. The phenomenon can be explained for an increase in activity in these regions to compensate for the other regions of neuron dysfunction or loss. Scarmeas et al. [39] suggested that the age-related increase of metabolism in some regions may be interpreted to compensate for the regions of metabolism decline to cope with the decrease of brain function in a memory condition. The functional preserve is the ability as well as in the resting state. The other interpretation for this aging effect is the different patterns of task performance between the youth and the elderly [31]. As described in the results section, we didn't found regions with positive correlation in the female group. In this study, a statistical threshold of $p < 0.05$ FWE-corrected and an extend threshold of 100 voxels were used for image display and region estimate. When we relax any of these conditions of use, regions with positive correlation appears in the female group. This indicates that both sexes have similar patterns of age-related glucose metabolism but different significance level.

Several limitations of this study should be illustrated. First, as described above, the partial volume effect ignored in this study is a confounding effect in analysis of age-related changes in the metabolism. Another issue is that estrogen use may influence cerebral glucose metabolism in adults [40]. Rasgon et al. found that estrogen use may protect cerebral metabolic from decline in postmenopausal women. We do not exclude the women with estrogen use in this study, which should be considered in the analysis of our results in the female. Further analysis of handedness effects on brain symmetry of glucose metabolism decline are needed to determine whether this is a factor. In addition, since all of the data derived from clinical database, we were unable to take cognitive performance test such as MMSE for each subject at this stage. It will be considered in the future work.

2 Functional PET Brain Network with Normal Aging

Function decline and organs aging is an inevitable physiological law of life. As one of the most important organs, aging brain tends to produce some specific alterations in morphological, physiological pathology and functional aspects. It is well known that normal aging is associated with a progressive decline in cognitive performance, including perception, attention, language and memory [3, 4, 41, 42]. Meanwhile, normal senescence is also highly related to some specific encephalopathies, such as Alzheimer's disease (AD) [43] and Parkinson's disease (PD) [44]. Therefore, aiming to assess the declining cognitive ability and supply a guiding for age-related encephalopathy in clinical, it is necessary to deeply understand the age-related changes in healthy brain.

An emerging approach for studying human brain system is graph theory which is represented by a set of nodes and links. It has been widely adopted to quantify complex system, e.g., in social sciences, biology or technology [45, 46]. The functional and structural systems of the human brain reveal age-related topological properties of complex networks, such as small-world characteristics, highly connected hubs, modularity, and network robustness [45–49]. Small-world properties, characterized by a high degree of clustering and a short average distance between any two nodes [50, 51], were analysed to reveal age-related global and local efficiency of information transfer in brain system. Some recent studies reported that, along with the normal aging, small-world network showed changed topological efficiency [48, 52–54]. For instance, a recent study on functional brain networks suggested that an older age group showed significantly reduced cost efficiency in comparison to a younger group [55]. A similar degeneration process of economical small-world networks was also found in a previous study about AD [56, 57]. Furthermore, changes in modular organization of human brain networks were proven to be associated with normal aging [47, 53]. Simultaneously, highly connected hubs are altered with normal aging, which has been reported in some previous studies [45, 47]. In addition, previous studies also found that normal aging processes significantly affect default mode network (DMN) [58–61], which is typically deactivated during external stimulation [62, 63]. Thus, a gradually forming evaluated system of brain networks with neural imaging technologies was adopted in assessing the aging brain and provided a guiding for age-related encephalopathy in clinical [45, 46].

However, up to now, few studies have constructed functional network via positron emission tomography (PET) data. Compared with other functional signals, PET can offer a more immediate way to indicate brain activity by offering the index of cerebral glucose metabolism. Here, for evaluating the age-related brain changes in normal individuals, the large-scale human brain functional network was constructed by node, defined as regional average cerebral glucose metabolism from PET data. Four main reasons indicate that the definition is reasonable and effective for assessing age-related brain functional changes. Firstly, during the resting state, the level of cerebral glucose metabolism is considered as a reliable index of neural activity [64]. Secondly, synapses are considered as the key sites for transferring information between neurons, and up to 75 % of the glucose consumption in the brain is used to maintain a baseline synaptic activity [11]. Thirdly, many studies have reported that the normal aging is accomplished by a decline of synaptic activity, which impacts the cognitive functions [6, 8]. Lastly, effective connectivity between PET regions has been found in previous studies [65, 66]. Thus, the definition of PET nodes can provide a complementary and convincible way to improve the evaluation of brain functional networks.

In the present study, large-scale functional networks (90 regions) in two age groups (110 older subjects, 113 younger subjects) were constructed by computing the partial correlation matrices of the regional mean intensity values from PET data. Afterwards, we investigated the brain functional topological properties, including small-world characteristics, hub regions and network robustness, revealing the brain functional changes associated with normal aging. Methodological robustness in the construction of PET network was also assessed.

2.1 Materials and Methods

2.1.1 Subjects

Two hundred and twenty-three healthy human subjects were selected from a physical examination database, and written informed consents for the future research were obtained from all subjects. They were separated into two age groups, 110 older subjects aged 51–65 years (mean age = 56.3 years, 73 male) and 113 younger subjects aged 26–40 years (mean age = 36.5 years, 73 male). Health status of all subjects were evaluated with a normal physical examination before imaging. Individuals with significant chronic or acute disease were excluded from subjects. Other criteria of subjects physical condition were as follows: native Mandarin Chinese speaker, right-handed, same average education years, no history of neurological disease, no brain trauma or clinical evidence of cognitive impairment.

2.1.2 PET Data Acquisition

All PET investigations were implemented with Hamamatsu SHR 22000 whole-body PET scanner system located at the Medical PET Center of Zhejiang University. The spatial resolution of the scanner is 3.5 mm full width at half maximum (FWHM) in sagittal or coronal plane and 3.2 mm FWHM in axial plane. There is a 600 mm patient aperture and an axial field-of-view of 225 mm in the scanner, which can deal with the whole head. A ^{68}Ge source for attenuation correction was used in the emission scan after a 10 min transmission scanning. All subjects were injected intravenously with 333–444 MBq (9–12 mCi) fluorodeoxyglucose (FDG) before resting in a dark, quiet room with ears open and eye closed for 50 min. Then each subject was scanned lying quietly at rest with eyes closed for 8 min. Nyquist frequency was acquired, after a ramp filter with the maximum-likelihood expectation maximization (MLEM) algorithm was used in reconstructions of PET images. Additionally, the acquisitions were performed with the approval of the Health Science Research Ethics Committee of Zhejiang University.

2.1.3 PET Data Preprocessing and Regional Parcellation

After using ImageJ (Wayne Rasband, National Institute of Mental Health, USA) and MRIcro software (http://www.mricro.com), Analyze Formats were acquired from raw PET data. Then the preprocessing was performed using matlab 6.5 (MathWorks Inc., Notich, MA, USA) and Statistical Parametric Mapping (SPM5, Wellcome Department of Cognitive Neurology, London, UK) software. Each data was normalized into the Montreal Neurological Institute (MNI, McGill University, Montreal, Canada) standard template using SPM5. An isotropic Gaussian kernel with 8 mm FWHM was used in spatial smoothing to increase the signal-to-noise ratio after

normalization. Then the proportional scaling was used for the intensity normalization [67–69]. Regional parcellation was completed using the anatomically automatic labeled (AAL) template image previously validated by Tzourio-Mazoyer et al. [70]. The brain was divided into 90 anatomical regions of interest (45 regions for each hemisphere) using this parcellation. Then we calculated mean intensity values of each region which represented the regional cerebral metabolic rates for glucose.

2.1.4 Partial Correlation Analysis

The functional connection was defined as statistical associations in the intensity values across subjects. Such a connection concept has been introduced by the previous studies [71, 72]. It is reasonable to investigate brain functional systems (networks) by calculating connectivity of the PET regions, since effective connectivity between PET regions has been found previously [65, 66]. So, the analytical procedure was performed by analysing the regional relation obtained above. The interregional correlation matrix $P_{ij}(i, j = 1, 2, \ldots, n$, here $n = 90)$ of each group (Fig. 7) was acquired by calculating the partial correlation coefficients across individuals between the mean intensity value of every pair of regions. The conditional dependences of arbitrary two regions partialled out the effects of the other 88 regions defined in the AAL template were represented by the partial correlations between them.

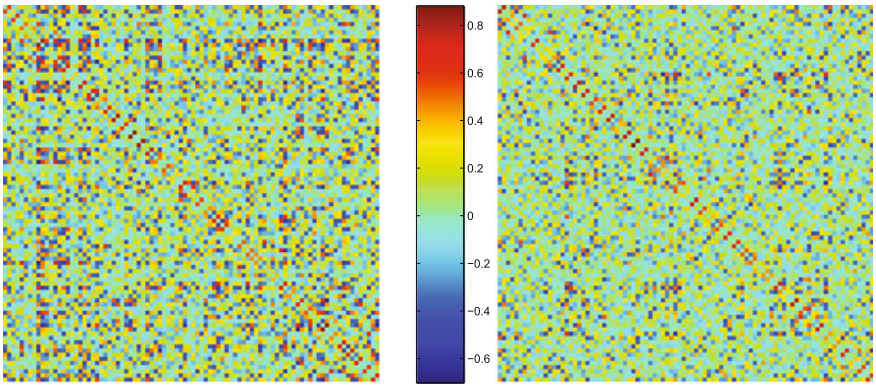

Fig. 7 The correlation matrices of two groups. The graphs show the correlation matrices acquired by calculating partial correlations (*left* for the older group and *right* for the younger group). The color bar in the *middle* indicates the partial correlation coefficient between regions. The rank and row successively represent the 90 brain regions (see Table 8 (Appendix))

Fig. 8 The binarized matrices ($S = 16\,\%$) of two groups. The graphs show the binarized matrices (*left* for the older group and *right* for the younger group) which are generated by setting threshold to the correlation matrices. The rank and row successively represent the 90 brain regions (see Table 8 (Appendix)). Such a threshold ($S = 16\,\%$) ensures that the networks of both of the groups have the same number of nodes and links, and also show changed efficiency of information transfer (C_p, L_p, E_{global}). In this graph, *white* and *black* indicate the 1 and 0

2.1.5 Construction of Functional Network

According to the prior studies [45, 67], functional networks of both groups could be acquired from their partial correlation matrices. The partial correlation matrix of each group was converted into a binarized matrix $B_{ij}[\,b_{ij}\,]$ (Fig. 8) by setting a threshold. Element of B_{ij} was 0 if the absolute value of the correlation between regions i and j was smaller than given correlation threshold and 1 otherwise. Topological organization of the human functional networks was represented by the binary matrices. Then a binary graph theoretical analysis [45, 46] was performed in the following.

2.1.6 Graph Theoretical Analysis

Sparsity selection. To perform a graph theoretical analysis, the binarized matrix B_{ij} is described as a network (graph) G defined by n nodes and k edges, where nodes indicate regions and edges indicate undirected links between regions according to nonzero elements of B_{ij}. A fixed sparsity S of each network, which was defined as the total number of edges k in a graph divided by the maximum possible number of edges, would be calculated after its correlation matrix was thresholded into the binarized matrix. It was stated briefly that same correlation threshold would lead to different number of edges (k, or S) between the both resulting graphs because of the difference in the low-level correlations (see Fig. 7). Therefore, alterations in the topological organization would not be solely reflected by the between-group difference in network parameters. Hence, a sparsity-specific threshold was set to ensure that the both undirected graphs had the same number of edges (k) or wiring cost

[55, 56]. Because a single and definitive threshold could not be selected currently, graphs with wide range of sparsity ($10\,\% < S < 50\,\%$) was generated by repeatedly thresholding each correlation matrix, then properties of them were estimated at each threshold value. Then small-world parameters between the two groups were compared as a function of independent sparsity of the precise selection of threshold. The range of sparsity ($10\,\% < S$) also ensured that every nodal pairs in both graphs had a connecting path (mentioned below) [73]. Then we estimated network properties including clustering coefficient, path length, global efficiency, nodal centrality and network robustness in the following steps.

Clustering coefficient. A cluster of node i is formed by directly connected nearest neighbours of the node [45]. Clustering coefficient C_i of a node i quantifies the number of connections existing in the cluster as a proportion of maximum possible connections [50]. C_p (Fig. 9) of a network is defined as the average of C_i over all nodes in a network and indicates the extent of local cliquishness or local efficiency of information transfer [50, 51].

Path length and global efficiency. Path length L_{ij} between node i and node j is defined as the minimum number of edges traversed from node i to node j. L_p (Fig. 10) is defined as the average L_{ij} of the all pairs nodes of the network and quantifies the ability of global efficiency of parallel information transfer [51]. Global efficiency (E_{global}, Fig. 11) inversely related to L_p but numerically easier to indicate the global efficiency of parallel information transfer was also estimated. E_{global} measure is $E_{global} = \frac{1}{n(n-1)} \sum_{i \neq j \notin G} \frac{1}{L_{ij}}$, L_{ij} means the path length of the node i and node j. Of

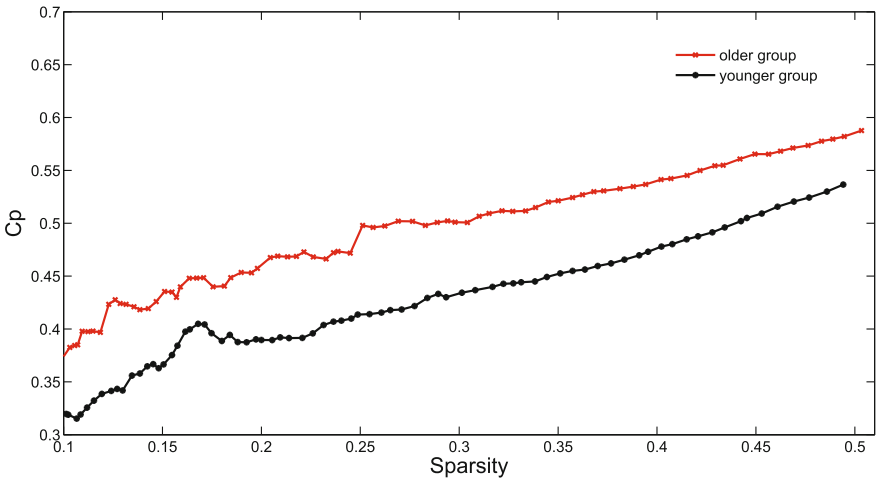

Fig. 9 Clustering coefficient (C_p) as a function of sparsity. The graph shows that, at a wide range of sparsity ($10\,\% < S < 50\,\%$), the older subjects (*red line*) have larger C_p value than the younger subjects (*black line*)

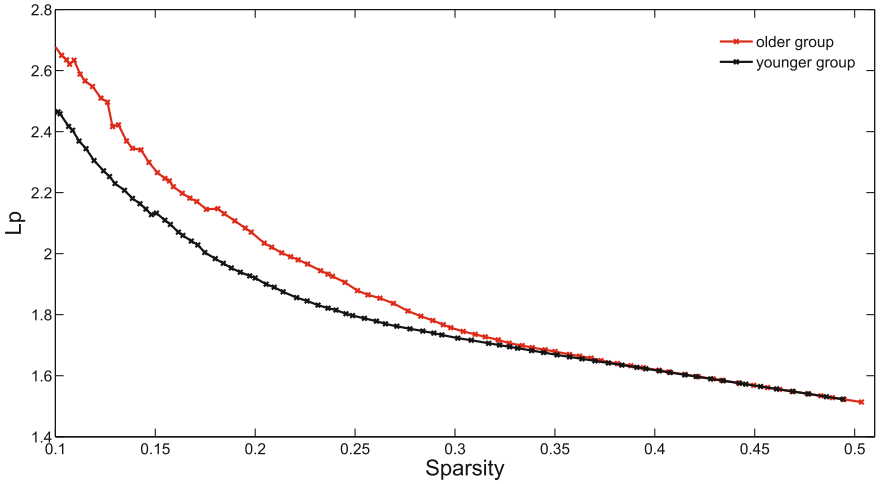

Fig. 10 Path length (L_p) as a function of sparsity. The graph shows that two groups have same L_p value when sparsity ranges from 33 to 50 % and the older group (*red line*) have larger L_p at $10\,\% < S < 33\,\%$

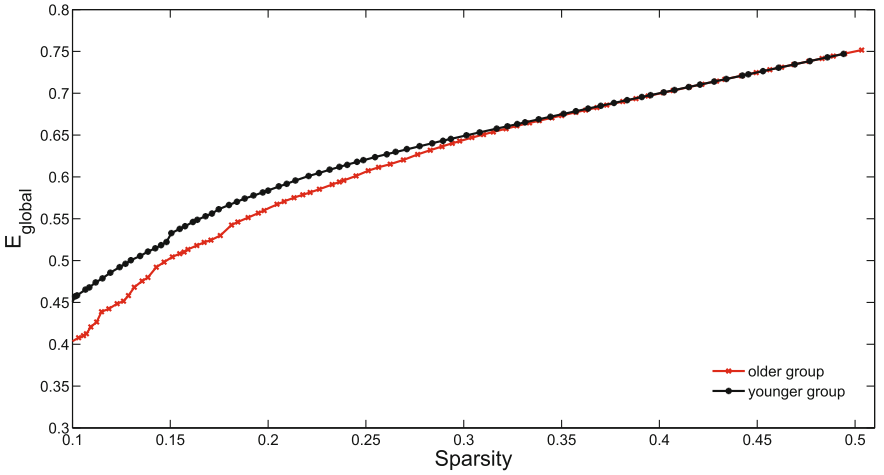

Fig. 11 Global efficiency (E_{global}) as a function of sparsity. E_{global} is numerically easier to indicate the global efficiency than L_p (see Materials and Methods). As the sparsity thresholds increase from 10 % to 33 %, E_{global} of both groups increase, and younger subjects (*black line*) have larger E_{global} values. At high sparsity threshold ($33\,\% < S < 50\,\%$), two groups show equal E_{global} values

note, the problem about the definition of L_p caused by nodal pairs without connecting path, can been eliminated by the range of sparsity ($10\,\% < S$, mentioned above).

Small-world analysis. In this study, small-world properties of networks in two groups were examined according to the C_p and L_p measured in the above steps.

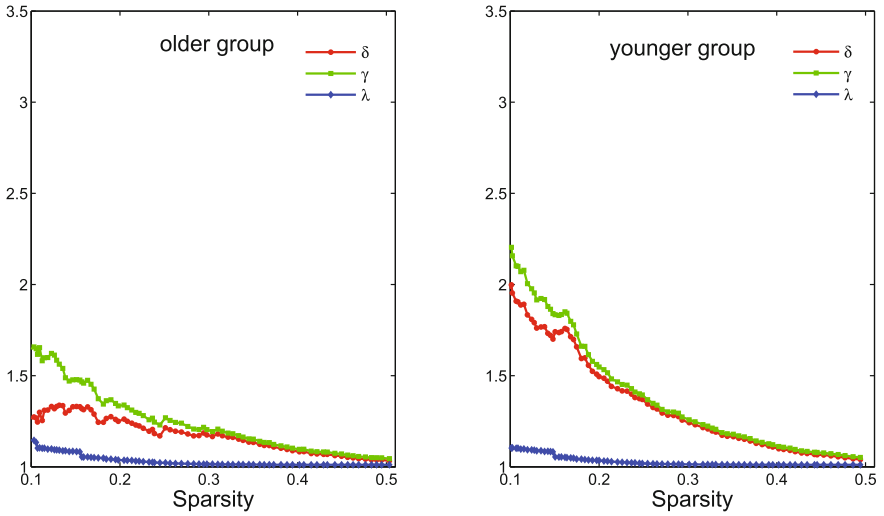

Fig. 12 Small-world parameters of networks. The graphs show the changes in δ (*red line*), γ (*green line*) and λ (*blue line*) in the networks of older (*left panel*) and younger (*right panel*) groups as a function of sparsity thresholds. At a wide range of sparsity, both networks have $\delta > 1$, that implies prominent small-world properties (see Materials and Methods). Note that, as the values of sparsity thresholds increase, the δ and γ values decrease rapidly, but the λ values decrease rapidly when sparsity range from 10 to 30 % then change slightly

A small-world network should meet the following criteria: $\lambda = L_p^{real}/L_p^{rand} \approx 1$ and $\lambda = C_p^{real}/C_p^{rand} > 1$ [50], or $\sigma = \gamma/\lambda$ [74, 75] (see Fig. 12), where the L_p^{rand} and C_p^{rand} are the mean path length and clustering coefficient of 1000 suitable random networks with the same number of nodes, edges, and degree (the degree k_i of a node i is the number of connections to that node) as the real network [50, 76]. Random graphs were generated by the random rewiring procedure [77, 78].

Betweeness centrality. The centrality (B_i) of node i is defined as the number of the shortest paths between all other node pairs pass through it [79]. A node with high value Bi is crucial to efficient communication in the network and is considered as the hub of the network [45]. Here B_i was calculated by using the MatlabBGL package (http://www.stanford.edu/~dgleich/programs/matlab_bgl/). Then normalized betweenness ($b_i = B_i/B$, see Fig. 13) was measured to estimate nodal characteristics of the networks, where B was the average B_i over all nodes in the network.

Network robustness. In this step, a simple analysis about network robustness was performed. Network robustness associated with the stability of a complex network refers to the degree of tolerance against random failures and targeted attacks [45]. In the current studies, robustness (tolerance) of the networks was investigated through removing nodes in the networks [75, 80, 81]. Firstly, to test the the nodal failure tolerance, one node was removed from the networks and changes in the size of the largest connected component were measured. Then other nodes were removed

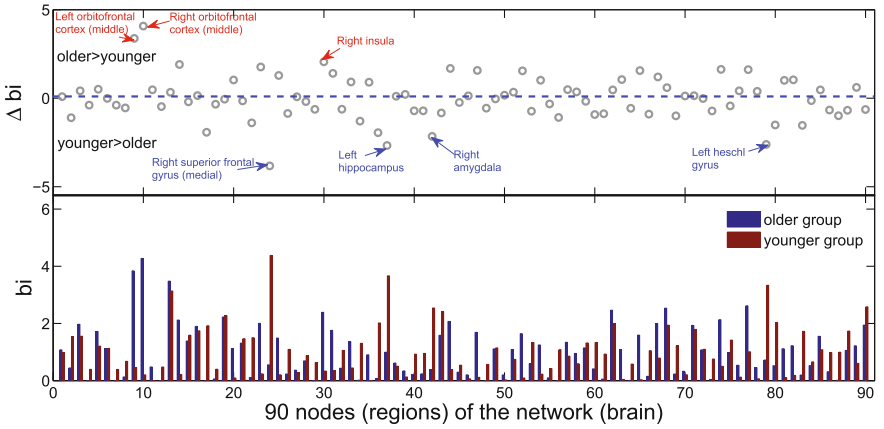

Fig. 13 Betweenness centrality (b_i) of two groups. The below graph shows the comparison (*red bar* for younger group and *blue bar* for older group) of normalized betweenness (b_i) in each node (region) between two groups. The *upper* graph shows the regional changes (Δb_i, $\Delta b_i = b_{iolder} - b_{iyounger}$) in normalized betweenness (b_i) between two groups. The regions labeled in the *upper* graph indicate significant changes in b_i between two groups (see Table 7). Note that these results were obtained from the brain networks with a sparsity of 16 %. Regions in networks of two groups showing high b_i value ($b_i > 2.0$) have been listed in the Tables 5 and 6

sequentially at random (Fig. 14). To address the attack tolerance, the above processes were repeated but we removed the nodes of high bi value in the targeted position (20 nodes of high bi value were removed from $NO.21$ to $NO.40$ in abscissa axis, showed in Fig. 14). To investigate the comparison of the network robustness between two groups, the procedures were repeated 1000 times for the networks of both groups. Then we calculated the mean relative of largest component (Fig. 14). Additionally, in order to investigate statistical differences, the 95 percentile points of each distribution were used as the critical values for a two-tailed test of the null hypothesis with a probability of type I error of 0.05, with every number of the removed nodes under two attacks.

2.1.7 Statistical Analysis

Correlation differences in statistical analysis. It is necessary to validate the significance difference of these correlations in two groups with statistical analysis of correlations between 4005 pairs of regions. The Z values approximately normally distributed were generated from correlation coefficients, after Fishers r-to-z transform. Then the transformed z values were compared by $A - Z$ statistic to determine the significance of the between-group differences in correlations [82]. A false discovery rate (FDR) procedure [64] was performed to adjust to the the multiple comparisons at a q value of 0.05.

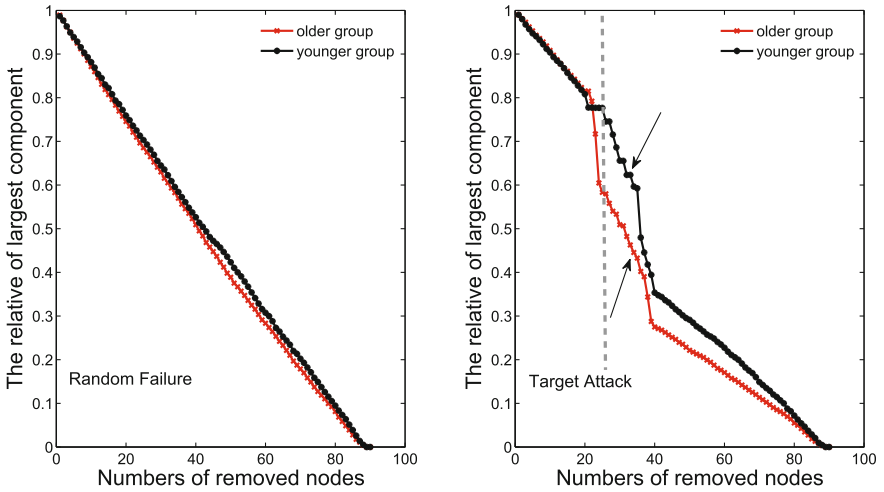

Fig. 14 Topological robustness in networks of two groups. The graphs show the relative size of the largest connected component as a function of the fraction of removed nodes by random failures or targeted attacks. As the response to random failures (*left panel*), the brain network in the older group (*red line*) is approximately as robust as that in the younger group (*black line*). *Right graph* shows that the older network displays remarkably reduced stability against targeted attack compared with the younger. Additionally, the statistical significant differences ($p < 0.05$) of two groups was found with the ranges of $23 < NO._{node} < 35$ and $40 < NO._{node} < 45$ in the *right graph*

Statistical differences in topological parameters. A nonparametric permutation test method was applied to determine statistical significance of the between-group differences. First of all, C_p, L_p, E_{gobal} and b_i of the two-groups networks with a given sparsity were separately computed. Secondly, to test the null hypothesis that the group differences might occur by chance, we then randomly reallocated each individual set of regional cerebral glucose metabolism to one or the other of the two groups. Thirdly, after recomputing the correlation matrix and obtaining binarized matrix, we recalculated the network parameters for each randomized group, using the same method. Lastly, this randomization procedure was repeated 1000 times and the 95 percentile points of each distribution were used as the critical values for a one-tailed test of the null hypothesis with a probability of type I error of 0.05. Then the procedure was repeated at every sparsity threshold value of the networks.

2.1.8 Methodological Robustness Analysis

It is necessary to test the methodological robustness in the construction of networks, because the PET networks are barely constructed by calculating the partial correlation matrices. In this study, the methodological robustness was estimated by reducing sample size in each group. Firstly, 5 individuals were separately removed from the both groups at random, to test methodological robustness against the reductions of

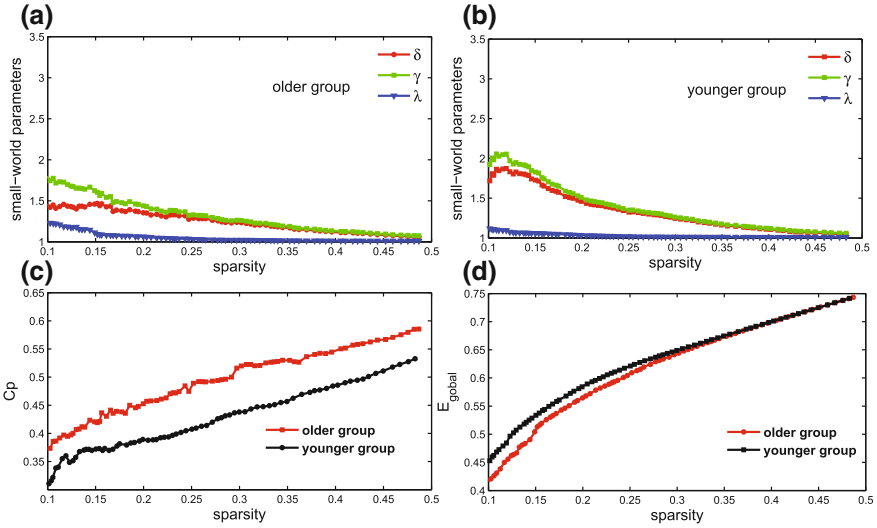

Fig. 15 Small-world properties in smaller-sample networks. **a** and **b**, The graphs show the small-world parameters (δ, γ and λ) of smaller-sample networks in older (**a**) and younger (**b**) groups. At a wide range of sparsity, both networks have $\delta > 1$, that implies prominent small-world properties (see Materials and Methods). **c** This graph shows that older subjects (*red line*) have larger C_p values than the younger subjects (*black line*). In the original networks, similar result of C_p was also shown in Fig. 9. **d** This graph shows the global efficiency (E_{global}) as a function of sparsity. As the sparsity thresholds increase from 5 to 30 %, E_{global} of both groups increase and younger subjects (*black line*) have larger E_{global} values

samples size in both groups. It is noted that quantities (5 nodes) of the removal individuals are limited by the size of the whole sample. After the above step was repeated 50 times, the mean smaller-sample networks (105 in older group and 108 in younger group) were obtained. As a comparison to the former networks, the small-world parameters (λ,γ and δ, see Fig. 15a, b), global efficiency (Fig. 15d) and local efficiency (Fig. 15c) in smaller-sample networks were calculated via the above methods. Furthermore, in order to determine statistical significance of the neo-networks differences, the nonparametric permutation test method was applied on $C_{[}p]$ and E_{gobal}. Methodological robustness was analysed by comparing the small-world properties between networks with different samples.

2.2 Results

2.2.1 Correlations of Regions in Two Groups

As is shown in Fig. 7, the interregional correlation matrices represent complex correlation patterns of both age groups. Statistical analysis further demonstrates

significant between-group correlation differences ($p < 0.05$, FDR-corrected) in various pairs of regions (Table 4). For instance, older subjects are found to show increased positive correlations in various pairs of cortical regions involved in the frontal, precentral and postcentral. In addition, decreased positive correlations in older group are observed in pairs of regions including hippocampus, amygdala. We also note several changed negative correlations in the older group. All pairs of regions with significant between-group changed correlation coefficients are listed in Table 4.

2.2.2 Small-World Topology Functional Networks

It has been demonstrated in the previous studies [67, 76, 83] that functional network of humans has small-world characteristics. In a small-world network, the nodes of the network have larger local interconnectivity than a random network, but the shortest path length between any pair of nodes is approximately equivalent to a comparable random network [50]. The small-world attributes of the functional networks in two age groups were also examined in the current study. As expected, both functional networks demonstrate small-world characteristics (Fig. 12, left for older group and right for younger group, $\delta > 1$ red line) over a wide range of sparsity ($10\,\% < S < 50\,\%$). Compared with the matched random networks, they have larger local cliquishness ($\gamma > 1$, green line) but an almost identical path length ($\lambda \approx 1$, blue line). Using computational modeling simulation approaches, Sporns et al. [84] propose the emergence of small-world topology when networks are evolved for high complexity of dynamic behavior defined as an optimal balance between global integration and local specialization. Therefore, our findings additionally support hypothesis that human brain has evolved into a complex but efficient neural architecture to maximize the power of information processing [76, 85].

2.2.3 Different Small-World Parameters Between Two Age Groups

As shown in Fig. 9, clustering coefficient (C_p) in networks of older group (red line in Fig. 9) are larger than those of younger group (black line in Fig. 9) over a wide range of sparsity ($10\,\% < S < 50\,\%$). Global efficiency (Fig. 11) in networks of younger group (red line in Fig. 11) are larger than those of older group (black line in Fig. 11), when sparsity ranged from 10 % to 33 %. Both groups show different small-world parameters, reduced global efficiency (E_{global}, Figs. 10 and 11) and increased local cliquishness (Fig. 9) in older group. Additional statistical analysis also reveals significant differences ($p < 0.05$) in the Cp values at $10\,\% < S < 50\,\%$, Lp values at $11\,\% < S < 25\,\%$ and E_{global} at $11\,\% < S < 25\,\%$. These results imply that older subjects are probably related to the loss of small-world characteristics in the large-scale functional brain systems. In addition, approximate results were obtained in previous studies about normal aging and even AD [54, 56, 57, 67].

Table 4 Comparisons of correlation between two groups

Regions		Correlation, r, (Z)	
		Young	Old
Increased positive correlation in older group			
Left orbitofrontal cortex (middle)	Left supplementary motor area	−0.15(−0.15)	**0.66(0.79)**
Left orbitofrontal cortex (superior)	Right inferior parietal lobule	−0.08(−0.08)	**0.72(0.91)**
Left orbitofrontal cortex (middle)	Right orbitofrontal cortex (inferior)	0.03(0.03)	**0.57(0.65)**
Left orbitofrontal cortex (middle)	Left orbitofrontal cortex (superior)	0.04(0.04)	**0.56(0.63)**
Left orbitofrontal cortex (middle)	Left olfactory	0.03(0.03)	**0.57(0.65)**
Left precental gyrus	Left supplementary motor area	0.02(0.02)	**0.62(0.73)**
Right precental gyrus	Right supplementary motor area	0.13(0.13)	**0.65(0.78)**
Left inferior frontal gyrus (opercular)	Right supplementary motor area	0.01(0.01)	**0.53(0.59)**
Right orbitofrontal cortex (middle)	Left superior frontal gyrus (medial)	0.12(0.12)	**0.64(0.76)**
Left olfactory	Left superior frontal gyrus (medial)	0.04(0.04)	**0.60(0.69)**
Left inferior frontal gyrus (triangular)	Right inferior parietal lobule	0.09(0.09)	**0.64(0.76)**
left postcentral gyrus	Left supramarginal gyrus	0.10(0.10)	**0.61(0.71)**
Decreased positive correlation in older group			
Left hippocampus	Left amygdala	**0.72(0.91)**	−0.13(−0.13)
Left superior frontal gyrus (dorsal)	Left middle frontal gyrus	**0.62(0.73)**	−0.23(−0.23)
Right rolandic operculum	Right precuneus	**0.58(0.66)**	0.06(0.06)
Increased negative correlation in older group			
Right orbitofrontal cortex (inferior)	Left supplementary motor area	0.01(0.01)	**−0.65(−0.78)**
Right inferior frontal gyrus (triangular)	Left superior frontal gyrus (medial)	0.11(0.11)	**−0.64(−0.76)**
Left orbitofrontal cortex (middle)	Left posterior cingulate gyrus	−0.03(−0.03)	**−0.62(−0.73)**
Left orbitofrontal cortex (middle)	Right inferior parietal lobule	−0.14(−0.14)	**−0.66(−0.79)**
Left orbitofrontal cortex (middle)	Left middle occipital gyrus	−0.01(−0.01)	**−0.53(−0.59)**
Left orbitofrontal cortex (middle)	Right putamen	−0.04(−0.04)	**−0.57(−0.65)**

(continued)

Table 4 (continued)

Regions		Correlation, r, (Z)	
		Young	Old
Right middle occipital gyrus	Right precuneus	−0.08(−0.08)	**−0.59(−0.68)**
Left thalamus	Right orbitofrontal cortex (middle)	−0.08(−0.08)	**−0.61(−0.71)**
Left thalamus	Left olfactory	−0.03(−0.03)	**−0.60(−0.69)**
Left thalamus	Right calcarine cortex	−0.01(−0.01)	**−0.58(−0.66)**
Right paracentral lobule	Right superior temporal gyrus	0.01(0.01)	**−0.56(−0.63)**
Right hippocampus	Left temporal pole (superior)	0.04(0.04)	**−0.61(−0.71)**
Left caudate	Right middle temporal gyrus	0.03(0.03)	**−0.56(−0.63)**
Right precuneus	Right Temporal pole (middle)	0.01(0.01)	**−0.56(−0.63)**
Decreased negative correlation in older group			
Left rolandic operculum	Right calcarine cortex	**−0.55(−0.62)**	−0.01(−0.01)
Left rolandic operculum	Right precuneus	**−0.61(−0.71)**	−0.09(−0.09)
Left paracentral lobule	Left heschl gyrus	**−0.54(−0.60)**	0.01(0.01)

This table lists pairs of regions with significant changed coefficients (change is larger than 0.5) between two groups. Coefficients in bold represent significant interregional association within group. The comparison of coefficients between two groups are also shown in Fig. 7. To determine the significance of between-group differences in correlation, a Z statistic was used in this study (see Materials and Methods). All Z value are significant ($p < 0.05$, FDR-corrected)

2.2.4 Hub Regions

The functional networks were constructed at a sparsity threshold of 16 % to investigate the nodal characteristics of each region in two age groups. After normalized betweenness centrality (b_i) of each region (Fig. 13) in both networks was measured (see Materials and Methods), hubs were defined as the regions with high betweenness centrality ($b_i > 2$, mean + sd). In the older group, 12 regions (Table 5) are identified as the hubs because of large values in b_i. In another group, 10 regions are identified as the hubs (Table 6). Our finding of some hub regions (including supplementary motor area, left hippocampus,) is consistent with a previous brain functional network study age-related changes [47].

2.2.5 Changed Regional Nodal Characteristics Between Two Groups

The regions (Fig. 14) with between-group changes in betweenness centrality are examined in this study. Compared with the younger subjects, the older show increased betweenness centrality ($\Delta b_i > 2$) in 3 regions (ORBmid.L, ORBmid.R, INS.R, listed

Table 5 Regions showing high betweenness ($b_i > 2$) in the network of older group

Regions	Abbreviations	Class	b_i	Degree, k_i
Left orbitofrontal cortex (middle)	ORBmid.L	paralimbic	3.84	41
Right orbitofrontal cortex (middle)	ORBmid.R	paralimbic	4.27	37
Left inferior frontal gyrus (triangular)	IFGtriang.L	association	3.48	29
Right inferior frontal gyrus (triangular)	IFGtriang.R	association	2.11	24
Left supplementary motor area	SMA.L	association	2.23	30
Left superior frontal gyrus (medial)	SFGmed.L	association	2.00	23
Right insula	INS.R	association	2.39	24
Right calcarine cortex	CAL.R	primary	2.07	27
Right inferior parietal lobule	IPL.R	association	2.46	28
Right precuneus	PCUN.R	association	2.53	33
Right putamen	PUT.R	subcortical	2.13	29
Left thalamus	THA.L	subcortical	2.61	28

This table lists the hub regions ($b_i > 2$) in the network of older group. Regions in bold show increased normalized betweenness (b_i) in older group compared with younger group (see Table 7). k_i denotes the the degree of region i. Note that these results were acquired from the brain networks with a sparsity of 16 %

Table 6 Regions showing high betweenness ($b_i > 2$) in the network of younger group

Regions	Abbreviations	Class	b_i	Degree, k_i
Left inferior frontal gyrus (triangular)	IFGtriang.L	association	3.14	22
Left supplementary motor area	SMA.L	association	2.28	18
Right superior frontal gyrus (medial)	SFGmed.R	association	4.38	27
Right posterior cingulate gyrus	PCG.R	paralimbic	2.02	12
Left hippocampus	HIP.L	paralimbic	3.67	24
Right amygdala	AMYG.R	paralimbic	2.54	22
Left calcarine cortex	CAL.L	subcortical	2.42	29
Left heschl gyrus	HES.L	association	3.33	32
Right heschl gyrus	HES.R	association	2.03	23
Right inferior temporal gyrus	ITG.R	association	2.58	26

This table lists the hub regions ($b_i > 2$) in the network of younger group. Regions in bold show decreased normalized betweenness (b_i) in older group compared with younger group (see Table 7). k_i denotes the degree of the region i. Note that these results were acquired from the brain networks with a sparsity of 16 %

in Table 7) and decreased betweenness centrality in 4 regions (SFGmed.R, HIP.L, AMYG.R, HES.L, listed in Table 7). Additional statistical analysis reveals significant differences ($p < 0.05$) in betweenness centrality of these regions. The changed nodal characteristics (Δb_i) of each region are also showed in Fig. 14 (upper panel). Together, our findings suggest that the roles of regions in managing information are profoundly affected by age [47].

Table 7 Regions showing significant changes in normalized betweenness (b_i) between two groups

Regions	Abbreviations	Normalized betweenness, b_i		Δb_i
		Old group	Young group	
Increased b_i in old group				
Left orbitofrontal cortex (middle)	ORBmid.L	**3.84**	0.47	+3.37
Right orbitofrontal cortex (middle)	ORBmid.R	**4.27**	0.20	+4.07
Right insula	INS.R	**2.39**	0.33	+2.06
Decreased b_i in old group				
Right superior frontal gyrus (medial)	SFGmed.R	0.55	**4.38**	−3.83
Left hippocampus	HIP.L	0.99	**3.67**	−2.68
Right amygdala	AMYG.R	0.39	**2.54**	−2.15
Left heschl gyrus	HES.L	0.72	**3.33**	−2.61

This table shows regions with changes in normalized betweenness (b_i) between two groups. Normalized betweenness (b_i) in bold indicate the betweenness centrality of the hub regions which are also showed in Tables 5 and 6

2.2.6 Reduced Network Robustness in Older Subjects

Figure 14 shows the network robustness of two age groups under the targeted attack and random failures. Both groups reveal similar network robustness to the random failures (Fig. 14). When the nodes were randomly removed, the sizes of the largest connected component in both groups reduced steadily and approximately (Fig. 14, left). Although network robustness of both groups reduced sharply due to the removing of 20 central nodes from $NO.21$ to $NO.40$, the younger network displayed remarkably stability against targeted attack compared with the older (Fig. 14, right). In addition, the statistical significant differences ($p < 0.05$) of two groups are only found in the targeted-attack procedure. The specific ranges are $23 < NO_{.node} < 35$ and $40 < NO_{.node} < 45$.

2.2.7 Small-World Parameters in Smaller-Sample Networks

Figure 15 shows the methodological robustness, in response to the decrease of samples size in both age groups. In the smaller sample networks, small-world characteristics are also revealed according to $\delta > 1$ (red lines) shown in Fig. 15a, b. Simultaneously, larger local efficiency (Fig. 15c) and lower global efficiency (Fig. 15d) in older group are found in smaller sample networks. Additional statistical analysis reveals significant differences ($p < 0.05$) in the C_p values at all range ($10\,\% < S < 50\,\%$), and E_{global} values at $11\,\% < S < 23\,\%$. These findings of two groups are compatible with the former results in the original networks.

2.3 Discussion

The current study, for the first time, demonstrates age-related changes in the topological organization of large-scale functional brain networks by utilizing PET data. Our main results are as follows: (1) that the observed data demonstrate age-related alterations in functional correlations among selective subsets of regions, (2) that the global topological organization of functional networks in older subjects are disrupted as indicated by altered small-world parameters, (3) that the regional nodal characteristic (centrality) is changed in older subjects, (4) that the functional network of older group shows reduced network robustness in response to the targeted attack, (5) that the methods to construct the functional PET networks demonstrate reasonable robustness.

2.3.1 Small-World Characteristics and Age-Related Changes

Our findings of high global and local efficiency in functional brain networks with both age groups are consistent with some previous studies [45, 55, 67, 86, 87]. Especially, another PET study [67], which compared the properties of whole-brain functional networks of normal, mild cognitive impairment (MCI) and AD individuals by using FDG-PET data, has reported that brain functional PET networks of all show small-world property. Experimental studies [88] and computational modeling simulations approaches [84] have also proposed the emergence of smallworld topology when networks evolved for high complexity of dynamic behavior defined as an optimal balance between global integration and local specialization [89]. Thus, Our findings provide additional support for the hypothesis that the human brain has evolved to maximize the cost efficiency of parallel information processing [84, 85].

We also find age-related changes of global and local efficiency (Figs. 9, 10 and 11) in the functional networks. The network may develop into a more local and less distributed organization, in the normal processes of brain senescence. This phenomenon suggests a degeneration process with normal aging, been proposed that in comparison to small-world networks, the lattice-like networks have a slow signal propagation speed and synchronizability [89]. Many psychiatric and neurological disorders described as dysconnectivity syndromes are associated with the regular topological organization that disturbs the optimal balance of a small-world network [90]. Previous studies have proposed the regular topological organization of brain networks in patients with diseases such as AD or schizophrenia [56, 86]. These convergent evidences from methodologically disparate studies suggest that both AD and schizophrenia are related to abnormal topological organization of structural and functional brain networks [45]. Therefore, our finding about the degeneration process shows that normal aging has high risk for dysconnectivity syndromes.

In particular, the above results in functional brain networks are conformed to a previous study about structural brain networks [54], which the middle group (mean age = 51 years) shows higher values in the global efficiency and lower values difference

in the local efficiency compared with the old group (mean age = 68 years). These evidences may suggest that age-related alterations in cortical functional networks can be related to structural deficits. Honey et al. [91] have found that the spontaneous neuronal which has been reported in some previous studies [45, 76]. It has dynamics can be structured at multiple temporal scales, proposing a tight association between functional and structural networks. Thus, it could be speculated that the age-related alterations in functional networks shown here are likely to be caused by structural impairments.

2.3.2 Betweenness Centrality and Age-Related Alterations

In a complex system, node betweenness represents an crucial metric which can be used to determine the relative importance of a node with a network and identify the pivotal nodes in the network [92]. As indicated above (see Results), 12 and 10 global hub regions (see Tables 5, 6 and Fig. 13) are identified in the older and younger respectively. These hub regions are mainly considered as recently evolved association and primitive limbic regions. It has been proven in the previous study that association regions contribute to the integrity of multiple functional systems, such as memory and attention systems, and are mainly involved in intelligent processing and maintenance of the senior spiritual activity [93]. Meanwhile, limbic regions which are highly interconnected with the prefrontal regions and subcortical regions, are closely related to emotion and a conscious state of mind [93]. Previous studies have reported that identified global hubs were mainly prefrontal and parietal regions, supplying a potential explanation for their well-documented activation by many cognitive functions [45]. In this study, the frontal and parietal regions are also considered as hub regions, especially in older group (see Tables 5 and 6). Furthermore, although the identified global hubs vary among two age groups, most of these regions are found to show high node betweenness in the functional and structural human brain networks [75, 88, 94, 95, 95]. In addition, it is noted that the substantial discrepancies of identified global hubs between this study and the previous studies can be caused by the different neuroimaging modalities, subjects characteristics and computational methods.

Age-related alterations of hub regions (e.g., SFG and HIP) are also found in this study (see Table 5 and Fig. 14). The most of these identified hub regions are association cortices regions (6/7 out of 10/12) in both age groups. This result is consistent with a previous study that association cortices regions tend to be hubs of the brain functional network regardless of age [55]. From younger group to older group, association cortices show significant changed node betweenness (see Tables 5, 6 and 7). These results support the view that age-related changes are characteristic of association cortex as opposed to primary cortex [96]. We find significant changes in node betweenness with decreasing and increasing in normal aging. This result is also similar to the finding by a previous study which indicated both negative and positive age effects on the regional efficiency in cortical regions [97]. Our finding is also consistent with a previous study that the ageing is associated with significantly reduced

nodal efficiency in the frontal neocortex [55]. Above results suggest that frontal which manage movement (see Tables 5 and 6) plays important roles in contacting information of both groups, but the importance of hippocampus closely related to mental activity is reduced in the older group, indicating the relative degradation of the aged mental activities. The similar findings have been reported in previous studies [96, 98, 99]. Overall, our finding demonstrates age-related changes in the nodal ability to manage information flow of PET networks.

In addition, PET investigations have revealed that the precuneus/posterior cingulate cortex and the medial prefrontal cortex, previously shown to be part of the DMN, display an elevated level of metabolic activity [100]. This result is consistent with our study that some elevated regions in DMN are the hubs (e.g. PCG.R, PCUN.R) which show nodal ability to manage the whole-brain PET network. Furthermore, a former study [58] has reported that magnitude of DMN co-activation in some regions (e.g. HIP.L and SFGmed.R) decreases with normal aging. In this study, these regions also show decreased centrality in older group. Hence, our whole-brain PET networks reveal similar regional characteristics to the previous DMN studies.

2.3.3 Topological Vulnerability in Functional Networks in Older Group

It has been demonstrated that small-world brain networks with embedded hubs exhibit surprising resilience to random failures and targeted attacks [75, 81]. Assuming that dynamic behavior of a network is strongly related to its fundamental configuration, it seems reasonable to suppose that the changes in network parameters reflect the disruptions in the general performance of the network such as stability and robustness. This hypothesis is supported by our results that the networks in older group are significantly vulnerable to targeted attacks on its pivotal nodes (hub regions) compared with younger group. The reduced topological stability is associated with senescent functional organization in older group such as smallworld architecture, and nodal centrality shown previously. Moreover, former studies have reported the vulnerable topological organization of brain structural cortical networks in patients with AD [57]. Thus, this evidence from our study suggests that normal senescence has risk for AD.

2.3.4 Methodology

In this study, we constructed large-scale human brain functional networks via PET data. It is reasonable to conclude that cerebral glucose metabolism from PET data represent the regional functional activity [10, 11]. Effective connectivity between PET regions has also been revealed in previous studies about investigating brain functional systems [65, 66].

According to results about methodological robustness, the similar small-world parameters (see Fig. 15) are obtained in responses to the decrease of the sample size. Small-world properties in both groups (Fig. 15a, b), reduced global efficiency

(Fig. 15d) and increased local efficiency (Fig. 15d) in older group are also found. Thus, it is reasonable to consider that this method demonstrates sufficiently reliable. While this study was a cross-sectional study, a longitudinal analysis would also be useful to investigate the changes of functional brain networks with normal aging. In future studies of functional brain network development, younger individuals are expected to be involved in farther experiments.

2.4 Conclusion

As mentioned above, by using PET data with graph theory analysis, this study demonstrates age-related changes in the topological organization of large-scale functional brain networks constructed via a robust method. These results indicate that normal senescence has a notable effect on the topological organization of functional brain networks. Our findings are also compatible with previous studies about the small-world properties, hub regions and network robustness of brain functional and structural networks, thus enhancing our understanding of the underlying physiology of normal aging in human brain.

Appendix

See Table 8

Table 8 Regions of interest included in AAL-atlas

Labels	Regions	Regions	Abbreviations
1	Precentral_L	Precental gyrus	PreCG.L
2	Precentral-R	Precental gyrus	PreCG.R
3	Frontal_L	Superior frontal gyrus, dorsolateral	SFGdor.L
4	Frontal_R	Superior frontal gyrus, orbital part	ORBsup.L
5	Frontal_Sup_Orb_L	Superior frontal gyrus, orbital part	ORBsup.L
6	Frontal_Sup_Orb_R	Superior frontal gyrus, orbital part	ORBsup.R
7	Frontal_Mid_L	Middle frontal gyrus	MFG.L
8	Frontal_Mid_R	Middle frontal gyrus	MFG.R
9	Frontal_Mid_Orb_L	Middle frontal gyrus, orbital part	ORBmid.L

(continued)

Table 8 (continued)

10	Frontal_Mid_Orb_R	Middle frontal gyrus, orbital part	ORBmid.R
11	FrontalJnf_Oper_L	Inferior frontal gyrus, opercular part	TFGoperc.L
12	FrontalJnf_Oper_R	Inferior frontal gyrus, opercular part	TFGoperc.R
13	Frontal Tnf Tri L	Inferior frontal gyrus, triangular part	TFGtriang.L
14	FrontalJnf_Tri_R	Inferior frontal gyrus, triangular part	TFGtriang.r
15	FrontalJnf_Orb_L	Inferior frontal gyrus, orbital part	ORBinf.L
16	FrontalJnf_Orb_R	Inferior frontal gyrus, orbital part	ORBinf.R
17	Rolandic_Oper_L	Rolandic operculum	ROL.L
18	Rolandic_Oper_R	Rolandic operculum	ROL.R
19	Supp_Motor_Area_L	Supplementary motor area	SMA.L
20	Supp_Motor_Area_R	Supplementary motor area	SMA.R
21	Olfactory _L	Olfactory cortex	OLF.L
22	Olfactory _R	Olfactory cortex	OLF.R
23	FrontaLSup_Medial_L	Superior frontal gyrus, medial	SFGmed.L
24	FrontaLSup-Medial-R	Superior frontal gyrus, medial	SFGmed.R
25	Frontal_Mid_Orb_L	Superior frontal gyrus, medial orbital	ORBsupmed.L
26	Frontal_Mid_Orb_R	Superior frontal gyrus, medial orbital	ORBsupmed.R
27	Rectus_L	Gyrus rectus	REC.L
28	Rectus_R	Gyrus rectus	REC.R
29	Insula_L	Insula	TNS.L
30	Tnsula_R	Insula	TNS.R
31	Cingulum_Ant_L	Anterior cingulate and paracingulate gyri	ACG.L
32	Cingulum_Ant_R	Anterior cingulate and paracingulate gyri	ACG.R
33	Cingulum_Mid_L	Median cingulate and paracingulate gyri	DCG.L
34	Cingulum_Mid_R	Median cingulate and paracingulate gyri	DCG.R

(continued)

Table 8 (continued)

Labels	Regions	Regions	Abbreviations
35	Cingulum_Post_L	Posterior cingulate gyrus	PCG.L
36	Cingulum_Post_R	Posterior cingulate gyrus	PCG.R
37	Hippocampus_L	Hippocampus	HTP.L
38	Hippocampus_R	Hippocampus	HTP.R
39	ParaHippocampal_L	ParaHippocampal gyrus	PHG.L
40	ParaHippocampal_R	ParaHippocampal gyrus	PHG.R
41	Amygdala_L	Amygdala	AMYG.L
42	Amygdala_R	Amygdala	AMYG.R
43	Calcarine_L	Calcarine fissure and surrounding cortex	CAL.L
44	Calcarine_R	Calcarine fissure and surrounding cortex	CAL.R
45	Cuneus_L	Cuneus	CUN.L
46	Cuneus_R	Cuneus	CUN.R
47	Lingual_L	Lingual gyrus	LING.L
48	Lingual_R	Lingual gyrus	LING.R
49	Occipital_Sup_L	Superior occipital gyrus	SOG.L
50	Occipital_Sup_R	Superior occipital gyrus	SOG.R
51	Occipital_Mid_L	Middle occipital gyrus	MOG.L
52	Occipital_Mid_R	Middle occipital gyrus	MOG.R
53	OccipitalJnf_L	Inferior occipital gyrus	IOG.L
54	OccipitalJnf_R	Inferior occipital gyrus	IOG.R
55	Fusiform_L	Fusiform gyrus	FFG.L
56	Fusiform_R	Fusiform gyrus	FFG.R
57	Postcentral_L	Postcentral gyrus	PoCG.L
58	PostcentraLR	Postcentral gyrus	PoCG.R
59	Parietal_Sup_L	Superior parietal gyrus	SPG.L
60	Parietal_Sup_R	Superior parietal gyrus	SPG.R
61	ParietalJnf_L	Inferior parietal, but supramarginal and angular gyri	IPL.L
62	Parietal_Inf_R	Inferior parietal, but supramarginal and angular gyri	IPL.R
63	SupraMarginal_L	SupraMarginal gyrus	SMG.L
64	SupraMarginal_R	SupraMarginal gyrus	SMG.R

(continued)

Table 8 (continued)

65	Angular_L	Angular gyrus	ANG.L
66	Angular_R	Angular gyrus	ANG.R
67	Precuneus_L	Precuneus	PCUN.L
68	Precuneus_R	Precuneus	PCUN.R
69	Paracentral_Lobule_L	Paracentral lobule	PCL.L
70	Paracentral_Lobule_R	Paracentral lobule	PCL.R
71	Caudate_L	Caudate nucleus	CAU.L
72	Caudate_R	Caudate nucleus	CAU.R
73	Putamen_L	Lenticular nucleus, putamen	PUT.L
74	Putamen_R	Lenticular nucleus, putamen	PUT.R
75	Pallidum_L	Lenticular nucleus, pallidum	PAL.L
76	Pallidum_R	Lenticular nucleus, pallidum	PAL.R
77	Thalamus_L	Thalamus	THA.L
78	Thalamus_R	Thalamus	THA.R
79	Heschl_L	Heschl gyrus	HES.L
80	HeschLR	Heschl gyrus	HES.R
81	Temporal_Sup_L	Superior temporal gyrus	STG.L
82	Temporal_Sup_R	Superior temporal gyrus	STG.R
83	Temporal_Pole_Sup_L	Temporal pole: superior temporal gyrus	TPOsup.L
84	Temporal_Pole_Sup_R	Temporal pole: superior temporal gyrus	TPOsup.R
85	Temporal_Mid_L	Middle temporal gyrus	MTG.L
86	Temporal_Mid_R	Middle temporal gyrus	MTG.R
87	Temporal_Pole JMid_L	Temporal pole: middle temporal gyrus	TPOmid.L
88	Temporal_Pole_Mid_R	Temporal pole: middle temporal gyrus	TPOmid.R
89	Temporal_Inf_L	Inferior temporal gyrus	ITG.L
90	Temporal_Inf_R	Inferior temporal gyrus	ITG.R

References

1. Chiappe, P., Siegel, L., Hasher, L.: Working memory, inhibition and reading skill. In: Shohov, S. (ed.) Advances in Psychology Research, pp. 30–51. Nova Science Publishers Inc., New York (2002)
2. Gur, R.C., Mozley, L.H., Mozley, P.D., Resnick, S.M., Karp, J.S., Alavi, A., Arnold, S.E., Gur., R.E.: Sex-differences in regional cerebral glucose-metabolism during a resting state. Science **267**, 528–531 (1995)
3. Madden, D.J., Turkington, T.G., Provenzale, J.M., Denny, L.L., Hawk, T.C., Gottlob, L.R., Coleman, R.E.: Adult age differences in the functional neuroanatomy of verbal recognition memory. Hum. Brain Mapp. **7**, 115–135 (1999)
4. Mattay, V.S., Fera, F., Tessitore, A., Hariri, A.R., Das, S., Callicott, J.H., Weinberger, D.R.: Neurophysiological correlates of age-related changes in human motor function. Neurology **58**, 630–635 (2002)
5. Miller, E., Li, L., Desimone, R.: Activity of neurons in anterior inferior temporal cortex during a short-term memory task. J. Neurosci. **13**, 1460–1478 (1993)
6. Pardo, J., Lee, J., Sheikh, S., Surerus-Johnson, C., Shah, H., Munch, K., Carlis, J., Lewis, S., Kuskowski, M., Dyskenb, M.: Where the brain grows old: decline in anterior cingulate and medial prefrontal function with normal aging. NeuroImage **35**, 1231–1237 (2007)
7. Parkin, A.J., Walter, B.M.: Recollective experience, normal aging, and frontal dysfunction. Psychol. Aging **7**, 290–298 (1992)
8. van Veen, V., Krug, M.K., Schooler, J.W., Carter, C.S.: Neural activity predicts attitude change in cognitive dissonance. Nat. Neurosci. **12**, 1469–1474 (2009)
9. Geinisman, Y., Detoledo-Morrell, L., Morrell, F., Heller, R.E.: Hippocampal markers of age-related memory dysfunction: behavioral, electrophysiological and morphological perspective. Prog. Neurobiol. **45**, 223–252 (1995)
10. Petit-Taboué, M.C., Landeau, B., Desson, J.F., Desgranges, B., Baron, J.C.: Effects of healthy aging on the regional cerebral metabolic rate of glucose assessed with statistical parametric mapping. NeuroImage **7**, 176–184 (1998)
11. Phelps, M.E., Huang, S.C., Hoffman, E.J., Selin, C., Sokoloff, L., Kuhl, D.E.: Tomographic measurement of local cerebral glucose metabolic rate in humans with (F-18) 2-fluoro-2-deoxy-D-glucose: validation of method. Ann. Neurol. **6**, 371–388 (1979)
12. Herholz, K., Salmon, E., Perani, D., Baron, J.-C., Holthoff, V., Frölich, L., Schönknecht, P., Ito, K., Mielke, R., Kalbe, E., Zündorf, G., Delbeuck, X., Pelati, O., Anchisi, D., Fazio, F., Kerrouche, N., Desgranges, B., Eustache, F., Beuthien-Baumann, B., Menzel, C., Schröder, J., Kato, T., Arahata, Y., Henze, M., Heiss, W-D.: NeuroImage **17**, 302–316 (2002)
13. Kalpouzos, G., Chételat, G., Baron, J., Landeau, B., Mevel, K., Godeaub, C., Barré, L., Constans, J., Viader, F., Eustache, F., Desgranges, B.: Voxel-based mapping of brain gray matter volume and glucose metabolism profiles in normal aging. Neurobiol. Aging **5**, 1–13 (2007)
14. Moeller, J.R., Ishikawa, T., Dhawan, V., Spetsieris, P., Mandel, F., Alexander, G.E., Grady, C., Pietrini, P., Eidelberg, D.: The metabolic topography of normal aging. J. Cereb. Blood Flow Metab. **16**, 385–398 (1996)
15. Willis, M.W., Ketter, T.A., Kimbrell, T.A., George, M.S., Herscovitch, P., Danielson, A.L., Benson, B.E., Post, R.M.: Age, sex and laterality effects on cerebral glucose metabolism in healthy adults. Psychiatry Res. **114**, 23–37 (2002)
16. Ernst, M., Zametkin, A.J., Phillips, R.L., Cohen, R.M.: Age-related changes in brain glucose metabolism ia adults with attention-deficit/hyperactivity disorder and control subjects. J. Neuropsychiatry Clin. Neurosci. **10**, 168–177 (1998)
17. Murphy, D.G.M., DeCarli, C., McIntosh, A.R., Daly, E., Mentis, M.J., Pietrini, P., Szczepanik, J., Schapiro, M.B., Grady, C.L., Horwitz, B., Rapoport, S.I.: Sex differences in human brain morphometry and metabolism: an in vivo quantitative magnetic resonance imaging and positron emission tomography study on the effect of aging. Arch. Gen. Psychiatry **53**, 585–594 (1996)

18. de Leon, M.J., George, A.E., Tomanelli, J., Christman, D., Kluger, A., Miller, J., Ferris, S.H., Fowler, J., Brodie, J.D., van Gelder, P., Klinger, A., Wolf, A.P.: Positron emission tomography studies of normalaging: a replication of PET III and 18-FDG using PET VI and 11-CDG. Neurobiol. Aging **8**, 319–323 (1987)
19. Kushner, M., Tobin, M., Alavi, A., Chawluk, J., Rosen, M., Fazekas, F., Alavi, J., Reivich, M.: Cerebellar glucose consumption in normal and pathologic states using fluorine-FDG and PET. J. Nucl. Med. **28**, 1667–1670 (1987)
20. Schlageter, N.L., Horwitz, B., Creasey, H., Carson, R., Duara, R., Berg, G.W., Rapoport, S.I.: Relation of measured brain glucose utilisation and cerebral atrophy in man. J. Neurol. Neurosurg. Psychiatry **50**, 779–785 (1987)
21. Yoshii, F., Barker, W.W., Chang, J.Y., Loewenstein, D., Apicella, A., Smith, D., Boothe, T., Ginsberg, M.D., Pascal, S., Duara, R.: Sensitivity of cerebral glucose metabolism to age, gender, brain volume, brain atrophy, and cerebrovascular risk factors. J. Cereb. Blood Flow Metab. **8**, 654–661 (1988)
22. Salmon, E., Maquet, P., Sadzot, B., Degueldre, C., Lemaire, C., Franck, G.: Decrease of frontal metabolism demonstrated by positron emission tomography in a population of healthy elderly volunteers. Acta Neurol. Belg. **91**, 288–295 (1991)
23. Wang, G.J., Volkow, N.D., Wolf, A.P., Brodie, J.D., Hitzemann, R.J.: Intersubject variability of brain glucose metabolic measurements in young normal males. J. Nucl. Med. **35**, 1457–1466 (1994)
24. Raz, N., Torres, I.J., Acker, J.D.: Age, gender, and hemispheric-differences in human striatum—a quantitative review and new data from in-vivo MRI morphometry. Neurobiol. Learn. Mem. **63**, 133–142 (1995)
25. Kumar, A., Braun, A., Schapiro, M., Grady, C., Carson, R., Herscovitch, P.: Cerebral glucose metabolic rates after 30 and 45 minute acquisitions: a comparative study. J. Nucl. Med. **33**, 2103–2105 (1992)
26. Brooks, R.A.: Alternative formula for glucose utilization using labeled deoxyglucose. J. Nucl. Med. **23**, 538–539 (1982)
27. Ibanez, V., Pietrini, P., Furey, M.L., Alexander, G.E., Millet, P., Bokde, A.L., Teichberg, D., Schapiro, M.B., Horwitz, B., Rapoport, S.I.: Resting state brain glucose metabolism is not reduced in normotensive healthy men during aging, after correction for brain atrophy. Brain Res. Bull. **63**, 147–154 (2004)
28. Yanase, D., Matsunari, I., Yajima, K., Chen, W., Fujikawa, A., Nishimura, S., Matsuda, H., Yamada, M.: Brain FDG PET study of normal aging in Japanese: effect of atrophy correction. Eur. J. Nucl. Med. Mol. Imaging **32**, 794–805 (2005)
29. Sowell, E.R., Peterson, B.S., Thompson, P.M., Welcome, S.E., Henkenius, A.L., Toga, A.W.: Mapping cortical change across the human life span. Nat. Neurosci. **6**, 309–315 (2003)
30. Salat, D.H., Buckner, R.L., Snyder, A.Z., Greve, D.N., Desikan, R.S., Busa, E., Morris, J.C., Dale, A.M., Fischl, B.: Thinning of the cerebral cortex in aging. Cereb. Cortex **14**, 721–730 (2004)
31. Hazlett, E.A., Buchsbaum, M.S., Mohs, R.C., Spiegel-Cohen, J., Wei, T.C., Azueta, R., Haznedar, M.M., Singer, M.B., Shihabuddin, L., Luu-Hsia, C., Harvey, P.D.: Age-related shift in brain region activity during successful memory performance. Neurobiol. Aging **19**, 437–445 (1998)
32. Posner, M.I., Rothbart, M.K.: Attention, self-regulation and consciousness. Philos. Trans. R. Soc. Lond. B Biol. Sci. **353**, 1915–1927 (1998)
33. Gur, R.C., Gunning-Dixon, F.M., Turetsky, B.I., Bilker, W.B., Gur, R.E.: Brain region and sex differences in age association with brain volume—a quantitative MRI study of healthy young adults. Am. J. Geriatr. Psychiatry **10**, 72–80 (2002)
34. Cabeza, R.: Hemispheric asymmetry reduction in older adults: the HAROLD model. Psychol. Aging. **17**, 85–100 (2002)
35. Cabeza, R., Anderson, N.D., Locantore, J.K., McIntosh, A.R.: Aging gracefully: compensatory brain activity in high-performing older adults. NeuroImage **17**, 1394–1402 (2002)

36. Grady, C.L., Bernstein, L.J., Beig, S., Siegenthaler, A.L.: The effects of encoding strategy on age-related changes in the functional neuroanatomy of face memory. Psychol. Aging **17**, 7–23 (2002)
37. Reuter-Lorenz, P.A., Jonides, J., Smith, E.S., Hartley, A., Miller, A., Marshuetz, C., Koeppe, R.A.: Age differences in the frontal lateralization of verbal and spatial working memory revealed by PET. J. Cogn. Neurosci. **12**, 174–187 (2000)
38. Kawachi, T., Ishii, K., Sakamoto, S., Matsu, M., Mori, T., Sasaki, M.: Gender differences in cerebral glucose metabolism: a PET study. J. Neurol. Sci. **199**, 79–83 (2002)
39. Scarmeas, N., Zarahn, E., Anderson, K.E., Hilton, J., Flynn, J., Van Heertum, R.L., Sackeim, H.A., Stern, Y.: Cognitive reserve modulates functional brain responses during memory tasks: a PET study in healthy young and elderly subjects. NeuroImage **19**, 1215–1227 (2003)
40. Rasgon, N.L., Small, G.W., Siddarth, P., Miller, K., Ercoli, L.M., Bookheimer, S.Y., Lavretsky, H., Huang, S.C., Barrio, J.R., Phelps, M.E.: Estrogen use and brain metabolic change in older adults. Psychiatry Res. **107**, 11–18 (2001)
41. Chiappe, P., Siegel, L.S., Hasher, L.: Working memory, inhibitory control, and reading disability. Mem Cogn. **28**, 8–17 (2000)
42. Aine, C.J., Sanfratello, L., Adair, J.C., Knoefel, J.E., Caprihan, A., Stephen, J.M.: Development and decline of memory functions in normal, pathological and healthy successful aging. Brain Topogr. **24**, 323–339 (2011)
43. McKhann, G., Drachman, D., Folstein, M., Katzman, R., Price, D., Stadlan, E.M.: Clinical diagnosis of Alzheimer's disease report of the nincdsadrda work group under the auspices of department of health and human services task force on Alzheimer's disease. Neurology **34**, 939–939 (1984)
44. Hughes, A.J., Daniel, S.E., Kilford, L., Lees, A.J.: Accuracy of clinical diagnosis of idiopathic parkinson's disease: a clinico-pathological study of 100 cases. J. Neurol. **55**, 181–184 (1992)
45. Bullmore, E., Sporns, O.: Complex brain networks: graph theoretical analysis of structural and functional systems. Nat. Rev. Neurosci. **10**, 186–198 (2009)
46. Bassett, D.S., Bullmore, E.T.: Human brain networks in health and disease. Curr. Opin. Neurol. **22**, 340–347 (2009)
47. Meunier, D., Achard, S., Morcom, A., Bullmore, E.: Age-related changes in modular organization of human brain functional networks. Neuroimage **44**, 715–723 (2009)
48. Micheloyannis, S., Vourkas, M., Tsirka, V., Karakonstantaki, E., Kanatsouli, K., Stam, C.J.: The influence of ageing on complex brain networks: a graph theoretical analysis. Hum. Brain Mapp. **30**, 200–208 (2009)
49. Sun, J., Tong, S., Yang, G.Y.: Reorganization of brain networks in aging and age-related diseases. Aging Dis. **3**, 181–193 (2012)
50. Watts, D., Strogatz, S.: Collective dynamics of small-world networks. Nature **393**, 440–442 (1998)
51. Latora, V., Marchiori, M.: Efficient behavior of small-world networks. Phys. Rev. Lett. **87**, 198701-1–198701-4 (2001)
52. Supekar, K., Musen, M., Menon, V.: Development of large-scale functional brain networks in children. PLoS Biol. **7**, e1000157 (2009)
53. Fair, D.A., Cohen, A.L., Power, J.D., Dosenbach, N.U., Church, J.A., Miezin, F.M., Schlaggar, B.L., Petersen, S.E.: Functional brain networks develop from a local to distributed organization. PLoS Comput. Biol. **5**, e1000381 (2009)
54. Wu, K., Taki, Y., Sato, K., Kinomura, S., Goto, R., Okada, K., Kawashima, R., He, Y., Evans, A.C., Fukuda, H.: Agerelated changes in topological organization of structural brain networks in healthy individuals. Hum. Brain Mapp. **33**, 552–568 (2012)
55. Achard, S., Bullmore, E.: Efficiency and cost of economical brain functional networks. PLoS Comput. Biol. **3**, e17 (2007)
56. Stam, C., Jones, B., Nolte, G., Breakspear, M., Scheltens, P.: Small-world networks and functional connectivity in Alzheimer's disease. Cereb. Cortex **17**, 92–99 (2007)
57. He, Y., Chen, Z., Evans, A., Breakspear, M., Scheltens, P.: Structural insights into aberrant topological patterns of large-scale cortical networks in Alzheimer's disease. J. Neurosci. **28**, 4756–4766 (2008)

58. Koch, W., Teipel, S., Mueller, S., Buerger, K., Bokde, A.L., Hampel, H., Coates, U., Reiser, M., Meindl, T.: Effects of aging on default mode network activity in resting state fMRI: does the method of analysis matter? Neuroimage **51**, 280–287 (2010)
59. Damoiseaux, J.S., Beckmann, C.F., Arigita, E.J., Barkhof, F., Scheltens, P., Stam, C.J., Smith, S.M., Rombouts, S.A.: Reduced resting-state brain activity in the default network in normal aging. Cereb. Cortex **18**, 1856–1864 (2008)
60. Fair, D.A., Cohen, A.L., Dosenbach, N.U., Church, J.A., Miezin, F.M., Barch, D.M., Raichle, M.E., Petersen, S.E., Schlaggar, B.L.: The maturing architecture of the brains default network. Proc. Natl. Acad. Sci. USA **105**, 4028–4032 (2008)
61. Bluhm, R.L., Osuch, E.A., Lanius, R.A., Boksman, K., Neufeld, R.W., Théberge, J., Williamson, P.: Default mode network connectivity: effects of age, sex, and analytic approach. Neuroreport **19**, 887–891 (2008)
62. Binder, J.R., Frost, J.A., Hammeke, T.A., Bellgowan, P.S., Rao, S.M., Cox, R.W.: Default mode network connectivity: effects of age, sex, and analytic approach. J. Cogn. Neurosci. **11**, 80–93 (1999)
63. Shulman, G.L., Corbetta, M., Buckner, R.L., Raichle, M.E., Fiez, J.A., Miezin, F.M., Petersen, S.E.: Top-down modulation of early sensory cortex. Cereb. Cortex **7**, 193–206 (1997)
64. Genovese, C., Lazar, N., Nichols, T.: Thresholding of statistical maps in functional neuroimaging using the false discovery rate. Neuroimage **48**, 870–878 (2002)
65. Horwitz, B., Tagamets, M., McIntosh, A.R.: Neural modeling, functional brain imaging, and cognition. Trends Cogn. Sci. **3**, 91–98 (1999)
66. Ferrarelli, F., Haraldsson, H.M., Barnhart, T.E., Roberts, A.D., Oakes, T.R., Massimini, M., Stone, C.K., Kalin, N.H., Tononi, G.: A [^{17}F]-fluoromethane PET/TMS study of effective connectivity. Brain Res. Bull. **64**, 10–113 (2004)
67. Seo, E.H., Lee, D.Y., Lee, J.M., Park, J.S., Sohn, B.K., Lee, D.S., Choe, Y.M., Woo, J.I.: Whole-brain functional networks in cognitively normal. PLOS One **8**, e53922 (2013)
68. Gavrilescu, M., Shaw, M.E., Stuart, G.W., Eckersley, P., Svalbe, I.D., Egan, G.F.: Simulation of the effects of global normalization procedures in functional MRI. Neuroimage **17**, 532–542 (2002)
69. Dukart, J., Mueller, K., Horstmann, A., Vogt, B., Frisch, S., Barthel, H., Becker, G., Möller, H.E., Villringer, A., Sabri, O., Schroeter, M.L.: Differential effects of global and cerebellar normalization on detection and differentiation of dementia in FDG-PET studies. Neuroimage **49**, 1490–1495 (2010)
70. Tzourio-Mazoyer, N., Landeau, B., Papathanassiou, D., Crivello, F., Etard, O., Delcroix, N., Mazoyer, B., Joliot, M.: Automated anatomical labeling of activations in SPM using a macroscopic anatomical parcellation of the MNI MRI single-subject brain. Neuroimage **15**, 273–289 (2002)
71. Worsley, K., Chen, J., Lerch, J., Evans, A.: Comparing functional connectivity via thresholding correlations and singular value decomposition. Philos. Trans. R. Soc. Lond. B Biol. Sci. **360**, 913–920 (2005)
72. Lerch, J.P., Worsley, K., Shaw, W.P., Greenstein, D.K., Lenroot, R.K., Giedd, J., Evans, A.C.: Mapping anatomical correlations across cerebral cortex (MACACC) using cortical thickness from MRI. Neuroimage **31**, 993–1003 (2006)
73. Liu, Y., Liang, M., Zhou, Y., He, Y., Hao, Y., Song, M., Yu, C., Liu, H., Liu, Z., Jiang, T.: Disrupted small-world networks in schizophrenia. Brain **131**, 945–961 (2008)
74. Humphries, M., Gurney, K., Prescott, T.: The brainstem reticular formation is a small-world, not scale-free, network. Proc. Biol. Sci. **273**, 503–511 (2006)
75. Achard, S., Salvador, R., Whitcher, B., Suckling, J., Bullmore, E.: A resilient, low-frequency, small-world human brain functional network with highly connected association cortical hubs. J. Neurosci. **26**, 63–72 (2006)
76. Sporns, O., Chialvo, D.R., Kaiser, M., Hilgetag, C.C.: Organization, development and function of complex brain networks. Trends Cogn. Sci. **8**, 418–425 (2004)
77. Maslov, S., Sneppen, K.: Specificity and stability in topology of protein networks. Science **296**, 910–913 (2002)

78. Milo, R., Shen-Orr, S., Itzkovitz, S., Kashtan, N., Chklovskii, D., Alon, U.: Network motifs: simple building blocks of complex networks. Science **298**, 824–827 (2002)
79. Freeman, L.: A set of measures of centrality based on betweenness. Sociometry **44**, 35–41 (1977)
80. Albert, R., Jeong, H., Barabási, A.L.: Error and attack tolerance of complex networks. Nature **406**, 378–382 (2000)
81. Kaiser, M., Hilgetag, C.: Edge vulnerability in neural and metabolic networks. Biol. Cybern. **90**, 311–317 (2004)
82. Cohen, J., Cohen, P., West, S.G., Aiken, L.S.: Applied Multiple Regression/Correlation Analysis for the Behavioral Sciences, 3rd edn. Routledge, New York (2013)
83. Bassett, D., Bullmore, E.: Small-world brain networks. Neuroscientist **12**, 512–523 (2006)
84. Sporns, O., Tononi, G., Edelman, G.: Theoretical neuroanatomy: relating anatomical and functional connectivity in graphs and cortical connection matrices. Cereb. Cortex. **10**, 127–141 (2000)
85. Kaiser, M., Hilgetag, C.: Nonoptimal component placement, but short processing paths, due to long-distance projections in neural systems. PLoS Comput. Biol. **2**, e95 (2006)
86. Bassett, D.S., Bullmore, E., Verchinski, B.A., Mattay, V.S., Weinberger, D.R., Meyer-Lindenberg, A.: Hierarchical organization of human cortical networks in health and schizophrenia. J. Neurosci. **28**, 9239–9248 (2008)
87. Wang, L., Zhu, C., He, Y., Zang, Y., Cao, Q., Zhang, H., Zhong, Q., Wang, Y.: Altered small-world brain functional networks in children with attentiondeficit-hyperactivity disorder. Hum. Brain Mapp. **30**, 638–649 (2009)
88. Chen, Z.J., He, Y., Rosa-Neto, P., Germann, J., Evans, A.C.: Revealing modular architecture of human brain structural networks by using cortical thickness from MRI. Cereb. Cortex **18**, 2374–2381 (2008)
89. Strogatz, S.H.: Exploring complex networks. Nature **410**, 268–276 (2001)
90. Catani, M., Ffytche, D.H.: The rises and falls of disconnection syndromes. Brain **128**, 2224–2239 (2005)
91. Honey, C.J., Kötter, R., Breakspear, M., Sporns, O.: Network structure of cerebral cortex shapes functional connectivity on multiple time scales. Proc. Natl. Acad. Sci. USA **104**, 10240–10245 (2007)
92. Wang, X.F., Chen, G.: Complex networks: small-world, scale-free and beyond. IEEE Circuits Syst. Mag. **3**, 6–20 (2003)
93. Mesulam, M.M.: From sensation to cognition. Brain **121**, 1013–1052 (1998)
94. He, Y., Dagher, A., Chen, Z., Charil, A., Zijdenbos, A., Worsley, K., Evans, A.: Impaired smallworld efficiency in structural cortical networks in multiple sclerosis associated with white matter lesion load. Brain **132**, 3366–3379 (2009)
95. Iturria-Medina, Y., Sotero, R.C., Canales-Rodríguez, E.J., Alemán-Gómez, Y., Melie-García, L.: Studying the human brain anatomical network via diffusion-weighted MRI and graph theory. Neuroimage **40**, 1064–1076 (2008)
96. Albert, M.L.: In: Knoefel, J. (ed.) Clinical Neurology Of Aging. Oxford University Press, New York (2010)
97. Gong, G., Rosa-Neto, P., Carbonell, F., Chen, Z.J., He, Y., Evans, A.C.: Age- and gender-related differences in the cortical anatomical network. J. Neurosci. **29**, 15684–15693 (2009)
98. Reijneveld, J.C., Ponten, S.C., Berendse, H.W., Stam, C.J.: The application of graph theoretical analysis to complex networks in the brain. Clin. Neurophysiol. **118**, 2317–2331 (2007)
99. Jhoo, J.H., Lee, D.Y., Choo, I.H., Seo, E.H., Oh, J.S., Lee, J.S., Lee, D.S., Kim, S.G., Youn, J.C., Kim, K.W., Woo, J.I.: Discrimination of normal aging, MCI and AD with multimodal imaging measures on the medial temporal lobe. Psychiatry Res. **183**, 237–243 (2010)
100. Raichle, M.E., MacLeod, A.M., Snyder, A.Z., Powers, W.J., Gusnard, D.A., Shulman, G.L.: A default mode of brain function. Proc. Natl. Acad. Sci. USA **98**, 676–682 (2001)

Investigation of Single- Versus Joint-Modality PET-MR Registration for 18F-Florbetapir Quantification: Application to Alzheimer's Disease

Liam Cattell, Julia A. Schnabel, Jerome Declerck and Chloe Hutton

Abstract Previous studies have demonstrated that quantification of ^{18}F-florbetapir uptake in the brain can be used to distinguish between populations of Alzheimers disease (AD) patients and healthy controls. Typically, quantification involves the calculation of standardised uptake value ratios (SUVRs), which requires registration to a template space in which regions of interest are defined. Consequently, SUVRs could be affected by the registration method used. We examine the effect of PET-based, MR-based and joint PET-MR registration on the SUVR. To achieve this, we introduce a joint-modality image-to-template registration framework that allows for variable contributions of PET and MR data to the registration process. We extend this further by proposing a method to determine the optimum combination of PET and MR information at each voxel. Following registrations of 100 subjects from the Alzheimers Disease Neuroimaging Initiative database, we show that there is a significant separation in mean SUVR between populations of AD patients and healthy controls for all registration methods. MR-only and PET-MR based methods slightly outperformed PET-only registration, however, diagnostic power was not affected by the registration method.

Keywords Registration · PET-MR · Florbetapir · SUVR

L. Cattell (✉) · J.A. Schnabel
Department of Engineering Science, Institute of Biomedical Engineering,
University of Oxford, Oxford, UK
e-mail: liam.cattell@eng.ox.ac.uk

J. Declerck · C. Hutton
Siemens Molecular Imaging, Oxford, UK

F. Gao et al. (eds.), *Computational Methods for Molecular Imaging*,
Lecture Notes in Computational Vision and Biomechanics 22,
DOI 10.1007/978-3-319-18431-9_17

1 Introduction

One of the pathologic biomarkers of Alzheimer's disease (AD) is the presence of neuritic plaques composed of the amyloid peptide, $A\beta_{42}$. To quantitatively assess the burden of $A\beta$ in an individuals brain, the ratio of cortical-to-cerebellar binding of the ^{18}F-florbetapir positron emission tomographic (PET) tracer is often used [3]. This ratio is known as the standardised uptake value ratio (SUVR). Usually, prior to SUVR calculation, the PET image is registered to a template space in which the cortical regions of interest are defined.

Although PET measures functional information, ^{18}F-florbetapir PET images contain some structural information that can be used for registration to a template. Florbetapir uptake in white matter is non-specific, and high in amyloid-positive and negative cases. However, in amyloid-positive individuals, the boundary between white matter and grey matter is lost, as specific tracer uptake occurs in grey matter (see Fig. 1).

Current methods for registration of ^{18}F-florbetapir data typically involve affinely or non-linearly registering the PET volume directly to a template [3, 5]. Nevertheless, it is widely accepted that using a structural magnetic resonance (MR) image to drive the registration is a suitable, or even preferable, alternative. It was shown that significantly different SUVRs were obtained when using a PET-based registration method and an MRI-based method with grey matter segmentation [7]. Nevertheless, the specific impact of the registration method without including grey matter segmentation has not been investigated.

If a patient has undergone both a PET scan and an MR scan, it may be beneficial to take advantage of all of the available information during the registration process. Therefore, another reasonable technique for registering the PET volume to a template space would be to use a joint-modality approach that combines information from both PET and MR.

In this work, we compare PET-based and MR-based methods for $A\beta$ quantification using non-linear registration. Furthermore, we investigate the influence of joint-modality PET-MR registration on the final SUVRs, by introducing a novel joint-modality registration framework, that allows for variable contributions of the PET and

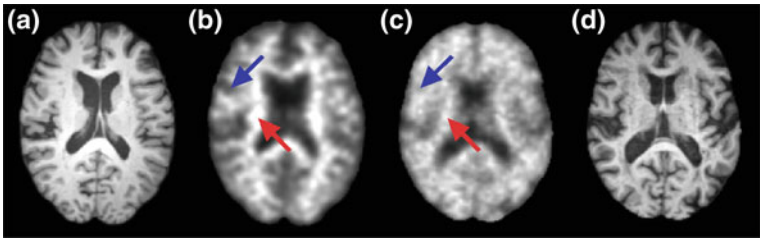

Fig. 1 An axial slice from MR and ^{18}F-florbetapir volumes of a cognitively normal individual **(a, b)** and an Alzheimer's disease patient **(c, d)**. Non-specific tracer uptake in white matter is visible in both cases (*red arrows*), but specific uptake only occurs in the grey matter of the diseased individual (*blue arrows*)

MR data during spatial normalisation to a PET-MR template space. To achieve this, we extend the log-domain local correlation coefficient (LCC) demons algorithm [6] by introducing a dual-modality cost function. Similarly to [2], the contribution of each modality to the registration process is controlled by a weighting parameter. We also extend the method to allow for a locally adaptive modality weighting (LAMW) that selects from a set of weighting factors, the best combination of PET and MR to give the maximum LCC at each voxel. Following affine and non-linear registrations, we compared cortex-to-cerebellar SUVRs of 100 subjects (50 AD, 50 healthy controls) from the Alzheimer's Disease Neuroimaging Initiative (ADNI).[1] We investigated five separate weightings of modality contributions (ranging from PET-only to MR-only), and tested our LAMW method.

The rest of this paper is structured as follows: In Sect. 2 we briefly review the log-domain LCC demons framework used for the non-linear registrations, and outline our contributions, namely the dual-modality LCC cost function and the LAMW method. In Sect. 3 we detail the dataset and template construction. Sections 4 and 5 present the experiments and results, respectively. Finally, Sect. 6 discusses the effect of PET-based versus MR-based versus joint-modality registration for Aβ quantification, and concludes this work.

2 Methods

2.1 Log-Domain Demons

The log-domain demons algorithm estimates the diffeomorphic transform between a fixed image F and a moving image M [9]. The transformation s is defined as the Lie group exponential map $s = \exp(\mathbf{v})$, where $\mathbf{v}$ is a stationary velocity field. The algorithm can be cast as the minimisation of a global energy function, consisting of a similarity criterion, used to measure the resemblance of the aligned images, and a regularisation term. In order for the optimisation to be well-posed, an auxiliary correspondence field c is introduced, to decouple the minimisation into two simple steps at each iteration.

$$E(F, M, c, s) = \frac{1}{\sigma_i^2}\mathrm{Sim}(F, M, c) + \frac{1}{\sigma_x^2}\| \log(s^{-1} \circ c)\|^2 + \frac{1}{\sigma_T^2}\mathrm{Reg}(s) \quad (1)$$

where σ_i accounts for the noise in the image, σ_x accounts for the spatial uncertainty of the correspondences, and σ_T controls the regularisation strength.

[1] http://adni.loni.ucla.edu/.

To account for locally varying intensity biases, Cachier et al. [1] proposed the local correlation coefficient (LCC) ρ as a similarity measure:

$$\rho(F, M) = \int \frac{\overline{FM}}{\sqrt{\overline{F^2} \cdot \overline{M^2}}} \tag{2}$$

where $\overline{F}$ is the local mean image of F, defined by Gaussian smoothing $\mathbf{G}_\sigma$ with a kernel size σ.

Given two images F' and M', and a symmetric formulation $F = F' \circ \exp(-\frac{\mathbf{v}}{2})$ and $M = M' \circ \exp(\frac{\mathbf{v}}{2})$, Lorenzi et al. [6] showed that optimisation of the energy function with respect to the update $\mathbf{u}$ can be computed:

$$\mathbf{u} = -\frac{2\Lambda}{\|\Lambda\|^2 - \frac{4}{\rho^2}\frac{\sigma_i^2}{\sigma_x^2}} \tag{3}$$

where

$$\Lambda = \left(\frac{\mathbf{G}_\sigma * (F\nabla M^T - M\nabla F^T)}{\mathbf{G}_\sigma * (FM)} + \frac{\mathbf{G}_\sigma * (F\nabla F^T)}{\mathbf{G}_\sigma * (F^2)} - \frac{\mathbf{G}_\sigma * (M\nabla M^T)}{\mathbf{G}_\sigma * (M^2)} \right) \tag{4}$$

2.2 Joint-Modality PET-MR LCC-Demons

Given a pair of PET and MR volumes, we extend the energy function to allow for two modalities:

$$E = -\frac{\alpha}{\sigma_{i_M}^2}\rho^2(F_M, M_M, \mathbf{u}) - \frac{(1-\alpha)}{\sigma_{i_P}^2}\rho^2(F_P, M_P, \mathbf{u}) + \frac{1}{\sigma_x^2}\|\mathbf{u}\|^2 \tag{5}$$

where α controls the contribution of each modality, and subscripts M and P denote MR and PET, respectively. Therefore, the update becomes:

$$\mathbf{u} = -\frac{2(\alpha\rho_M^2\Lambda_M + (1-\alpha)\rho_P^2\Lambda_P)}{\alpha\rho_M^2\|\Lambda_M\|^2 + (1-\alpha)\rho_P^2\|\Lambda_P\|^2 - 4\frac{\sigma_i^2}{\sigma_x^2}} \tag{6}$$

Hence, the PET-MR LCC-demons algorithm can be described by the following iterations:

2.2.1 Algorithm 1

Joint Modality PET-MR LCC-Demons Registration

- Given the current transformation $s = \exp(\mathbf{v})$, use (6) to compute update $\mathbf{u}$
- For fluid-like regularisation, regularise $\mathbf{u}$ by convolving with a Gaussian filter, such that $\mathbf{u} \leftarrow G * \mathbf{u}$
- Let $\mathbf{v} \leftarrow \mathbf{v} + \mathbf{u}$
- For diffusion-like regularisation, regularise $\mathbf{v}$ by convolving with a Gaussian filter, such that $\mathbf{v} \leftarrow G * \mathbf{v}$

2.3 Locally Adaptive Modality Weighting

Fixing the modality weighting α for all subjects and all brain regions could be improved upon by using a personalised, locally variable weighting. Therefore, we extend our proposed PET-MR registration method, by introducing an adaptive α map. Given a set of α values $\{\alpha_1, \ldots, \alpha_n\}$, the algorithm selects the best value at each voxel, resulting in a locally varying α map for each subject. This can be summarised in Algorithm 2:

2.3.1 Algorithm 2

PET-MR LCC-Demons Registration with LAMW

- For each iteration:
  - For $i = 1, \ldots, n$:
    Run one iteration of Algorithm 1 with α_i. This generates F_{Mi}, M_{Mi}, F_{Pi}, and M_{Pi}
    Compute the mean squared correlation
    $\text{MSLCC}_i = \frac{1}{2}(\rho(F_{Mi}, M_{Mi})^2 + \rho(F_{Pi}, M_{Pi})^2)$
  - Create a spatially-varying α map by selecting the α value which gives the largest MSLCC at each voxel.
  - Run one iteration of Algorithm 1 using the α map. This generates the final fixed and moving images for this iteration.

3 Materials

3.1 ADNI Data and Initialisation

T1-weighted MR and ^{18}F-florbetapir PET volumes for 110 subjects were collected from the ADNI database. In our proposed registration method we assume that PET and MR volumes of each subject are rigidly registered. Therefore prior to PET-MR registration, PET volumes were registered to their corresponding MR volume using SPM8,[2] and results were checked visually. A brain mask was then constructed from the tissue segmentations of the MR images (obtained using SPM8), and all of the images were skull-stripped. Finally, the MR volumes were rigidly registered to the nonlinear MNI152 brain template used by FSL.[3] The resulting transformations were also applied to the PET volumes.

3.2 Template Construction

An MR template was constructed iteratively from five AD brains and five healthy brains (chosen at random from the set of 110 subjects), using the method proposed in [4]. This removes the bias associated with selecting a single subject as the template. To ensure that the PET-MR registration is not influenced by any residual misregistration between the PET and MR templates, a synthetic PET template was constructed from the MR template, using weighted combinations of its tissue segmentations. The two templates are shown in Fig. 2.

4 Experiments

4.1 Affine and Non-linear Registration

The MR volumes of the 100 subjects (50 AD, 50 healthy controls) excluded from the template creation were affinely registered to the MR template using FSL's FLIRT. The resulting transformations were applied to the corresponding PET volumes. The 100 subjects then underwent PET-MR LCC-demons registrations for a range of fixed modality weightings: $\alpha = \{0, 0.25, 0.5, 0.75, 1\}$. The values $\alpha = 0$ and $\alpha = 1$ correspond to single modality PET-to-PET and MR-to-MR LCC-demons registrations, respectively. Following this experiment, the subjects were registered to the templates using the LAMW method described in Sect. 2.3. The set of combination weightings used to determine the locally optimal was $\alpha = \{0, 0.25, 0.5, 0.75, 1\}$.

[2] http://www.fil.ion.ucl.ac.uk/spm/software/spm8/.

[3] http://fsl.fmrib.ox.ac.uk/fsl/fslwiki/.

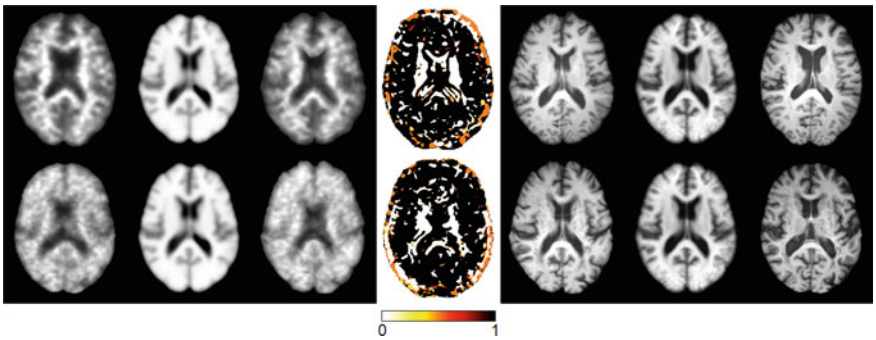

Fig. 2 An axial slice from 3D registration results using the LAMW method, for a healthy control (*top*) and an Alzheimer's disease patient (*bottom*). The columns (*left to right*) show: affine-registered PET image, pseudo-PET template, LAMW-registered PET image, α map (*white* PET-only registration updates, *black* MR-only registration updates), LAMW-registered MR image, MR template, affine-registered MR image

4.2 Standardised Uptake Value Ratio

Following the registrations, SUVRs were computed from the ratio of florbetapir retention in regions of interest (ROIs) to the cerebellum. The cortical regions we used were shown to have prominent uptake of Aβ in AD versus control [3]: anterior cingulate, posterior cingulate, parietal, temporal, precuneus and medial orbital frontal. A t-test was used to determine if there was a significant separation between the mean SUVRs of the two groups (AD and healthy control). Using the mean SUVR as a discrimination threshold, receiver operating characteristic (ROC) analyses were performed for each registration method. The areas under the curve (AUC) were calculated, in addition to the sensitivity and specificity at the SUVR threshold proposed in [3] (identifiable Aβ for SUVR > 1.08).

4.3 Dice Overlap

To quantitatively evaluate the accuracy of the registration results, the Dice overlap was computed between cortical regions in each subject's MR and the MR template [10]. To create the cortical region atlases, the MR images (in native space) were first non-linearly registered to MNI space using SPM8. Then, using the resulting inverse transformation, the Automatic Anatomic Labelling (AAL) atlas [8] was resampled into native space. Finally, any transformations applied to the MR volumes were also applied to the corresponding atlas. Paired t-tests between each registration method and every other were used to assess whether any differences in Dice overlap were statistically significant.

Table 1 Mean (standard deviation) Dice overlap of all regions over all subjects, mean SUVR, area under curve (AUC), and sensitivity and specificity at a cut-off of 1.08, by registration method: affine, PET-only ($\alpha = 0$), combined PET-MR with fixed combination weighting ($\alpha = \{0.25, 0.5, 0.75\}$), MR-only ($\alpha = 1$), and joint-modality with a locally adaptive modality weighting (LAMW)

	Affine	$\alpha = 0$	$\alpha = 0.25$	$\alpha = 0.5$	$\alpha = 0.75$	$\alpha = 1$	LAMW
Dice overlap	0.68 **(0.15)**	0.69 (0.16)	0.70 (0.16)	**0.71** (0.16)	**0.71** (0.16)	**0.71** (0.16)	0.70 (0.16)
SUVR AD	1.37 (0.29)	1.35 **(0.27)**	1.37 **(0.27)**	1.38 (0.28)	1.39 (0.29)	1.40 (0.29)	1.37 (0.28)
SUVR controls	1.07 (0.27)	1.07 **(0.24)**	1.07 (0.25)	1.08 (0.25)	1.08 (0.25)	1.08 (0.26)	1.07 (0.25)
AUC	0.77	**0.78**	**0.78**	**0.78**	**0.78**	**0.78**	**0.78**
$\text{Sensitivity}_{1.08}$ (%)	80	78	80	**82**	**82**	**82**	**82**
$\text{Specificity}_{1.08}$ (%)	68	**70**	**70**	**70**	68	68	**70**

The best results are highlighted in bold

5 Results

Table 1 presents the mean (standard deviation) Dice overlap of all regions over all subjects, mean (standard deviation) SUVR, AUC, and sensitivity and specificity at a cut-off of 1.08. For all registration methods, AD patients and controls were clearly separated by mean SUVR, which was significantly higher in AD versus control ($p < 0.01$, corrected). Following ROC analyses, all of the non-linear registration methods resulted in the same AUC, suggesting that these methods have similar overall performance with respect to classification of Alzheimer's disease versus healthy control. This is further indicated by the sensitivity and specificity at a cut-off of 1.08, which do not vary greatly between registration methods. Mean Dice values were significantly greater for non-linear registration methods compared to affine registration methods ($p < 0.05$, corrected for 21 comparisons).

Example registration results for the LAMW method, and their final spatially-varying α maps, are shown in Fig. 2. Whilst, the LAMW method only outperforms PET-to-PET registration, the spatially-varying maps in Fig. 2 suggest that the optimum combination of modalities is spatially variant.

6 Discussion and Conclusion

This work provides a first investigation into the direct effect of registration on ^{18}F-florbetapir quantification. Our results suggest that using some structural information during registration of PET volumes to a template could be beneficial, and could further inform the registration process. Our results also suggest that the optimum combination of modalities is spatially-varying, although further investigation is required to refine the estimation of the α map. We have demonstrated that non-linear

methods produce more accurate registration results, even when MR data are unavailable. Although rigid PET-to-MR registration may have influenced our results, this was not the focus of our investigation, and we therefore used a well-tested, off-the-shelf package for this step (SPM8), and checked the results visually. Regardless of the registration methods presented here, there is a significant separation between populations of AD and healthy controls. Although the absolute difference in mean SUVR differs with the registration method used, classification of Alzheimers disease patients versus cognitively normal controls based purely on SUVR is not affected by the registration method.

References

1. Cachier, P., Bardinet, E., Dormont, D., Pennec, X., Ayache, N.: Iconic feature based nonrigid registration: the PASHA algorithm. Comput. Vis. Image Underst. **89**, 272–298 (2003)
2. Cattell, L., Schnabel, J., Declerck, J., Hutton, C.: Combined PET-MR brain registration to discriminate between Alzheimer's disease and healthy controls. In: WBIR, pp.134–143 (2014)
3. Fleisher, A., Chen, K., Liu, X., Roontiva, A., Thiyyagura, P., Ayutyanont, N., Joshi, A., Clark, C., Mintun, M., Pontecorvo, M., Doraiswamy, P., Johnson, K., Skovronsky, D., Reiman, E.: Using positron emission tomography and florbetapir F18 to image cortical amyloid in patients with mild cognitive impairment or dementia due to Alzheimer disease. Arch. Neurol. **68**(11), 1404–1411 (2011)
4. Guimond, A., Meunier, J., Thirion, J.-P.: Average brain models: A convergence study. Comput. Vis. Image Underst. **77**(2), 192–210 (2000)
5. Hutton, C., Declerck, J., Mintun, M., Pontecorvo, M., Devous, M., Joshi, A.: Quantification of florbetapir F18 PET: comparison of two methods.In: Paper presented at the Annual Congress of the European Association of Nuclear Medicine (2013)
6. Lorenzi, M., Ayache, N., Frisoni, G., Pennec, X.: LCC-Demons: a robust and accurate symmetric diffeomorphic registration algorithm. NeuroImage **81**, 470–483 (2013)
7. Saint-Aubert, L., Nemmi, P., Peran, P., Barbeau, E., Payoux, P., Chollet, F., Pariente, J.: Comparison between PET template-based method and MRI-Based method for cortical quantification of florbetapir (AV-45) uptake in vivo. Eur. J. Nucl. Med. Mol. Imaging **41**(5), 836–843 (2014)
8. Tzourio-Mazoyer, N., Landeau, B., Papathanassiou, D., Crivello, F., Etard, O., Delcroix, N., Mazoyer, B., Joliot, M.: Automated anatomical labelling of activations in SPM using a macroscopic anatomical parcellation of the MNI MRI single subject brain. NeuroImage **15**(1), 273–289 (2002)
9. Vercauteren, T., Pennec, X., Perchant, A., Ayache, N.: Symmetric log-domain diffeomorphic registration: a demons-based approach. Med. Image Comput Comput-Assist Interv, 754–761 (2008)
10. Zijdenbos, A., Dawant, B., Margolin, R., Palmer, A.: Morphometric analysis of white matter lesions in MR images: method and validation. IEEE Trans. Med. Imaging **13**(4), 716–724 (1994)